The thermo-mechanical evolution of the subduction-collision systems

Alessandro Regorda

Università degli Studi di Milano
Facoltà di Scienze e Tecnologie
Dipartimento di Scienze della Terra *"Ardito Desio"*

Université Cote d'Azur
Laboratoire Géoazur

Corso di Dottorato in Scienze della Terra - Ciclo XXIX
École doctorale Sciences fondamentales et appliquées

The thermo-mechanical evolution of the subduction-collision systems

Tesi di Dottorato di Ricerca di

Alessandro Regorda

05/04/2017

Tutors
Prof. Anna Maria Marotta
Prof. Maria Iole Spalla
Prof. Jean-Marc Lardeaux

Coordinatore
Prof. Elisabetta Erba

Anno Accademico
2015/2016

Contents

List of Figures

List of Tables

Abstract

The aim of this work was to develop a 2D thermo-mechanical model to analyse in detail the effects of the shear heating and mantle wedge hydration on the thermal state and dynamics of an ocean/continent subduction system. The thermal setting and dynamics that result from models with shear heating and/or mantle hydration are directly compared to a model that does not account for either (*Marotta and Spalla*, 2007) to analyse their effects on both the strain rate and the viscosity. The new model show the activation of short-wavelength mantle convection related to the hydration and the serpentinisation of the mantle wedge, with the consequent recycling of oceanic and continental subducted material. The effects of the subduction velocities on the size of the hydrated area are also analysed, and predictions of the pressure-temperature evolutions of crustal markers and the thermal field, which affect different portions of subduction systems, are used to infer the thermal regimes that affect the models. Similarly, the model can help to understand extensively both the distribution and the evolution, in time and space, of metamorphic conditions characterised by contrasting P/T ratios in subduction systems.

In a second phase, P-T predicted by the model has been compared with natural P_{max}-T estimates related to the Variscan metamorphism, from both the present domains of the Alps and from the French Central Massif. However, the model did not allow to compare simulated P-T paths with successive metamorphic stages recorded and preserved by the rocks during their metamorphic evolution, because of the lack of exhumation of subducted material up to the shallowest portion of the crust. Then, the model has been implemented by the introduction of the atmosphere and erosion-sedimentation mechanism, to verify that a free upper boundary could allow the rising of material up to the upper continental crust. The analysis of the simulated paths suggests the possibility to have two cycles of subduction and collision involved in the evolution of the Variscan belt. The hypothesis of two successive subduction systems is in agreement with geodynamics models proposed by many authors (e.g. *Matte*, 2001; *Guillot et al.*, 2009a; *Lardeaux*, 2014a). On these results, a model characterised by two opposite subduction systems has been developed, to verify that it could represent a better evolutionary system for the reconstruction of the Variscan orogeny. Lastly, a comparison between the new model and P-T data of Variscan metamorphism has been performed.

Chapter 1

Subduction Zones

1.1 Introduction

Subduction zones are the deep and superficial expressions of Earth's 55000 km of convergent plate margins (*Stern*, 2002; *Heuret and Lallemand*, 2005), almost equal to the cumulative length of mid-ocean ridges (60000 km), and 4/5 of them are distributed around the Pacific Ocean (*Lallemand*, 1999) (Figure 1.1). The subduction of the plates is driven by the sinking of the oceanic lithosphere in the underlying asthenosphere, as a consequence of the cooling, and the relative increase of density, that occurs during the drifting from the positive thermal anomaly in the mid-ocean ridges. In fact, the subsidence of the ocean floor is proportional to the square root of the age. Mantle lithosphere is widely accepted to be slightly more dense than underlying asthenosphere by 1–2% (*Stern*, 2002). The gravitational instability of the oceanic lithosphere is determined by the cooling for conduction of the mantle in contact with the overlying oceanic crust. The sinking of the lithosphere also provides most of the forces needed to drive the plates and cause mid-ocean-ridge to spread (*Stern*, 2002).

The geometry of the subduction zones has been extensively investigated with geophysical and geochemical methods, by mean which mainly the shallower portions have been studied. Subduction zones are strongly asymmetric for the upper hundred kilometres and their geometric features are defined by deep trenches, lines of volcanoes parallel to the trenches and inclined planar arrays of deep earthquakes that extend down to the 660 km discontinuity (Wadati-Benioff zone) (*Stern*, 2002). The maximum depth of seismicity (φ) in a subduction zone can be determined as

$$\varphi = V \times A$$

where V is the subduction velocity and A the age of the subducted plate (from *Lallemand*, 1999). Deep seismicity develops between 325 and 690 km, with the highest concentration

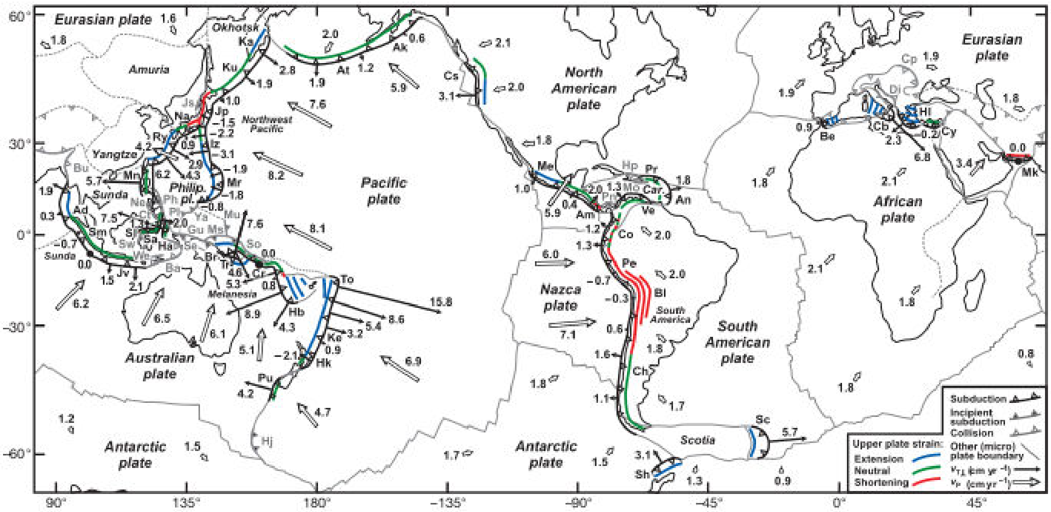

Figure 1.1: Map of the convergent margins on the Earth with the velocities of the plates (from *Schellart et al.*, 2007).

between 500 and 650 km (*Lallemand*, 1999; *Stern*, 2002). Therefore, earthquakes in subduction zones occur at enormously greater depths than elsewhere on Earth, where seismicity is limited to the uppermost 20 km.

Subduction zones represent also the principal recycling system of the Earth. The subduction of the lithosphere delivers oceanic crust and sediments deep into the mantle, where they are re-equilibrated in conditions of increasing pressure and temperature. The subducted material not recycled in the upper few hundred kilometres can either stagnate in correspondence of the transition zone at 660 km deep or sink to the core-mantle boundary (Figure 1.2, where this residue may be reheated for a billion years or so until it is resurrected as a mantle plume (*Hofmann*, 1997; *Stern*, 2002). There is a continuum from subduction, involving normal oceanic lithosphere, to collision, involving continental lithosphere (*Stern*, 2002).

Uyeda and Kanamori (1979) and *Uyeda* (1987) recognised two fundamentally contrasting subduction zones, controlled by the strength of mechanical coupling between downgoing and overriding plates:

1. Chilean-type, characterised by high seismicity at the interface between the lower and the upper plates, low dip angle of the subducted slab, bulging of the lower plate and well developed accretionary wedges (Figure 1.3a);

2. Mariana-type, characterised by extension in the upper plate with opening of back-arc basins, subsidence in correspondence of the margin, absence of the accretionary wedge and high dip angle of the subducted slab (Figure 1.3b).

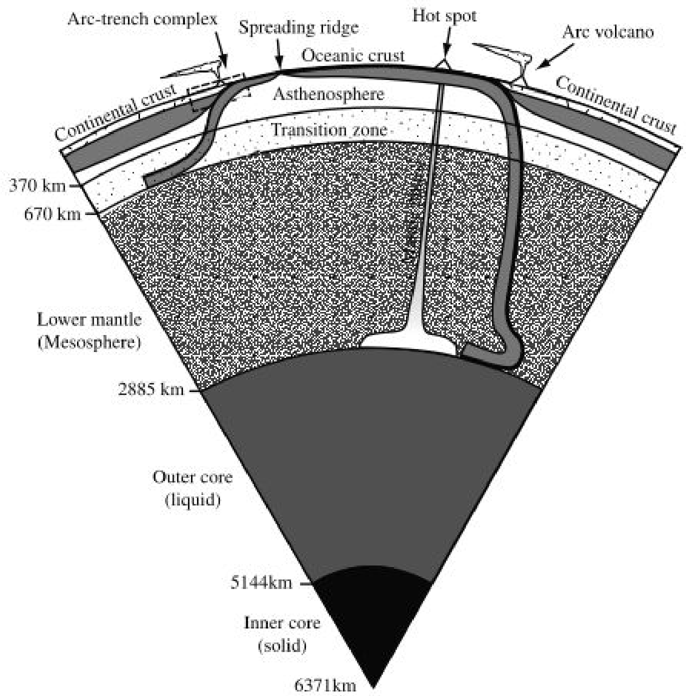

Figure 1.2: Vertical sketch of the Earth. It shows both the subducted plates stagnating at the transition zone and the subducted plates sank to the core-mantle boundary (from *Stern*, 2002).

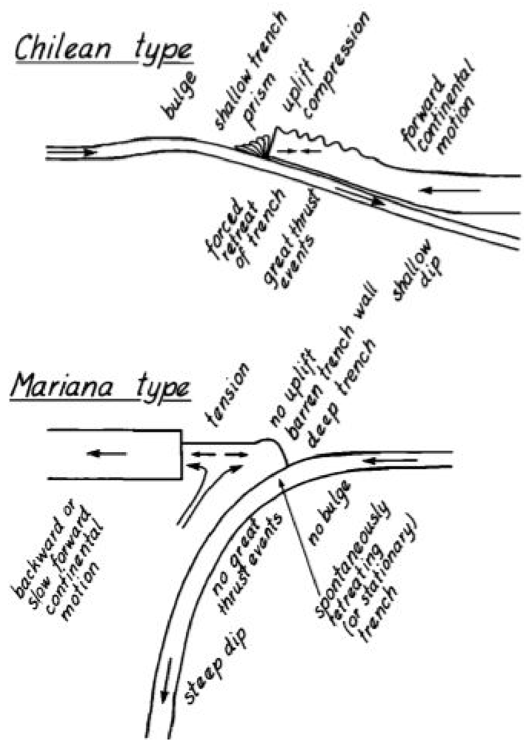

Figure 1.3: Differences between Chilean- and Mariana-type subduction (from *Uyeda and Kanamori*, 1979).

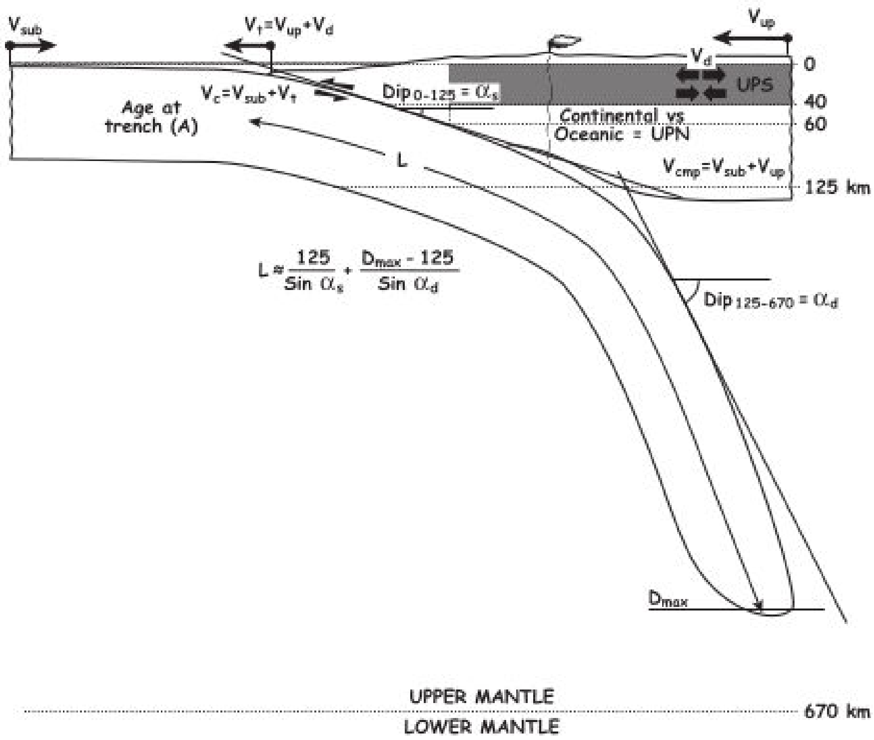

Figure 1.4: Sketch of a subduction zone. It shows the geometric features of the slab, as the length of the slab (L), maximum depth reached (D_{max}), the velocities of the plates (v_{sup}, v_{up}), the deformation (UPS) and the nature (UPN) of the upper plate (from *Lallemand et al.*, 2005).

1.2 Relations between upper and lower plate

1.2.1 Forces acting in the subduction zones

The geometry of the subducted plate can be defined by its dip angle, its length and the maximum depth reached (*Lallemand et al.*, 2005) (Figure 1.4). Usually, the dip angle of the slab increases gradually from the surface, up to a depth between 80 and 150 km. Below this depth the angle remains almost constant up to the transition zone, where it could bend (*Jarrard*, 1986; *Lallemand et al.*, 2005). Therefore, two mean dip angle can be identified (*Lallemand et al.*, 2005):

- $\alpha_s = 32° \pm 11°$, the mean dip angle of the subducted plate up to 125 km deep;
- $\alpha_d = 58° \pm 14°$, the mean dip angle of the subducted slab below 125 km deep.

The slab dip is proportional to the velocity of the upper plate, in particular for what concerns α_s. In fact, there are higher angles with the increase of the velocities, from negative values (in case of a backward movements of the plate) to positive values (in case of forward movements of the plate) (*Lallemand et al.*, 2005). A relation is also evident between the nature of the upper plate and the slab dip, with higher angles occurring

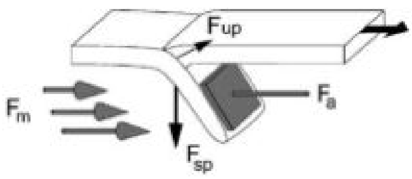

Figure 1.5: Sketch of a subduction zone showing the forces operating on the slab and at the interface between the plates: the slab pull force (F_{sp}), the slab anchoring force (F_a), the suction/pushing force (F_{up}) and the pressure force generated by mantle flow (F_m) (from *Heuret and Lallemand*, 2005).

in presence of intra-oceanic subduction. Another parameter which influences the dip angle of the subducted plate is the thermal state of the overriding plate. In particular, for colder thermal states in the upper plate there is a decreasing of the efficiency of the convective cells above the slab, with a consequent decrease of the dip angle (*Lallemand et al.*, 2005). These observations have been confirmed also by numerical models (*Roda et al.*, 2011), which have shown also a lacking of a relation between the slab dip and both the direction of the subduction and the age of the subducted plate (*Cruciani et al.*, 2005; *Lallemand et al.*, 2005; *Roda et al.*, 2011), in particular for slab with a thickness lower than 100 km (*Roda et al.*, 2011).

The kinematics of the plates and the deformation associated to the subduction zones are influenced by many forces (*Heuret and Lallemand*, 2005; *Lallemand et al.*, 2005) (Figure 1.5):

1. the slab pull, defined as the mass excess of the slab relative to the surrounding mantle (F_{sp});

2. the anchor force, defined as the viscous resistance of the mantle during the sinking of the slab as well as the forward or rearward motion of the slab (F_a);

3. the coupling between the plates along the interplate zone, which includes both the interplate friction and pressure and the bending/unbending of the slab (F_{up});

4. the regional mantle flow and the corner flow (F_m).

The combination of the forces acting in a subduction zone generates stresses in both the subducting and the overriding plates, either deforming the upper plate or determining a migration of the trench. Three models can be identified based on how these forces interact (*Heuret and Lallemand*, 2005):

1. the "upper plate motion controlled model", for which the subduction hinge is affected by upper plate motion through two kind of forces: 1) a suction/push force (F_{up}) which acts on the plate interface, making the upper plate interdependent with the subducting plate, and allowing upper plate motion to be transmitted to the top

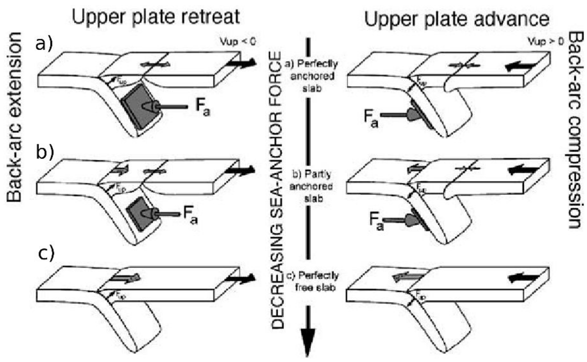

Figure 1.6: Sketch of the "upper plate motion controlled model", with $F_a \neq 0$ (a) and (b), and with $F_a = 0$ (c) (from *Heuret and Lallemand*, 2005).

of the slab; and 2) the anchoring force (F_a), which is the viscous resistance force opposed by the asthenosphere to any lateral migration of the slab and trench that may be induced by F_{up}. Then, two cases can be distinguished, for $F_a \neq 0$ and for $F_a = 0$. In the first case the migration of the trench is inversely proportional to the anchor force, and whole (Figure 1.6a) or part of the movement (Figure 1.6b) is converted into back-arc deformation: if the movement is toward the trench there is compression, otherwise there is extension, with a consequent opening of a back-arc basin. Differently, in the second case every movements of the overriding plate is transferred to the subducted plate, determining a migration of the trench without deformation inside the upper plate (Figure 1.6c);

2. the "slab rollback model", driven by the slab pull force $F_{sp} = K\Delta\rho L A^{1/2}$, where $\Delta\rho$ is the density difference between slab and mantle, L and A are the length and the age of the slab respectively, and K is a constant. The bending moment (M_b) related to this force produce a retreating of both the trench and the subducted plate (rollback), with a consequent extension in the upper plate. Therefore, this model can be associated to old and cold plates, which sink faster in the asthenosphere (Figure 1.7);

3. the "mantle flow induced model", controlled by the pressure generated by the mantle flow F_m acting normally on one side of the slab. This pressure determines a movement of the slab which causes a deformation in the back-arc of the overriding plate. The deformation can be extensive (Figure 1.8a) or compressive (Figure 1.8b), depending on the direction of the flow.

1.2.2 Accretion and tectonic erosion

The interaction between the plates is essential to understand the structural evolution, the kinematics and the exhumation of rocks inside the accretionary wedges. Two models of

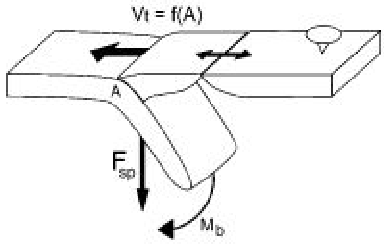

Figure 1.7: Sketch of the "slab rollback model". V_{up} is upper plate absolute motion, V_t is the trench absolute motion, F_{sp} is the slab pull force, M_b is the bending moment and A is the slab age (from *Heuret and Lallemand*, 2005).

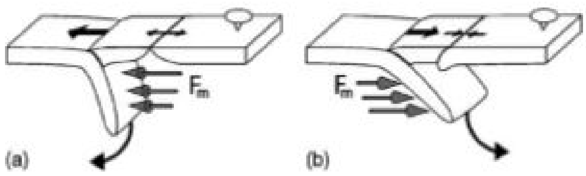

Figure 1.8: Sketch of the "mantle flow induced model". F_m is the pressure force generated by mantle flows on one side of the slab (from *Heuret and Lallemand*, 2005).

accretion of the wedge can be identified (*Malavieille*, 2010):

1. models of frontal accretion, for which can be distinguished models with high basal friction and with low basal friction. Models with high basal friction are characterised by an high taper angle and by growth through imbrication of long tectonic units bounded by low-angle thrusts (Figure 1.9a). Backthrusts are minor and develop within the body of the wedge. Wedges with a low basal friction are characterized by a low taper angle and by growth through frontal accretion of new tectonic units involving forward propagation of a basal décollement (Figure 1.9b);

2. models of basal accretion, characterised by multiple décollement. In these models two growth mechanisms act simultaneously: 1) frontal accretion above the upper décollement ("décollement 2" in Figure 1.9c), and 2) deep underplating of thrust slices, with basal accretion at the rear due to duplex formation above a basal lower detachment ("décollement 1" in Figure 1.9c). These mechanisms produce a variable taper, which is lower in the frontal part, where there is frontal accretion, and higher in the rear part, where there is basal accretion.

As the accretion act to increase the dimensions of a wedge, the tectonic erosion decrease them. Two processes of tectonic erosion can be distinguished (*Von Huene and Lallemand*, 1990):

- frontal erosion, in which the sediments are removed by the frontal margin of the wedge;

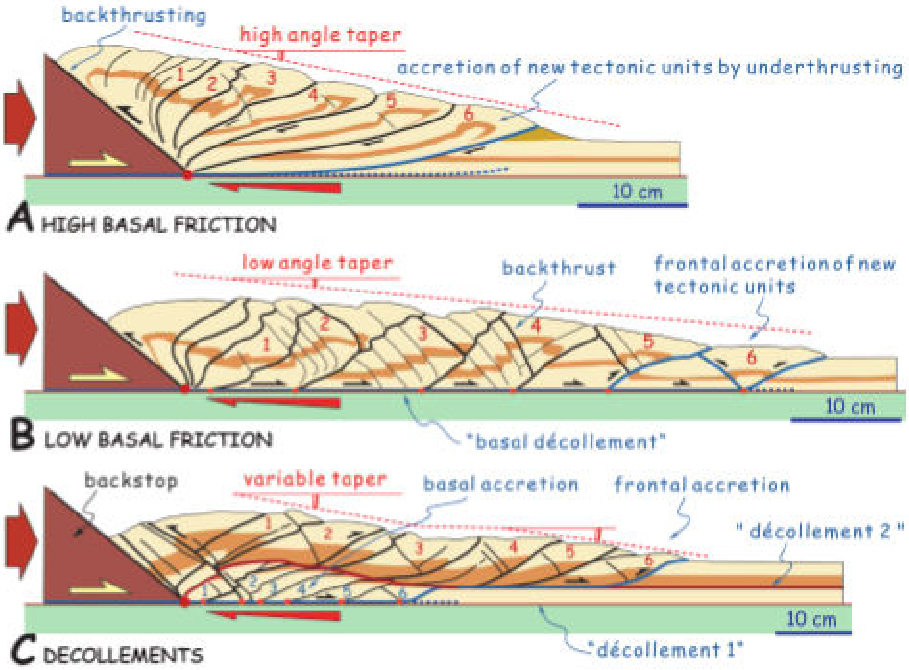

Figure 1.9: Models without erosion showing the main mechanisms of wedge accretion and the corresponding critical taper (from *Malavieille*, 2010).

- basal erosion, in which the sediments are removed by the lower and rear portion of the wedge.

Erosion margins are habitually associated to either seamount or horst and graben. In presence of horst and graben, the erosion is due to the opportunity of the graben to receive sediments, derived from the accretionary wedge, and carry them to deep. The fluids contained in the subducted sediments are released as the pressure increases, inducing overpressures in the overlying wedge and fracturing it (*Lallemand*, 1999). Bathymetric highs of the oceans can cause effects similar to those provoked by continental collision. A basaltic plateau can determine an orogenic collision only in case of bodies with an extension higher than 50x100 km and a thickened crust of at least 30 km (*Cloos*, 1993). For what concerns the seamounts, there can be collision if they are higher than 8 km, but generally they cause only temporarily deformations in the geometry of the accretionary wedge (*Cloos*, 1993; *Ruh*, 2016) (Figure 1.10). From the perspective of lithospheric buoyancy, continental or arc crust 25 km thick or more would appear to be subductable where the lithosphere is 200 km thick. However, where surface geothermal gradients are $> 25°C/km$ the part of crust deeper than 15-20 km has a temperature $> 400°C$, so, in the case that the lower crust is quartzo-feldspathic (with at least 10% free quartz), there is negligible strength and hence negligible coupling to the olivine-rich mantle. Therefore, quartzose continentals or arcs crust thicker than 15-20 km are not sufficiently coupled to their mantle roots to enable intact subduction (*Cloos*, 1993).

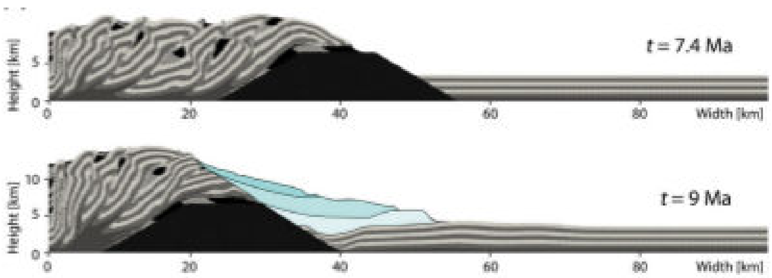

Figure 1.10: Deformation of an accretionary wedge during the passage of a seamount. Blue tones indicate landslides, rose indicates landslide detachment and blue and rose stripes indicate detachment buried by landslide (from *Ruh*, 2016).

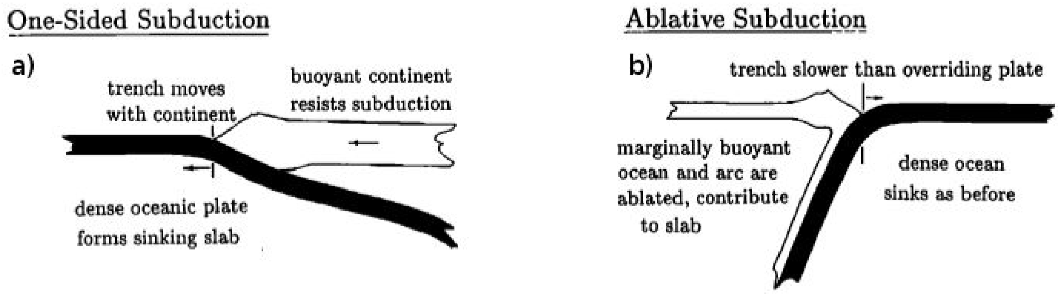

Figure 1.11: Sketches showing one-sided (a) and ablative subduction (b) (from *Tao and O'Connell*, 1992).

In addition to the one-sided subduction characterised by an accretionary wedge (Figure 1.11a), *Tao and O'Connell* (1992) proposed a model of "ablative subduction" to interpret observations concerning slab profiles, interplate seismicity, back arc tectonics, and complex processes such as double subduction and subduction polarity reversal (Figure 1.11b). In this model the slab profile results strongly influenced by ablation of the overriding plate. When ablation is weak, as when a buoyant continent borders the trench, deformable slabs adopt shallow, Chilean-type profiles. These profiles develop over time from an initially steep shape. Differently, for higher ablation rates, as might occur in an ocean-ocean convergence, slabs adopt Mariana-type profiles. Differences between Chilean- and Mariana-type subductions may result from disparities in ablation rate and subduction duration. The occurrence of ablation might not be easily detected at depth, because material from subducting and ablating plates adhere closely as a single slab (*Tao and O'Connell*, 1992).

1.3 Phase transitions

As a subducted plate descends, it is progressively heated and squeezed, changing the mineralogy and volatile content of sediments, crust, and mantle lithosphere. One of the most important transition is that of the Mg_2SiO_4's polymorphs. At $\sim$410 km depth olivine changes into β-spinel structure (wadsleyite), which at $\sim$520 km depth changes into γ-spinel structure (ringwoodite). Then, at $\sim$660 km depth there is the transition of

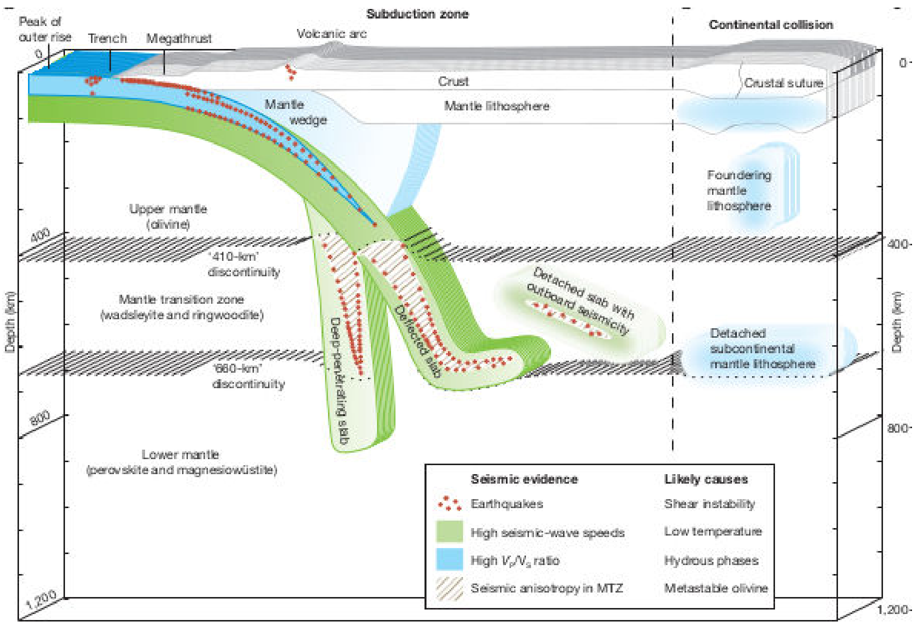

Figure 1.12: Sketches of a subduction zone showing the phases stable through the subduction zone and the behaviour of the subducted plate (from *Green et al.*, 2010).

the ringwoodite into perowskite ($MgSiO_3$) + magnesiowustite (MgO) (*Stern*, 2002; *Green et al.*, 2010). The transition olivine-wadsleyite occurs at the boundary between the upper mantle and the transition zone, while the transition ringwoodite-perowskite + magnesiowustite takes place at the boundary between the transition zone and the lower mantle (*Green et al.*, 2010) (Figure 1.12). The wadsleyite-ringwoodite transition do not causes large changes in density, while olivine-wadsleyite and ringwoodite-perowskite + magnesiowustite transitions determine a significative increase of density, of 6% and 8% respectively (*Stern*, 2002). In the subducted lithosphere the olivine-wadsleyite transition occurs shallower than 410 km, whereas the ringwoodite-perovskite + magnesiowustite occurs deeper than 660 km. This is due to the positive Clapeyron slope (dP/dT) of the olivine-wadsleyite reaction, while the slope for the ringwoodite-perovskite + magnesiowustite transition is negative. Therefore, the first transition occurs shallower in the slab than in the mantle, causing an increase of the relative density of the subducting lithosphere and favouring continued sinking. Differently, the second transition occurs deeper in the slab than in the mantle, decreasing the relative density of the slab (*Stern*, 2002).

Another important transition concerns the breakdown of the serpentine. Serpentine (antigorite, $Mg_{48}Si_{34}O_{85}(OH)_{62}$) contains 12.3 wt% H_2O and, together with chlorite (13.0 wt% H_2O), dominates the water budget of hydrous peridotite up to $\sim$150 km depth (Figure 1.13a). In peridotites serpentine forms during low-grade hydration, and its maximum temperature stability is 720°C (*Schmidt and Poli*, 1998). The phases with large contributions to the water budget of subducting MOR basalt are lawsonite, chlorite, and amphi-

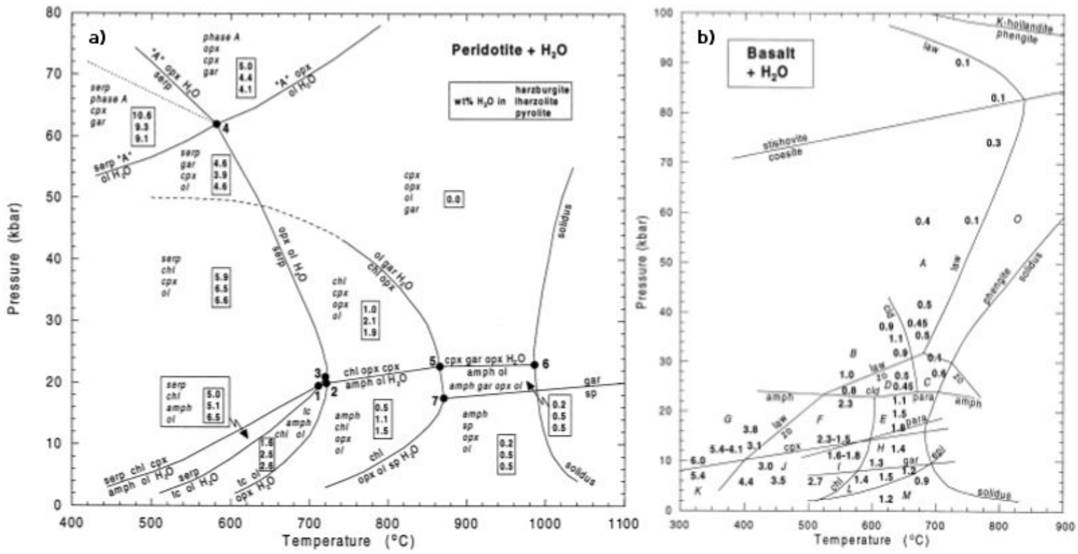

Figure 1.13: a) Phase diagram for H_2O-saturated average mantle peridotite and maximum H_2O contents bound in hydrous phases in average peridotites. Upper value: harzburgite; middle value: lherzolite; lower value: pyrolite. The italic labels are assemblages in a given stability field. b) Maximum H_2O contents bound in hydrous phases in H_2O-saturated MOR basalt. 'A' = phase A, amph = amphibole, chl = chlorite, cld = chloritoid, cpx = clinopyroxene, epi = epidote, gar = garnet, law = lawsonite, ol = olivine, opx = orthopyroxene, para = paragonite, serp = serpentine, sp = spinel, tc = talc, zo = zoisite (from *Schmidt and Poli*, 1998).

bole. Lawsonite contains 11.2 wt% H_2O, chlorite in basalt contains about 12 wt% H_2O and amphibole only contains 2.1 wt% H_2O but forms 20–60 wt% of a basalt (*Schmidt and Poli*, 1998) (Figure 1.13b).

During the descend of the slab, many different reactions involving hydrous phases modify the water contents through the transition from blueschists to dry eclogites. As antigorite can remain stable up to 8 GPa and lawsonite is stable up to 10 GPa, water is released continuously from subducted materials up to great depths, approximately 250-300 km depth (*Schmidt and Poli*, 1998; *Stern*, 2002). This has been observed also in recent numerical models, which have shown that some fluids subducted within the oceanic crust do not rise in the overlying wedge but migrate toward the underlying lithospheric mantle, with the chance to be carried to the bottom of the upper mantle (*Faccenda*, 2014).

The releasing of large amounts of fluids by the slabs consequent to the dehydration reactions can trigger earthquake and back-arc vulcanism (*Peacock*, 1990). Recent seismic studies show dip layers, associated to the slab, characterised by seismic velocities lower by 5-15% than in the mantle, usually between 40 and 150 km depth (*Abers*, 2005). Generally, they are considered hydrated metabasalts which, at high pressures, become eclogites with seismic velocities similar to those of the mantle (*Rondenay et al.*, 2008). The fluids released by the subducted slab mostly (60-90%) remain in the cold corner of the mantle wedge and a portion of this H_2O will give raise to serpentine diapirs (*Schmidt and Poli*, 1998).

The mantle wedge is the portion of the mantle above the subducted slab, where cold subducted oceanic crust and sediments come into contact with the hotter mantle. The thermal gradient produced after the cooling of the asthenosphere in contact with the slab determines the activation of convective flows in the mantle wedge. In fact, hotter mantle from the external portion of the wedge move toward the trench, taking place of the cooled mantle strongly coupled with the slab (*Stern*, 2002). The hydration of the mantle wedge, as a consequence of hydrated mineral breakdown reactions in the descending plate, determines a decrease of the viscosity of at least one order of magnitude (*Billen and Gurnis*, 2001; *Billen*, 2008). Numerical models seem to confirm that a mean viscosity of 10 19 Pa·s for the serpentinized mantle wedge could be a realistic value (*Gerya and Stockhert*, 2002; *Arcay et al.*, 2005; *Roda et al.*, 2010a). This low viscosity hydrated mantle facilitates the activation of small convective cells, favouring the exhumation of subducted oceanic and continental material at the base of the crust of the upper plate (*Honda and Saito*, 2003; *Meda et al.*, 2010; *Le Voci et al.*, 2014).

1.4 Metamorphic gradients

The study of the metamorphism has progressed from a static to a dynamic approach, as a consequence of the evolution from the use of index minerals to reconstruction of P-T-t paths to understand the metamorphic evolution. The meaning of every metamorphism classification is to describe the observed types on the Earth and to link them to the forces and the mechanisms producing them.

For the first time in 1912 Barrow identified zones characterised by index minerals, which series

$$Chl \rightarrow Bt \rightarrow Grt \rightarrow St \rightarrow Ky \rightarrow Sil$$

is called Barrowian sequence and is characterised by intermediate P/T ratios. Differently, the series

$$Chl \rightarrow And \rightarrow Sil$$

is characterised by low P/T ratios and is called Buchan.

Successively, *Eskola* (1920) introduced the concept of *metamorphic facies*, linking the mineralogic association to the metamorphic environment in terms of PT conditions. After that *Miyashiro* (1961) introduced the concept of *metamorphic facies series*, while few years later *Ernst* (1971a,b, 1973) associated different tectonics environments to the metamorphic facies.

Metamorphic series with high P/T ratios are generally associated with P-T conditions that are peculiar of active oceanic subduction (*Spear*, 1993; *Kornprobst*, 2002; *Nicollet*, 2010). This type of metamorphic facies association, which is deduced from regional scale metamorphic settings inferred by fieldwork (*Miyashiro*, 1961; *Ernst*, 1973), is referred to as either Franciscan or Sanbagawa metamorphic sequence. Barrovian or Dalradian metamorphic series, which are characterised by intermediate P/T ratios, are traditionally considered in the geological literature to have been developed during continental collisions (*England and Richardson*, 1977; *Thompson*, 1981; *England and Thompson*, 1984; *Thompson and England*, 1984; *Spear*, 1993). Metamorphic facies series that are characterised by low P/T ratios (Abukuma or Buchan-type metamorphism) have generally been associated with abnormally high geothermal gradients, such as those detected in arc regions. *Miyashiro* (1973) developed the idea of paired metamorphic belts based on the juxtaposition of orogenic crustal sections characterised by Sanbagawa- and Abukuma-type metamorphic facies series.

In case of a thermally and mechanically stable lithosphere, a "stable geotherm" can be calculated (∼25°C/km) (*Carslaw and Jaeger*, 1959; *England and Thompson*, 1984; *Thompson and England*, 1984), while in case of perturbation of the lithosphere three different geotherms can be inferred (*Cloos*, 1993) (Figure 1.14):

- a "perturbed geotherm" in correspondence of subduction, characterised by a lower thermal gradient (varying from ∼6°C/km in cold subduction to ∼10°C/km in warm subduction zone);
- a "relaxed geotherm" in correspondence of continental collision following oceanic subduction ($t \rightarrow \infty$), characterised by a higher thermal gradient consequent to the high radioactive energy due to the thickening of the crust (∼33°C/km);
- geotherms associated to spreading ridges or active arc volcanoes, characterised by very high gradients (∼60°C/km).

1.4.1 Prograde and retrograde paths

Geological units which have recorded regional metamorphism generally show a spatial variation of the metamorphic facies, in relation to the evolution of the recorded P-T conditions. Rocks that have recorded high grade metamorphic conditions should have passed through lower grade metamorphic facies, so the sequence of successive re-equilibrations makes possible to recreate the P-T path of metamorphic unit. This kind of path, characterised by an increase of the metamorphic grade in time, is called prograde gradient (*Kornprobst*, 2002). On the other hand, mineralogic association developed in P-T peak conditions can be successively re-equilibrated under different metamorphic P-T conditions. The succession of different associations in time can define a P-T path, that, usually, is associated to decrease of pressure and temperature. This type of evolution is called retrograde (*Kornprobst*, 2002). By the means of the prograde and the retrograde gradients, the geodynamic history of the metamorphic series and, then, of the P-T condition in time can be recreated. Variations of pressure depend directly by the variations of the

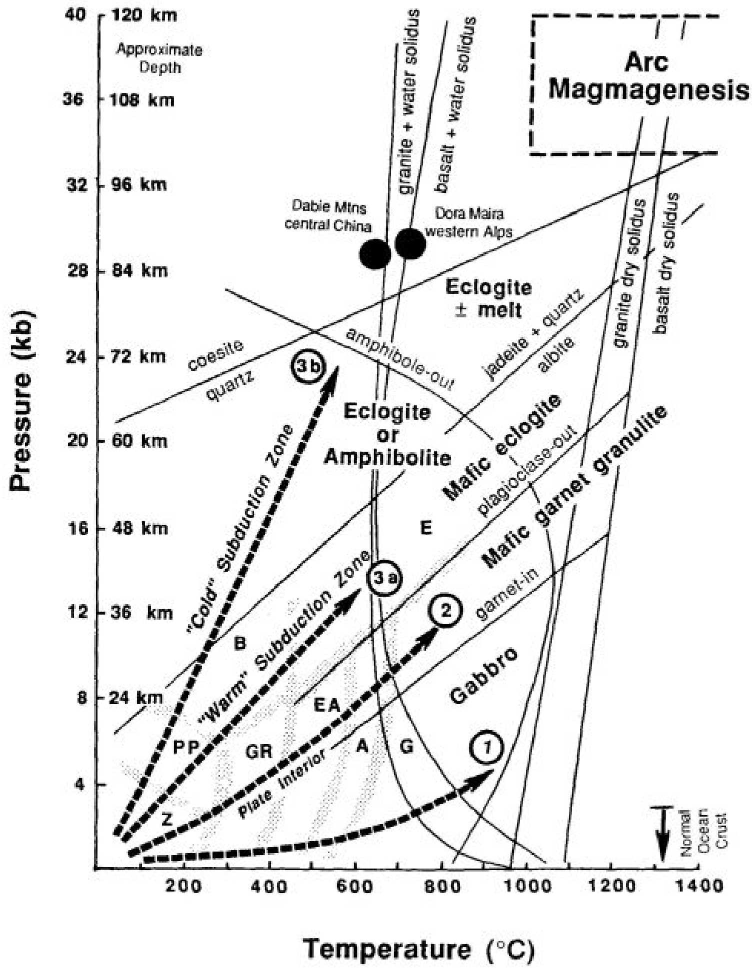

Figure 1.14: Petrogenetic grid for metamorphism and arc magma generation. Z = zeolite; PP = prehnite-pumpellyite; B = blueschist; GR = greenschist; EA = epidote-amphibolite; A = amphibolite; E = eclogite; G = granulite. Pressure-temperature trajectories are: (1) low P/T ratio near spreading ridges or active arc volcanoes; (2) normal geothermal gradients in unperturbed lithosphere; (3a) high P/T ratio in warm subduction zones; and (3b) in cold subduction zones (from *Cloos*, 1993).

depth and, consequently, they allow to determine either the burial, in case of an increase of pressure, and the exhumation, in case of a decrease of pressure. Differently, variations of temperature are more difficult to interpret, because the thermal conductivity of rocks is very low and the diffusion of heat is slower than spatial movement. *Thompson* (1981); *England and Thompson* (1984) realised a series of monodimensional models to evaluate the main factors controlling the regional metamorphism consequent to thickening or thinning of the continental lithosphere.

Generally, prograde P-T paths are characterised by an increase of pressure consequent to burial of metamorphic units. The shape of the paths mainly depends by the velocity of the burying (v) of the lithological units, as

$$v = V sin\alpha$$

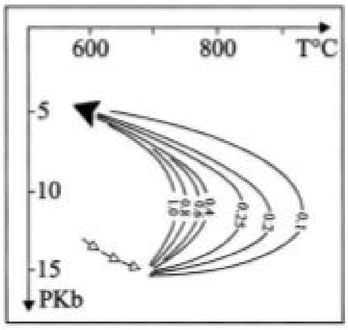

Figure 1.15: Shapes of retrograde paths in relation to the exhumation velocities (from *Kornprobst*, 2002).

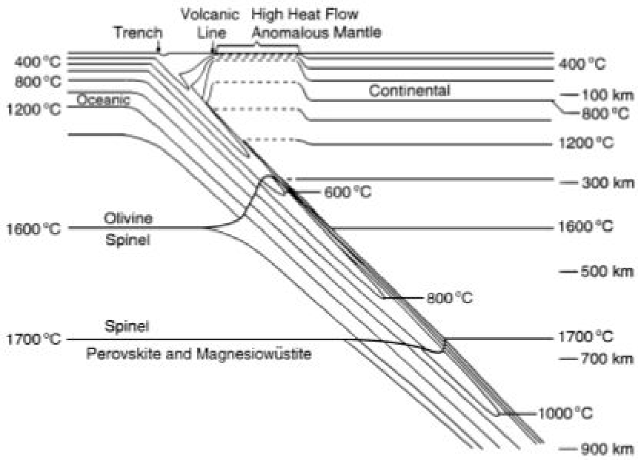

Figure 1.16: Isotherms in a typical descending lithosphere (from *Turcotte and Schubert*, 2002).

where V is the velocity of convergence and α the slab dip. Differently, retrograde paths are often associated to decompression resulting from the uplift of units. The shape of these paths is variable and it depends by the velocity of exhumation (*Kornprobst*, 2002) (Figure 1.15). Between these two partial trajectories a stage of thermal reequibration can be identified, often characterised by lacking of lithospheric motions.

The subduction of oceanic lithosphere determines a rapid burial, some cm/yr, of a plate, which undergoes a prograde path of low temperature, due to the thermal depression produced by the deepening of the isotherms (Figure 1.16). The P/T ratio varies in different portions of the subducted plate for two reasons: 1) the pressure at the bottom of the oceanic crust is higher than at the top (up to 0.2 GPa), as a consequence of its thickness, and 2) there is a warming at the top of the lithosphere, as consequence of the production of viscous heating (*Kornprobst*, 2002).

The burial of tectonic units can be also related to the thickening and the consequent thermal perturbation of either the crust or the lithosphere. For what concerns the crust, two mechanisms can be identified (*Thompson*, 1981; *England and Thompson*, 1984; *Thompson and England*, 1984):

1. crustal thickening by overthrusting. In this instance a doubling of thickness results from the emplacement of one entire crustal sequence upon another. Considering the mechanical perturbation as instantaneous (as suggested by the Peclet number), there are no thermal variations inside the units, neither above nor below the thrust (Figure 1.17a). The result is a saw tooth shape geotherm (Figure 1.17d). Then, for this model the prograde evolution is characterised only by pressure increase. After the perturbation, the first controlling mechanism is the thermal re-equilibration by conduction between the over- and underthrusted units, producing an attenuation of the saw tooth profile. During this phase, in the lower unit the temperature increases, while in the upper unit there is a decrease of temperature. After that, the controlling mechanism is the radiogenic decay, determining an increase of temperature in both units (Figure 1.17d). So, two different paths can be identified in this model: 1) for the upper unit there is not a prograde evolution and the phase of thermal re-equilibration determines a decrease of temperature. The retrograde path is characterised by an intial phase in which there is an increase of temperature associated to the beginning of the exhumation, followed by a phase characterised by a decrease of both temperature and pressure; 2) for the lower unit the prograde path is characterised by an increase of pressure with constant temperature and during the thermal re-equilibration this unit warms up. The retrograde path is similar to that observed for the upper unit.

2. homogeneous thickening of the crust, with the shortening assumed to take place instantaneously (Figure 1.17b). In this case the final geotherm has a higher slope than the initial one and in time there is a gradual warming in both the units, which brings the geotherm back at the initial slope (Figure 1.17e). During the early stages, the main mechanism for the warming is the heat flow from the mantle, while later the increase of temperature is related to the radiogenic decay. For this model the P-T paths of the two units are comparable and three phases can be distinguished: 1) a prograde path characterised by increase of pressure with a constant temperature; 2) a thermal re-equilibration that warms up both units at constant pressure; 3) a retrograde evolution characterised by an initial increase of temperature followed by a decrease of both temperature and pressure.

For what concern the homogeneous thickening of the lithosphere, with the shortening assumed to take place instantaneously (Figure 1.17c), the final geotherm has a higher slope than the initial one. As for the homogeneous thickening of the crust, in time there is a gradual warming in both the units, which brings the geotherm back at the initial slope (Figure 1.17e). In this case, the heat flow toward the crust is lower than in the case of the shortening of the only crust, because the negative thermal anomaly in the lithosphere is accentuated. This causes a less increase of temperature during the early

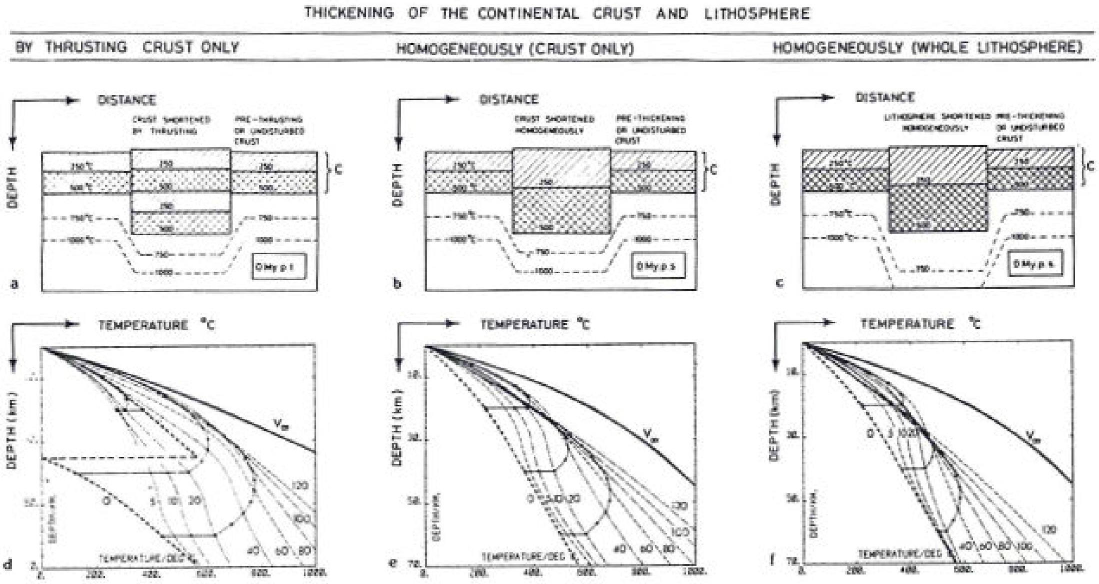

Figure 1.17: Models of thickening of the crust (panels a, b, d and e) and of the lithosphere (panels c and f). a) Thickening of the crust by thrusting; b) shortening by homogeneous thickening of the crust; c) shortening by homogeneous thickening of the lithosphere; d) evolution of the geotherms following thrusting; e) evolution of the geotherms following homogeneous thickening of the crust; f) evolution of the geotherms following homogeneous thickening of the lithosphere (from *England and Thompson*, 1984).

stages of the post-thickening evolution. For this model the P-T paths of the two units are comparable, as in the model of crust thickening, and three phases can be distinguished: 1) a prograde path characterised by an increase of pressure with a constant temperature; 2) a thermal re-equilibration that warms up both units at constant pressure; 3) a retrograde evolution characterised by an initial increase of temperature followed by a decrease of both temperature and pressure.

Uplift of tectonic units can be related to either erosion or tectonic exhumation. In the first case the exhumation is due to the crustal thickening, and the consequent formation of topographic relieves, following the continental collision. The erosion of the relieves is balanced by isostatic uplift that bring lower crust up to shallower depths. The velocity of exhumation is lower than 1 mm/yr and the retrograde path is very differents from the prograde, with the chance to have high temperatures associated to partial melting. In case of tectonic exhumation, the uplift is consequent to subduction and collision during which decoupling and overthrusting can be observed. In these environments the velocity of exhumation is higher, up to 1 cm/yr, and is associated to a lesser increase of temperature. Therefore, the shape of the retrograde path can give useful hints about the orogenic stage during which the uplift takes place (*Kornprobst*, 2002).

1.4.2 HP-LT metamorphism

Generally is difficult to determine prograde paths in units showing HP-LT metamorphic conditions because they are subjected to intense sin- and post-metamorphism deformations and only some portions can show the prograde evolution (*Kornprobst*, 2002). One example is the Zermatt-Saas unit that shows a prograde evolution from 1.5 GPa and 500°C to 2.0 GPa and 600°. This path is characterised by the following reactions observed in the metabasalts:

- clinozoisite + glaucophane → garnet + omphacite + paragonite
- clinozoisite + glaucophane + paragonite → garnet + jadeite + quartz + H_2O
- lawsonite → clinozoisite + kyanite + quartz + H_2O

These reactions indicate a prograde evolution from blueschist to the eclogite facies (*Kornprobst*, 2002).

Another example of prograde path can be observed in the Ivozio Complex metabasites, characterised by a multi-stage structural and metamorphic re-equilibration during Alpine time (*Zucali et al.*, 2004; *Zucali and Spalla*, 2011; *Delleani et al.*, 2012). In fact, a S_1 foliation developed from 0.5 GPa to 1.3 GPa at a temperature of 300-500°C and successively re-equilibrated to P < 1.8 GPa and T < 600° indicates a prograde evolution with a geothermal gradient of ∼10°C/km. The post-D_{1a} stage is characterised by the static growth of lawsonite at 520-600° and 1.8 GPa, while during post-D_{1b} stage lawsonite is replaced by omphacite + zoisite + kyanite assemblages at P > 1.5 GPa and T > 580°C. The subsequent development of the S_2 foliation occurred at decreasing pressure and temperature. S_{2a} occurred at P < 1.8 GPa and T between 500 and 600°C, while S_{2b} at P = 0.5-1.3 GPa and T = 300-500°C. The retrograde path is marked by a first temperature increase at constant or decreasing pressure, related to a geothermal gradient between 12 and 10°C/km (stages S_{2a} and S_{2b}) (*Zucali and Spalla*, 2011) (Figure 1.18).

For retrograde paths associated to exhumation of HP-LT metamorphic units, the exhumation-paragenesis overprints heterogeneously on the prograde paragenesis of high pressure and often crystallises during heterogeneous deformations, allowing to some portions not to be deformed and poorly re-equilibrated. The metamorphic evolution is in relation to the decrease of pressure due to the uplift and the retrograde P-T-t path can have different shapes related to the mechanism of exhumation.

For example in the Monviso metabasites three stages of re-equilibration, successive to the paragenesis of high pressure, can be identified and the retrograde path shows a higher temperature than the prograde path (Figure 1.19). Differently, the eclogitic metagabbro of the Voltri Massif undergoes the amphibolite facies and the greenschist facies during their exhumation path, with a significant increase of temperature than in the Monviso metabasites (*Kornprobst*, 2002) (Figure 1.19). The retrograde paths observed in the HP-LT units

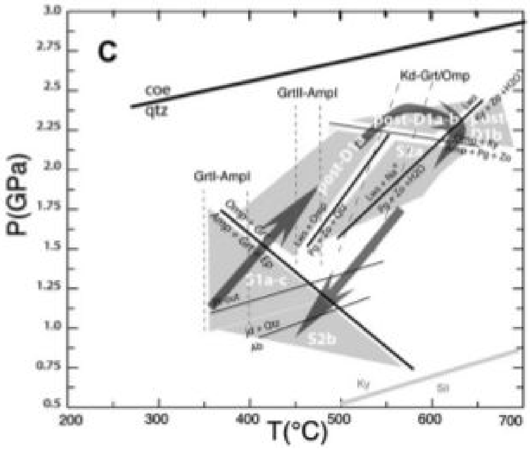

Figure 1.18: P-T-t path of the Ivozio Complex metabasites (from *Zucali and Spalla*, 2011).

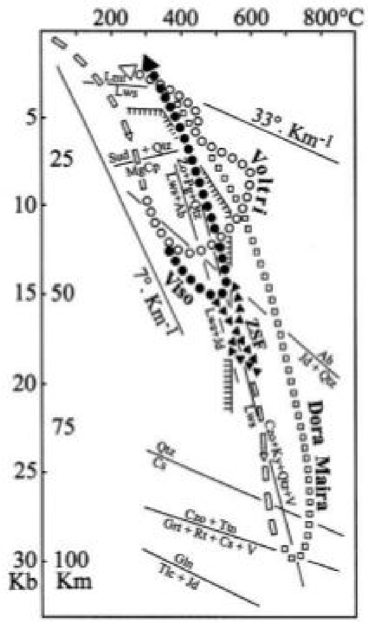

Figure 1.19: Examples of prograde and retrograde paths in the Western Alps (from *Kornprobst*, 2002).

of the Voltri massif and in the Monviso metabasites show an exhumation associated to a thermal re-equilibration with temperatures higher than the LT conditions characterising the subduction environment. The trajectory with a higher slope of the Monviso units indicates a rapid exhumation after the HP peak developed in a thermally depressed environment. Differently, the trajectory of the Voltri units indicates a slow exhumation, associated to a partial thermal re-equilibration, maybe associated to a variation of the regional thermal regime. The exhumation of these units is probably related to the crustal thickening consequent to a continental collision (*Kornprobst*, 2002).

A great discrepancy in retrograde paths can be observed also between the western and eastern parts of the French Massif Central. In all cases the retromorphosis of eclogites begins with the destabilisation of omphacite through the reaction omphacite → diopside + plagioclase, while garnet is replaced by coronas of amphibole and plagioclase. The omphacite breakdown corresponds to a discontinuous precipitation reaction giving rise to symplectitic textures. However, the microstructures related to the retrograde evolutions of the studied eclogites are different, suggesting contrasting thermal evolutions. For example, in the Najac area and in the western Limousin areas, authors have shown that temperature decreases with pressure, while in eastern Limousin or Rouergue the decompression is isothermal. Differently, in the Lyonnais area a retrograde path showing an increase of temperature at the beginning of decompression is described. In summary, in the western part of the French Massif Central, eclogites are retromorphosed under amphibolite facies conditions, while in the eastern French Massif Central they are retromorphosed under granulite facies conditions (*Mercier et al.*, 1991a; *Lardeaux*, 2014a).

1.5 Exhumation processes

Eclogites have been reported since the first petrological description by *Hauy* (1822), and recognised from many locations in the world with ages ranging from Proterozoic to Phanerozic times (e.g. *Spalla et al.*, 1996; *Godard*, 2001; *Guillot et al.*, 2009b). Different eclogite classifications were proposed (e.g *Coleman et al.*, 1965; *Banno*, 1970), in which eclogites were discriminated on the basis of their mode of occurrence, mineral and bulk compositions, and geodynamic setting (*Godard*, 2001). Following the classifications of *Coleman et al.* (1965), eclogites can be differentiated in three groups:

- Group A; eclogites of this group are included in kimberlites, basalts, or as layers in ultramafic rocks;
- Group B; eclogites of this group occur as bands or lenses within migmatite gneissic terrains;
- Group C (ophiolitic eclogites); eclogites of this group occur as bands or lenses within alpine-type metamorphic rocks.

The compositions range from olivine basalt for Group A to tholeiitic basalts for Group C (*Coleman et al.*, 1965).

The occurrences of pelitic rocks metamorphosed under eclogite facies conditions suggest that these rocks were subducted to great depths before the exhumation. The discovery of coesite in Alpine metasediments (*Chopin*, 1984; *Smith*, 1984) introduced the term of UHP metamorphism and demonstrated that continental crust can be subducted to a depth greater than 100-120 km (*Spalla et al.*, 1996; *Guillot et al.*, 2009b). The exhumation of HP and UHP rocks can occur in two contrasting types of convergent zones: the Pacific and Alpine-types (*Bally*, 1981). The Pacific-type subduction is characterized by long-lasting subduction of oceanic lithosphere, while the Alpine-type initially involves the consumption of an oceanic domain followed by the subduction of continental margins (*Bally*, 1981; *Guillot et al.*, 2009b).

Based on the the lithology, the peak P-T conditions, and the exhumation patterns of metamorphic rocks, *Guillot et al.* (2009b) proposed three major types of exhumation processes:

1. accretionary-type subduction zones, in which the exhumation of HP metasedimentary rocks is favoured by underplating. In this case the exhumation is slow and can be long-lasting;

2. the serpentinite-type subduction zones, in which the exhumation of HP to UHP takes place in a 1 to 10 km thick serpentinite subduction channel. The serpentinite matrix originates from both subducted abyssal peridotites and hydated mantle wedge. Exhumation velocity is low to intermediate and the exhumation is driven by the buoyancy and the low-viscosity of the serpentinite;

3. the continental-type subductions, in which the exhumation of UHP rocks of continental origin is fast, short-lived and occurs at the transition from oceanic subduction to continental subduction. It is driven by buoyancy forces and asthenospheric return flow. This type is similar to the Alpine-type defined by *Bally* (1981).

A subduction zone may evolve from one type to others during its life and two different types may co-exist along one subduction zone.

Accretionary-type subduction

When a slab is parallel to a buttress, deeply subducted rocks are prevented from exhumation (Figure 1.20a). Differently, a wide open wedge allows the exhumation of deeply subducted rocks that originated from the upper and lower plates. In intermediate geometries, deeply subducted rocks are exhumed close to the trench in pro-wedge exhumation (Figures 1.20b-c-d), vertically in plug uplift (Figure 1.20b) and also near the buttress in retro-wedge exhumation (Figure 1.20c) (*Guillot et al.*, 2009b; *Ernst*, 2005). The HP-LT rocks in accretionary-type subduction zones are dominated by clastic sedimentary rocks with no mantle-derived material, suggesting that the protoliths of HP-LT rocks are sediments deposited on the sea floor. The exhumation of only upper crustal rocks implies that lower crustal rocks of slabs are deeply subducted. The maximum pressures recorded in exhumed rocks vary from 0.7 to 2.0 GPa and plot along geotherms ranging between 5 and 14°C/km, which are similar to those of modern subduction zones. Several eclogites show pressures equivalent to a depth of about 75 km. This is much deeper than the maximum depth (20-40 km) observed in most active accretionary wedges. Another common feature

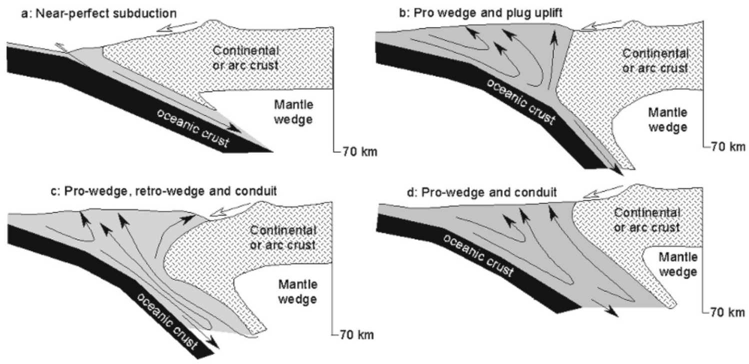

Figure 1.20: Sketch of accretionary prisms. a) Slab parallel to the buttress, which prevents the exhumation of HP rocks; b) wide accretionary wedge at shallow depth, in which rocks are exhumed only from shallow depth with pro-wedge and plug uplift exhumation; c) wide accretionary wedge at shallow depths and intermediate wedge at high depths, in which rocks can be exhumed from high depths, with pro-wedge, retro-wedge and conduit exhumation; d) wide accretionary wedge both at shallow and at deep levels, which allow the exhumation of HP rocks from great depths at front, middle and rear of the wedge (from *Guillot et al.*, 2009b).

of HP-LT rocks is slow exhumation rates ranging between 1 and 5 mm/year, which are independent of subduction velocities (*Guillot et al.*, 2009b).

Serpentinite-type subduction zones

In paleo-subduction zones, serpentinites are commonly associated with HP-LT rocks and have been considered as fragments of oceanic lithosphere. The contacts between eclogitic lenses and the matrix serpentinites are interpreted to be primary (*Coleman*, 1971; *Guillot et al.*, 2009b). HP-LT units exhumed in serpentinite-type subduction zones are dominated by highly sheared serpentinites containing weakly defomed blocks of metabasites, ranging in size from metric to decametric. The metasediments are highly deformed and minor in volume, less than 10% of the massifs. Serpentinites in oceanic subduction zones are mostly originated from abyssal peridotites and their hydration likely took place during the ridge hydrothermal. Moreover, some serpentinites can also derive from hydrated mantle wedges. Regarding the metamorphic conditions, most eclogitic blocks reached HP between 1.8 and 2.5 GPa and relatively low temperatures, which defines paleo-geothermal gradients lower than 10°C/km. The exhumation velocities vary between 3 and 10 mm/year, which are faster than those recorded in accretionary wedge environments. Also in this case the exhumation velocity remains independent of the subduction velocity (*Agard et al.*, 2009; *Guillot et al.*, 2009b).

Continental-type subductions

The discovery of diamonds (*Sobolev and Shatsky*, 1990) and coesite (*Chopin*, 1984; *Smith*, 1984) in subducted crustal rocks demonstrated that continental rocks can be subducted below 100 km of depth. The protoliths of UHP rocks are predominantly upper continental crust, such as granite gneisses, and metasedimentary rocks (quartzites, metapelites, and marbles). Mafic plutonic rocks are present in subduction zones, but they correspond to intrusions in continental crust prior to the subduction. The occurrence of gabbro and peridotite with contemporaneous gneiss suggests that these rocks were probably present in the continent-ocean transition where the lower crust is thin or totally absent (*Guillot et al.*, 2009b). Garnet peridotites are associated with continental rocks and their exhumation is explained by decoupling of the continental slice from the descending oceanic lithosphere due to the positive buoyancy of continental rocks within the subduction channel (*Ernst*, 1999). UHP rocks commonly record pressures ranging from about 2.5 GPa up to P > 7 GPa and temperatures varying between 500°C and 1335°C. However, most UHP rocks of continental origin record pressures between 2.5 and 4.0 GPa (*Hacker*, 2006), and the UHP conditions are mostly recorded in garnet-bearing peridotites. UHP metamorphism develops under low geothermal gradients, ranging from 5 to 10°C/km in most terranes. Estimated exhumation velocities in UHP rocks of continental origin are faster than 6 mm/year (*Guillot et al.*, 2009b).

Chapter 2

Numerical modelling and the *SubMar code*

The limitations of the human mind are such that it cannot grasp the behaviour of its complex surroundings and creations in one operation. Thus the process of subdividing all systems into their individual components or "elements", whose behaviour is readily understood, and then rebuilding the original system from such components to study its behaviour is a natural way in which the engineer, the scientist, or even the economist proceeds (*Zienkiewicz and Taylor*, 2000). A numerical model can be obtained by the resolution of discrete problems, such that the solution is determined dividing the system in a finite number of elements, or of continuous problems, for which problems can be solved by mathematical techniques. There are different methods of discretisation, developed by both engineers and mathematics, and all of them imply an approximation of the continuous system, which get better with the increase of the discrete variables. In particular, mathematics have developed a *finite difference method*, while engineers a *finite element method* (*Zienkiewicz and Taylor*, 2000). The *SubMar* code used in this work (*Marotta et al.*, 2006) is based on the *finite element method*.

2.1 Governing equations of the *SubMar* code

The mechanical behaviour of Earth materials which compose the crust and the mantle is described by means of the following equations:

$$\nabla \cdot \mathbf{v} = 0 \tag{2.1}$$

$$-\nabla p + \nabla \cdot \boldsymbol{\tau} + \rho\,\mathbf{g} = 0 \tag{2.2}$$

$$\rho\, c_p \left(\frac{\partial T}{\partial t} + \mathbf{v} \cdot \nabla T \right) = \nabla \cdot (K\, \nabla T) + H_r \tag{2.3}$$

which are the mass conservation equation (2.1), the momentum conservation equation (2.2) and the energy conservation equation (2.3), where ρ is the density, $\boldsymbol{\tau}$ is the deviatoric stress, c_p is the specific heat at a constant pressure, p is the pressure, T is the temperature, K is the thermal conductivity, H_r is the radiogenic energy, $\mathbf{v}$ is the velocity and $\mathbf{g}$ is gravitational acceleration. These equations are solved by using finite element method, as explained in the Section 2.2. For the entire system a Newtonian rheology has been considered, such as

$$\tau_{ij} = 2\,\mu\,\dot{\varepsilon}_{ij} \tag{2.4}$$

where $\dot{\varepsilon}_{ij} = \frac{1}{2}(\frac{\partial u_i}{\partial x_j} + \frac{\partial u_j}{x_i})$ is the infinitesimal strain rate tensor.

The momentum conservation equation is integrated using the penalty formulation (Section 2.6), while the energy conservation equation is integrated using the Petrov-Galerkin method (Section 2.3). The use of the Lagrangian particle technique (*Christensen*, 1992; *Marotta et al.*, 2006) makes it possible to compositionally differentiate the crust from the mantle. Different numeric indexes of the particles (markers) make it possible to differentiate continental-type from oceanic-type markers (*Marotta et al.*, 2006). The position of the individual markers during the dynamic evolution of the system is calculated by solving the equation

$$\frac{d\mathbf{x}}{dt} = \mathbf{u} \tag{2.5}$$

using the Runge-Kutta scheme at the first order, where $\mathbf{x}$ and $\mathbf{u}$ are the position and the velocity of each marker, respectively. These scheme has been tested by means of a benchmark (Zalesak disc test), to evaluate its accuracy (Appendix A.1). $\mathbf{u}$ is evaluated interpolating the velocities in the nodal points of the element containing the marker by the means of the shape functions used in the numerical approximation (*Marotta et al.*, 2006; *Marotta and Spalla*, 2007) (Section 2.2). Since some studies have shown that numerical instabilities can result at the interface between two fluids causing artificial mixing of the markers, a benchmark on the Rayleigh-Taylor instability test has been performed (*van Keken et al.*, 1997; *Thieulot*, 2014) (Appendix A.2).

At every time step, the composition C_e of each element of the grid is determined by the quantity of the different type of markers in the element, such as

$$C_e = C_e^c + C_e^o \qquad \text{, with} \qquad C_e^o = \frac{P_e^o}{P_e^0} \quad \text{and} \quad C_e^c = \frac{P_e^c}{P_e^0} \tag{2.6}$$

in which P_e^o and P_e^c are the numbers of the oceanic and continental markers in the element e, respectively, and P_e^0 is the maximum number of markers of every type that the element can contain. Since the dimension of the elements is not constant, P_e^0 depends on the element considered, while C_e^o and C_e^c vary between 0 and 1. Considering an incompressible fluid with a viscosity that depends on both the temperature and the composition of the

Symbol	Physical quantity	Factor
$\mathbf{x}'$	Coordinates	$\mathbf{x} \cdot \frac{1}{L_0}$
$\mathbf{u}'$	Velocity	$\mathbf{u} \cdot \frac{L_0}{\kappa_0}$
t'	Time	$t \cdot \frac{L_0^2}{\kappa_0}$
p'	Pressure	$p \cdot \frac{L_0}{\kappa_0 \mu_0}$
T'	Temperature	$\frac{T - T_0}{T_b - T_s}$
μ'	Viscosity	$\mu \cdot \frac{1}{\mu_0}$
K'	Thermal conductivity	$K \cdot \frac{1}{\rho_0 c_p \kappa_0}$
κ'	Thermal diffusivity	$\kappa \cdot \frac{1}{\kappa_0}$

Table 2.1: Dimensionless factors (from *Marotta et al.*, 2006).

element, it can be written that

$$\mu = \mu^m[1 - C^o - C^c] + \mu^o C^o + \mu^c C^c \tag{2.7}$$

where

$$\mu^i = \mu_0^i(C)\, e^{\frac{E_a^i}{nR}\left(\frac{1}{T} - \frac{1}{T_0}\right)} \tag{2.8}$$

Taking into account the elemental composition C_e (Equation 2.6), the density of each element can be expressed as

$$\rho_e = \rho_0\big[1 - \alpha(T - T_0)\big] + (\rho^o - \rho_0)C_e^o + (\rho^c - \rho_0)C_e^c \tag{2.9}$$

where ρ_0 is the reference density of the mantle at the reference temperature T_0, and ρ^o and ρ^c are the average density of the oceanic and continental crust, respectively (*Marotta et al.*, 2006). Introducing Equations 2.4 and 2.6 in the Equation 2.2, the momentum conservation equation becomes

$$\begin{aligned} -\frac{\partial \bar{p}}{\partial x} + \frac{\partial}{\partial x}\left(2\mu\frac{\partial u}{\partial x}\right) + \frac{\partial}{\partial y}\left[\mu\left(\frac{\partial u}{\partial y} + \frac{\partial v}{\partial x}\right)\right] = 0 \\ -\frac{\partial \bar{p}}{\partial y} + \frac{\partial}{\partial y}\left(2\mu\frac{\partial v}{\partial y}\right) + \frac{\partial}{\partial x}\left[\mu\left(\frac{\partial u}{\partial y} + \frac{\partial v}{\partial x}\right)\right] + \\ + \alpha\,\rho_0(T - T_0)\mathbf{g} - (\rho^o - \rho_0)C^o\mathbf{g} - (\rho^c - \rho_0)C^c\mathbf{g} = 0 \end{aligned} \tag{2.10}$$

in which x and u are the horizontal components of the coordinates and the velocities, respectively, and y and v the vertical components, and $\bar{p} = p + \rho_0\,\mathbf{g}\,y$ is the pressure which take into account both the lithostatic and the dynamic components. By the means of the factors in Table 2.1 the Equation 2.10 can be written dimensionless, as

$$
\begin{aligned}
-\frac{\partial \bar{p}'}{\partial x'} + \frac{\partial}{\partial x'}\left(2\mu'\frac{\partial u'}{\partial x'}\right) + \frac{\partial}{\partial y'}\left[\mu'\left(\frac{\partial u'}{\partial y'} + \frac{\partial v'}{\partial x'}\right)\right] = 0 \\
-\frac{\partial \bar{p}'}{\partial y'} + \frac{\partial}{\partial y'}\left(2\mu'\frac{\partial v'}{\partial y'}\right) + \frac{\partial}{\partial x'}\left[\mu'\left(\frac{\partial u'}{\partial y'} + \frac{\partial v'}{\partial x'}\right)\right] + \\
+ R_a\,\rho_0(T' - T_0') - R_c^o\,C^o - R_c^c\,C^c = 0
\end{aligned}
\tag{2.11}
$$

in which R_a, R_C^o and R_c^c are the dimensionless Rayleigh numbers with respect to the temperature and the oceanic and continental composition, respectively (*Marotta et al.*, 2006). They can be expressed as

$$R_a = \frac{\alpha\,\rho_0\,\mathbf{g}\,L_0^3}{\kappa_0\,\mu_0}(T_b - T_s) \tag{2.12}$$

with T_b and T_s are the temperatures at the bottom and at the surface of the system, respectively.

$$
\begin{cases}
R_c^o = \dfrac{\mathbf{g}\,L_0^3}{\kappa_0\,\mu_0}(\rho^o - \rho_0) \\
R_c^c = \dfrac{\mathbf{g}\,L_0^3}{\kappa_0\,\mu_0}(\rho^c - \rho_0)
\end{cases}
\tag{2.13}
$$

related to the maximum difference of density between the mantle and the oceanic and the continental crust, respectively (*Marotta et al.*, 2006).

Using the dimensionless factors listed in Table 2.1, the energy conservation equation in 2D can be written as

$$\frac{\partial T'}{\partial t'} + u'\frac{\partial T'}{\partial x'} + v'\frac{\partial T'}{\partial y'} = \frac{\partial}{\partial x'}\left(\kappa'\frac{\partial T'}{\partial x'}\right) + \frac{\partial}{\partial y'}\left(\kappa'\frac{\partial T'}{\partial y'}\right) \tag{2.14}$$

2.2 Finite element method

The developing of a finite element method can be divided in 5 stages:

1. the continuous system is divided in a finite number of "elements" with imaginary lines (2D) or surfaces (3D);

2. elements are interconnected by a discrete number of nodal point and the behaviour of each element is defined by a finite number of nodal parameters that are the variables of the problem. The elements are called *linears* if the nodal point are only at the vertexes of each element, or *quadratics* if there are nodal points also at the middle of each side. Higher-order elements can have nodal points also in the interior;

3. a set of function (*displacement functions*) is chosen to define uniquely the state of

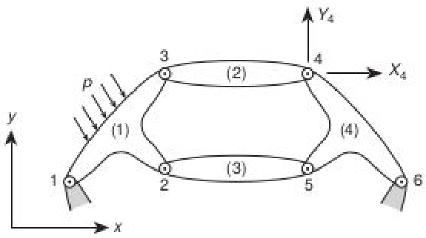

Figure 2.1: A structure built up from elements interconnected by a variable number of nodes (from *Zienkiewicz and Taylor*, 2000).

displacement within each element and on its boundaries in terms of its nodal displacements;

4. the displacement functions define uniquely the state of deformation within each element. These deformations with an eventual pre-existed deformation ε_0 and the rheological proprieties define the state of stresses of the system;

5. a system of nodal forces balancing the stresses and the distributed loading is determined, obtaining a relation as

$$\mathbf{q} = \mathbf{K} \cdot \mathbf{a} + \mathbf{f}_p + \mathbf{f}_{\varepsilon_0} \tag{2.15}$$

Stage 1

Figure 2.1 shows a two-dimensional system assembled from individual elements and interconnected by a variable number of nodes for each element. In this example there are 4 elements and the nodes are globally numbered from 1 to 6. As a starting point it will be assumed that the characteristics of each element are precisely known. The resulting of the forces acting at the nodes 1, 2 and 3 of the element labelled 1 are uniquely defined by the displacements of these nodes, the distributed loading acting on the element (p), and its possible initial strain, which may be due to temperature or shrinkage. The forces and the corresponding displacements are defined by appropriate components (U, V and u, v) in a common coordinate system (*Zienkiewicz and Taylor*, 2000).

Stage 2

Listing the forces acting on all the nodes of the element (three nodes for the element (1) in the case illustrated in Figure 2.1) as a matrix we have

$$\mathbf{q}^1 = \begin{Bmatrix} \mathbf{q}_1^1 \\ \mathbf{q}_2^1 \\ \mathbf{q}_3^1 \end{Bmatrix} \qquad \text{where} \qquad \mathbf{q}_1^1 = \begin{Bmatrix} U_1^1 \\ V_1^1 \end{Bmatrix}, \quad \mathbf{q}_2^1 = \begin{Bmatrix} U_2^1 \\ V_2^1 \end{Bmatrix}, \quad \mathbf{q}_3^1 = \begin{Bmatrix} U_3^1 \\ V_3^1 \end{Bmatrix} \tag{2.16}$$

and for the corresponding nodal displacements

$$\mathbf{a}^1 = \begin{Bmatrix} \mathbf{a}_1^1 \\ \mathbf{a}_2^1 \\ \mathbf{a}_3^1 \end{Bmatrix} \qquad \text{where} \qquad \mathbf{a}_1^1 = \begin{Bmatrix} u_1^1 \\ v_1^1 \end{Bmatrix}, \quad \mathbf{a}_2^1 = \begin{Bmatrix} u_2^1 \\ v_2^1 \end{Bmatrix}, \quad \mathbf{a}_3^1 = \begin{Bmatrix} u_3^1 \\ v_3^1 \end{Bmatrix} \tag{2.17}$$

Assuming linear elastic behaviour of the element, the characteristic relationship will be in the form

$$\mathbf{q}^1 = \mathbf{K}^1 \cdot \mathbf{a}^1 + \mathbf{f}_p^1 + \mathbf{f}_{\varepsilon_0}^1 \tag{2.18}$$

where $\mathbf{f}_{\varepsilon_0}^1$ represents the nodal forces associated to the initial deformation, $\mathbf{f}_p^1$ represents the nodal forces associated to the distributed loads and $\mathbf{K}^1 \cdot \mathbf{a}^1$ represents the nodal forces associated to nodal displacements. $\mathbf{K}$ is called *stiffness matrix*.

For a generic element *e* with *m* nodal points, the vectors of the nodal forces $\mathbf{q}^e$ and of the nodal displacements $\mathbf{a}^e$ can be represented as

$$\mathbf{q}^e = \begin{Bmatrix} \mathbf{q}_1^e \\ \mathbf{q}_2^e \\ \vdots \\ \mathbf{q}_m^e \end{Bmatrix} \qquad \text{and} \qquad \mathbf{a}^e = \begin{Bmatrix} \mathbf{a}_1^e \\ \mathbf{a}_2^e \\ \vdots \\ \mathbf{a}_m^e \end{Bmatrix} \tag{2.19}$$

with each $\mathbf{q}_i^e$ and $\mathbf{a}_i^e$ possessing the same number *n* of components (or *degrees of freedom*). Therefore, the stiffness matrices of the element will always be square and of the form

$$\mathbf{K}^e = \begin{bmatrix} \mathbf{K}_{ij}^e & \cdots & \mathbf{K}_{im}^e \\ \vdots & \ddots & \vdots \\ \mathbf{K}_{mj}^e & \cdots & \mathbf{K}_{mm}^e \end{bmatrix} \tag{2.20}$$

in which *j* is the nodal points influencing *i-esim* node.

Considering the *i-esim* node of the *e-esim* element, the Equation 2.18 can be written as

$$\mathbf{q}_i^e = \mathbf{K}_{i,1}^e \cdot \mathbf{a}_1^e + \mathbf{K}_{i,2}^e \cdot \mathbf{a}_2^e + \cdots + \mathbf{K}_{i,nnode}^e \cdot \mathbf{a}_{nnode}^e + \mathbf{f}_{p_i}^e + \mathbf{f}_{\varepsilon_{0i}}^e = \\ = \sum_{inode=1}^{nnode} \mathbf{K}_{i,inode}^e \cdot \mathbf{a}_{inode}^e + \mathbf{f}_{p_i}^e + \mathbf{f}_{\varepsilon_{0i}}^e \tag{2.21}$$

in which *nnode* is the number of nodes in the *j-esim* element. The numbering of the local nodes, or rather of each element, must follow the same criteria (for example clockwise).

If m elements have a node i in common the resulting force is

$$\mathbf{q}_i = \mathbf{q}_i^1 + \mathbf{q}_i^2 + \cdots + \mathbf{q}_i^m = \sum_{e=1}^{m} \mathbf{q}_i^e = \sum_{e=1}^{m} \left[\underbrace{\sum_{inode=1}^{nnode} \mathbf{K}_{i,inode}^e \cdot \mathbf{a}_{inode}^e}_{\text{stiffness matrix in local coordinates}} + \mathbf{f}_{p_i}^e + \mathbf{f}_{\varepsilon_0 i}^e \right] \quad (2.22)$$

The first summation can be done on all the elements (*nelem*) instead that only on the elements with the node in common (m), because only the elements which include point i will contribute non-zero forces. Considering the number of nodes of all the system (*npoin)* instead of the number of nodes of the element (*nnode*), the stiffness matrix can be written in global coordinates. Therefore, for each element the stiffness matrix has null values except for the nodes belonging to the own element, and the Equation 2.22 can be written as

$$\mathbf{q}_i = \sum_{e=1}^{nelem} \left[\underbrace{\sum_{inode=1}^{npoin} \mathbf{K}_{i,inode}^e \cdot \mathbf{a}_{inode}^e}_{\text{stiffness matrix in global coordinates}} + \mathbf{f}_i^e \right] \quad (2.23)$$

where

$$\mathbf{f}^e = \mathbf{f}_p^e + \mathbf{f}_{\varepsilon_0}^j$$

In order that the *i-esim* node is in equilibrium, the resulting of the forces $\mathbf{q}_i$ must either have a zero value or be or equal to an external force applied. Thus, considering all the force components, it is found that

$$\mathbf{r}_i = \sum_{e=1}^{nelem} \mathbf{q}_i^e \quad (2.24)$$

So, Equation 2.23 can be written as

$$\mathbf{K} \cdot \mathbf{a} = \mathbf{r} - \mathbf{f} \quad (2.25)$$

In which the submatrices are

$$\mathbf{K}_{i,inode} = \sum_{e=1}^{nelem} \mathbf{K}_{i,inode}^e \qquad \text{and} \qquad \mathbf{f}_i = \sum_{e=1}^{nelem} \mathbf{f}_i^e \quad (2.26)$$

This simple rule for assembly is very convenient because as soon as a coefficient for a particular element is found it can be put immediately into the appropriate location specified in the computer, additioning all the coefficients in that location (*Zienkiewicz and Taylor*, 2000) (Figure 2.2).

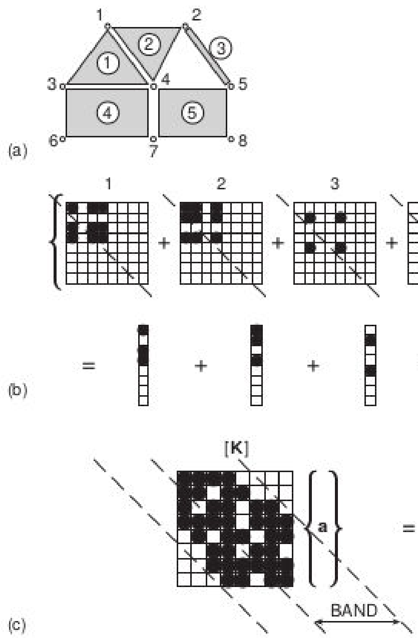

Figure 2.2: Example for the assembly of the stiffness matrix. a) System constituted by 5 elements and 8 nodes; b) construction of the stiffness matrix in global coordinates for each element; c) assembly of the stiffness matrix (from *Zienkiewicz and Taylor*, 2000).

Stage 3

The displacement $\mathbf{u}(x, y)$ in any internal point of the element can be approximated to a vector $\hat{\mathbf{u}}(x, y)$. In the instance of an element *e* constituted by 3 nodal points (*i*, *j*, *m*), it can be defined as

$$\mathbf{u}(x, y) \approx \hat{\mathbf{u}}(x, y) = \sum_k \mathbf{N}_k \cdot \mathbf{a}_k^e = \begin{bmatrix} \mathbf{N}_i & \mathbf{N}_j & \mathbf{N}_m \end{bmatrix} \cdot \begin{bmatrix} \mathbf{a}_i \\ \mathbf{a}_j \\ \mathbf{a}_m \end{bmatrix}^e = \mathbf{N} \cdot \mathbf{a}^e \tag{2.27}$$

in which **a** is the vector of the nodal displacement and **N** the vector of the displacement functions. In this way, the displacement for all points of the element is approximated as linear function of the nodal displacement. The displacement functions must be chosen to reflect the nodal displacement if the values of the coordinates are changed. For example, for the node *i*

$$\hat{\mathbf{u}}(x_i, y_i) = \sum_{i=1}^{nnode} \mathbf{N}_i \cdot \mathbf{a}_i^e = \mathbf{N}_i(x_i, y_i)\mathbf{a}_i + \mathbf{N}_j(x_i, y_i)\mathbf{a}_j + \mathbf{N}_m(x_i, y_i)\mathbf{a}_m = \mathbf{a}_i \tag{2.28}$$

from which it is deduced that $\mathbf{N}_j(x_i, y_i) = \mathbf{N}_m(x_i, y_i) = 0$ and $\mathbf{N}_i(x_i, y_i) = 1 = N_i\mathbf{I}$. The same holds for the other nodal points of the element. In all the other points inside the element $0 < \mathbf{N} < 1$.

Stage 4

With displacements known at all points within the element the strains at any point can be determined. These will always result in a relationship that, using Equation 2.28, can be written in matrix notation as

$$\boldsymbol{\varepsilon} \approx \hat{\varepsilon} = \begin{bmatrix} \varepsilon_{xx} \\ \varepsilon_{yy} \\ \varepsilon_{xy} \end{bmatrix} = \begin{bmatrix} \frac{\partial u}{\partial x} \\ \frac{\partial v}{\partial y} \\ \frac{1}{2}(\frac{\partial u}{\partial y} + \frac{\partial v}{\partial x}) \end{bmatrix} = \begin{bmatrix} \frac{\partial}{\partial x} & 0 \\ 0 & \frac{\partial}{\partial y} \\ \frac{1}{2}\frac{\partial}{\partial y} & \frac{1}{2}\frac{\partial}{\partial x} \end{bmatrix} \cdot \begin{bmatrix} u \\ v \end{bmatrix} = \mathbf{S} \cdot \mathbf{u}(x,y) = \mathbf{S} \cdot \mathbf{N} \cdot \mathbf{a} \quad (2.29)$$

The vector of the displacement **a** in the Equation 2.29 can be written as

$$\begin{bmatrix} \mathbf{u} \\ \mathbf{v} \end{bmatrix} \approx \begin{bmatrix} \hat{\mathbf{u}} \\ \hat{\mathbf{v}} \end{bmatrix} = \begin{bmatrix} N_i\mathbf{I} & N_j\mathbf{I} & N_m\mathbf{I} \end{bmatrix} \cdot \begin{bmatrix} \mathbf{a}_i \\ \mathbf{a}_j \\ \mathbf{a}_m \end{bmatrix} =$$

$$= \begin{bmatrix} N_i & 0 & N_j & 0 & N_m & 0 \\ 0 & N_i & 0 & N_j & 0 & N_m \end{bmatrix} \cdot \begin{bmatrix} u_i \\ v_i \\ u_j \\ v_j \\ u_m \\ v_m \end{bmatrix} = \begin{bmatrix} N_i u_i + N_j u_j + N_m u_m \\ N_i v_i + N_j v_j + N_m v_m \end{bmatrix} \quad (2.30)$$

and integrating the Equation 2.30 in the Equation 2.29 it is obtained that

$$\boldsymbol{\varepsilon} = \begin{bmatrix} \frac{\partial}{\partial x} & 0 \\ 0 & \frac{\partial}{\partial y} \\ \frac{1}{2}\frac{\partial}{\partial y} & \frac{1}{2}\frac{\partial}{\partial x} \end{bmatrix} \cdot \begin{bmatrix} N_i u_i + N_j u_j + N_m u_m \\ N_i v_i + N_j v_j + N_m v_m \end{bmatrix} =$$

$$= \begin{bmatrix} \frac{\partial N_i}{\partial x} u_i + \frac{\partial N_j}{\partial x} u_j + \frac{\partial N_m}{\partial x} u_m \\ \frac{\partial N_i}{\partial y} v_i + \frac{\partial N_j}{\partial y} v_j + \frac{\partial N_m}{\partial y} v_m \\ \frac{1}{2}(\frac{\partial N_i}{\partial y} u_i + \frac{\partial N_j}{\partial y} u_j + \frac{\partial N_m}{\partial y} u_m + \frac{\partial N_i}{\partial x} v_i + \frac{\partial N_j}{\partial x} v_j + \frac{\partial N_m}{\partial x} v_m) \end{bmatrix} \quad (2.31)$$

in which the components u and v do not depend by x and y because they are the displacement in the nodes. Eventually, they can depend by the time if the problem is not stationary. Therefore, the Equation 2.31 can be written as

$$\boldsymbol{\varepsilon} = \begin{bmatrix} \frac{\partial N_i}{\partial x} & 0 & \frac{\partial N_j}{\partial x} & 0 & \frac{\partial N_m}{\partial x} & 0 \\ 0 & \frac{\partial N_i}{\partial y} & 0 & \frac{\partial N_j}{\partial y} & 0 & \frac{\partial N_m}{\partial y} \\ \frac{1}{2}\frac{\partial N_i}{\partial y} & \frac{1}{2}\frac{\partial N_i}{\partial x} & \frac{1}{2}\frac{\partial N_j}{\partial y} & \frac{1}{2}\frac{\partial N_j}{\partial x} & \frac{1}{2}\frac{\partial N_m}{\partial y} & \frac{1}{2}\frac{\partial N_m}{\partial x} \end{bmatrix} \cdot \begin{bmatrix} u_i \\ v_i \\ u_j \\ v_j \\ u_m \\ v_m \end{bmatrix} = \mathbf{B} \cdot \mathbf{a} \tag{2.32}$$

With the shape functions N_i, N_j, and N_m already determined, the matrix **B** can easily be obtained.

Knowing the deformation and the rheological properties of the material, the stress for each point inside the element can be expressed as

$$\boldsymbol{\sigma} = \boldsymbol{\sigma}_0 + \mathbf{D}(\boldsymbol{\varepsilon} - \boldsymbol{\varepsilon}_0) \quad \rightarrow \quad \begin{bmatrix} \sigma_{xx} \\ \sigma_{yy} \\ \sigma_{xy} \end{bmatrix} = \begin{bmatrix} \sigma_{0xx} \\ \sigma_{0yy} \\ \sigma_{0xy} \end{bmatrix} + \mathbf{D} \begin{bmatrix} \varepsilon_{xx} - \varepsilon_{0xx} \\ \varepsilon_{yy} - \varepsilon_{0yy} \\ \varepsilon_{xy} - \varepsilon_{0xy} \end{bmatrix} \tag{2.33}$$

where $\mathbf{D}$ is the matrix containing the rheological properties of the material and σ_0 and ε_0 are stresses and deformations pre-existing. Under plane stress conditions, from the Hooke's law

$$\begin{cases} \varepsilon_{xx} - \varepsilon_{0xx} = \dfrac{\sigma_{xx}}{E} - \dfrac{\nu}{E}\sigma_{yy} \\ \varepsilon_{yy} - \varepsilon_{0yy} = -\dfrac{\nu}{E}\sigma_{xx} + \dfrac{\sigma_{yy}}{E} \\ \varepsilon_{xy} - \varepsilon_{0xy} = \dfrac{(1+\nu)}{E}\sigma_{xy} = \dfrac{1}{2\mu}\sigma_{xy} \end{cases}$$

from which the components of the stress can be written as

$$\begin{cases} \sigma_{xx} = \dfrac{E}{1-\nu^2}(\varepsilon_{xx} - \varepsilon_{0xx}) + \dfrac{E\nu}{1-\nu^2}(\varepsilon_{yy} - \varepsilon_{0yy}) \\ \sigma_{yy} = \dfrac{E\nu}{1-\nu^2}(\varepsilon_{xx} - \varepsilon_{0xx}) + \dfrac{E}{1-\nu^2}(\varepsilon_{yy} - \varepsilon_{0yy}) \\ \sigma_{xy} = \dfrac{E(1-\nu)}{1-\nu^2}(\varepsilon_{xy} - \varepsilon_{0xy}) \end{cases} \tag{2.34}$$

and substituting the Equations 2.34 in the Equation 2.33 it is obtained that

$$\begin{bmatrix} \sigma_{xx} \\ \sigma_{yy} \\ \sigma_{xy} \end{bmatrix} = \frac{E}{1-\nu^2} \begin{bmatrix} 1 & \nu & 0 \\ \nu & 1 & 0 \\ 0 & 0 & 1-\nu \end{bmatrix} \cdot \begin{bmatrix} \varepsilon_{xx} - \varepsilon_{0xx} \\ \varepsilon_{yy} - \varepsilon_{0yy} \\ \varepsilon_{xy} - \varepsilon_{0xy} \end{bmatrix} = \mathbf{D} \cdot \begin{bmatrix} \varepsilon_{xx} - \varepsilon_{0xx} \\ \varepsilon_{yy} - \varepsilon_{0yy} \\ \varepsilon_{xy} - \varepsilon_{0xy} \end{bmatrix}$$

$$\Downarrow$$

$$\boldsymbol{\sigma} = \mathbf{D} \cdot \boldsymbol{\varepsilon} = \mathbf{D} \cdot \boldsymbol{\varepsilon}_{tot} - \mathbf{D} \cdot \boldsymbol{\varepsilon}_0 \tag{2.35}$$

Stage 5

To make the nodal forces statically equivalent to the stresses and to the distributed forces, the work expended by the nodal forces and the work expended by the stresses and the distributed forces must be equal.

- *Nodal forces*: considering a virtual nodal displacement $\delta\mathbf{a}^e$ for the element e, the work due to the nodal forces is

$$L^e_{ext} = \sum_{inode=1}^{nnode} \mathbf{q}^e_{inode} \cdot \delta\mathbf{a}^e_{inode} = \delta\mathbf{a}^{e^T} \cdot \mathbf{q}^e \tag{2.36}$$

- *Stresses and distributed forces*: considering the distributed forces $\mathbf{b} = \begin{bmatrix} b_x \\ b_y \end{bmatrix}$, the work of a unit volume is

$$L_{\mathbf{b}} = \mathbf{b} \cdot \delta\mathbf{u} = \delta\mathbf{u}^T \cdot \mathbf{b} \tag{2.37}$$

while for the stresses $\boldsymbol{\sigma} = \begin{bmatrix} \sigma_{xx} & \sigma_{xy} \\ \sigma_{yx} & \sigma_{yy} \end{bmatrix}$ the work is

$$L_{\boldsymbol{\sigma}} = \delta\boldsymbol{\varepsilon}^T \cdot \boldsymbol{\sigma} \tag{2.38}$$

Taking into account that $\delta\boldsymbol{\varepsilon} = \mathbf{B} \cdot \delta\mathbf{a}^e$ and $\delta\mathbf{u}(x, y) = \mathbf{N} \cdot \delta\mathbf{a}$, adding Equations 2.37 and 2.38 and integrating on the volume of the element the internal work of the element is

$$L^e_{int} = \int_{V_e} \delta\mathbf{a}^T \cdot (\mathbf{B}^T \cdot \boldsymbol{\sigma} - \mathbf{N}^T \cdot \mathbf{b}) dV \tag{2.39}$$

The Equations 2.36 and 2.39 must be equal, therefore

$$\delta\mathbf{a}^{e^T} \cdot \mathbf{q}^e = \delta\mathbf{a}^T \int_{V_e} (\mathbf{B}^T \cdot \boldsymbol{\sigma}) dV - \int_{V_e} (\mathbf{N}^T \cdot \mathbf{b}) \mathbf{dV}$$

$$\Downarrow$$

$$\mathbf{q}^e = \int_{V_e} (\mathbf{B}^T \cdot \boldsymbol{\sigma}) dV - \int_{V_e} (\mathbf{N}^T \cdot \mathbf{b}) \mathbf{dV} \tag{2.40}$$

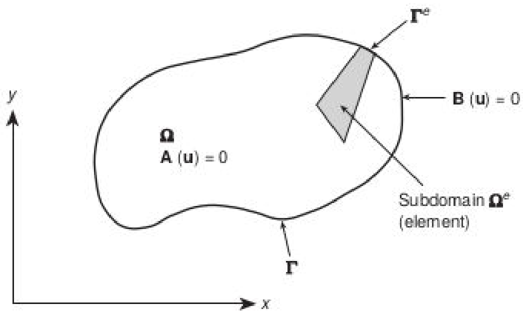

Figure 2.3: Example of boundaries Γ of a domain Ω (from *Zienkiewicz and Taylor*, 2000).

Introducing the Equations 2.32 and 2.33 into the Equation 2.40, it can be obtained that

$$\mathbf{q}^e = \underbrace{\int_{V_e} (\mathbf{B}^T \cdot \mathbf{D} \cdot \mathbf{B}) dV \cdot \mathbf{a}^e}_{\mathbf{K} \cdot \mathbf{a}} + \underbrace{\int_{V_e} (\mathbf{B}^T \cdot \boldsymbol{\sigma}_0) dV}_{\mathbf{f}_p} - \underbrace{\int_{V_e} (\mathbf{B}^T \cdot \mathbf{D} \cdot \boldsymbol{\varepsilon}_0) dV}_{\mathbf{f}_{\boldsymbol{\varepsilon}_0}} - \underbrace{\int_{V_e} (\mathbf{N}^T \cdot \mathbf{b}) dV}_{\mathbf{f}_\mathbf{b}} \tag{2.41}$$

which is in the same form of the Equation 2.15.

The error between the numerical solution and the analytic solution is of order $O(h^2)$, where h is the dimension of the grid. Generally, the dimension of the elements of the grid is reduced only in some portions of the system, to avoid to increase too much compute times.

2.3 Galerkin method

Posing the problem to be solved in its most general terms, an unknown function $\mathbf{u}$ has to be found such that it satisfies a certain differential equation set

$$\mathbf{A}(\mathbf{u}) = \begin{Bmatrix} A_1(\mathbf{u}) \\ A_2(\mathbf{u}) \\ \vdots \\ A_n(\mathbf{u}) \end{Bmatrix} = \mathbf{0} \tag{2.42}$$

in a domain Ω (line, area or volume), together with certain boundary conditions

$$\mathbf{B}(\mathbf{u}) = \begin{Bmatrix} B_1(\mathbf{u}) \\ B_2(\mathbf{u}) \\ \vdots \\ B_n(\mathbf{u}) \end{Bmatrix} = \mathbf{0} \tag{2.43}$$

defined on the boundaries Γ of the domain Ω (*Zienkiewicz and Taylor*, 2000) (Figure 2.3).

The function needed may be a scalar quantity or may represent a vector. Similarly, the differential equation may be a single one or a set of simultaneous equations and does not need to be linear. The finite element process, being one of approximation, will seek the solution in the approximate form of the Equation 2.27.

A solution of the system given by the Equations 2.42 and 2.43 can be obtained recasting the problem in the integral form

$$\int_{\Omega} \mathbf{G}_j(\mathbf{u})d\Omega + \int_{\Gamma} \mathbf{g}_j(\mathbf{u})d\Gamma = \mathbf{0} \tag{2.44}$$

in which $\mathbf{G}_j$ and $\mathbf{g}_j$ prescribe known functions or operators. To obtain the approximation in such integral forms the method of weighted residuals (the Galerkin method) can be used.

As the set of differential Equations 2.42 has to be zero at each point of the domain Ω, it follows that

$$\int_{\Omega} \mathbf{v}^T \mathbf{A}(\mathbf{u}) = 0 \rightarrow \int_{\Omega} [v_1 A_1(\mathbf{u}) + v_2 A_2(\mathbf{u}) + \cdots + v_n A_n(\mathbf{u})] d\Omega = 0 \tag{2.45}$$

where

$$\mathbf{v} = \begin{Bmatrix} v_1 \\ v_2 \\ \vdots \\ v_n \end{Bmatrix} \tag{2.46}$$

is a set of arbitrary functions equal in number to the number of equations $\mathbf{A}(\mathbf{u})$ involved. In the same way, functions $\bar{\mathbf{v}} \equiv -\mathbf{v}$ must be found such that

$$\int_{\Omega} \bar{\mathbf{v}}^T \mathbf{B}(\mathbf{u}) = 0 \rightarrow \int_{\Omega} [\bar{v}_1 B_1(\mathbf{u}) + \bar{v}_2 B_2(\mathbf{u}) + \cdots + \bar{v}_n B_n(\mathbf{u})] d\Omega = 0 \tag{2.47}$$

Therefore, the integral statement that

$$\int_{\Omega} \mathbf{v}^T \mathbf{A}(\mathbf{u}) d\Omega + \int_{\Omega} \hat{\mathbf{v}}^T \mathbf{B}(\mathbf{u}) d\Omega = 0 \tag{2.48}$$

is satisfied for all $\mathbf{v}$ and $\hat{\mathbf{v}}$ and it is equivalent to the satisfaction of the differential Equations 2.42 and their boundary conditions 2.43.

$\mathbf{v}$ and $\hat{\mathbf{v}}$ have to be chosen in function of the differential equation to solve. The integral statement 2.48 allow an approximation to be made if, in place of any function $\mathbf{v}$, we put a finite set of approximate functions

$$\mathbf{v} = \sum_{j=1}^{n} \mathbf{w}_j \delta \mathbf{a}_j \qquad \bar{\mathbf{v}} = \sum_{j=1}^{n} \bar{\mathbf{w}}_j \delta \mathbf{a}_j \tag{2.49}$$

in which $\delta \mathbf{a}_j$ are arbitrary parameters and n is the number of unknowns entering the problem. Inserting the approximation 2.49 into the Equation 2.48, it can be obtained that

$$\delta \mathbf{a}^T \left[\int_\Omega \mathbf{w}_j^T \mathbf{A}(\sum_i \mathbf{N}_i \cdot \mathbf{a}_i) d\Omega + \int_\Omega \bar{\mathbf{w}}_j^T \mathbf{B}(\sum_i \mathbf{N}_i \cdot \mathbf{a}_i) d\Omega \right] = 0 \tag{2.50}$$

and since $\delta \mathbf{a}_j$ is arbitrary, there is a set of equations which is sufficient to determine the parameters $\mathbf{a}_j$ as

$$\int_\Omega \mathbf{w}_j^T \mathbf{A}(\sum_i \mathbf{N}_i \cdot \mathbf{a}_i) d\Omega + \int_\Omega \bar{\mathbf{w}}_j^T \mathbf{B}(\sum_i \mathbf{N}_i \cdot \mathbf{a}_i) d\Omega = 0 \tag{2.51}$$

$\mathbf{A}(\sum_i \mathbf{N}_i \cdot \mathbf{a}_i)$ represents the residual obtained by substitution of the approximation into the differential equation and $\mathbf{B}(\sum_i \mathbf{N}_i \cdot \mathbf{a}_i)$ represents the residual of the boundary conditions. So, the Equation 2.51 is a weighted integral of such residuals. The approximation may thus be called the method of weighted residuals (*Zienkiewicz and Taylor*, 2000). In the Galerkin method $\mathbf{v} \equiv \mathbf{N}_i$ and $\bar{\mathbf{v}} \equiv -\mathbf{N}_i$, obtaining symmetric Stiffness matrices, and the Equation 2.51 can be written as

$$\int_\Omega N_j \mathbf{A}(\sum_i \mathbf{N}_i \cdot \mathbf{a}_i) d\Omega + \int_\Omega N_j \mathbf{B}(\sum_i \mathbf{N}_i \cdot \mathbf{a}_i) d\Omega = 0 \tag{2.52}$$

These integral form permits the approximation to be determined element by element, and dividing the system in *nelem* elements, it can be written as

$$\sum_{ielem=1}^{nelem} \left[\int_\Omega N_j \mathbf{A}(\sum_i \mathbf{N}_i \cdot \mathbf{a}_i) d\Omega + \int_\Omega N_j \mathbf{B}(\sum_i \mathbf{N}_i \cdot \mathbf{a}_i) d\Omega \right] = 0 \tag{2.53}$$

2.4 Local coordinates

If the elements have an irregular shape it is not possible to determine the integral exactly. In this case it is useful to develop the method in the local coordinates of the element *(s,t)* and to come back to the global coordinates *(x,y)* at the end of the calculation. In local coordinates,

$$\begin{aligned} \frac{\partial N_i}{\partial s} &= \frac{\partial N_i}{\partial x}\frac{\partial x}{\partial s} + \frac{\partial N_i}{\partial y}\frac{\partial y}{\partial s} \\ \frac{\partial N_i}{\partial t} &= \frac{\partial N_i}{\partial x}\frac{\partial x}{\partial t} + \frac{\partial N_i}{\partial y}\frac{\partial y}{\partial t} \end{aligned} \tag{2.54}$$

which can be written in matrices, as

$$\begin{bmatrix} \frac{\partial N_i}{\partial s} \\ \frac{\partial N_i}{\partial t} \end{bmatrix} = \underbrace{\begin{bmatrix} \frac{\partial x}{\partial s} & \frac{\partial y}{\partial s} \\ \frac{\partial x}{\partial t} & \frac{\partial y}{\partial t} \end{bmatrix}}_{\mathbf{J} = \text{Jacobiano}} \cdot \begin{bmatrix} \frac{\partial N_i}{\partial x} & \frac{\partial N_i}{\partial y} \end{bmatrix} \tag{2.55}$$

from which, inverting the Jacobian matrix, it is obtained that

$$\begin{bmatrix} \frac{\partial N_i}{\partial x} & \frac{\partial N_i}{\partial y} \end{bmatrix} = \begin{bmatrix} \mathbf{J} \end{bmatrix}^{-1} \cdot \begin{bmatrix} \frac{\partial N_i}{\partial s} & \frac{\partial N_i}{\partial t} \end{bmatrix} \tag{2.56}$$

The Jacobian matrix can be evaluated knowing the relation between system of global coordinates and that of the local coordinates. For every point has to be valid the relation

$$x = \sum_{i=1}^{nnode} N_i x_i$$

which introduced in the Jacobian matrix gives

$$\mathbf{J} = \begin{bmatrix} \frac{\partial}{\partial s}\left(\sum_{i=1}^{nnode} N_i x_i\right) & \frac{\partial}{\partial s}\left(\sum_{i=1}^{nnode} N_i y_i\right) \\ \frac{\partial}{\partial t}\left(\sum_{i=1}^{nnode} N_i x_i\right) & \frac{\partial}{\partial t}\left(\sum_{i=1}^{nnode} N_i y_i\right) \end{bmatrix} = \begin{bmatrix} \sum_{i=1}^{nnode} x_i \frac{\partial N_i}{\partial s} & \sum_{i=1}^{nnode} y_i \frac{\partial N_i}{\partial s} \\ \sum_{i=1}^{nnode} x_i \frac{\partial N_i}{\partial t} & \sum_{i=1}^{nnode} y_i \frac{\partial N_i}{\partial t} \end{bmatrix} =$$

$$= \begin{bmatrix} \frac{\partial N_1}{\partial s} & \frac{\partial N_2}{\partial s} & \dots & \frac{\partial N_{nnode}}{\partial s} \\ \frac{\partial N_1}{\partial t} & \frac{\partial N_2}{\partial t} & \dots & \frac{\partial N_{nnode}}{\partial t} \end{bmatrix} \cdot \begin{bmatrix} x_1 & y_1 \\ x_2 & y_2 \\ \vdots & \vdots \\ x_{nnode} & y_{nnode} \end{bmatrix} \tag{2.57}$$

For what concerns $d\Omega$, it also depends on dx and dy, with

$$dx = \frac{\partial x}{\partial s} ds + \frac{\partial x}{\partial t} dt \quad \text{and} \quad dy = \frac{\partial y}{\partial s} ds + \frac{\partial y}{\partial t} dt$$

, which can be written in matrices, as

$$\begin{bmatrix} dx \\ dy \end{bmatrix} = \begin{bmatrix} \frac{\partial x}{\partial s} & \frac{\partial x}{\partial t} \\ \frac{\partial y}{\partial s} & \frac{\partial y}{\partial t} \end{bmatrix} \cdot \begin{bmatrix} ds \\ dt \end{bmatrix} \tag{2.58}$$

obtaining

$$d\Omega = dx\, dy = det\, \mathbf{J} \cdot ds\, dt \tag{2.59}$$

2.5 Gauss quadrature

In case of complex problems the integration is determined with numerical methods, as the Gauss quadrature. In this case, in place of specifying the position of a given number of sampling points *a priori*, the points of integration can be determined to aim an increase of the accuracy. Considering

$$\int_a^b f(\xi)d\xi = \sum_{i=1}^{N} H_i f(\xi_i) \tag{2.60}$$

where H_i is the weight in every point and N, which are the Gauss points, depends on both the order of the partial derivative and the accuracy of the quadrature. The function is approximated by a polynomial of order $(N-1)$. For example, in case of a 2-dimensional system

$$K_{ij} = \int_{-1}^{1}\int_{-1}^{1} K(s,t)ds\,dt = \int_{-1}^{1}\left(\sum_{i=1}^{N} H_i K(s_i)\right)dt = \sum_{j=1}^{N}\sum_{i=1}^{N} H_j H_i K(s_i,t_j) \tag{2.61}$$

with K determined in the Gauss points of coordinates (s,t).

2.6 Penalty formulation

The penalty formulation of the mass conservation equation is based on a relaxation of the incompressibility constraint, such as

$$\nabla \cdot \mathbf{v} + \frac{\bar{p}}{\lambda} = 0 \tag{2.62}$$

so that the normalised modified pressure can be written as

$$\bar{p}' = -\lambda\left(\frac{\partial u'}{\partial x'} + \frac{\partial v'}{\partial y'}\right) \tag{2.63}$$

where λ is the penalty parameter, that can be interpreted as a bulk viscosity and has the same dimension, that is equivalent to say that the material is weakly compressible (*Thieulot*, 2014). It can be shown that if one chooses λ to be a sufficiently large number, the continuity equation (2.1) will be approximately satisfied in the finite element solution. The value of λ is often recommended to be 6 to 7 orders of magnitude larger than the shear viscosity (*Donea and Huerta*, 2003; *Thieulot*, 2014). In *SubMar* λ is chosen as $\lambda = \mu\sqrt{r_p}$ with r_p denoting the machine relative precision (*Marotta et al.*, 2006).

Chapter 3

Hydration and shear heating in the *SubMar* code

3.1 Model setup

The numerical integration (as described in the Chapter 2) is performed in a 2D rectangular domain that is 1400 km wide and 700 km deep. The domain is discretised by a non-deforming irregular grid that is composed of 4438 quadratic triangular elements and 9037 nodes and has a denser nodal distribution near the contact region between the plates, where the most significant gradients in temperature and velocity fields are expected. The size of the elements varies from 10 km to 80 km horizontally and from 5 km to 20 km vertically, with the smaller elements located in the active margin region to depths of up to 300 km (Figure 3.1).

The model simulates the thermo-mechanical evolution of a crust-mantle system during three tectonic phases: 1) active convergence of a continent-ocean-continent system that drives the closure of a 2500-km-wide ocean (Figure 3.2), 2) continental collision, and 3) a post-collisional phase. The physics of the crust-mantle system during the three tectonic phases is synthesised in Section 2.1.

The boundary conditions are set in terms of velocities and temperatures that are prescribed at the borders of the 2D domain. The velocity boundary conditions vary depending on the tectonic phase; during the pre-collisional and collisional phases, a velocity of 3 cm/yr, 5 cm/yr or 8 cm/yr is prescribed along the bottom of the oceanic crust. To facilitate the subduction of the ocean, the same velocity is also fixed along a 45° dipping plane that extends from the trench to a depth of 100 km (Figure 3.2). During the post-collisional phase, the system undergoes pure gravitational evolution. Stress-free conditions are assumed along the upper boundary of the 2D domain, and no-slip conditions are assumed along the other boundaries. The thermal boundary conditions correspond to fixed temperatures at the top (300 K) and the bottom (1600 K) of the model, zero thermal flux at

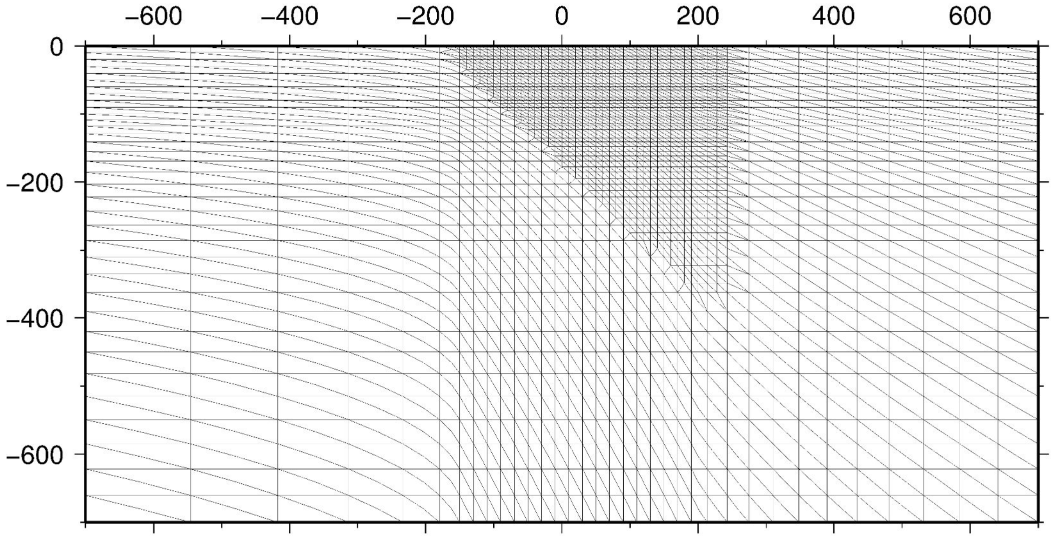

Figure 3.1: Grid with quadratic triangular elements used for the implementation of the model.

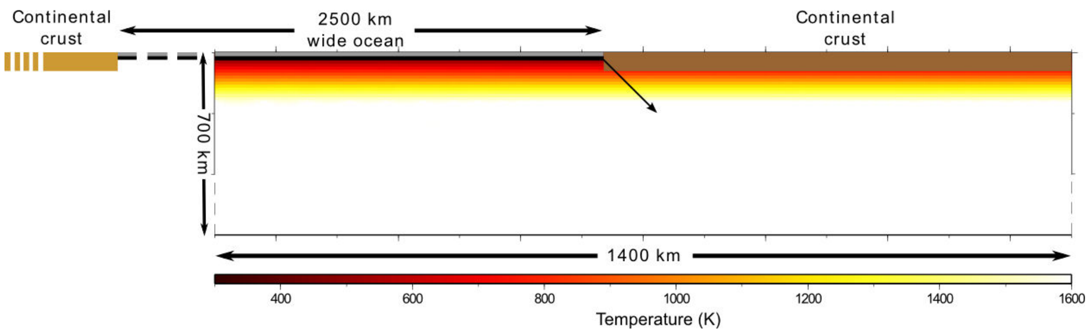

Figure 3.2: Setup and initial thermal configuration of the numerical model. Brown, grey and black colours indicate the continental crust, the upper oceanic crust and the lower oceanic crust, respectively. The distances are not to scale.

the right vertical sidewall and fixed temperature along the left side.

The initial thermal structure corresponds to a simple conductive thermal configuration throughout the lithosphere with temperatures that vary from 300 K at the surface to 1600 K at the base of the lithosphere, which is located at a depth of 80 km under both the oceanic and continental domains. This configuration corresponds to an oceanic lithosphere of approximately 40 Ma based on the cooling of a semi-infinite half space model (*Turcotte and Schubert*, 2002) and to a thinned continental passive margin based on a medium to slow spreading rate of 2-3 cm/yr. The 1600 K isotherm defines the base of the lithosphere throughout the system's evolution.

At the beginning of the evolution, 288061 markers identified by different indexes, are spatially distributed (Figure 3.2) with a density of 1 marker per 0.25 km^2 to define the upper oceanic crust, the lower oceanic crust and the continental crust. All of the properties (conductivity, specific heat at a constant pressure, density and viscosity) depend on the

	Continental Crust	Oceanic Crust Lower	Oceanic Crust Upper	Mantle	Serpentinised Mantle
Rheology	Dry Granite	-	Diabase	Dry Dunite	-
E (kJ/mol)	123	-	260	444	-
n	3.2	-	2.4	3.41	-
μ_0 **(Pa · s)**	$3.47 \cdot 10^{21}$	10^{19}	$1.61 \cdot 10^{22}$	$5.01 \cdot 10^{20}$	10^{19}
ρ_0 **(kg/m^3)**	2640	2961	2961	3200	3000
K (W/m · K)	3.03	2.10	2.10	4.15	4.15
H_c **(μW/m^3)**	2.5	0.4	0.4	0.002	0.002
References	a, d, f	b, f, i, j, k	a, b, c, f	c, d, e, f, j	d, f, g, h, i

Table 3.1: Values of the material and rheological parameters used in the models. a) *Ranalli and Murphy* (1987); b) *Afonso and Ranalli* (2004); c) *Kirby* (1983); d) *Haenel et al.* (1988); e) *Chopra and Peterson* (1981); f) *Dubois and Diament* (1997), *Best and Christiansen* (2001); g) *Roda et al.* (2011); h) *Schmidt and Poli* (1998); i) *Gerya and Stöckhert* (2006); j) *Roda et al.* (2012); and k) *Gerya and Yuen* (2003).

composition such that within each element e, the value of property can be expressed as

$$P^e = P_m \left[1 - \sum_i C_i^e\right] + \sum_i P_i C_i^e \tag{3.1}$$

where P_m is the value of the property for the mantle, and P_i is the value of the property for the serpentinizsed mantle ($i = sm$), upper oceanic crust ($i = oc_U$), lower oceanic crust ($i = oc_L$) and continental crust ($i = cc$). Table 3.1 summarises the material properties and rheological parameters.

3.2 Implementation of the model

3.2.1 Hydration of the mantle wedge

Numerical and petrological models have demonstrated the dominant role of mantle wedge hydration in the cyclic uplift and burial of deeply subducted material prior to continental collision (*Schmidt and Poli*, 1998; *Gerya and Stockhert*, 2002; *Gorczyk et al.*, 2006, 2007; *Yamato et al.*, 2007; *Ernst and Liou*, 2008; *Agard et al.*, 2009; *Meda et al.*, 2010; *Roda et al.*, 2010b, 2012; *Le Voci et al.*, 2014). In ocean-continent subduction systems, low viscosity hydrated mantle (*Billen and Gurnis*, 2001; *Hirth and Kohlstedt*, 2003; *Billen*, 2008; *Guillot et al.*, 2009b; *Hirth and Guillot*, 2013; *Nagaya et al.*, 2016) facilitates the exhumation and underplating of subducted oceanic and continental material at the base of the crust of the upper plate. The hydration of the mantle wedge is possible because of the transport of water to great depths, which is associated with the dehydration of the subducting oceanic crust (*Schmidt and Poli*, 1998; *Liu et al.*, 2007; *Faccenda et al.*, 2009; *Faccenda and Mancktelow*, 2010).

To define the geometry oh the hydrated wedge it is necessary to determine the maximum dehydration depth of the oceanic crust Y_{dehydr}, below which the water content in hydrous phases in H_2O-saturated MORB basalt is negligible, using the stability field of lawsonite (*Schmidt and Poli*, 1998; *Roda et al.*, 2010b) as follows

$$Y_{dehydr} = -0.8755 \cdot T_{imarc} + 714.35 \tag{3.2}$$

where Y_{dehydr} is calculated for each oceanic crustal marker with temperature T_{imarc} up to a depth of 300 km. *Schmidt and Poli* (1998) indicate that a significant water budget should be available until a depth of about 150–200 km, however, the exhumation of subducted continental rocks show evidence of stishovite that induce to consider the transport of water up to 250-300 km deep (*Liu et al.*, 2007). Furthermore, *Faccenda et al.* (2009); *Faccenda and Mancktelow* (2010); *Faccenda* (2014) have shown that tectonic stresses can influence the hydration pattern in the subducted slab, allowing the fluids to penetrate in the slab and favouring their transport to great depths, up to the base of the upper mantle.

The progressive hydration of the mantle wedge is defined by the stability field of serpentine, which is calculated for each element by using the following two equations (*Roda et al.*, 2010b)

$$\begin{aligned} Y_{hydr} &= -0.3394 \cdot T_{elem} + 268.09 \qquad \text{above 66 km depth} \\ Y_{hydr} &= -0.9540 \cdot T_{elem} + 993.28 \qquad \text{below 66 km depth} \end{aligned} \tag{3.3}$$

where Y_{hydr} represents the maximum hydration depth, and T_{elem} is the elemental temperature. Each element with an average depth and temperature (Y_{elem}, T_{elem}) is considered to be hydrated if $Y_{hydr} < Y_{elem} < Y_{dehydr}$, where Y_{hydr} is calculated from Equation 3.3. The subducting plate limits the hydrated area from below. Specifically, to better delineate the geometry of the lower border of the hydrated area, the subducted plate was subdivided into segments of equal length; the deepest dehydrated oceanic crust marker for each segment is identified at each time during the system's dynamic evolution. The line that connects these markers defines the lower limit of the hydrated area.

The hydration is simulated assuming a constant viscosity of 10^{19} Pa·s and a density of 3000 kg/m^3 in the mantle with pressure and temperature conditions that are within the stability field of serpentine (*Honda and Saito*, 2003; *Arcay et al.*, 2005; *Roda et al.*, 2010b) and neglecting the effects of water migration (*Quinquis and Buiter*, 2014).

3.2.2 Shear heating

The energy conservation equation (2.3) has been modified taken into account also the energy produced by both shear heating (H_s) and adiabatic heating (H_a), as follow

$$\rho\, c_p \left(\frac{\partial T}{\partial t} + \mathbf{v} \cdot \nabla T \right) = \nabla \cdot (K\, \nabla T) + H_r + H_s + H_a \tag{3.4}$$

where

$$H_s = \tau_{ij} \dot{\varepsilon_{ij}} = 2\, \mu_{eff}\, \dot{\varepsilon_{ij}} \dot{\varepsilon_{ij}} \qquad \text{and} \qquad H_a = T\, \alpha\, \frac{Dp}{Dt} \tag{3.5}$$

in which α is the thermal coefficient of expanision and μ_{eff} is the effective viscosity.

Latent heat of serpentinisation has not been taken into account because, at large scale, can be considered to be balanced by the latent heat produced by both the de-serpentinisation and the melting (*Pérez-Gussinyé et al.*, 2001; *Rupke et al.*, 2004; *Rüpke et al.*, 2013). Furthermore, it has been suggested that the latent heat of serpentinization is $2.9 \cdot 10^5$ J/kg (*Emmanuel and Berkowitz*, 2006), resulting in an increase in temperature of 300°C (*Rüpke et al.*, 2013), and therefore the serpentine would cease to be stable. However, since the serpentinisation exists on large scale, the latent heat of hydration-dehydration must have a minor impact on the thermal field, likely because the circulation of fluids is an efficient mechanism to carry the heating away.

Outside the lithosphere, the effective viscosity coincides with the viscosity determined by Equation 2.8, so that

$$\mu_{eff} = \mu_{visc}$$

Differently, within the lithosphere the viscous rheology is combined with a brittle/plastic rheology and the effective viscosity is defined as

$$\mu_{eff} = min(\mu_{visc}, \mu_{plast}) \tag{3.6}$$

Different yield criteria are used in geosciences to define the plastic yield of rocks, such as the Drucker-Prager, the von-Mises-Hencky and the Tresca criteria. The Drucker-Prager criterion states that yielding depends on both the second invariant of the stress deviator and the first invariant of the stress tensor. Although the Drucker-Prager criterion is simple and predicts a smooth and symmetric failure surface, which facilitates its implementation in numerical models, it has a major limitation in overestimating the rock strength and in predicting errors that are larger than other yield criteria (*Colmenares and Zoback*, 2002; *Alejano and Bobet*, 2012). The Drucker-Prager criterion can be considered as an extension of the von-Mises-Hencky criterion and states that yielding occurs when the second invariant of the stress, which is defined by the magnitude of either the maximum and intermediate principal stress components, reaches a value that is characteristic of the material (*Ranalli and Murphy*, 1987). The von-Mises-Hencky criterion is similar to the Tresca criterion, although the latter states that yielding depends on the magnitude of only the maximum principal stress. Because the Tresca criterion is a more conservative plastic yielding criterion, it has been used to determine the plastic viscosity.

The Tresca criterion requires the principal stress difference as well as the principal stresses themselves to be less than the yield stress σ_Y (*Turcotte and Schubert*, 2002), such that

$$|\sigma_1| \leq \sigma_Y \,, \qquad |\sigma_2| \leq \sigma_Y \,, \qquad |\sigma_1 - \sigma_2| \leq \sigma_Y \tag{3.7}$$

After taking minor mathematical steps, the plastic viscosity can be defined as

$$\mu_{plast} = min(\mu_1, \mu_2, \mu_3) \tag{3.8}$$

with

$$\mu_1 = \frac{\sigma_Y - p}{2\dot{\varepsilon_1}} \,, \qquad \mu_2 = \frac{\sigma_Y - p}{2\dot{\varepsilon_2}} \,, \qquad \mu_3 = \frac{\sigma_Y - p}{2(\dot{\varepsilon_1} - \dot{\varepsilon_2})} \tag{3.9}$$

where p is the pressure, and ε_i are the principal strain rates.

The yield stress σ_Y is defined by assuming the following simplified formulation of Byerlee's law criterion:

$$\sigma_Y = \beta \cdot y \qquad \text{with} \qquad \beta = 40 \text{ MPa/km} \tag{3.10}$$

where the effects of pore fluid pressure are neglected, ρ is the density and y is the depth.

To verify the implementation of shear and adiabatic heating, the benchmark experiment proposed by *Gerya* (2011) has been performed, comparing the outcomes of the two codes. The results of the benchmark are shown in Appendix A.3.

3.3 Results

Four model types have been developed to analyse the impact of shear heating and mantle hydration on the system's thermo-mechanics. We use the following acronyms to refer to each of these models followed by the value of the prescribed velocity, which is expressed in cm/yr:

- SIN-SIN - models without shear heating or mantle hydration (reference model from *Marotta and Spalla*, 2007);
- CUM-SIN - models with shear heating and without mantle hydration;
- SIN-CUM - models without shear heating and with mantle hydration;
- CUM-CUM - models with both shear heating and mantle hydration.

3.3.1 Global dynamics

To determine the role of mantle hydration and shear heating mechanisms on the dynamics of the wedge area, the main thermo-mechanical features predicted by the SIN-CUM and CUM-CUM models have been compared to those predicted by the reference SIN-SIN model (Marotta and Spalla, 2007). As in the SIN-SIN model, when only mantle hydration is allowed (SIN-CUM model) convective flow develops underneath the overriding continental plate during the active phase (Figure 3.3a). By the time, this convective flow progressively enlarges at the bottom of the study domain because of the progressive burial of the subducting oceanic plate (Figure 3.3b). This large scale mantle flow causes a mechanical erosion of continental material from the base of the upper plate and it intensifies with the increase of the prescribed velocity (Figure 3.3c), with a consequent temperature increase in the mantle wedge. The introduction of mantle hydration has a dual effect: first, it decreases the friction between the two plates, leading to a small amount of eroded crustal material from the upper plate; second, it reduces the temperature increase in respect to the model without hydration (Figure 3.3d). Conversely, both in the SIN-SIN and in the SIN-CUM models the temperature in the subducting oceanic lithosphere decreases with increasing velocity, as shown by the maximum depth reached by the 800 K isotherm in the different models. For example, it reaches a depth of approximately 300 km in the SIN-CUM.3 model (continuous blue line in Figure 3.4a), of approximately 370 km in the SIN-CUM.5 model (continuous green line in Figure 3.4a) and of 450 km in the SIN-CUM.8 model (continuous red line in Figure 3.4a). The colder thermal state for higher prescribed velocities determines a larger hydrated area during the early stages of the evolution of the SIN-CUM model (see Section 3.3.2 for more details).

Mantle hydration greatly affects the dynamics in the mantle wedge area, where short-wavelength convective cells appear in the low-viscosity hydrated domain. These cells favour the recycling of both continental crust, which was eroded by the upper plate, and upper oceanic crust, which belongs to the subducting lithosphere (Figures 3.5a and b). The convective cells remain active throughout the entire active evolution of the system (Figure 3.5b) and are better defined with high velocities (compare panels c and d to panel b of Figure 3.5). The recycling and mixing of large amounts of continental and oceanic crust and mantle is in agreement with other models in which hydration is taken into account (*Gerya and Yuen*, 2003; *Stöckhert and Gerya*, 2005; *Roda et al.*, 2012; *Li et al.*, 2015).

Figure 3.6 shows the viscosity, strain rate and total energy patterns predicted by model SIN-CUM.5 (a_i and b_i) compared to those that were predicted by model SIN.SIN.5 (c_i). During the active phase, the viscosity inside the cold subducting lithosphere is approximately 2 orders of magnitude higher than the viscosity in the non-hydrated wedge area and up to 6 orders of magnitude higher than the viscosity in the hydrated domain (Figure 3.6a_1). In addition, the strain rate is high in both the lower plate and the wedge

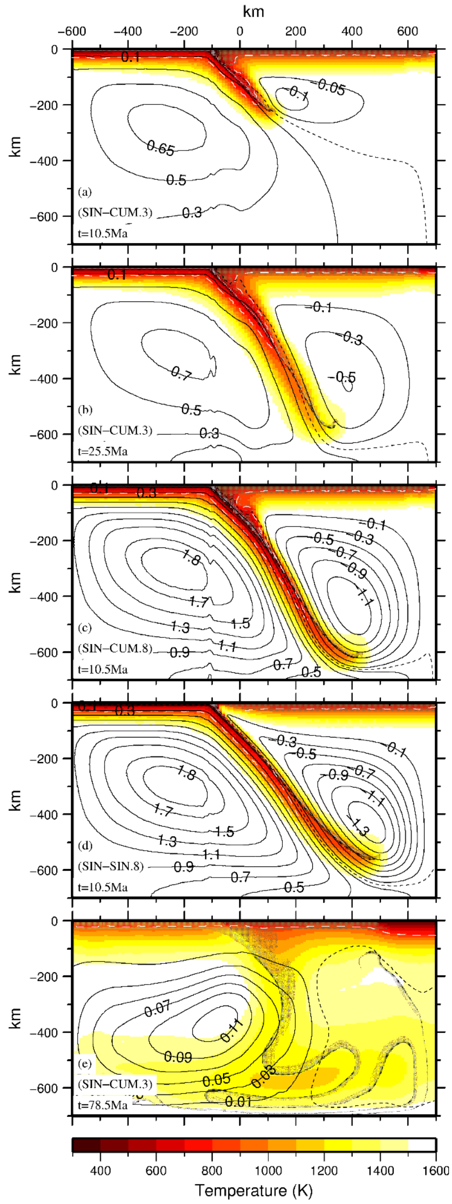

Figure 3.3: Large-scale temperature field (colours) and streamline patterns (solid black lines) for model SIN-CUM.3 at 10.5 Ma (panel a), model SIN-CUM.3 at 25.5 Ma (panel b), model SIN-CUM.8 at 10.5 Ma (panel c) and model SIN-SIN.8 at 10.5 Ma (panel d) after the beginning of active convergence and model SIN-CUM.3 at 78.5 Ma after the continental collision (panel e). The dashed white lines indicate the 800 K isotherm. Black, grey, dark brown and light brown points represent the lower oceanic crust, upper oceanic crust, continental crust of the upper plate, and continental crust of the lower plate, respectively.

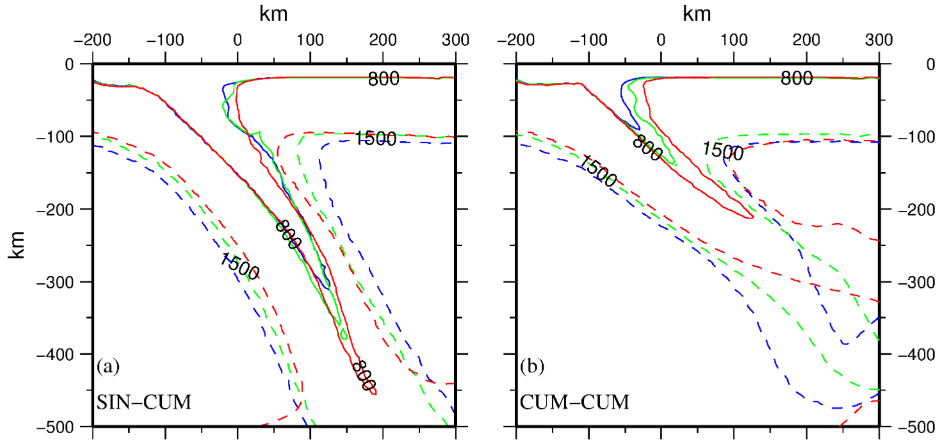

Figure 3.4: Thermal configurations predicted by the SIN-CUM models (panel a) and CUM-CUM models (panel b) in terms of the maximum depth of the 800 K isotherms (solid lines) and 1500 K isotherms (dashed lines). Different colours are used to distinguish between models with different prescribed velocities (blue for 3 cm/yr, green for 5 cm/yr and red for 8 cm/yr).

area, varying from 10^{-16} 1/s in the lower plate to 10^{-13} 1/s near the subduction zone and in the wedge area (Figure 3.6a$_2$). Maximum strain rates are located along the contact area between the lower and the upper plates, where the velocity gradients are very high and strong compositional variations occur. In contrast, the upper plate is characterised by strain rates less than 10^{-16} 1/s.

Since the SIN-SIN and the SIN-CUM models do not account for shear heating, the total energy depends exclusively on radiogenic decay, which is up to 3 orders of magnitude higher in the continental crust than in the mantle. As consequence, the large amount of recycled continental crustal material in the models that take into account hydration is responsible for the high radiogenic energy in the hydrated wedge, approximately 1-2 order of magnitude higher than in the non-hydrated mantle and 1-2 orders of magnitude less than in the continental crust of the upper plate (Figure 3.6a$_3$).

The velocity field that characterise the pure gravitational phase is comparable in all models, both in the SIN-SIN end in the SIN-CUM models, regardless of the subduction velocity that was prescribed during the previous active phase. This is due to the inertial forces that during this phase are negligible, so that only the gravitational forces drive the system (Figure 3.3e). At longer times, the entire system undergoes thermo-mechanical relaxation, and the maximum intensity of the velocity field in the wedge area becomes negligible with respect to the active phase. Furthermore, the convective mantle flow below the lower plate decreases by at least one order of magnitude compared to the flow during the active phase. This flow expands laterally towards the subducted plate reducing the shallow dip of the subducted lithosphere, producing a rising of recycled oceanic and continental crustal material and the doubling of the crust by the end of the pure gravitational phase (Figure 3.3e). This is accompanied by a global thermal re-equilibration of

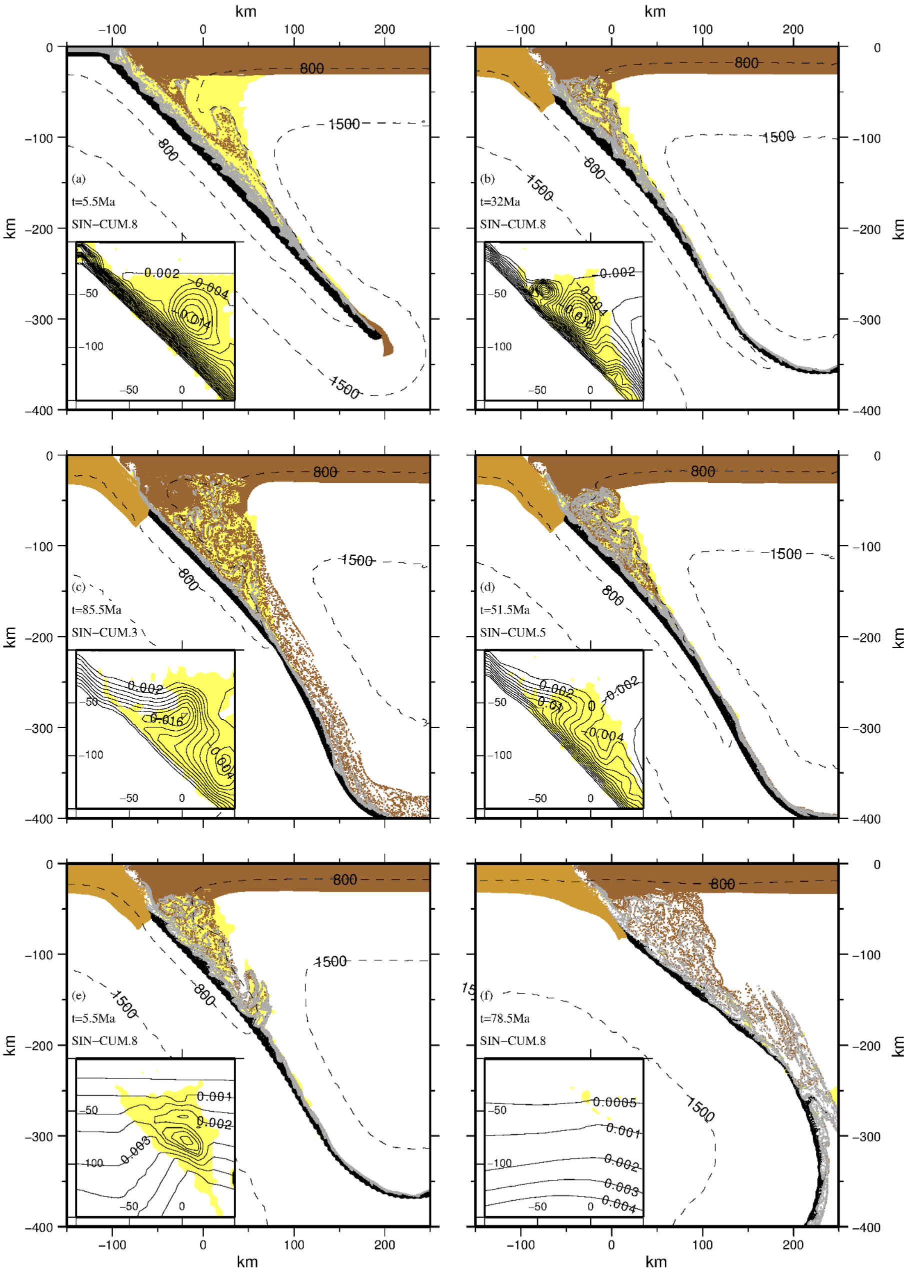

Figure 3.5: Temperature field in terms of the 800 K and 1500 K isotherms (dashed black lines) and streamline patterns (black solid lines in the insets) surrounding the wedge area in the SIN-CUM models at different times and for different subduction velocities. Panel (a): model SIN-CUM.8 at 5.5 Ma after the beginning of active convergence. Panel (b): model SIN-CUM.8 at 32 Ma after the beginning of active convergence. Panel (c): model SIN-CUM.3 at 85.5 Ma after the beginning of active convergence. Panel (d): model SIN-CUM.5 at 51.5 Ma after the beginning of active convergence. Panel (e): model SIN-CUM.8 at 5.5 Ma after the continental collision. Panel (f): model SIN-CUM.8 at 78.5 Ma after the continental collision. The yellow areas represent the hydrated wedge domains. Black, grey, dark brown and light brown points represent the lower oceanic crust, upper oceanic crust, continental crust of the upper plate, and continental crust of the lower plate, respectively.

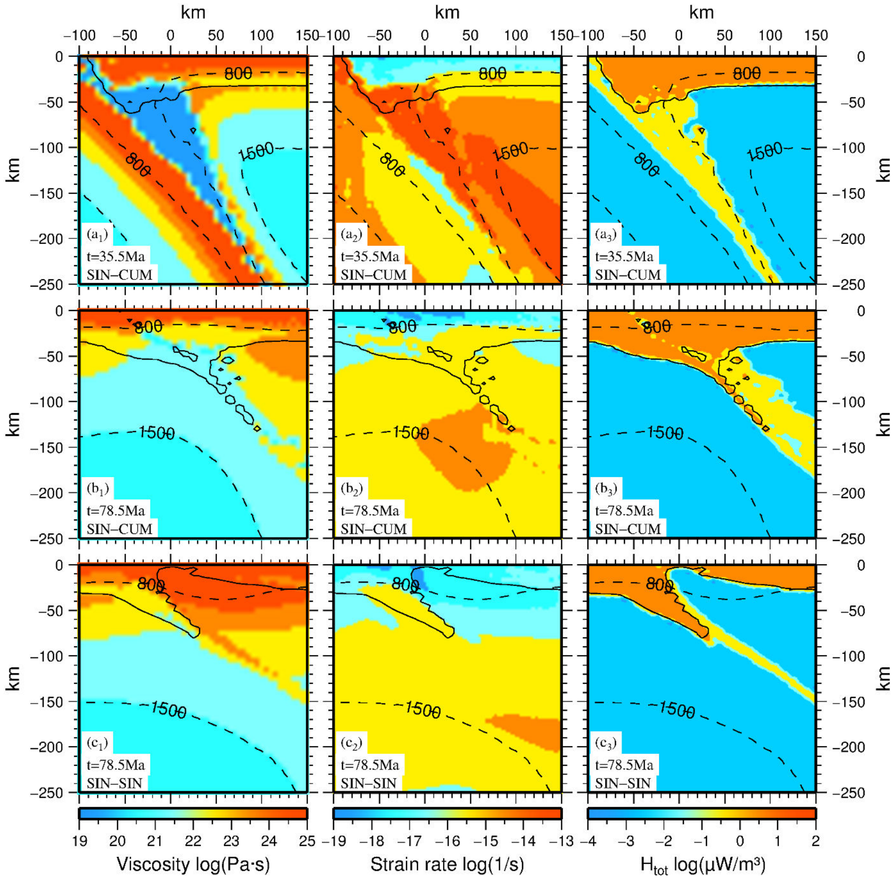

Figure 3.6: Distributions of the effective viscosity (panels a_1, b_1 and c_1), strain rate (panels a_2, b_2 and c_2) and total energy (panels a_3, b_3 and c_3) that were predicted by model SIN-CUM.5 at 35.5 Ma after the beginning of active convergence (panels a_i), model SIN-CUM.5 at 78.5 Ma after the continental collision (panels b_i) and model SIN-SIN.5 at 78.5 Ma after the continental collision (panels c_i). The dashed black lines indicate the 800 K and 1500 K isotherms. The black solid lines indicate the base of the continental crust.

the system in which the subducted lithosphere slowly warms while the temperature in the non-hydrated mantle wedge decreases because of the deactivation of the convective flow below the upper continental plate (Figure 3.3e; Figures 3.5e and f). In the SIN-SIN model the cooling affects the entire mantle wedge, while in the SIN-CUM models it affects only the external non-hydrated portion of the wedge. Differently, the hydrated area of the wedge behaves as the subducted lithosphere, showing a gradual increase of temperatures. In addition to the general warming of the system due to the natural thermal reequilibration that occurs during the pure gravitational phase in all models, the doubling of the crust in the SIN-CUM models causes an additional warming in the subduction complex due to the large amount of radiogenic energy (Figure 3.6b_3).

The new thermal field impacts the viscosity and the strain rate, which show significantly different trends in both the wedge area and the subducted lithosphere with respect to the previous active phase (Figures 3.6b_1 and b_2). Specifically, the viscosity decreases in the interior of the subducted lithosphere and increases in the wedge area by up to 3 orders of magnitude (Figure 3.6b_1), whereas the strain rate decreases in the entire domain by at least 3 orders of magnitude due to general decreases in velocity (Figure 3.6b_2) with small spatial gradients that are caused by crust-mantle compositional variations. The increase of viscosity in the wedge area is of the same order of magnitude both in the SIN-SIN and in the SIN-CUM models but with different values of viscosity. In fact, the viscosity in the wedge area of the SIN-CUM models during the active phase is lower than that in the SIN-SIN models (10^{19} and 10^{21}-10^{22} Pa·s, respectively), because of the stability of the serpentine in the hydrated area. In the same way, during the gravitational phase the viscosity is still lower in the wedge of the SIN-CUM models than in the SIN-SIN models (10^{22} and 10^{24}-10^{25} Pa·s, respectively), because of the higher temperatures due to the doubling of the crust.

In the SIN-CUM models the global warming observed in the subduction zone produces a gradual decrease of the extension of the area in which the serpentine is stable, which cause the de-hydration of the wedge and the consequent deactivation of the short-wavelength convective cells. In fact, for at least the first 10 Ma of the pure gravitational evolution, short-wavelength convective cells persist in the wedge area because of the significant extension of the hydrated domain (Figure 3.5e). Subsequently, these local dynamics quickly vanish with the concurrent disappearance of the hydrated area (Figure 3.5f).

The introduction of shear heating (CUM-CUM models) has significant impacts on the large-scale thermo-mechanics of the system throughout its active evolution. In particular, it generally increases the temperatures, decreases the magnitude of the convective flow, and reduces the dip of the slab. In addition, the higher the subduction velocity is, the lower the slab dip is (Figures 3.7a, b and d).

Warming of the subducting lithosphere also occurs, which is adequately demonstrated by the configuration of the 1500 K isotherm and by the shallower maximum depths that are reached by the 800 K isotherm with respect to the SIN-CUM models (approximately 220 km for CUM-CUM.8 compared to more than 400 km for SIN-CUM.8, approximately 140 km for CUM-CUM.5 compared to 370 km for SIN-CUM.5, and approximately 90 km for CUM-CUM.3 compared to 300 km for SIN-CUM.3; Figures 3.4a and b, red, green and blue continuous lines, respectively). The introduction of shear heating and the resulting increase of temperatures in the wedge area cause a reduction of the extent of the area in which the serpentine is stable and consequently of the low-viscosity hydrated domain. In spite of the decrease of the hydrated area, short-wavelength convective flows remain active, favouring also in these models the recycling of both continental and oceanic crustal material (Figures 3.8a and b).

The total energy in the non-hydrated mantle of the CUM-CUM models (Figure 3.9a_4) results to be up to 4 orders of magnitude higher than that of the SIN-CUM models (Figure 3.6a_3) because of the large amount of energy from shear heating (Figure 3.9a_3). Dif-

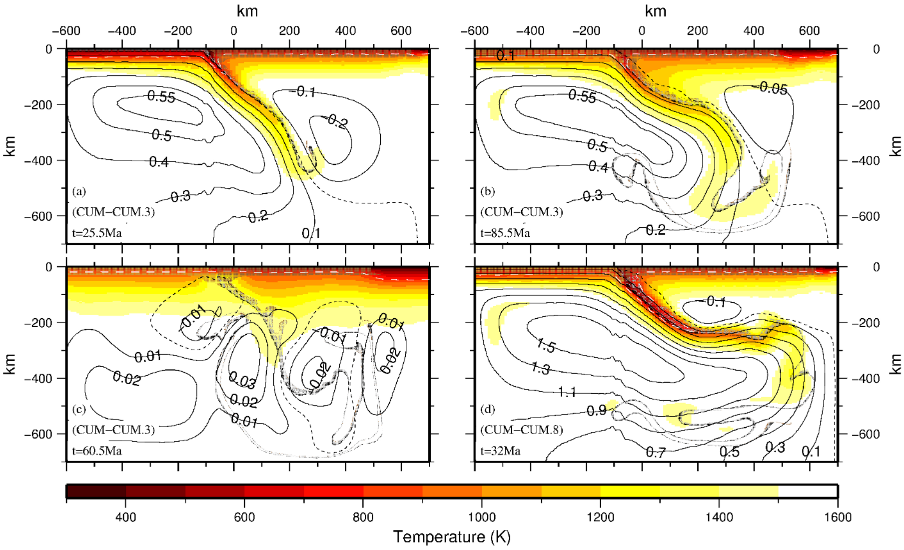

Figure 3.7: Large-scale temperature field (colours) and streamline patterns (black solid lines) for the model CUM-CUM.3 at 25.5 Ma (panel a) and 85.5 Ma (panel b) after the beginning of active convergence and at 60.5 Ma (panel c) after the continental collision. Panel d shows the same for model CUM-CUM.8 after 32 Ma of active subduction. The dashed white lines indicate the 800 K isotherm. Black, grey, dark brown and light brown points represent the lower oceanic crust, upper oceanic crust, continental crust of the upper plate, and continental crust of the lower plate, respectively.

ferently, the total energy in the hydrated area differs by less than 1 order of magnitude, because of the low viscosity and the consequent very low energy produced by shear heating (approximately 2-3 orders of magnitude lower than in the non-hydrated mantle). To further stress the role of the hydration mechanism on the local thermal state of the wedge area, panels b_i of Figure 3.9 shows the viscosity, strain rate, dissipated viscous energy and total energy predicted by a model in which hydration is not taken into account (CUM-SIN models). The higher temperatures predicted in the subduction complex of the CUM-SIN models are caused by the large amount of energy from shear heating, which is up to 6 orders of magnitude higher in the wedge area than in the upper plate, where energy is primarily generated by radiogenic decay. Thus, the total energy in the wedge area is approximately 1 order of magnitude higher than in the continental crust of the upper plate. The results show that the temperature increase driven by shear heating in the CUM-CUM models is less than that in the CUM-SIN models, because of the low viscosity and the consequently smaller amount of dissipated energy that characterise the hydrated area. In particular, the shear heating produced in the mantle wedge of the CUM-SIN models is at least 2 orders of magnitude higher than that produces in the hydrated wedge of the CUM-CUM models.

During the pure gravitational phase, the thermo-mechanical evolution of the CUM-CUM models is characterised by a progressive thermal erosion of the subducted slab that is consumed in approximately 60 Ma in models with low and medium subduction velocities that are prescribed during the active phase (Figures 3.7c). The warming of the

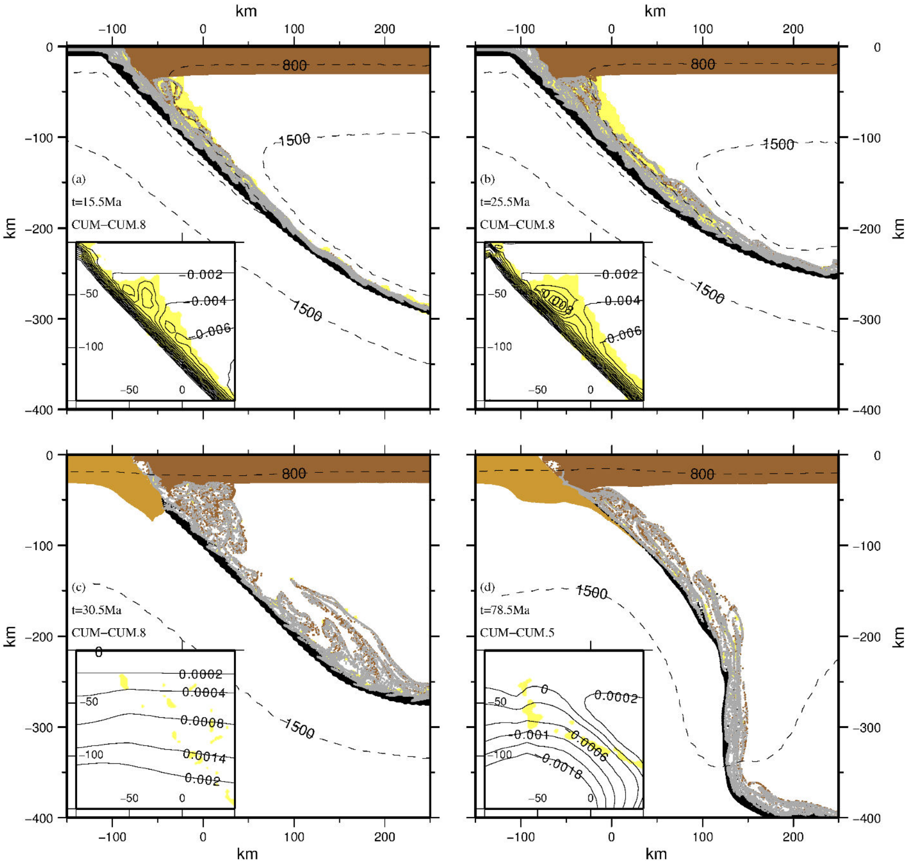

Figure 3.8: Temperature field in terms of the 800 K and 1500 K isotherms (dashed black lines) and streamline patterns (black solid lines in the insets) surrounding the wedge area for the CUM-CUM models at different times and for different subduction velocities. Panel (a): model CUM-CUM.8 at 15.5 Ma after the beginning of active convergence. Panel (b): model CUM-CUM.8 at 25.5 Ma after the beginning of active convergence. Panel (c): model CUM-CUM.8 at 30.5 Ma after the continental collision. Panel (d): model CUM-CUM.5 at 78.5 Ma after the continental collision. The yellow areas represent the hydrated wedge domains. Black, grey, dark brown and light brown points represent the lower oceanic crust, upper oceanic crust, continental crust of the upper plate, and continental crust of the lower plate, respectively.

subduction zone is similar to that observed in the SIN-CUM models, because during this phase the strain rates and the consequent energy produced by shear heating are very low, so that the total energy of the system strongly depends by the radiogenic decay. A peculiar feature of the CUM-CUM models is that during the gravitational phase, although at different times, slices of subducted crust separate from the slab and rise to shallower depths (Figures 3.8c and d), which widens the area that is occupied by recycled crustal material in the supra-subductive mantle.

3.3.2 Dynamics of the hydrated area

When both hydration and shear heating are allowed (CUM-CUM models), hydration of the mantle wedge starts within 1 Ma after the beginning of the evolution at all of the prescribed velocities and continues over a period that decreases as the prescribed velocity increases (Figures 3.10a_1, b_1 and c_1). Specifically, the hydration lasts 87.8 Ma in

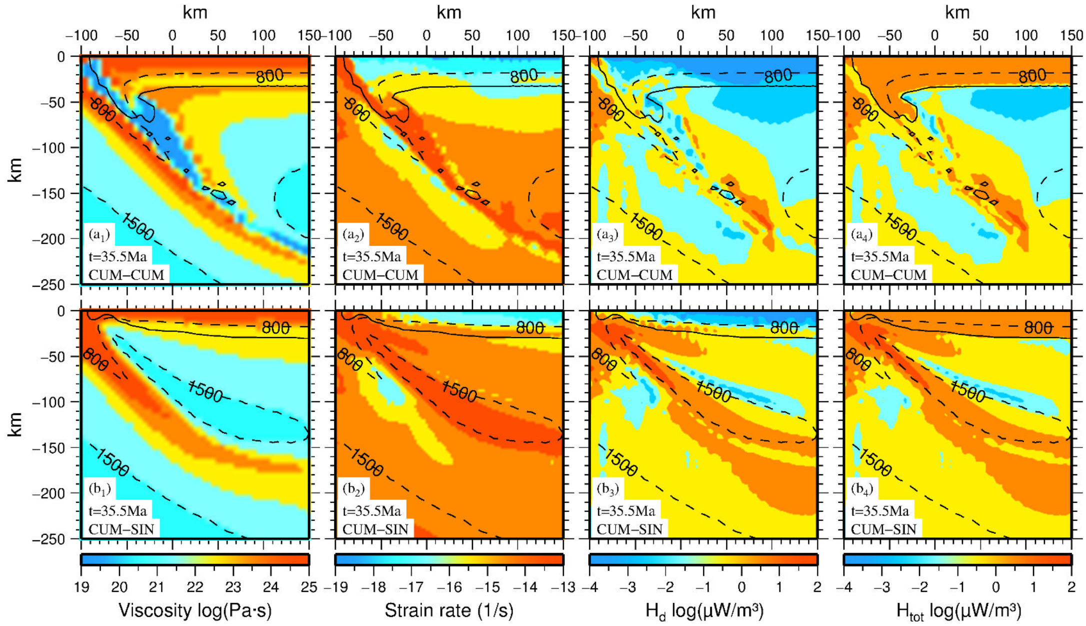

Figure 3.9: Distributions of the effective viscosity (panels a_1 and b_1), strain rate (panels a_2 and b_2), energy due to shear heating (panels a_3 and b_3) and total energy (panels a_4 and b_4) that were predicted by model CUM-CUM.5 at 35.5 Ma after the beginning of active convergence (panels a_i) and by model CUM-SIN.5 at 35.5 Ma after the beginning of active convergence (panels b_i). The dashed black lines indicate the 800 K and 1500 K isotherms, and the black solid lines indicate the base of the continental crust.

the CUM-CUM.3 model, 55.7 Ma in the CUM-CUM.5 model and 50.3 Ma in the CUM-CUM.8 model.

During the active phase, the maximum extent of the hydrated area increases with the increase of the prescribed velocity from approximately 2500 km^2 in model CUM-CUM.3 to 4250 km^2 in model CUM-CUM.5 to 8160 km^2 in model CUM-CUM.8 (Figures 3.10a_1, b_1 and c_1, respectively). This is due to the lower temperatures in the subducted slab predicted for models with intermediate and high convergence velocities and the consequent wider area in which serpentine is stable.

The evolution of the hydrated area is different for models with different prescribed velocity. In particular, models CUM-CUM.3 and CUM-CUM.5 show two maxima of extension after approximately 24 Ma and 52 Ma for CUM-CUM.3 and after approximately 22 Ma and 48 Ma for CUM-CUM.5. Differently, in model CUM-CUM.8 there is a progressive enlargement of the hydrated area, until a maximum just before the continental collision. At the collision, the hydrated area decreases abruptly in all models, by approximately 500 km^2 in CUM-CUM.3 and CUM-CUM.5 and by approximately 750 km^2 in CUM-CUM.8. This decrease follows the partial subduction of the continental crust of the lower plate, which confines the low viscosity hydrated channel between the upper plate and the subducting lithosphere (Figures 3.10a_5, b_5 and c_4). During the early stages of the post-collisional phase the hydrated area of all models gradually decrease, disappearing after 3.3 Ma in CUM-CUM.3, after 4.8 Ma in CUM-CUM.5 and after 18 Ma in CUM-

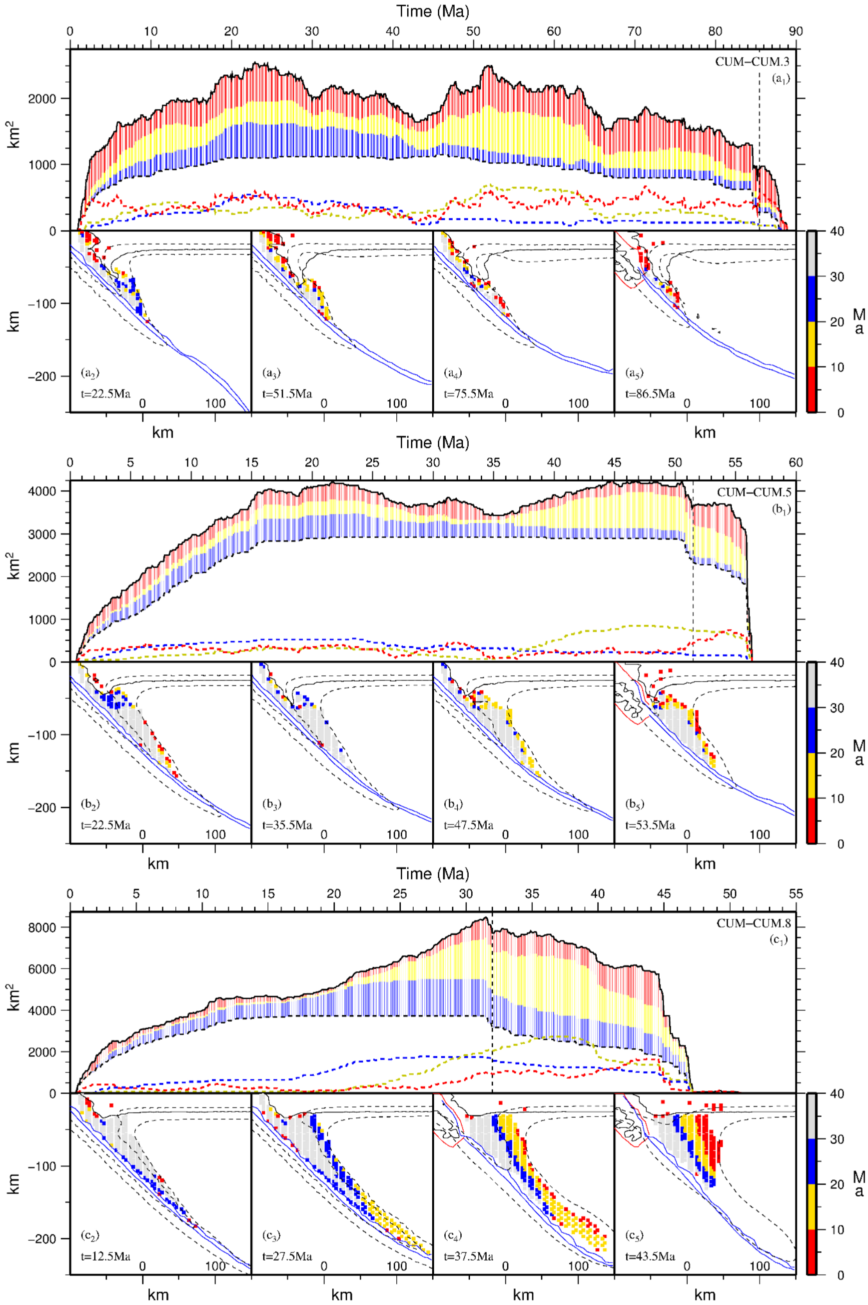

Figure 3.10: Panels a_1, b_1 and c_1 show the variations with time of the dimension of the total hydrated area (continuous black line) and of the main hydrated area (dashed black line) for models CUM-CUM.3, CUM-CUM.5 and CUM-CUM.8, respectively. Dashed coloured lines and coloured areas indicate the variations with time of the dimensions of the second-order hydrated domains (red for time spans shorter than 10 Ma, yellow for time spans between 10 Ma and 20 Ma, and blue for time spans between 20 Ma and 30 Ma). The vertical dashed lines indicate the beginning of the collision. Panels a_2-a_5, b_2-b_5 and c_2-c_5 show the areal configurations of the hydrated mantle domains at different times during the evolution of models CUM-CUM.3, CUM-CUM.5 and CUM-CUM.8, respectively. The hydrated elements are coloured according to the time span during which the element remains hydrated. The elements whose hydration time spans are longer than 30 Ma (grey) constitute the main hydrated area. The dashed black lines in panels a_2-a_5, b_2-b_5 and c_2-c_5 indicate the 800 K and 1500 K isotherms, and the black, red and blue solid lines identify the upper continental crust, the lower continental crust and the upper oceanic crust, respectively.

CUM.8. So, the duration of hydration during the pure gravitational phase increases with the increase of the pescribed velocity as results of the lower temperatures characterising the subducted slab for higher subduction rates before continental collision.

In all the models a main triangular hydrated area develops by a unique cycle that lasts longer than 30 Ma. The main hydrated area is characterised by an initial high gradient growth phase, an intermediate low gradient phase during which the extent remains almost constant, and a final phase with a large gradient decrease (black dashed lines in panels a_1, b_1 and c_1 and grey areas in panels a_2-a_5, b_2-b_5 and c_2-c_5 in Figure 3.10). During the initial phase, both the maximum extension and the mean growth rate of the main hydrated area increase with the increase of the prescribed velocity: 875 km^2 and 110 km^2/Ma, respectively, in CUM-CUM.3 (Figure 3.10a_1), 2875 km^2 and 171 km^2/Ma, respectively, in CUM-CUM.5 (Figure 3.10b_1), and 3750 km^2 and 302 km^2/Ma, respectively, in CUM-CUM.8 (Figure 3.10c_1). During the entire active phase, the main hydrated areas extend from maximum depths of 110 km for slow velocities (CUM-CUM.3; Figure 3.10a_3) to 150 km for medium and high velocities (CUM-CUM.5 and CUM-CUM.8; Figures 3.10b_3 and c_3, respectively) to shallow depths, where they extend along a narrow 45° dipping channel between the overriding and the subducting lithosphere. The occurrence of these shallow hydrated domains is related to the erosion of the upper plate that occurs during the early evolution of the system.

Second-order hydrated domains also develop in different positions with respect to the main hydrated area although they persist for shorter time periods. The occurrence and locations of the secondary hydrated areas are controlled by the periodic fluctuations in the thermal state that characterise the margins of the main hydrated area and determine the growth of both the external and deep portions of the total hydrated areas. In particular, three domains of short-period hydration can be identified: less than 10 Ma, between 10 and 20 Ma and between 20 and 30 Ma (red, yellow and blue colours in Figure 3.10, respectively).

Two main episodes of short-period growth occur for models CUM-CUM.3 (Figures 3.10a_1, a_2 and a_3) and CUM-CUM.5 (Figures 3.10b_1, b_2 and b_3) in correspondence of the two absolute maxima observed in the extension of the total hydrated area. For both models the first episode is related to short-period hydration of 20-30 Ma (Figures 3.10ai and bi), while the second epsode is related to short-period of 10-20 Ma (yellow colours in Figures 3.10a_i and b_i). In addition, for CUM-CUM.3 model in both episodes there is hydration for period less than 10 Ma (red colours in Figures 3.10ai). For model CUM-CUM.5 a third episode occurs after the collision, between 52 and 56 Ma. This short-period hydration (less than 10 Ma) balances the decrease of the hydrtaed area caused by the longer periodicities, determining an enlargement of approximately 500 km^2 toward the external portion of the wedge (Figure 3.10b_5).

The more stable thermal field that characterizes the active phase of the high velocity model (CUM-CUM.8) allows only one brief episode of growth before the collision at approximately 27 Ma (Figure 3.10c_1). This episode is associated with short-periods of hydration that last between 20 and 30 Ma (blue colour in Figures 3.10c_i) and contributes to the expansion in depth and towards the margins of the main hydrated area (Figure 3.10c_3). Similar to model CUM-CUM.5, an episode of short-period hydration of less than 10 Ma (red colour in Figures 3.10c_i) occurs after the collision between 42 Ma and 44 Ma; this contrasts with the decrease of the longer periodicities and controls the marginal widening of the hydrated area of approximately 775 km^2 (Figure 3.10c_5).

To stress the role of shear heating on the dynamics of the hydrated area, the main similarities and differences between the CUM-CUM and SIN-CUM models are discussed below. The general evolution of the hydrated area is similar in the models with and without shear heating and is characterised by three features:

1. hydration starts within 1 Ma after the beginning of the active phase (Figures 3.11a_1, b_1 and c_1);

2. during the initial phase, the growth rate of the hydration area increases with increasing velocity; specifically, approximately 500 km^2/Ma for SIN-CUM.3, 1041.7 km^2/Ma for SIN-CUM.5 and 1666.7 km^2/Ma for SIN-CUM.8 (Figures 3.11a_1, b_1 and c_1, respectively);

3. main and second-order hydrated domains develop; the latter are predominantly located along the external and deepest portions of the main hydrated area and increase the hydrated area after the collision by several hundreds of square kilometres, up to 4800 km^2 for high velocities (SIN-CUM.8 model) (Figure 3.11c_1).

However, in the framework of the general dynamics, several differences can be identified:

1. hydration lasts longer than in the respective models with shear heating because of the persistence of PT conditions under which serpentine is stable for a longer time interval during the post-collisional phase (42.4 Ma for SIN-CUM.3, 32.7 Ma for SIN-CUM.5 and 33.2 for SIN-CUM.8, Figures 3.11a_1, b_1 and c_1, respectively);

2. the extent of the main hydrated area increases with decreasing velocity during the active phase (black lines in Figures 3.11a_1, b_1 and c_1);

3. all of the SIN-CUM models show an increase in the extent of the hydrated area during the pure gravitational phase that is due to the occurrence of brief episodes of growth that last less than 30 Ma (red, yellow and blue colours in Figure 3.11) and are located in the shallow and external portion of the wedge (Figures 3.11a_5, b_5 and c_5);

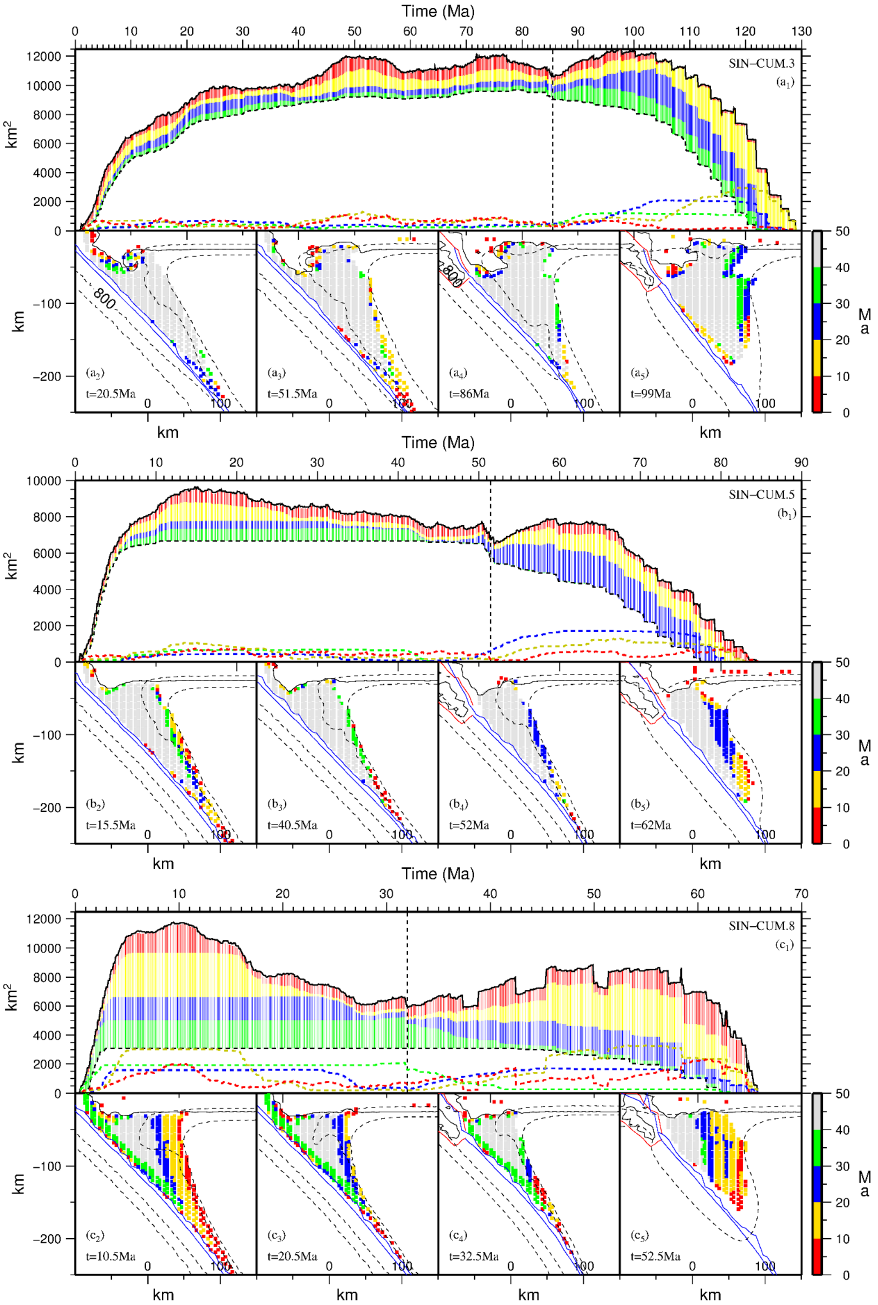

Figure 3.11: Panels a_1, b_1 and c_1 show the variations with time of the dimensions of the total hydrated area (continuous black line) and of the main hydrated area (dashed black line) for models SIN-CUM.3, SIN-CUM.5 and SIN-CUM.8, respectively. Dashed coloured lines and coloured areas indicate the variations with time of the dimensions of the second-order hydrated domains (red for time spans shorter than 10 Ma, yellow for time spans between 10 Ma and 20 Ma, blue for time spans between 20 Ma and 30 Ma and green for time spans between 30 Ma and 40 Ma). The vertical dashed lines indicate the beginning of the collision. Panels a_2-a_5, b_2-b_5 and c_2-c_5 show the areal configurations of the hydrated mantle domains at different times during the evolution of models SIN-CUM.3, SIN-CUM.5 and SIN-CUM.8, respectively. The hydrated elements are coloured according to the time span during which the element remains hydrated. The elements whose hydration time spans are longer than 40 Ma (grey) constitute the main hydrated area. The dashed black lines in panels a_2-a_5, b_2-b_5 and c_2-c_5 indicate the 800 K and 1500 K isotherms. The black, red and blue solid lines in the same panels identify the upper continental crust, the lower continental crust and the upper oceanic crust, respectively.

4. the main hydrated area persists for a minimum of 40 Ma (grey colour in Figure 3.11), and the second-order hydrated domains last for slightly longer than in the CUM-CUM models (periodicities between 30 Ma and 40 Ma; green colour in Figure 3.11).

All of these effects are ascribable to the lower and more stable thermal field that is predicted in the absence of an additional energy budget from shear heating. In all SIN-CUM models, the thermal field in the wedge area changes during successive evolutionary stages. In particular, during the early stages of active subduction the slower the velocity, the warmer and smaller the wedge domain is. Differently, during the advanced stages of active subduction, the slower the prescribed velocity is, the colder the temperature in the wedge and the larger the main hydrated area. In particular, model SIN-CUM.3 undergoes both progressive and continuous cooling throughout the active subduction phase (Figures 3.11a_2-a_4), while model SIN-CUM.8 is characterised by an initial cooling phase until 10 Ma and a successive rapid warming with a significant decrease in the extent of the hydrated area (Figures 3.11c_2-c_4).

3.3.3 Metamorphic Facies

Traditionally, three metamorphic series with different P/T ratios are identified and they are associated to different phases of evolution of subduction/collision complexes (see Section 1.4). However, it has been suggested that different metamorphic facies can coexist in the same geodynamic environment contemporaneously. For example, the different members of the Leptino-Amphibolitic Complex in the French Massif Central show significantly contrasted metamorphic P-T conditions recorded during their evolution, from Blueschist to HP-Granulite facies (*Lardeaux et al.*, 2014). Furthermore, *Roda et al.* (2012) show that the thermal gradient in a subduction zone can vary in time and space for the same subduction rate. These data suggest that a thermal gradient could be no peculiar of a single geodynamic process, but contrasted gradients and thermal state can be recorded in the same geological environment as function of the path that rocks underwent during their evolutions. The P-T conditions recorded by the markers during both the evolutionary stages of the models have been compared to P-T conditions peculiar of metamorphic facies to investigate the distribution and the evolution of metamorphic environments characterising subduction/collision complexes during successive stages of their dynamics.

During the whole evolution of the SIN-CUM model, at the base of the crust of the upper plate P-T conditions are compatible with Amphibolite facies exclusively (Figure 3.12). This is due to the dynamics in the hydrated wedge that prevents mantle flow from both reaching the internal portions of the wedge and warming the crust of the upper plate. In fact, in the hydrated portion of the wedge there is the activation of short wavelength

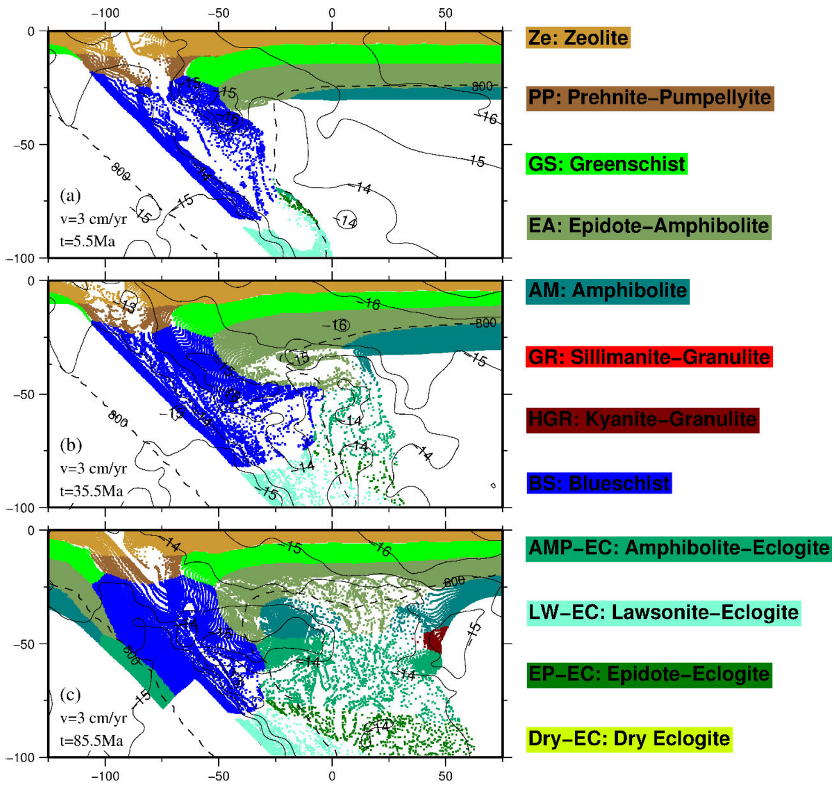

Figure 3.12: Distribution of metamorphic facies (identifies by different colours) during the active subduction phase for SIN-CUM.3 model. The legend of the colours of the facies is represented on the right of the figure. Dashed black lines indicate 800 K isotherm. Continous black lines indicate the contours of areas with equal the strain rates.

convective cells that favour the recycling of cold subducted material. In SIN-CUM.5 and in SIN-CUM.8 models the mantle flow is more intense, producing a slight increase of temperature after 30 Ma. This warming is essential to develop P-T conditions compatible with Sillimanite-Granulite facies farther than 150 km from the trench (Figure 3.13, panels b and c). Chlorite is stable in the lithospheric mantle below the crust of the upper plate for the whole duration of the active phase. The increasing of the mantle flow produces also an increase of temperature in the external portion of the wedge, reducing the extension of the area in which Serpentine is stable. As a consequence, lower the velocity of subduction greater the extension of the hydrated area (Figure 3.13).

During the early stages, Blueschist facies conditions characterise the crustal material subducted up to 75 km depth, both oceanic deriving from the lower plate and continental tectonically eroded by the upper plate (Figure 3.12a). With the progress of the evolution, the area characterised by P-T conditions in the stability field of Serpentine enlarges toward more external portions from the trench, causing a large amount of crust to be recycled under Amphibole-Eclogite and Epidote-Eclogite facies conditions, below 50 km depth (Figures 3.12b and c). In the shallowest portions of the wedge, the recycled crustal material is primarily continental and it records metamorphic conditions characterised by

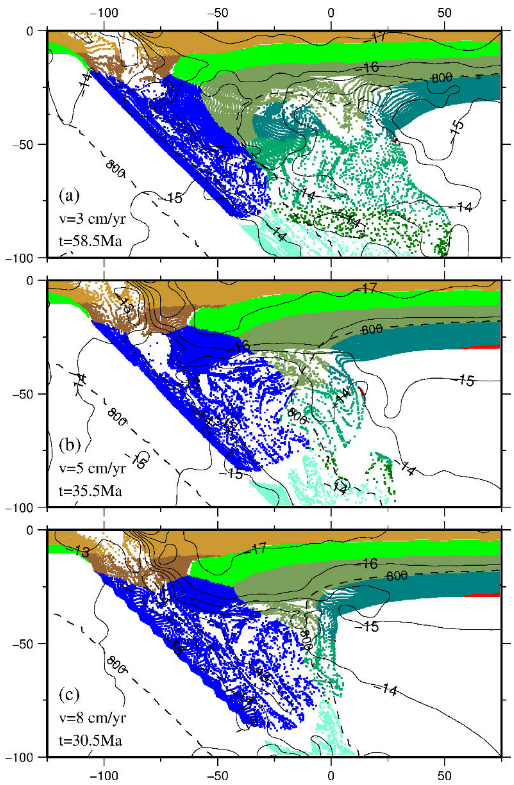

Figure 3.13: Distribution of metamorphic facies (identifies by different colours) during the active subduction phase for models SIN-CUM.3 (panel a), SIN-CUM.5 (panel b) and SIN-CUM.8 (panel c). The legend of the colours of the facies is the same represented in Figure 3.12. Dashed black lines indicate 800 K isotherm. Continous black lines indicate the contours of areas with equal the strain rates.

intermediate P/T ratios, as Epidote-Amphibolite and Amphibolite facies conditions (Figures 3.12b and c). In SIN-CUM.5 model, after 35 Ma Kyanite-Granulite facies conditions develop in the most external portion of the hydrated wedge, at a depth of approximately 50 km (Figure 3.13b). The temperature in the internal portion of the subducted plate is lower for higher subduction velocities, because of the increase of cold material subducted during the same time span. As a consequence, the extension of the area charcaterised by Blueschist facies conditions increases with the increase of velocity (Figure 3.13). Chlorite is stable in the shallower and external portion of the mantle wedge, where the subducted crust is characterised by Amphibolite, Kyanite-Granulite and Amphibole-Eclogite facies conditions.

Strain rates higher than 10^{-14} 1/s are localised where low viscosities are assumed (10^{19} Pa·s), both in correspondence of the trench and in the hydrated area. Near the trench, highest strain rates are developed by oceanic and continental crust under Zeolite, Prehnite-Pumpellyite and Blueschist facies conditions (Figures 3.12a and b). During the latter stages of evolution, high strain rates are developed also under Greenschist and Epidote-Amphibolite facies conditions (Figure 3.12c). In the hydrated domain highest strain rates are developed by continental and oceanic crust under P-T conditions compatible with Epidote-Ampibolite, Blueschist, Amphibole-Eclogite and Lawsonite-Eclogite facies (Figure 3.12). Amphibolite facies conditions develop primarily in portions of the hydrates domain with strain rates between 10^{-14} 1/s and 10^{-15} 1/s (Figure 3.12). At the collision, strain rates higher than 10^{-14} 1/s can develop also in the continental crust of the lower plate, under P-T conditions compatible with Zeolite, Prehnite-Pumpellyite and Blueschist facies (Figure 3.12c). Strain rates higher than 10^{-13} 1/s can be observed under Blueschist facies conditions for SIN-CUM.5 model (Figure 3.13b) and under Blueschist and Epidote-Amphibolite facies conditions for SIN-CUM.8 model (Figure 3.13c).

Metamorphic facies with high P/T ratios, traditionally considered characteristic of active subductions, remain stable until the early stages of the post-collisional phase, although a general warming of the system due to a thermal re-equilibration. In particular, Blueschist conditions are satisfied until approximately 5.5 Ma for SIN-CUM.3 model (Figure 3.14a), 8.5 Ma for SIN-CUM.5 model (Figure 3.14b) and 10.5 Ma for SIN-CUM.8 model (Figure 3.14c), while Amphibole-Eclogite conditions are satisfied until approximately 30 Ma in broad portions below 40 km depth (Figure 3.14d). The extension of the area characterised by these facies decreases at the expense of both the gradually increase of the extension of the area characterised by Kyanite-Granulite facies conditions and the appearance and widening of the area satisfying Sillimanite-Granulite P-T field at 30 km depth. Kyanite-Granulite becomes the most extended metamorphic facies during the final stages (Figures 3.14g, h and i), while Sillimanite-Granulite facies conditions develop stably after approximately 32.5 Ma for SIN-CUM.3 model (Figure 3.14d), 35.5 Ma for SIN-CUM.5 model (Figure 3.14e) and 55.5 Ma for SIN-CUM.8 model (Figure 3.14f). In SIN-CUM. 5 model the area with P-T conditions compatible with Sillimanite-Granulite facies (Figure 3.14e) is larger than both in SIN-CUM.3 model and in SIN-CUM.8 model, farther than 100 km from the trench. On the contrary, in SIN-CUM.8 there is the slowest growth of the area characterised by Kyanite-Granulite facies conditions and the final extension of the area characterised by Sillimanite-Granulite facies is lesser than in SIN-CUM.3 model (Figures 3.14f and d, respectively). The portion of the mantle wedge in the stability field of Serpentine reduces progressively, to the detriment of the growth of the area in the stability field of Chlorite. At the end of the evolution, Amphibole and Spinel are stable in the lithospheric mantle in correspondence of Sillimanite-Granulite and Kyanite-Granulite facies conditions in the crust.

Strain rates higher than 10^{-14} 1/s can be observed in SIN-CUM.3 model and in SIN-CUM.8 model until approximately 15 Ma under Epidote-Amphibolite, Amphibole-Eclogite and Epidote-Eclogite facies conditions, and until 30 Ma only in a small area under Epidote-Amphibolite conditions. In SIN-CUM.5 model high strain rates persist until 8.5 Ma under Amphibolite, Kyanite-Granulite and Amphibole-Eclogite facies conditions (Figure 3.14b).

For what concerns the CUM-CUM model,low viscosity assumed in the hydrated area

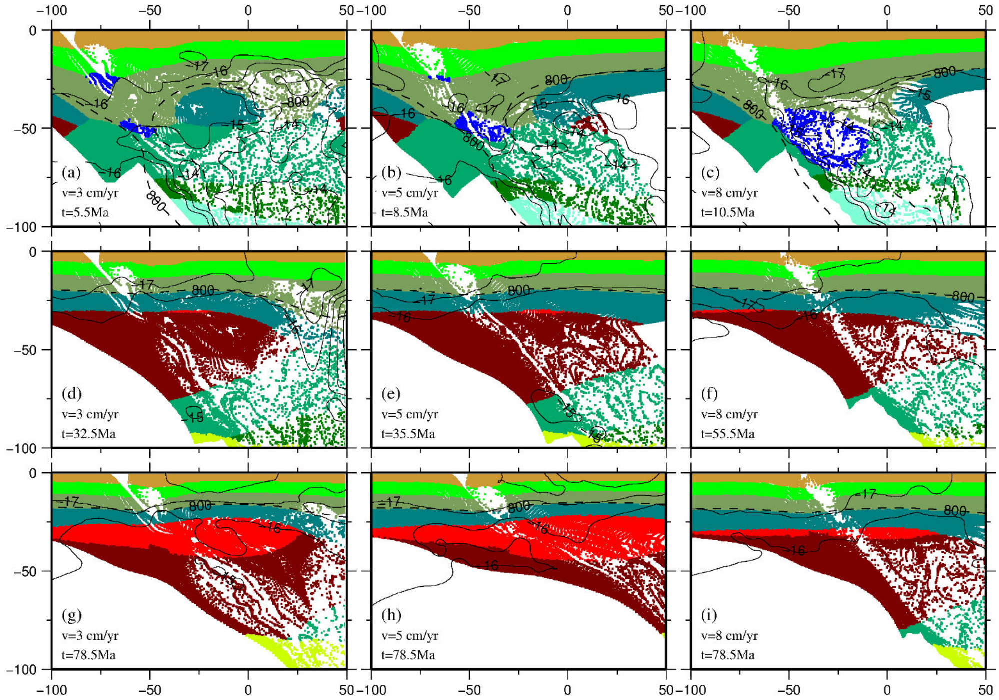

Figure 3.14: Distribution of metamorphic facies (identifies by different colours) during the post-collisional phase for models SIN-CUM.3 (panels a, d and g), SIN-CUM.5 (panels b, e and h) and SIN-CUM.8 (panels c, f and i). The legend of the colours of the facies is the same represented in Figure 3.12. Dashed black lines indicate 800 K isotherm. Continous black lines indicate the contours of areas with equal the strain rates.

(10^{19} Pa·s) do not affect highly the production of viscous heating, although high strain rates. Differently, high viscosities in the non-hydrated mantle produces high values of viscous heating in the external portion of the wedge, with a consequent increase of temperature. This increase of temperature causes a decrease of the extension of the area in the stability field of Serpentine, with a consequent reduction of both the hydrated domain and the area affected by recycling of subducted material. Differently from SIN-CUM model, the area with P-T conditions compatible with the stability field of Serpentine is wider for higher velocity of subduction, because of lower temperatures in the subducted plate.

As in the SIN-CUM models, metamorphic facies with intermediate and high P/T ratios develop simultaneously during the active subduction phase. Amphibolite and Sillimanite-Granulite facies conditions develop at the base of the crust of the upper plate (Figure 3.15). Moreover, Sillimanite-Granulite facies occupies a thin portion further than 100 km after 20 Ma of evolution (Figures 3.15d, e and f). In CUM-CUM.3 model, continental crust in a portion at about 30 km depth and 75-100 km far from the trench has P-T conditions compatible with Sillimanite-Granulite facies, starting from 60 Ma of evolution (Figure 3.15g).

Zeolite, Prehnite-Pumpellyite and Blueschist facies conditions develop in correspondence of the trench and Blueschist, Amphibole-Eclogite and Epidote-Eclogite facies con-

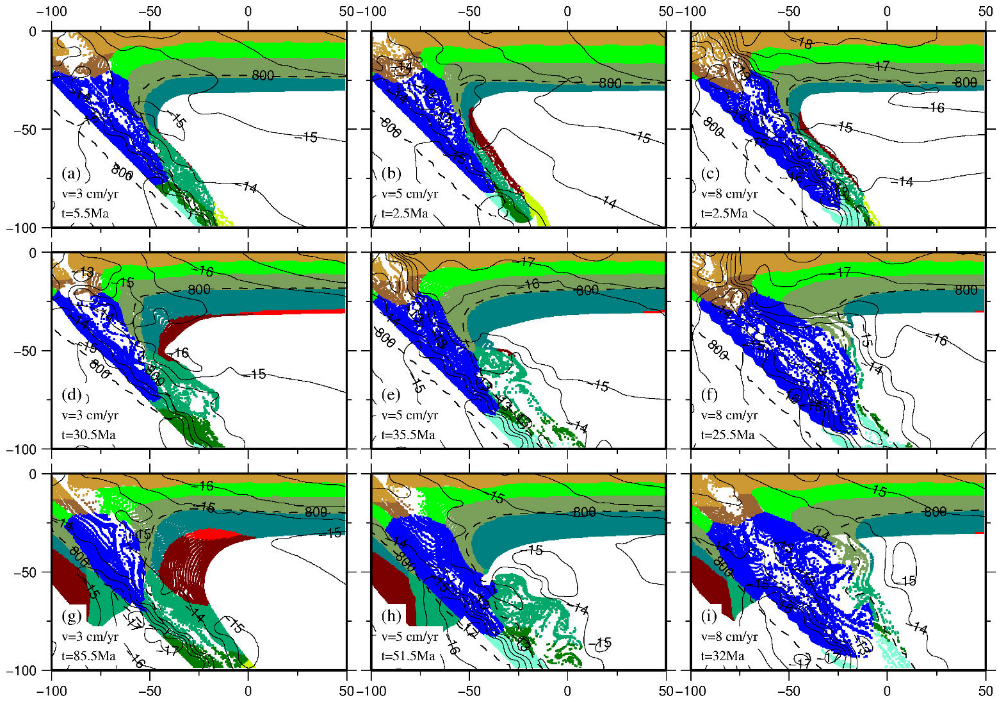

Figure 3.15: Distribution of metamorphic facies (identifies by different colours) during the active subduction phase for models CUM-CUM.3 (panels a, d and g), CUM-CUM.5 (panels b, e and h) and CUM-CUM.8 (panels c, f and i). The legend of the colours of the facies is the same represented in Figure 3.12. Dashed black lines indicate 800 K isotherm. Continous black lines indicate the contours of areas with equal the strain rates.

ditions characterise the hydrated area. The area characterised by Blueschist conditions is more extended for higher velocities (Figure 3.15). These metamorphic facies are recorded by both oceanic crust derived by the lower plate and continental crust tectonically eroded by the upper plate. Lawsonite-Eclogite conditions are attained in the early stages of evolution below 80 km depth in all models (Figures 3.15a, b and c) and they remain stable also in latter stages of active subduction evolution for CUM-CUM.5 and CUM-CUM.8 models (Figures 3.15e, f, h and i). At the collision, part of the continental crust of the lower plate shows P-T conditions compatible with Blueschist facies (Figures 3.15g, h and i).

Continental crust eroded by the upper plate develop P-T conditions compatible with Kyanite-Granulite in the external portion of the hydrated area, starting from 30 Ma of evolution for CUM-CUM.3 model (Figure 3.15d) and within 5 Ma of evolution for CUM-CUM.5 and CUM-CUM.8 models (Figures 3.15b and c, respectively). In CUM-CUM.5, Kyanite-Granulite facies can be recorded also after 35 Ma, by both continental crust of the upper plate and oceanic crust (Figure 3.15e).

Highest strain rates, higher than 10^{-13} 1/s, can develop during the whole active evolution in domains in the P-T field of Zeolite, Prehnite-Pumpellyite, Blueschist, Amphibole-Eclogite and Epidote-Eclogite facies. As in SIN-CUM models, higher the velocities larger the extension of the area in which strain rates higher than 10^{-13} 1/s can be developed

(Figure 3.15).

Metamorphic facies with a high P/T ratio can be observed also during the early stages of the post-collisional phase. In particular, areas under Blueschist facies conditions survive until 2.5 Ma for CUM-CUM.3 model and for CUM-CUM.5 model (Figures 3.16a and b, respectively), and until 10.5 Ma for CUM-CUM.8 model (Figure 3.16c). The progressive warming of the system induce an enlargement of the area characterised by P-T conditions compatible with Kyanite-Granulite and Sillimanite-Granulite facies, with a slower growth for faster subduction velocities. For CUM-CUM.3 model Kyanite-Granulite facies grows until 10.5 Ma of evolution of the pure gravitational phase, when is the most extended facies between 30 km and 70 km deep (Figure 3.16d); for CUM-CUM.5 model it grows until 25.5 Ma, when occurs in the whole thickened crust between 30 km and 70 km deep (Figure 3.16e); for CUM-CUM.8 model it reaches the maximum extension at the end of the evolution (Figure 3.16i). The extension of Sillimanite-Granulite facies at the end of the evolution is larger for lower prescribed velocities of subduction. It extends up to about 150 km far from the trench, with a maximum thickness between about 30 km in CUM-CUM.3 model and about 15 km in CUM-CUM.8 model (Figures 3.16g, h and i). Strain rates higher than 10^{-14} 1/s can be observed only in the early stages in CUM-CUM.8 model, in correspondence of Blueschist, Amphibole-Eclogite and Epidote-Eclogite facies conditions (Figure 3.16c).

3.3.4 Predicted P-T

Below, P- and T-peak conditions of the markers that reside in the mantle wedge at the end of the active subduction evolution are analysed. This is essential to verify that markers which recorded intermediate P/T conditions during the early stages of the active evolution were not carried in depth, having the chance to be exhumed during the following stages of evolution. Two P- and T-peak conditions are discriminated: one characterising the active phase, P_{maxA} and T_{maxA}, and one characterising the post-collisional phase P_{maxC} and T_{maxC}. In the following Figures, the three coloured areas indicate metamorphic gradients for low (red - Abukuma or Buchan gradients), intermediate (yellow - Dalradian or Barrovian gradients) and high (light blue - Franciscan or Sanbagawa gradients) P/T ratios under which crustal rocks, occupying different positions in an evolving convergent margin, can be re-equilibrated.

The recycling of abundant continental and oceanic crustal material is triggered during the subduction phase (Figure 3.17) because of the activation of short-wavelength convective cells in the mantle wedge, which reflect the P-T conditions of the involved crustal markers. An analysis of the P_{maxA}-T trend indicates that large amounts of continental crust from the upper plate, which correspond to areas of approximately 6700, 8000 and 7000 km^2 for subduction rates of 3, 5 and 8 cm/yr, respectively, record P_{maxA}-T condi-

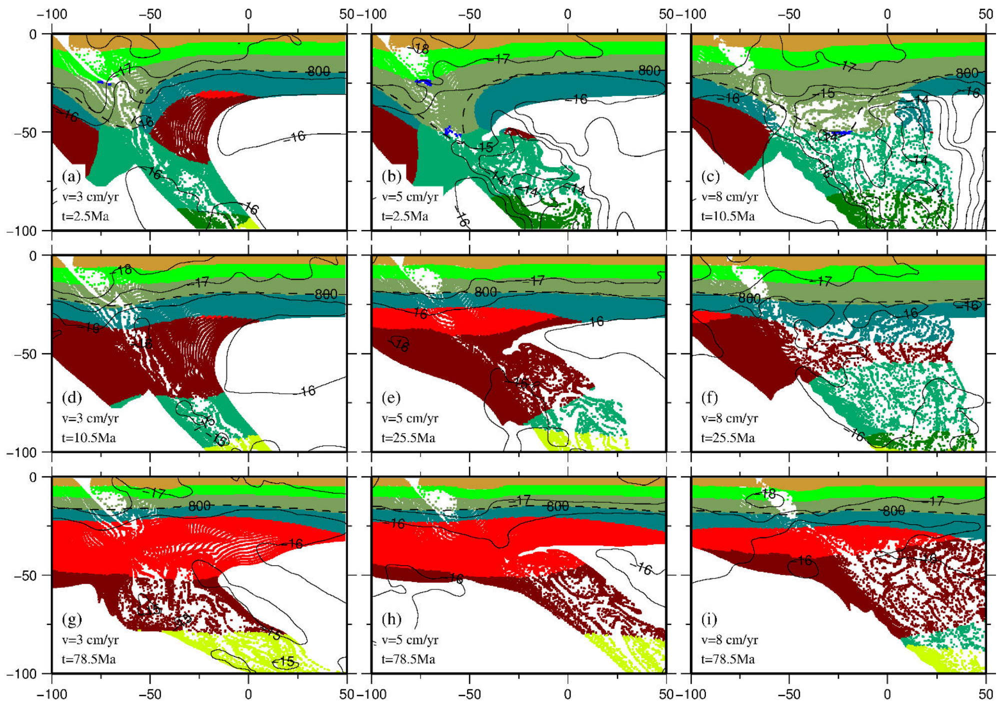

Figure 3.16: Distribution of metamorphic facies (identifies by different colours) during the post-collisional phase for models CUM-CUM.3 (panels a, d and g), CUM-CUM.5 (panels b, e and h) and CUM-CUM.8 (panels c, f and i). The legend of the colours of the facies is the same represented in Figure 3.12. Dashed black lines indicate 800 K isotherm. Continous black lines indicate the contours of areas with equal the strain rates.

tions with intermediate P/T ratios (represented by the yellow area), which are warmer than those that were prescribed by the initial continental geotherm. For these markers, P_{maxA} was recorded during the early stages of the active subduction phase until approximately 10 Ma in P-T conditions compatible with Greenschist, Epidote-Amphibolite and Amphibolite facies conditions (Figures 3.17a and b). Differently, their T_{maxA} values show that they could have recorded P-T conditions compatible with Sillimanite-Granulite facies during their path (Figures 3.17c and d). From these, it can be deduced that these markers have recorded their P-T_{maxA} under Sillimanite-Granulite facies conditions in the upper plate during the early stages of active evolution, and then they were never deeply involved in the subduction system, but they were displaced while remaining within (or coherent with) the continental crust of the upper plate from the external portion of the convergent margin toward the wedge area, characterised by a colder thermal regime.

A smaller area of both oceanic and continental material (ranging from 2,000 km^2 for a subduction rate of 3 cm/yr to 1000 km^2 for a subduction rate of 8 cm/yr) records high P/T ratios that reach pressures of up to 3 GPa and temperatures up to 800 K during sinking. After being subducted, the materials that are involved in mantle wedge recycling are uplifted because of the formation of convective cells in the hydrated area. As a consequence of the cold thermal state observed in the hydrated area, their P-T conditions are colder than the initial continental geotherms (represented by the green area). These

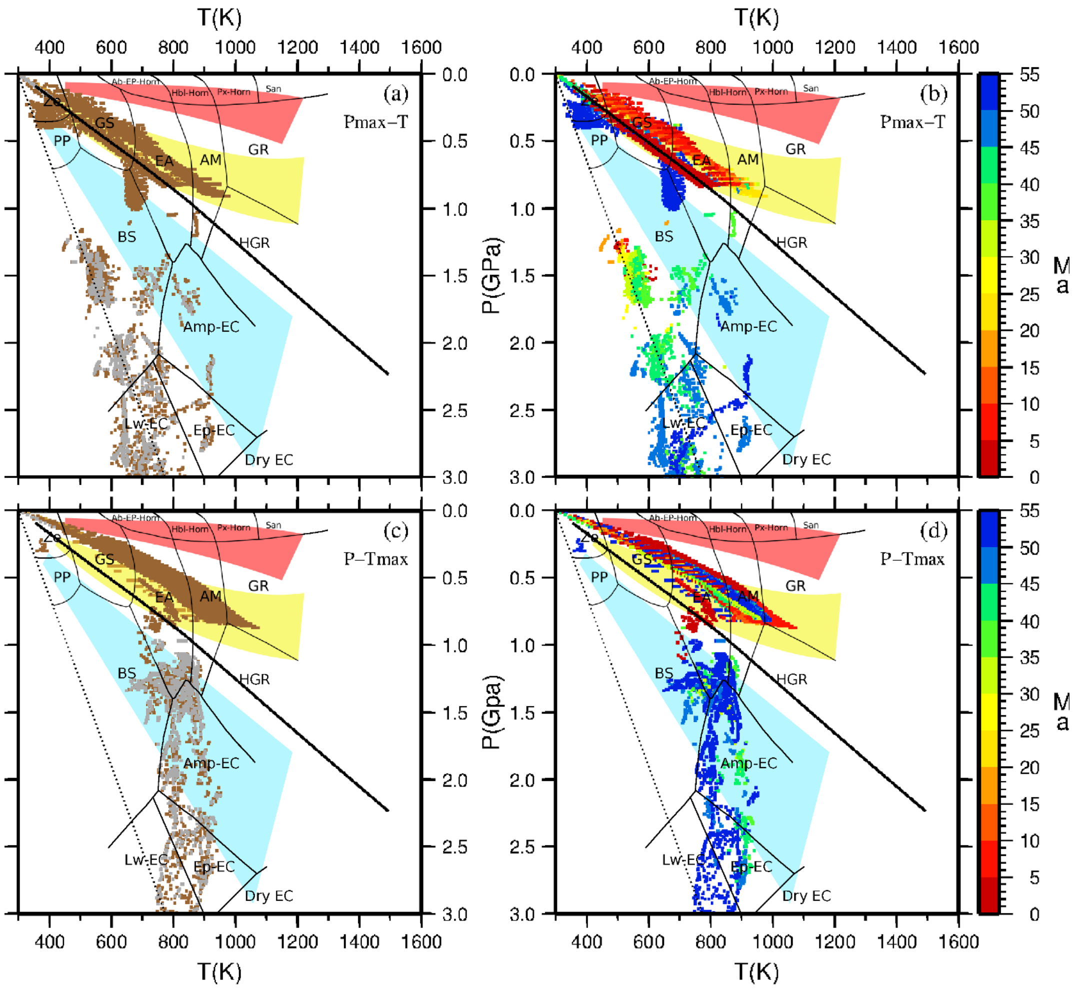

Figure 3.17: Predicted P_{maxA} -T (panels a and b) and P-T_{maxA} (panels c and d) distributions of the markers that have been partially exhumed during the active phase for the model SIN-CUM.5. In panels a and c, gray, dark brown and light brown points represent the upper oceanic crust, the continental crust of the upper plate and the lower plates, respectively. In panels b and d, the markers are coloured according to the age at which P_{maxA} and T_{maxA} conditions are reached. The thick black lines represent the unperturbed continental geotherm. The red areas indicate metamorphic gradients for low P-T series (Abukuma or Buchan metamorphism), the yellow areas for medium P-T series (Dalradian or Barrovian metamorphism), and the light blue areas for high P-T series (Franciscan or Sanbagawa metamorphism).

markers show compatibility with P-T conditions of different metamorphic facies; some of them reach their P_{maxA} under Blueschist conditions and the ages of their pressure peak are distribute during the whole evolution, while some other markers record their P_{maxA} values under P-T conditions compatible with Amphibole-Eclogite, Epidote-Eclogite and Lawsonite-Eclogite facies during the latter stages of evolution (Figures 3.17b). T_{maxA} values recorded in conditions characterised by high P/T ratio are reached primarily in the latter stages (Figures 3.17d).

Panel a of Figure 3.18 shows the predicted pressures and temperatures that are recorded by all of the crustal markers, both oceanic and continental, at different times during the entire active subduction phase for the SIN-CUM models. Different colours are used to differentiate successive time intervals from the beginning of the evolution. The global thermal configuration of the system does not change significantly with time; the non-subducted markers in the upper plate (P < 0.8 GPa) have intermediate P/T ratios, while the subducted markers in both the upper and lower plates (P > 0.8 GPa) have high P/T ratios. These results indicate that intermediate P/T ratios can coexist with high P/T ratios within an active subduction complex (Figure 3.18a).

During the pure gravitational phase (Figure 3.19), a large amount of continental crust that belongs to the upper plate rises to shallower depths, which is consistent with the accretion of crustal material in the wedge at the end of the active subduction phase (an area that ranges from approximately 3500 km^2 in models SIN-CUM.3 and SIN-CUM.5 to 730 km^2 in model SIN-CUM.8). Following the collision, the concentration of P_{maxC}-T values of the continental markers from the lower plate (Figure 3.19a) shift from the Franciscan to Barrovian fields from the beginning to the end (red to blue colours in Figure 3.19a, respectively) of the gravitational phase, whereas the P_{maxC}-T values of the continental markers from the upper plate remain in the Barrovian field during the entire gravitational phase. The P_{maxC}-T distribution (Figure 3.19a) shows that the maximum T values are 1300 K for models SIN-CUM.3 and SIN-CUM.5 and 1200 K for model SIN-CUM.8.

After the continental collision, in all the SIN-CUM models a cold thermal regime compatible with an active subduction phase is maintained in the system for few Ma. In fact, a large amount of markers, both oceanic and continental, develop P_{maxC}-T conditions compatible with Blueschist, Amphibole-Eclogite and Epidote-Eclogite facies during the early stages of the post-collisional phase (Figure 3.19a). After that there is a progressive increase of temperature with time (Figure 3.18b) and T_{maxC} values are mainly recorded at the end of the evolution (e.g., Figure 3.19b) under P-T values characterising Greenschist, Epidote-Amphibolite, Amphibolite, Sillimanite-Granulite and Kyanite-Granulite facies. All markers record intermediate to high P/T ratios with a migration toward P-T conditions that are warmer than the initial continental geotherm (black line in Figure 3.18b).

The velocities that are prescribed during the active subduction phase influence the distribution of the P-T_{maxC} values. In particular, for low velocities (model SIN-CUM.3), the markers that record P > 0.5 GPa have temperatures that range between 800 K and 1300 K and are characterised by intermediate to high P/T ratios. For intermediate velocities (model SIN-CUM.5), the markers are distributed along a narrow curved area with a maximum temperature of approximately 1400 K at approximately 1.5 GPa. These markers plot in the Barrovian field, with the exception of markers with P > 2 GPa, which are characterised by Franciscan-type P/T ratios. Finally, for high velocities (model SIN-CUM.8), continental markers from the lower plate only appear at pressures lower than 2 GPa and lie within a narrow curved area with a maximum temperature of 1200 K at approximately 2 GPa. Continental markers that belong to the upper plate and upper

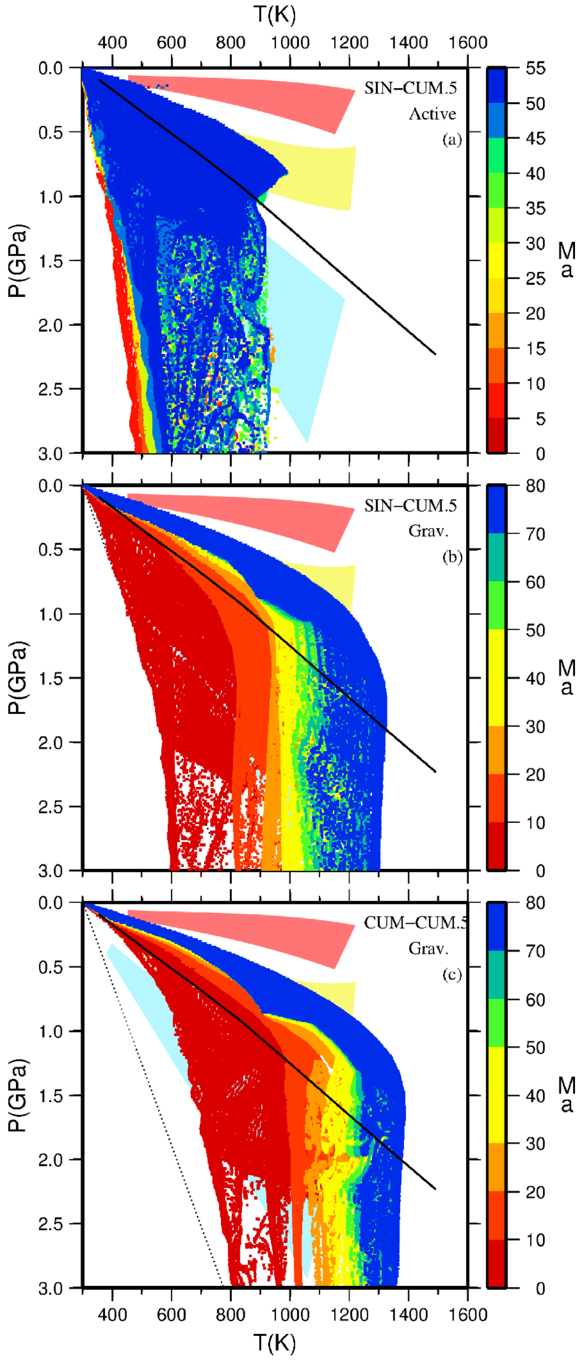

Figure 3.18: Predicted pressures and temperatures recorded by both oceanic and continental crustal markers at different times during: Panel a) the active subduction phase of model SIN-CUM.5; panel b) the pure gravitational phase of model SIN-CUM.5; and panel c) the pure gravitational phase of model CUM-CUM.5. Different colours indicate successive time intervals from the beginning of the simulation. The thick black lines represent the unperturbed continental geotherms. The red, yellow, and light blue areas indicate the metamorphic gradients for the low P-T series (Abukuma or Buchan metamorphism), medium P-T series (Dalradian or Barrovian metamorphism), and high P-T series (Franciscan or Sanbagawa metamorphism), respectively.

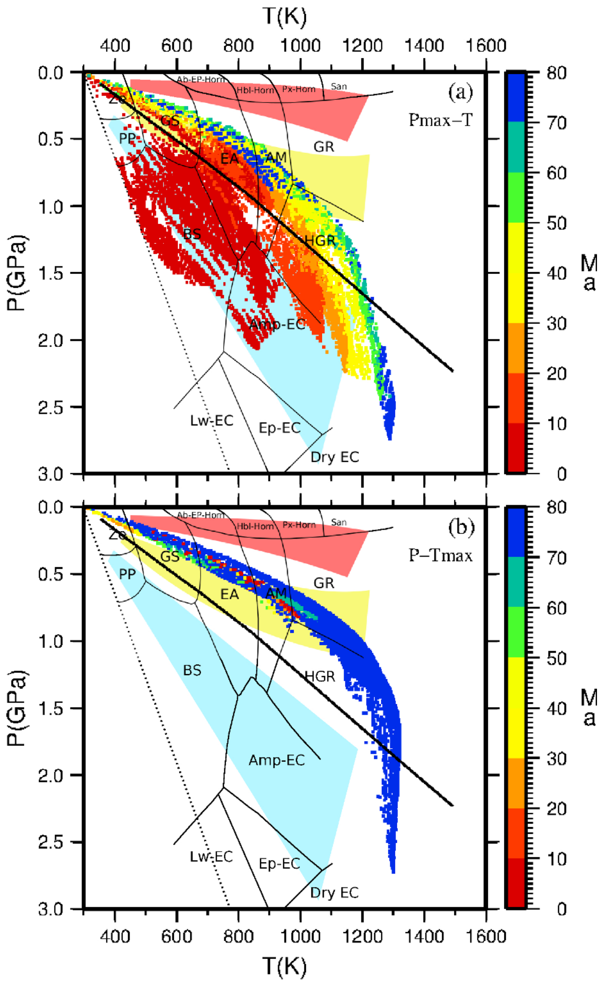

Figure 3.19: Predicted P_{maxC}-T (panel a) and P-T_{maxC} (panel b) distributions of the markers that have been partially exhumed during the post-collisional phase for the model SIN-CUM.5. The markers are coloured according to the age at which P_{maxC} and T_{maxC} conditions are reached. The thick black lines represent the unperturbed continental geotherm. The red areas indicate metamorphic gradients for low P-T series (Abukuma or Buchan metamorphism), the yellow areas for medium P-T series (Dalradian or Barrovian metamorphism), and the light blue areas for high P-T series (Franciscan or Sanbagawa metamorphism).

oceanic markers record temperatures between 800 K and 1300 K and pressures of up to 3 GPa. The majority of the markers (corresponding to an area of approximately 2000 km^2) record intermediate P/T ratios with the exception of a few markers with pressures greater than 1.5 GPa that exhibit high P/T ratios.

When shear heating is included in a model that already accounts for mantle hydration, the following features can be identified. During the active phase, a discontinuous distribution of P_{maxA}-T values of the markers is observed, which shows a gap in pressure whose extent is different for different velocities (Figures 3.20 and 3.21). In particular, in model CUM-CUM.3, a small number of continental and oceanic markers (corresponding to a total area of approximately 100 km^2) are distributed in one cluster and are limited by temperatures between 800 K and 1000 K and pressures from 2 GPa to 2.5 GPa (Figures

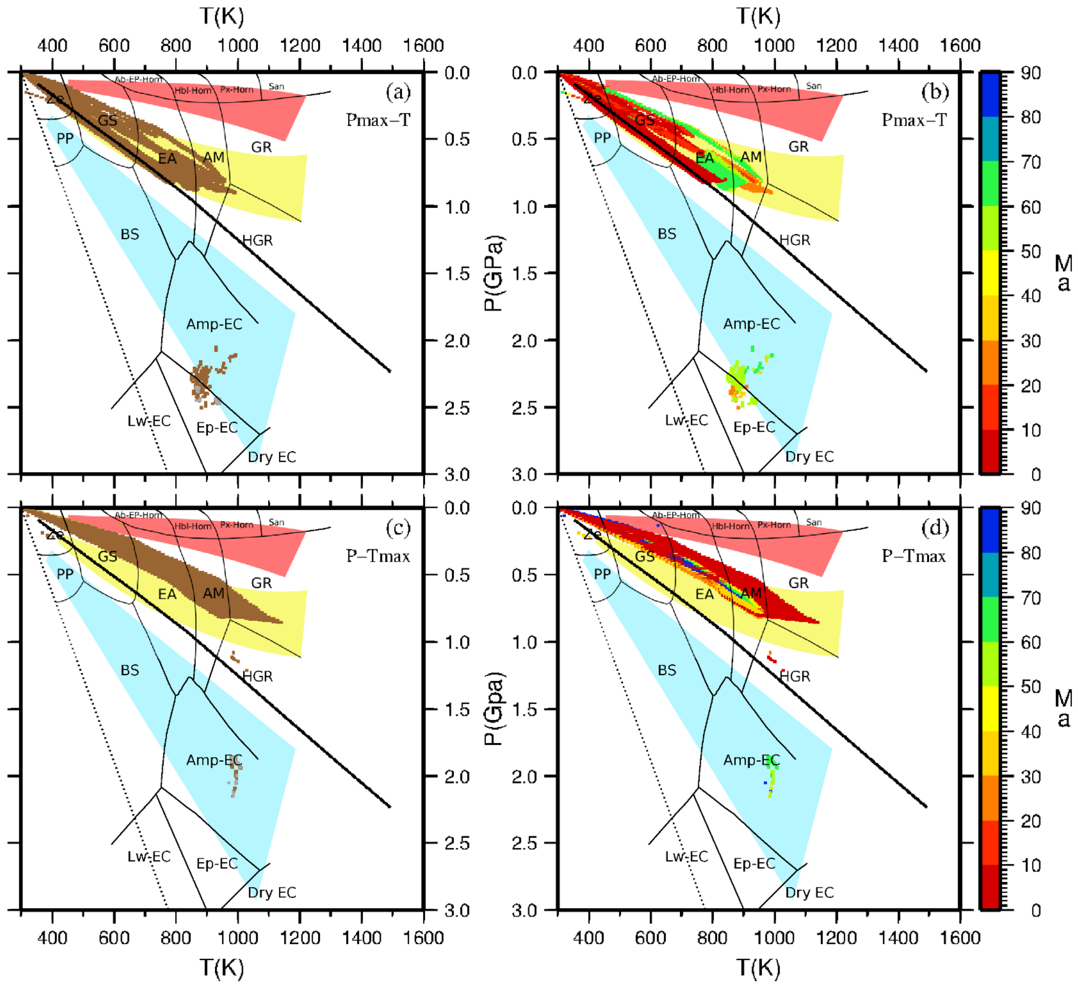

Figure 3.20: Predicted P_{maxA}-T (panels a and b) and P-T_{maxA} (panels c and d) distributions of the markers that have been partially exhumed during the active phase for the model CUM-CUM.3. In panels a and c, gray, dark brown and light brown points represent the upper oceanic crust, the continental crust of the upper plate and the lower plates, respectively. In panels b and d, the markers are coloured according to the age at which P_{maxA} and T_{maxA} conditions are reached. The thick black lines represent the unperturbed continental geotherm. The red areas indicate metamorphic gradients for low P-T series (Abukuma or Buchan metamorphism), the yellow areas for medium P-T series (Dalradian or Barrovian metamorphism), and the light blue areas for high P-T series (Franciscan or Sanbagawa metamorphism).

3.20). In models CUM-CUM.5 and CUM-CUM.8, a remarkably larger number of continental and oceanic markers (corresponding to total areas of approximately 1400 km^2 and 1000 km^2, respectively) exhibit P > 1.5 GPa with temperatures between 600 K and 1000 K for model CUM-CUM.5 (Figures 3.21) and between 500 K and 1000 K for model CUM-CUM.8.

P-T_{maxA} conditions show an increase in the T_{maxA} of about 100 K, in respect to the SIN-CUM models (Figures 3.21 and 3.21, panels c and d). This increase of temperature determines an increase in the amount of the continental markers plotting under Sillimanite-Granulite facies conditions. The P-T_{maxA} distribution of model CUM-CUM.3 shows similar features to the P_{maxA}-T distribution with a narrower range of temperatures (approx-

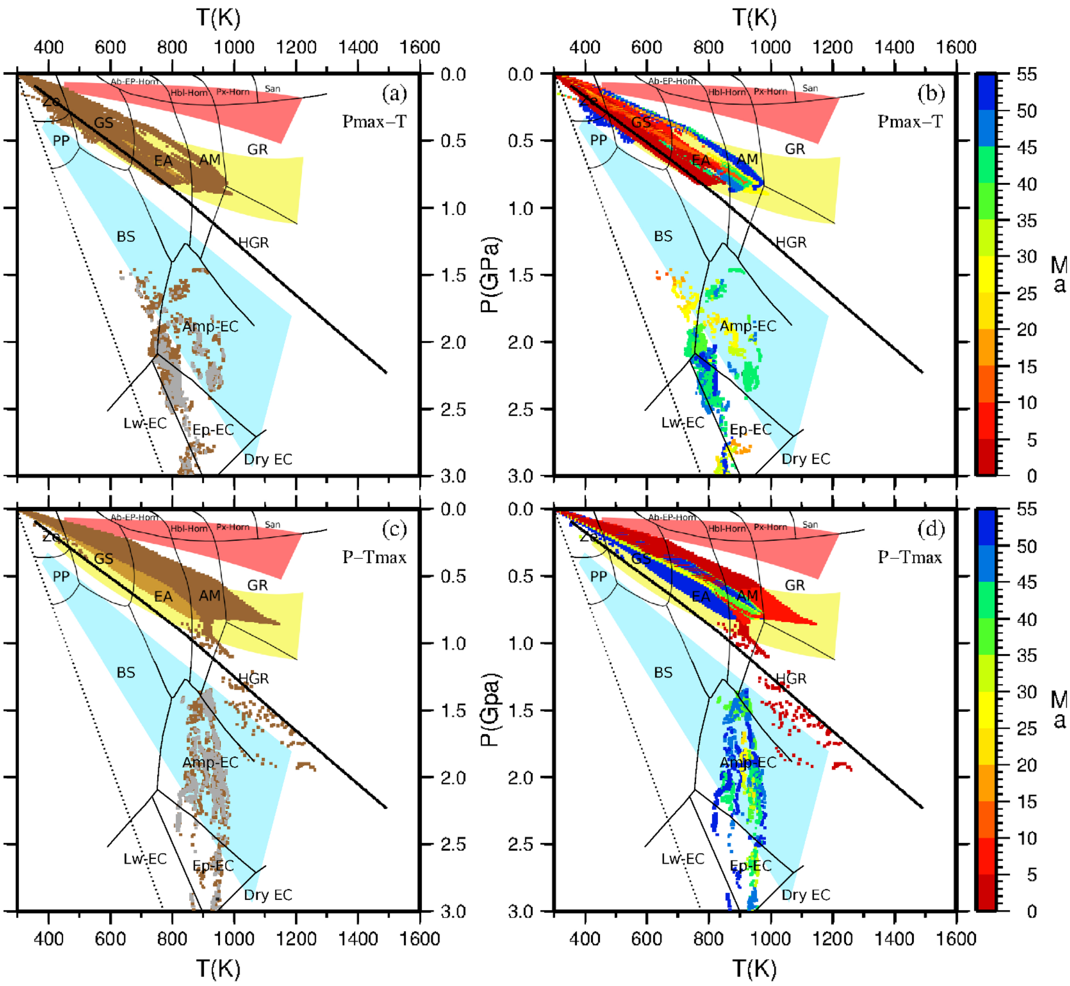

Figure 3.21: Predicted P_{maxA}-T (panels a and b) and P-T_{maxA} (panels c and d) distributions of the markers that have been partially exhumed during the active phase for the model CUM-CUM.5. In panels a and c, gray, dark brown and light brown points represent the upper oceanic crust, the continental crust of the upper plate and the lower plates, respectively. In panels b and d, the markers are coloured according to the age at which P_{maxA} and T_{maxA} conditions are reached. The thick black lines represent the unperturbed continental geotherm. The red areas indicate metamorphic gradients for low P-T series (Abukuma or Buchan metamorphism), the yellow areas for medium P-T series (Dalradian or Barrovian metamorphism), and the light blue areas for high P-T series (Franciscan or Sanbagawa metamorphism).

imately 50 K at approximately 1000 K) and pressures between 2.3 GPa and 2.7 GPa. In contrast, in models CUM-CUM.5 and CUM-CUM.8, the markers with P-T_{maxA} values greater than 1 GPa cluster in two groups that depend on the time at which they have recorded their thermal peak (Figure 3.21). One group, which is composed of both continental and oceanic markers with maximum temperatures of approximately 1000 K and high P/T ratios, record their thermal peaks during the second half of the active evolution (Figure 3.21b). The second group, which is composed only by continental crustal markers of the upper plate with temperatures between 1000 K and 1300 K and pressures between 1.3 GPa and 2 GPa, record their thermal peaks during the first 5 Ma of active evolution (Figure 3.21b), reaching conditions compatible with Kyanite-Granulite facies

(Figures 3.21c and d). Their P/T ratios are lower than the P/T ratios that are recorded by the first group and are similar to the initial continental geotherm. Then, continental markers of both CUM-CUM.5 and CUM-CUM.8 models show a migration in time of T_{max} with P > 1 GPa toward lower temperatures and conditions with higher P/T ratios. During the entire active subduction phase different P-T conditions, from intermediate (Barrovian) to high (Franciscan), can be developed at the same in time in thermally contrasted portion of the same subduction system. In particular, Kyanite-Granulite facies conditions can affect the external portion of the mantle wedge, while the more internal portion is affected by Blueschist conditions. Even though some continental markers record P-T_{maxA} conditions under Kyanite-Granulite facies during the early stages (Figure 3.21d), they remain in the mantle wedge until the beginning of post-collisional phase.

During the pure gravitational phase, the distribution of the P_{maxC}-T values and P-T_{maxC} values are very similar in all of the CUM-CUM models and include a wide range of temperatures (approximately 500 K at 1.5 GPa) for the P_{maxC}-T values and a narrow range (approximately 100 K at every depth) for the P-T_{maxC} values. The P_{maxC}-T values exhibit intermediate to high P/T ratios, whereas the P-T_{maxC} values are mainly characterised by intermediate P/T ratios (data with high P/T ratios occur only above 2 GPa). As in the SIN-CUM models, high P/T ratios for the P_{maxC} values are recorded until 10 Ma of pure gravitational evolution, while the T_{maxC} values are recorded during the last stages of the pure gravitational evolution. In the CUM-CUM models, a progressive increase in temperature occurs in the entire system during the pure gravitational phase (Figure 3.18c) and, as expected, the warming trend is higher than in the SIN-CUM models (Figure 3.18b). Consequently, as in the SIN-CUM models, the majority of the markers show intermediate P/T ratios at the end of the evolution, whereas high and intermediate P/T ratios coexist during the early stages of the pure gravitational phase (red colour in Figure 3.18c).

3.4 Discussion

The introduction of the hydration of the mantle wedge determines significant variations of the thermodynamics of the subduction system. In the hydrated portion of the mantle wedge, the activation of small convective cells during the early stages of active subduction favours the recycling and partial exhumation of buried oceanic and continental crust. These dynamics last few Ma after the collision, before the thermal re-equilibration of the system with the consequent increase of temperature in the wedge and the decrease of the area in which serpentine is stable. The introduction of shear heating slightly affects the thermal state in the hydrated area because the decrease in the mantle viscosity is greater than the increase in the strain rates, which produces a small amount of energy by shear heating. Accordingly, radiogenic decay remains the principal source of internal energy. The recycling of crustal material affects the dynamics and thermal state during the pure gravitational phase because the large amount of crustal material that was tectonically eroded from the upper plate and recycled in the wedge thickens the continental crust and thus increases the temperature in the models with mantle hydration. In general, the introduction of mantle hydration has no effect on the large-scale dynamics. Its effects are limited to the subduction zone during both the active subduction and the pure gravitational phases. In contrast, shear heating causes a shallower subduction geometry, which is more evident for higher prescribed subduction velocities. Different subduction velocities induce different thermal states in the interior of the subducting plate. In particular, the temperature in the subducting oceanic plate increases with decreasing velocity because the cold subducted material is slowly replaced, and the external hot mantle is more efficient at warming the subducting plate.

Generally the hydrated area has a rather triangular shape, as already suggested by previous models characterised by different setups (*Arcay et al.*, 2005; *Hebert et al.*, 2009; *Quinquis and Buiter*, 2014). In the CUM-CUM models, the higher the subduction velocity, the larger the extents of both the main triangular hydrated area and the entire hydrated area. This occurs because of the lower temperatures that characterise the interior of the subducted plate and the resulting thermal depression at the bottom of the hydrated area. For all models, the evolution of the hydrated area is characterised by an initial increase of extension, a successive phase of stability and a final phase of rapid decrease. Differently, in the SIN-CUM models, the prescribed velocities has a second-order impact on the maximum extent of the entire hydrated area, as already suggested by other models that do not take into account shear heating (*Hebert et al.*, 2009). Indeed, the extent of the hydrated domain in model SIN-CUM.8 during the early stages of active subduction is comparable to the extent during the late stages of active subduction in model SIN-CUM.3, which occurs because a large amount of cold material is quickly subducted at the beginning of the evolution of model SIN-CUM.8, which thermally depresses the subduction zone.

The thermal state during the pure gravitational phase remains comparable to that of active subduction until approximately 10 Ma of evolution; subsequently, the system progressively warms. In both the SIN-CUM and CUM-CUM models, small-scale convective cells remain active in the wedge area during the early post-collisional stages until wedge dehydration is reached, with resulting increased viscosity. Thus, the system maintains a cold thermal state at the beginning of the gravitational phase and then warms up because of the high radiogenic decay in the large amount of continental material that accumulated in the wedge. Consequently, at the end of the evolution, the models with mantle hydration are characterised by warmer thermal regimes than those without hydration. The progressive warming of the system generates a thermal environment in which the markers primarily experience P-T conditions that are compatible with Barrovian- (or Dalradian)-type metamorphism at the end of the evolution with a final thermal gradient that is higher than the initial continental geotherm. In all of the models, the highest T_{maxC} values are reached at the end of the evolution, whereas the markers record their P_{maxC} during the early stages of the gravitational evolution before the uplift of the subducted plate.

Despite the peculiar significance that has been traditionally assigned to metamorphic facies series, the P-T conditions predicted by the models show that contrasting P-T conditions, such as intermediate (Barrovian) to high P/T ratios (Franciscan), can exist simultaneously during active subduction. Markers that record Barrovian-type P_{maxA}-T conditions during subduction, come from and remain in the continental crust of the upper plate and have trajectories that indicate that they are carried by mantle flow from the bottom of the crust toward the more internal and shallower portion of the mantle wedge. The markers that record Franciscan-type P_{maxA}-T conditions are exhumed by the activation of convective cells and the resulting recycling of crustal material that was either tectonically sampled from the subducting plate or ablated by the upper plate in the mantle wedge. In particular, during the phase of oceanic subduction, P-T conditions compatible with Amphibolite and Sillimanite-Granulite facies are stable at the bottom of the continental crust of the upper plate, while P-T conditions compatible with Kyanite-Granulite facies can be developed in the continental crust in the external and shallow portion of the hydrated wedge. The thermal anomaly induced by the subduction at the bottom of the continental crust of the upper plate is due to the large scale convective mantle flow induced by the sinking of the slab. However, in the continental crust only intermediate P/T ratios can be recorded, while metamorphic facies series characterised by low P/T ratios can not be developed. Therefore, an additional source of heat should be taken into account to develop Abukuma-type metamorphism, such as heat and fluids transfers related to arc magmatism (arc-related metamorphism). P-T conditions under Epidote-Amphibolite and Amphibolite facies can also develop in the shallower and warmer portion of the wedge by recycled markers, both continental and oceanic. At the same time, in the internal portion of the wedge the recycle of continental and oceanic markers happens in a colder thermal state, compatible with metamorphic facies characterised by high P/T ratio. In this area markers can develop Blueschist, Amphibole-Eclogite and Epidote-Eclogite facies conditions. The occurrence of contrasted metamorphic conditions in the wedge is related to the hydration and the consequent recycling of subducted material. As consequence, recycled oceanic and continental crust are spread in portion of the wedge characterised by different thermal gradients, the further from the slab, the warmer.

The coexistence of metamorphic facies characterised by contrasted P-T gradients is observed also during the early stage of the post-collisional gravitational evolution. In fact, metamorphic facies with high P/T ratios (as Blueschist or Amphibole-Eclogite facies) remain stable after the collision for a period during which areas characterised by P-T conditions in the stability fields of facies with intermediate P/T ratio enlarge (as Kyanite-

Granulite facies). The duration of this metamorphic pattern is related to the thermal condition of the system. In fact, the warming of the subduction complex does not occur suddenly, and some Ma are necessary to thermally re-equilibrate the slab and the wedge, characterised by high P/T ratios, with the surrounding warmer mantle. Differently from the oceanic subduction phase, during the post-collisional phase the thermal anomaly in the continental crust is due to the high radiogenic energy consequent to the thickened of the crust.

Chapter 4

The Variscan belt

4.1 The Variscan orogeny

The Variscan belt, extending from Southern Iberia to Poland, is the more significant geological event in the basement of Europe (*von Raumer et al.*, 2003) (Figure 4.1) and it is part of a 1000 km broad and 8000 km long Paleozoic mountain system, which extended from the Caucasus to the Appalachian and Ouachita mountains of northern America at the end of the Carboniferous (*Matte*, 2001). It results from the successive collision of a series of terranes (Armorican terrane assemblage and Gondwana) against Laurussia and Avalonia during Devonian - Carboniferous times (e.g. *Giorgis et al.*, 1999; *Matte*, 2001; *von Raumer et al.*, 2003; *Marotta and Spalla*, 2007; *Compagnoni and Ferrando*, 2010; *Edel et al.*, 2013; *Lardeaux et al.*, 2014) (Figure 4.2). The final convergence between the supercontinents of Laurussia, to the north, and Gondwana, to the south, was associated with an intensive deformation of the assembled Avalonia and Armorican terrane assemblage (*Edel et al.*, 2013). These two microplates became separated by oceanic sutures and drifted during the early Palaeozoic, prior to docking against Baltica and Laurentia before the Devono-Carboniferous collision (*Matte*, 2001). Avalonia and Armorica have been defined essentially on the basis of paleomagnetism and paleobiostratigraphy, but geological studies allow smaller microplates, separated by oceanic sutures, to be defined within Armorica (*Matte*, 2001; *Franke*, 2000), even if the corresponding small oceans (500 km) are difficult to detect from palaeomagnetism and palaeobiostratigraphy. All these microplates have a peculiar common upper Proterozoic basement (Avalonian-Cadomian) comprising low-grade, thick turbiditic sediments and island arc-type volcanic and plutonic rocks that were formed at the northern (active) margin of Rodinia (*Matte*, 2001). Avalonia comprises the northern foreland of the Variscan belt and is geologically well defined because it lies between major sutures: the Iapetus and the Tornquist Caledonian sutures to the north separating Avalonia from North America and from Baltica, respectively, and the Rheic Variscan suture to the south. Avalonia drifted northward independently from

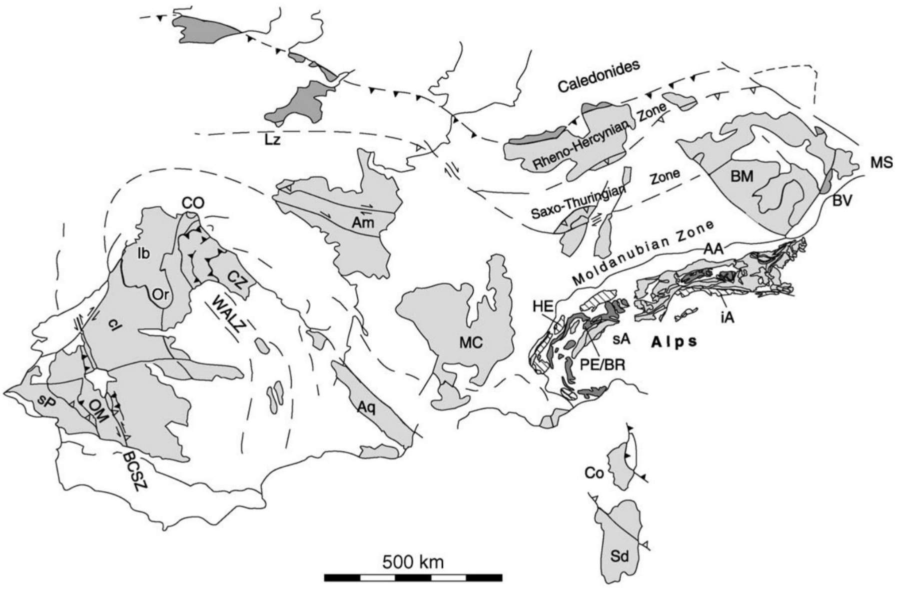

Figure 4.1: Geological map of Variscan basement areas in Central Europe. AA: Austroalpine; Am: Armorican Massif; Aq: Aquitaine; BCSZ: Badajoz-Cordoba Shear Zone; BM: Bohemian Massif; BV: Brunovistulicum; cI: Central Iberian Zone; CO: Cabo Ortegal Complex; CZ: Cantabrian Zone; Co: Corsica; HE: Helvetic Zone; iA: Intra-Alpine; Ib: Iberia; Lz,: Lizard; MC: French Central Massif; MS: Moravo-Silesian; Or: Ordenes ophiolites; OM: Ossa Morena Zone; PE/BR: Penninic/Brianconnais; sA: Southalpine; Sd: Sardinia; sP: South Portuguese Zone; WALZ: West Asturias Leon Zone (from *von Raumer et al.*, 2003).

Armorica during the early Palaeozoic (*Trench and Torsvik*, 1991), detaching from Gondwana during Ordovician times and opening the Rheic Ocean, while the Iapetus closed by southward and then northward subduction beneath the Taconic arc of Newfoundland (*Pickering*, 1989). Armorica is not defined precisely on the basis of palaeomagnetic data and, in fact, while for some authors (e.g. *Tait et al.*, 1997) Armorica drifted northward later than Avalonia, opening a very large ocean, for other authors (e.g. *Torsvik*, 1998) it remained more or less closed to Gondwana during its northward drift, from Ordovician to Devonian times. Geologically it does not represent a coherent microplate because it includes fragments separated by oceanic sutures underlined by eclogites that show MORB geochemical affinities, such as the Southern Brittany-Northern Massif Central suture in France (*Matte*, 2001).

The main sections of the Variscan belt show opposite vergences of nappes and recumbent folds migrating toward external Carboniferous basins. Sutures are found on both sides of the belt and they are the roots of large nappes containing ophiolitic rocks and/or HP/UHP rocks (*Matte*, 2001) (Figure 4.3):

1. on the southern side of the belt, the Galicia-Southern Brittany suture runs from the Coimbra-Cordoba Shear Zone in central Iberia (CCSZ) to southern Britanny, northern Massif Central and further east to the southern Bohemian nappes. This suture is located between the Armorican terrane assemblage and Gondwana. The CCSZ is considered as the root zone of the western Iberian nappes as the South

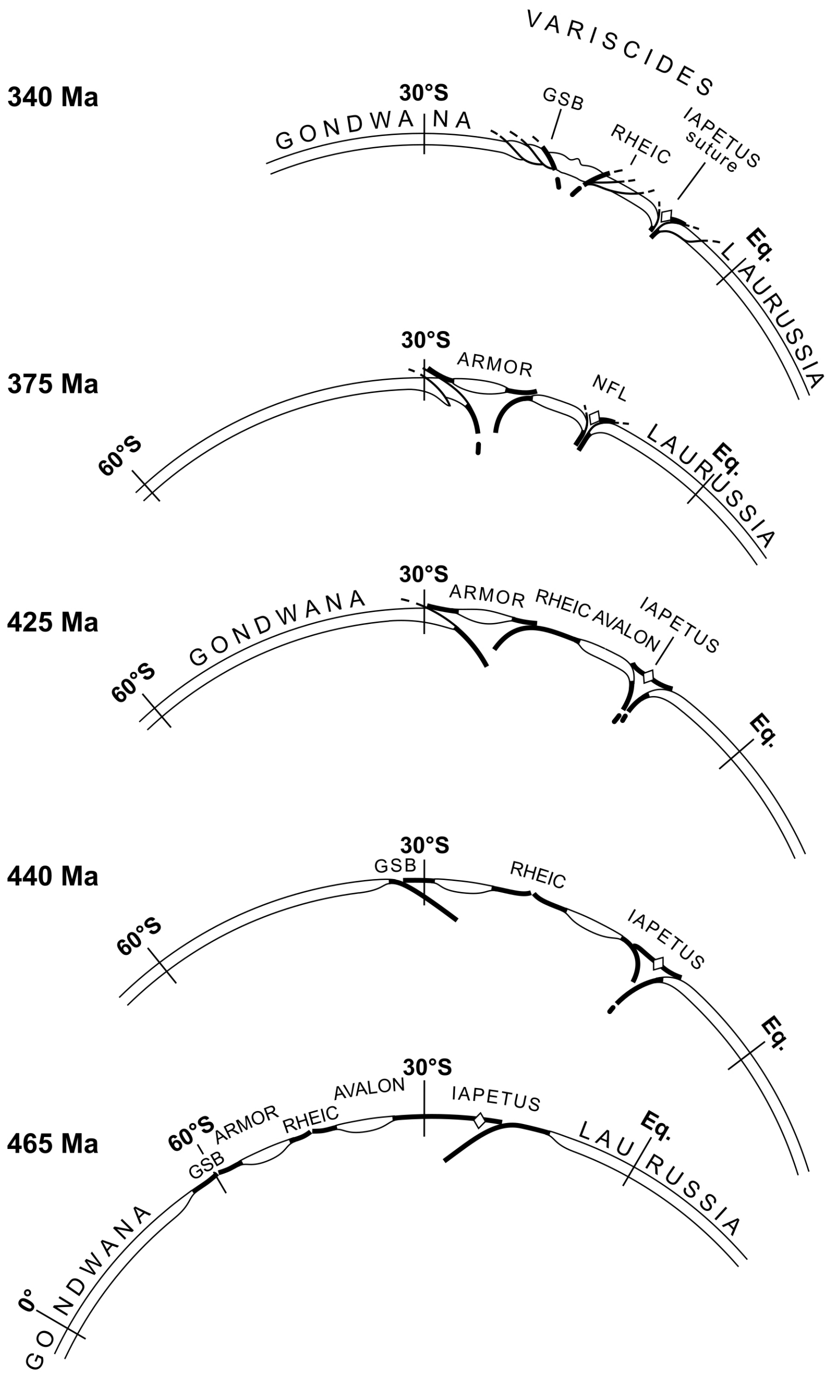

Figure 4.2: Plate tectonic sketch at lithospheric scale showing the movements of continents between 465 and 340 Ma. GSB: Galicia-Southern Brittany ocean and suture (from *Matte*, 2001).

Armorican Shear Suture Zone, running through southern Brittany to the northern Massif Central, must be considered as the root of the ophiolitic southern Brittany-Massif Central nappes. Ophiolitic rocks are dated between 500 and 400 Ma and the HP/UHP metamorphism between 430 and 360 Ma (*Matte*, 2001). This suture, which forms the root of large nappes transported to the East (Western Iberia) and to the South (Massif Central), may be related to a N-S eo-Variscan suture, running from the French external Alps to Sardinia and forming the root of W-verging pre-Permian nappes. The translation toward SW of the French external Alps from Northern Europe, in prolongation with the Bohemian Massif, is related to the dextral wrenching from Carboniferous to Permian times along a N030° strike-slip fault, in response to oblique collision between Laurussia and Gondwana (*Matte*, 2001; *Guillot et al.*, 2009a; *Edel et al.*, 2013) (Figure 4.4);

2. on the northern side of the belt, two sutures are relatively well defined from southern England, through Germany to Poland: the Teplá suture, located between the Saxothuringian plate and the southern Gondwana-derived fragments, and the Rhenohercynian suture, located between Avalonia and Armorica (*Franke*, 2000; *Matte*, 2001; *Schulmann et al.*, 2009; *Edel et al.*, 2013). They are the roots of NW-transported nappes, showing HP/UHP metamorphism in the ophiolitic rocks of the Teplá suture and its continental footwall. The oceanic rocks are dated at around 500 Ma and the HP metamorphism took place around 380 Ma. The Rhenohercynian suture corresponds to a younger Lower Devonian oceanic basin which opened and closed later (*Matte*, 2001; *Franke*, 2000).

Armorica can be considered as a small continental plate between the northern sutures (Teplá and Rhenohercynian sutures) and the southern suture (Galicia-southern Brittany suture). The two corresponding main oceanic basins (the Rheic and the Galicia-southern Brittany oceans) closed by opposite subduction, as indicated by the occurrence of HP/UHP metamorphism (430 and 360 Ma) on both sides of the belt. In France, Armorica includes Central Brittany and Normandy between the southern Brittany-Massif Central suture and the Rhenohercynian suture. In the Bohemian massif, Armorica correponds to two microplates: the Saxothuringian and the Barrandian (*Matte*, 2001).

4.2 The French Central Massif

The european basement of the Variscan Belt experienced a long-lasting evolution from Cambrian-Ordovician rifting to Carboniferous collision and orogenic collapse (*Matte*, 2001; *Faure et al.*, 2005, 2008). In France, the Variscan Belt is well exposed in the Massif Central and Massif Armoricain, where two contrasted paleogeographic and tectonic domains are recognized. The Nort-sur-Erdre Fault corresponds to the suture zone between

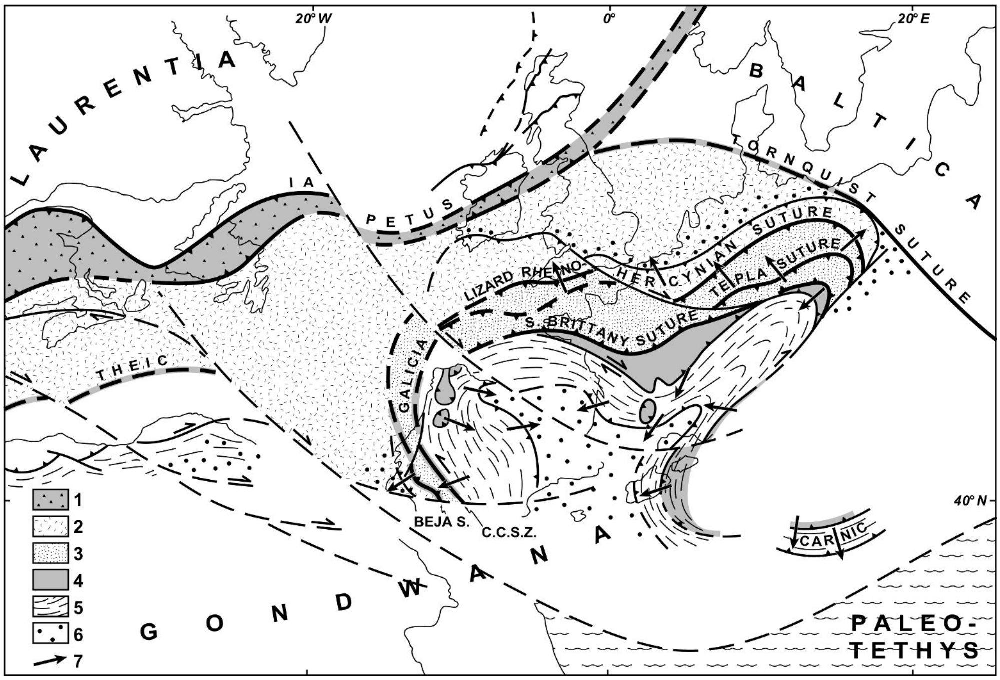

Figure 4.3: Configuration of the Variscan belt of Western Europe and northern Africa at 270 Ma, showing the main sutures and extension of the Avalonia and Armorica continental microplates. 1) Iapetus Caledonian suture and Ordovician island arc; 2) Avalonia; 3) Armorica; 4) ophiolitic nappes rooted in the Galicia-Southern Brittany suture; 5) Schistose nappes in the southern Variscides; 6) Carboniferous (Visean to Westphalian) foredeep basins; 7) main vergence of nappes. CCSZ: Coimbra-Cordoba Shear Zone; Beja S: Beja suture (from *Matte*, 2001).

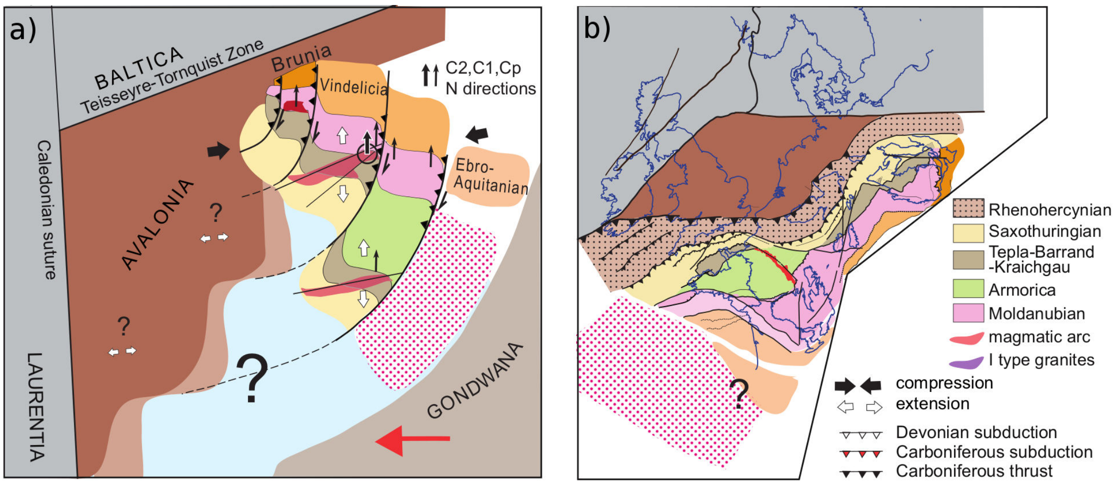

Figure 4.4: Model of evolution of the Variscides during the Carboniferous. Panel a): situation at 330–328 Ma, showing shortening of the Variscan belt between Gondwana and Laurussia and major dextral wrenching along reactivated transform boundaries; panel b): situation at the end of the Carboniferous (from *Edel et al.*, 2013).

the Armorican domain to the north and the Gondwana margin to the south (Galicia-Southern Brittany suture) (*Matte*, 2001; *Faure et al.*, 2008). The Massif Central belongs to the western part of the Variscan chain and it is the largest area where Variscan metamorphic and plutonic rocks are exposed, with the entire massif belonging to the northern Gondwanian margin (*Mercier et al.*, 1991b; *Faure et al.*, 2009). P-T estimates of the Variscan metamorphism in the French Central Massif are presented in Tables B.2 and B.4.

The Massif Central is a stack of metamorphic nappes, in which six main units are recognized, from the bottom to the top and from the south to the north (*Ledru et al.*, 1989; *Faure et al.*, 2009; *Lardeaux et al.*, 2014; *Lardeaux*, 2014a) (Figure 4.5):

1. the southernmost turbidites foreland basin (Visean-late Mississipian) contains olistoliths of Palaeozoic sedimentary rocks and it extends southward below the coastal plain of the Mediterranean Sea and up to the Pyrénées, ;

2. the Paleozoic fold-and-thrust belt of the Montagne Noire area is composed of weakly metamorphosed sediments (early Cambrian to early Carboniferous continental margin to platform series) and it is deformed in kilometres-scale south-verging recumbent folds and thrust sheets;

3. the Para-autochthonous unit overthrusts the southern fold-and-thrust belt and it is composed primarily of metapelite and metagreywacke with minor limestones, quartzites and volcanic rocks, metamorphosed under greenschist to epidote-amphibolite facies conditions. In the northern part of the Massif Central it appears as tectonic windows surrounded by the Lower Gneiss Unit;

4. the Lower Gneiss Unit (LGU) is composed primarily by metapelites, metagreywackes, metarhyolites ans metagranites metamorhposed under amphibolite facies considitions, plus minor amphibolites. The geochemical characteristics of the metabasites indicate an origin as basaltic members of alkaline magmatic series, sometimes in close association with alkaline rhyolites volcanic tuffs. This association of bimodal alkaline magmatic rocks with terrigenous detrital sediments indicates that the members of the LGU, as well as the Para-autochthonous unit, are remnants of the northern Gondwana passive margin. Prograde Barrovian-type metamorphic sequences are recognised in different areas of the massif, with different ages depending on their involvement in the nappe stacking (*Burg et al.*, 1989);

5. the Upper Gneiss Unit (UGU) is composed of rocks which experienced Silurian to lower Devonian HP to UHP metamorphism (eclogite and/or HP granulite facies), locally reaching coesite eclogite facies in the Mont du Lyonnais area (*Paquette et al.*, 1995; *Lardeaux et al.*, 2001). This unit is characterised by the occurrence of a bimodal association called 'Leptyno-Amphibolitic Complex' (LAC), interpreted as

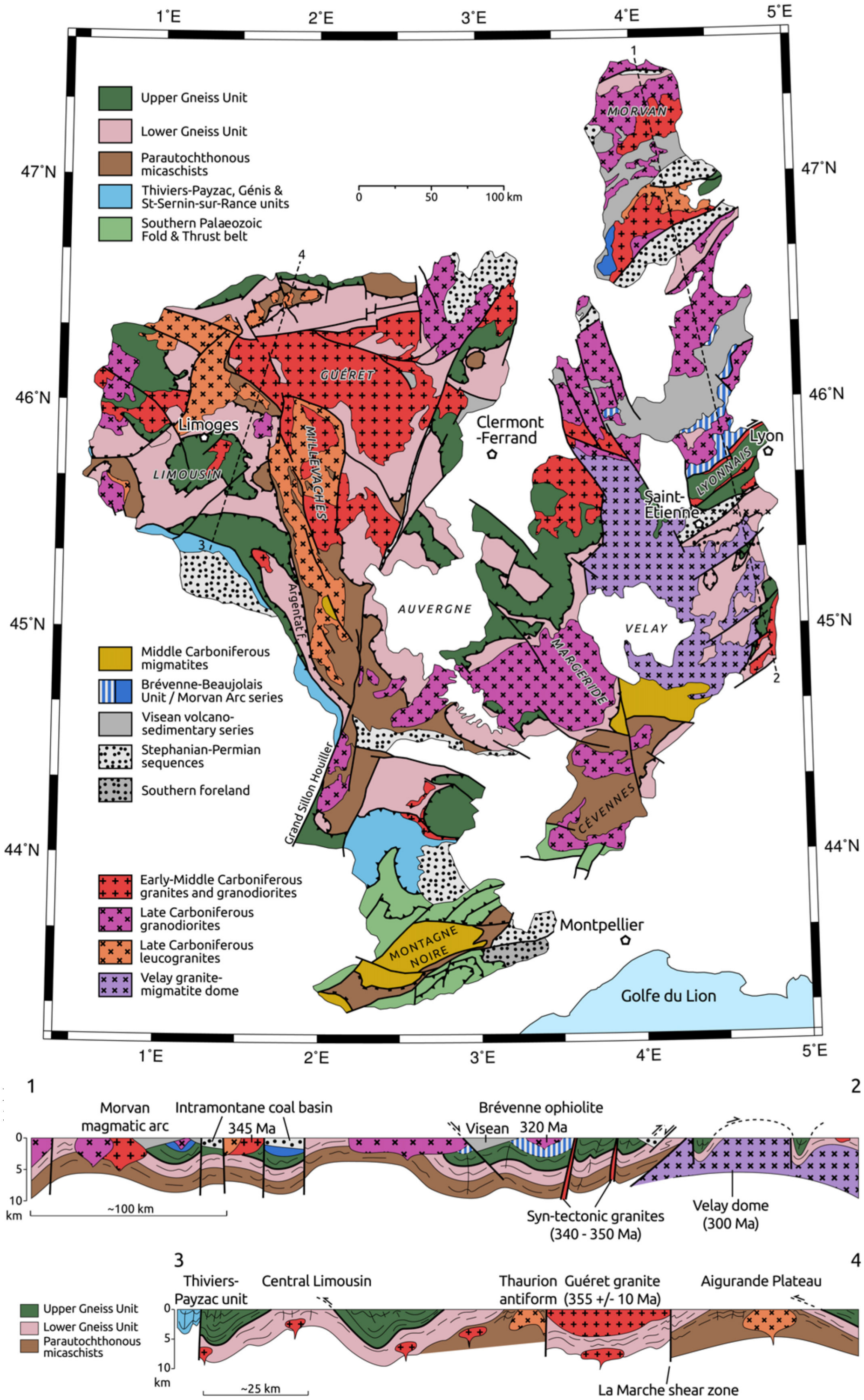

Figure 4.5: Geological map of the French Massif Central and simplified geological cross-sections. 1-2, eastern cross-section; 3-4, western cross-section (from Lardeaux et al., 2014).

formed during the rifting that led to the separation of Armorica from north Gondwana (*Faure et al.*, 2005). The LAC is a peculiar association of mafic/ultramafic rocks (basalts, gabbros, spinel/garnet peridotites) and felsic rocks (rhyolites, granites and tuffs). In general, it is located at the base of the UGU (Figure 4.6), while the upper part consists of migmatites formed by MP to HP partial melting of para- and/or orthogneisses, driven by a strong decompression. The eclogites derive from meta-basalts and meta-gabbros and can be regarded as the variably fractionated members of a tholeiitic suite. On the top of this eclogitic complex, various types of HP granulites crop out (basic granulites, acid and aluminous granulites and granulitic orthogneisses). The metabasites were derived from continental tholeiites, while quartzo-feldspathic granulites were derived from rhyolites, granites or continental sediments. This lithological association is typical for a thinned continental margin at the ocean-continent transition (OCT). Therefore, the lowermost part of the UGU can be interpreted as a subducted and exhumed Cambro-Ordovician OCT (*Ledru et al.*, 1989; *Faure et al.*, 2009; *Lardeaux et al.*, 2014; *Lardeaux*, 2014a);

6. the uppermost units are identified by the Brévenne and Morvan units in the eastern Massif Central and by the by the Thiviers-Payzac unit in the western Massif Central. The Brévenne unit is an ophiolitic complex composed of mafic magmatic rocks (pillow basalts, dolerites and diabases, gabbros, pyroclastites), serpentinites, scarce trondjhemites and siliceous sediments (radiolarites, siltites). Geochemical and geochronological investigations indicate that the Brévenne ophiolite was originated in a back-arc setting during late Devonian times and then deformed under greenschist facies conditions. The Morvan arc is localised northern then the Brévenne unit and it consists of weakly metamorphosed middle to late Devonian calk-alkaline volcanic and volcaniclastic rocks. To the west, the Thiviers-Payzac unit forms the highest tectonic unit in the south Limousin. It has received different local names depending on the area, nevertheless, similar lithological, metamorphic and structural features are recognized in all these areas (*Duguet et al.*, 2007). It is composed of Cambrian greywackes, quartzites and rhyolites intruded by Ordovician granite and metamorphosed under epidote-amphibolite facies. In the South Limousin, some small outcrops of gabbro, mafic metavolcanic rocks (pillow lavas in places), radiolarian cherts, siliceous red shales and Middle Devonian limestones form the Génis Unit. The structural and paleogeographic setting of this unit is not yet settled and it is interpreted either as an uppermost ophiolitic nappe similar to the Devonian Brévenne ophiolite or as an early Carboniferous olistostrome reworking Devonian ophiolites (*Ledru et al.*, 1989; *Faure et al.*, 2009; *Lardeaux et al.*, 2014; *Lardeaux*, 2014a).

In the evolution of the Massif Central basement, two cycles of subduction/collision

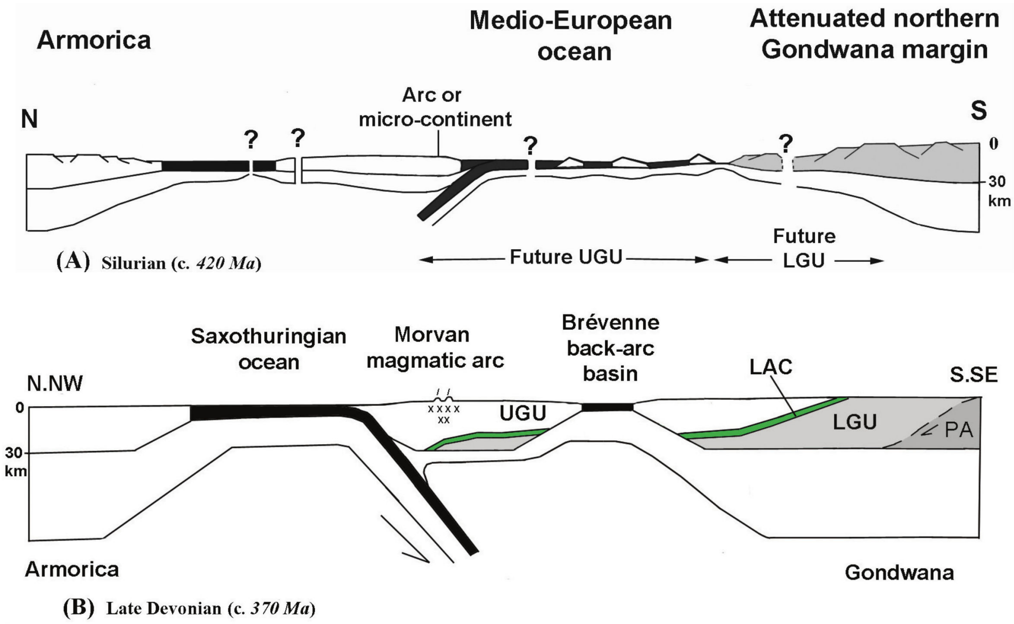

Figure 4.6: Model of the geodynamic evolution of the Massif Central showing the Eo-Variscan north-directed subduction (panel a) and the Variscan south-directed subduction (panel b). UGU: Upper Gneiss Unit; LGU: Lower Gneiss Unit; PA: Para-autochthonous units; LAC: Leptyno-Amphibolitic Complex (from *Lardeaux*, 2014a).

can be identified, with possibly opposite polarities (*Faure et al.*, 2005, 2009; *Lardeaux*, 2014a):

- an early Paleozoic Eo-Variscan cycle, corresponding to the rifting of the Armorica from Gondwana during the Ordovician to the early Silurian and their successive collision during late Silurian-early Devonian driven by a northward subduction. In fact, rock associations, metamorphic history and finite strain pattern depicted in the Monts du Lyonnais Unit are regarded as the record of a north-dipping subduction that led to the closure of the Galicia-Massif Central (or Medio-European) oceanic domain (Figure 4.6a);

- a Variscan cycle, representing the late Devonian to Carboniferous collision of Gondwana and Laurussia through a south-directed subduction of the Rheic Ocean. The direction of this second subduction event is argued by the position of the Morvan arc to the north and Brévenne back-arc to the south (Figure 4.6b).

The protoliths of the eclogites widespread in the Massif Central show various chemical characters and represent basic magmas of oceanic affinities emplaced in originally various site. The maximum P-T conditions are similar for all the eclogites, while the retrograde evolutions during the exhumation show differences between the western and eastern parts of the Massif Central, suggesting contrasting thermal evolutions. In fact, the retrograde P-T path in the central and western parts of Massif Central is characterised by isothermal decompression into the upper amphibolite facies, while in the eastern part an

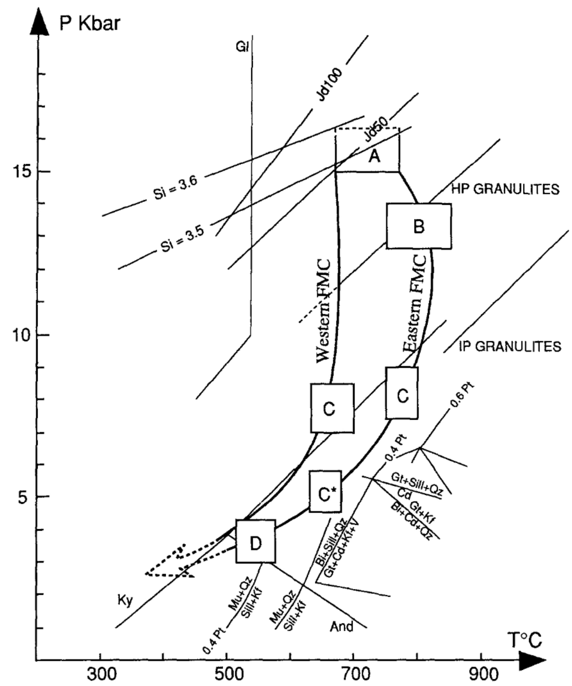

Figure 4.7: PT diagram illustrating the contrasting retrograde P-T paths of HP metamorphic rocks in the French Massif Central (from *Mercier et al.*, 1991a).

increase in temperature occurs at the beginning of the retrograde P-T path, resulting in granulite facies mineral assemblages (*Mercier et al.*, 1991a,b) (Figure 4.7).

The tectonic architecture of the Massif Central can be well illustrated by three mainly NS-orientated cross-sections over the eastern, the central and western parts, through which the main metamoprhic and deformative stages can be reconstructed.

4.2.1 Eastern Massif Central

In the eastern cross-section four domains can be recognised (*Lardeaux et al.*, 2014) (section 1-2 in Figure 4.5):

- Visean unmetamorphosed volcanics, sediments and granodiorites rocks unconformably overlie or intrude older rocks (320-335 Ma);
- the middle to late Devonian Morvan magmatic arc and Brévenne back-arc ophiolite (360-370 Ma). To the south, the Brévenne unit is separated by a dextral wrench fault, underlay syntectonic granites (340-350 Ma) (*Costa et al.*, 1993);
- the Upper Gneiss Unit in the Monts du Lyonnais area is characterised by migmatitic ortho- and paragneisses at the top (380-390 Ma) and by the Leptyno-Amphibolitic Complex at the bottom, including quartz or coesite bearing eclogites (*Lardeaux et al.*, 2001) (data ML2 in Table B.2) and garnet peridotites (*Gardien et al.*, 1988; *Costa et al.*,

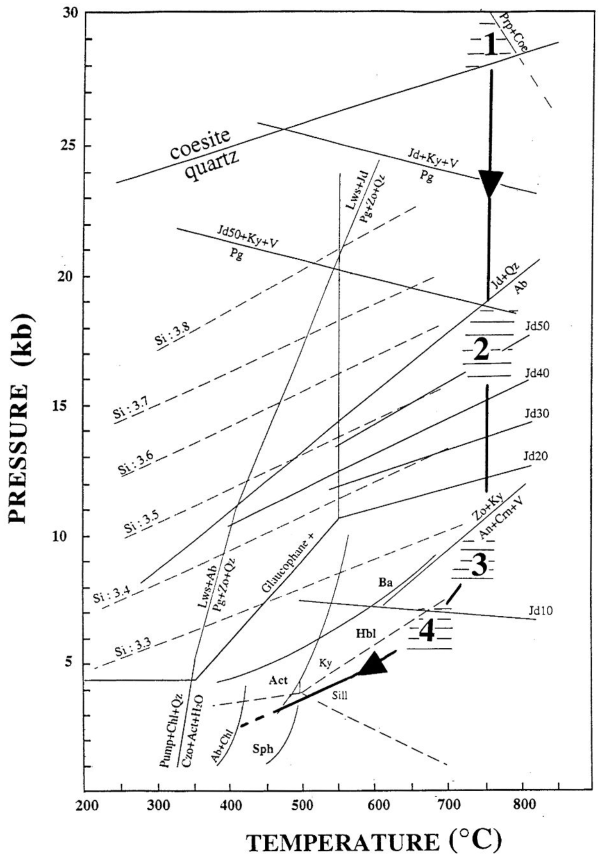

Figure 4.8: P-T path of the Monts du Lyonnais coesite-bearing eclogite (from *Lardeaux et al.*, 2001).

1993) (data ML1). Eclogites and related garnet amphibolites also occur to the north, in the Morvan, and to the SE, in the Maclas-Tournon area (*Gardien and Lardeaux*, 1991; *Ledru et al.*, 2001) (data Mc1). The age of HP/UHP metamorphism is uncertain but in the Monts du Lyonnais a successive deformative stage is recorded under amphibolite facies conditions with partial melting and it corresponds to a NW–SE crustal shortening dated 340-360 Ma (*Mercier et al.*, 1991a; *Lardeaux et al.*, 1989; *Costa et al.*, 1993) (Figure 4.8). A late transpressive regime led to development of a regional-scale fold system, correlated with the deformative event observed in the Brévenne unit. With the exception of the initial stage of UHP, a similar evolution has been identified for the Maclas area where the eclogites are retromorphosed under granulites and then under amphibolite facies conditions (*Gardien and Lardeaux*, 1991; *Ledru et al.*, 2001) (Figure 4.9).

- the Lower Gneiss Unit of the Pilat Unit is divided from the previous unit by a thrust zone developed under amphibolite facies conditions. This unit is composed of meta-sediments, meta-rhyolites, meta-basalts and numerous meta-granites metamorphosed under amphibolite facies conditions. This unit is characterised by a

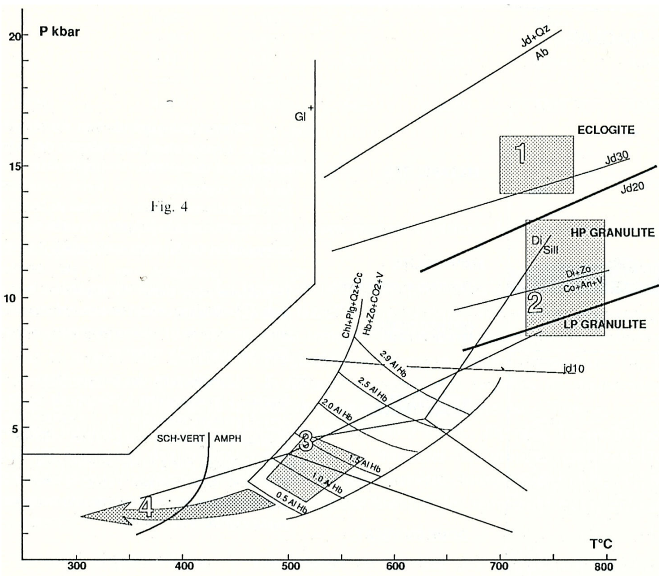

Figure 4.9: P-T path of the Monts du Lyonnais. 1: P-T conditions of the eclogitic stage; 2: P-T conditions of the granulitic stage; 3: P-T conditions of the amphibolitic stage (from *Gardien and Lardeaux*, 1991).

well-developed N-dipping foliation and stretching lineation developed under conditions of retrograde metamorphism from HT to greenschist facies. The metamorphism recorded under greenschist facies condiction is superimposed on a foliation related to the earlier Variscan compressional events (350-380 Ma) associated with southward emplacement of nappes and HP-HT metamorphism (*Malavieille et al.*, 1990). A late HT-LP event (295-320 Ma), synchronous with crustal extension, is related to the intrusion of a large granitic pluton (the Velay Dome). Three melting events can be identified in the southern envelope of the Velay dome: 1) a first melting episode occurred within the biotite stability field (315-325 Ma) which led to the complete disappearance of muscovite and to the formation of migmatites. It is interpreted as the result of internal heating linked to the decay of heat producing elements accumulated in a thickened crust. It resulted in the formation of a partially molten middle crust with decoupling between the lower and upper crust, late-collisional extension and crustal thinning; 2) a second episode of melting related to the emplacement of the Velay granites (approximately 305 Ma). This HT event synchronous with crustal extension is considered to result from intrusion of hot mantle-derived and lower crustal magmas triggering catastrophic melting in the middle crust; 3) a third episode of melting corresponding to emplacement of late granites (295-305 Ma) generated from melting of specific lithologies triggered by injection of mafic magmas (*Barbey et al.*, 2015). This strong tectono-thermal event is interpreted as the record of the post-orogenic collapses of the eastern Massif Central (*Ledru et al.*, 2001).

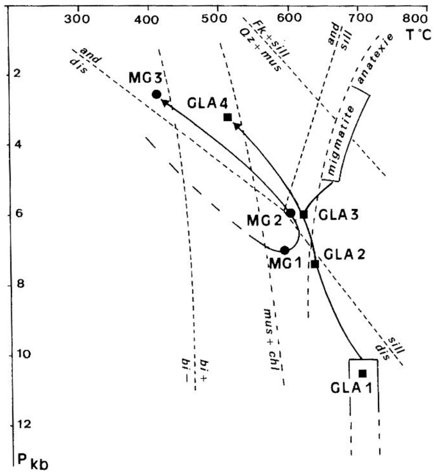

Figure 4.10: P-T paths of different units of the Aigurande Plateau. GLA: Leptyno-Amphibolitic Complex; MG: micaschist-gneiss series (from *Faure et al.*, 1990).

4.2.2 Western Massif Central

The structure observed in the western cross-section is consistent with the eastern architecture and five domains can be recognised from the north to the south (*Lardeaux et al.*, 2014) (section 3-4 in Figure 4.5):

- the Upper Gneiss Unit is represented by a synformal klippen in the Aigurande Plateau (data PA) and others two to the south in the Limousin (data Li3 and Li7). The Aigurande Plateau is an ENE-WSW trending antiform folding a nappe composed of the LAC and migmatites thrusted upon a micaschist-gneiss series. The eclogites observed in the LAC show an early HP stage, followed by a retrograde evolution firstly in amphibolite facies conditions and then under conditions of LP associated to a partial anatectic event. The evolution of the micaschist-gneiss series is characterised by a prograde metamorphism up to amphibolite facies conditions, overprinted by a LP metamorphism (Figure 4.10). In the Limousine, the UGU is composed primarily of plagioclase-rich gneisses, locally with an anatectic imprint, and numerous bodies of amphibolitised quartz bearing eclogites, which derive from MORB-type basalts and gabbros;

- para-autochthonous units underlie the LGU and are well exposed as tectonic windows in the Thaurion anticline and Aigurande Plateau. These units are composed mainly of micaschists and paragneisses with rare metavolcanics and quartzites;

- a peculiar characteristic of the western cross-section, in the Limousine area, is the occurrence of dismembered ophiolite bodies including numerous peridotites and forming a transported suture zone now separating the UGU and the LGU. These ophiolite bodies are associated with scarce zoisite bearing eclogites equilibrated

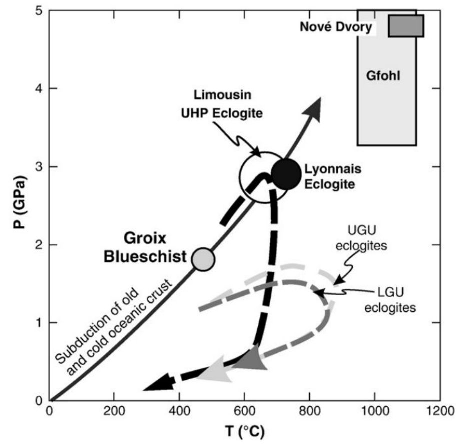

Figure 4.11: Comparison of the P-T path determined for the UHP Limousin eclogites with P-T conditions of Variscan LT/HP and UHP rocks (Nove Dvory and Gföhl are UHP terranes in the Bohemian massif) and with UGU and LGU P-T path determined for other Limousin eclogites (from *Berger et al.*, 2010).

under UHP conditions (data Li6). The well-preserved assemblages of these eclogites indicate a fast exhumation to mid-crustal level, which is followed by an upper Devonian anatectic HT-MP event (*Berger et al.*, 2010) (Figure 4.11);

- the Lower Gneiss Unit is well exposed in the core of the antiforms, as the Tulle Antiform in the Limousine (data Li1). It consists mainly of calc-alkaline orthogneisses metamorphosed under amphibolite facies conditions and associated with paragneisses and minor amphibolites. The entire series is partly migmatised (375-385 Ma) (*Faure et al.*, 2008);

- the uppermost Thiviers-Payzac low-grade unit (TPU) consists of metagreywackes, metasandstones and metapelites with minor amounts of quartzites, graphite schists, marbles and amphibolites. The foliation presents a well-developed NW–SE trending mineral and stretching lineation along which shear criteria indicate a top-to-the NW shearing associated to the superposition of the TPU upon the UGU. In the Quercy area (data TP1), the micaschists experienced a clockwise prograde metamorphic P-T path ending with an isobaric heating. The peak conditions correspond to the amphibolite facies conditions coeval with the top-to-the NW shearing (*Duguet et al.*, 2007).

4.2.3 Central Massif Central

A third cross-section can be analysed to enlighten the metamorphic evolution of the domains belonging to the central-southern Massif Central (Figure 4.12):

- the Upper Gneiss Unit is represented in the Haut-Allier, Artense, Cezallier, Marvejols and Rouergue metamorphic units. Eclogites in the LAC of the Haut-Allier and

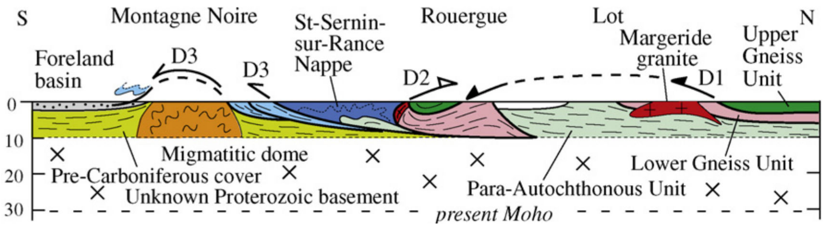

Figure 4.12: Simplified geological cross-sections throughout the central French Massif Central (from *Faure et al.*, 2009).

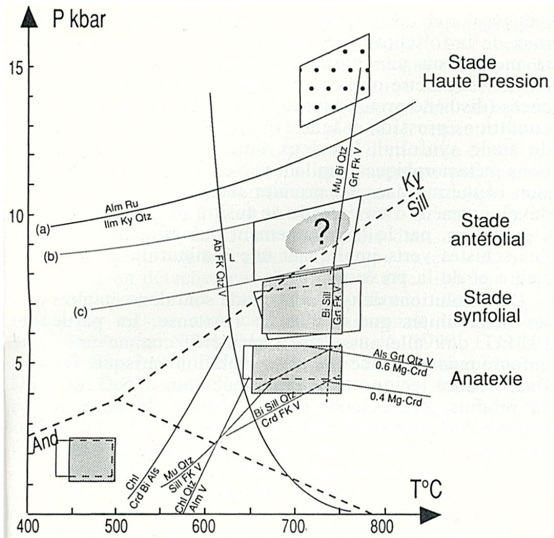

Figure 4.13: P-T paths of the paragneisses from the Artense unit. In white the UGU; in grey the LGU; HP relicts are shown by points (from *Mercier et al.*, 1992).

Marvejols areas show HP metamorphism dated at 420-450 Ma (data HA1) and 410-420 Ma (data Ma1), respectively. Moreover, in the Marvejols the eclogites are retromorphosed under granulite and amphibolite facies conditions, at 360-400 Ma and 345-360 Ma, respectively (*Pin and Peucat*, 1986; *Ledru et al.*, 1989; *Mercier et al.*, 1991b). In the Artense area relicts of HP have been observed in both the paragneisses and the amphibolites (data Ar1). In the Artense unit the evolution is characterised by an initial HP metamorphic imprint followed by a decompression associated to an increase of temperature, reaching granulite facies conditions. Differently, during the last stage the exhumation is characterised by a decrease of temperature under amphibolite facies conditions (*Mercier et al.*, 1992) (Figure 4.13). A retrograde P-T path is observed also to the south, in the Rouergue. All the klippen of the Rouergue unit (Lévézou, Najac and Le Vibal, data Ro1, Ro2 and Ro3, respectively) show HP relict metamorphism, recorded at approximately 415 Ma, followed by slightly different paths during the exhumation. However, all of them show a similar final mineral assemblage (340-350 Ma) recorded under amphibolitic facies conditions (*Burg et al.*, 1989) (Figure 4.14);

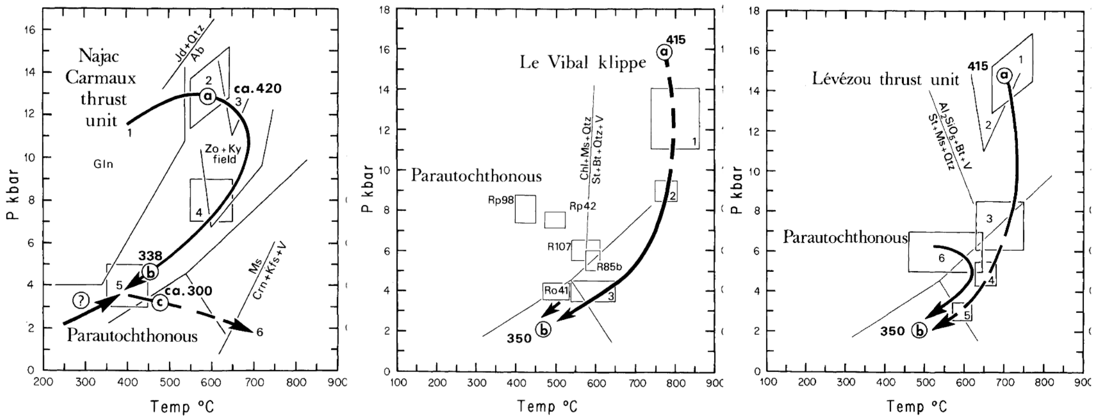

Figure 4.14: P-T paths of the klippen of the Rouergue area (from *Burg et al.*, 1989).

- the Lower Gneiss Unit of the Artense area is composed of metapelites and metamorphosed orthogneisses (data Ar2). The members of this unit do not show relicts of HP metamorphism and they underwent a retrograde metamorphic evolution after the coupling with the UGU. The older metamorphic imprint of the paragneiss is recorded under amphibolite facies conditions and is coeval with the main foliation. This unit suffered a successive anatectic event during the decompression (*Mercier et al.*, 1992) (Figure 4.13);

- in the southernmost portion of the Massif Central, the Montagne Noire exposes the Palaeozoic Fold-Thrust Belt and the southern foreland basin. It is classically divided into three units, characterised by late Visean-early Namurian south-verging recumbent folds: the southern and northern parts, composed of Palaeozoic sedimentary series, and the axial zone, composed of cores of gneisses and migmatites surrounded by micaschists. Two large lithological units form the axial zone, a basement orthogneissic complex and the Cambro-Ordovician covers, have a contact marked by amphibolite layers. Both the axial and the outer zones experienced a polyphase metamorphic evolution and, despite a pervasive anatexis, several rock types considered as protoliths are preserved as restites. The most pervasive metamorphism is a HT-LP event, with minor variations between the southern and northern part. Moreover, an earlier eclogite facies metamorphism is preserved in the mafic rocks, while in both the orthogneisses and the pelitic rocks it has been entirely deleted by the late LP metamorphism (*Demange*, 1985; *Faure et al.*, 2014) (Figure 4.15).

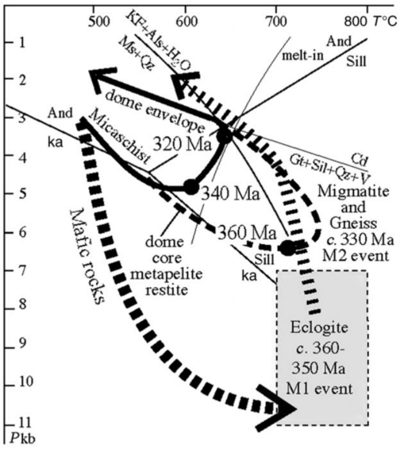

Figure 4.15: P-T-t paths of different rocks from the Montagne Noire (from *Faure et al.*, 2014).

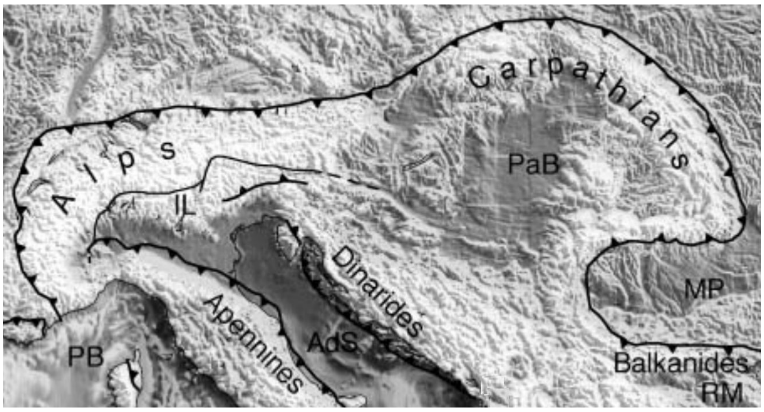

Figure 4.16: Digital terrain model of the Mediterranean region. AdS: Adriatic Sea; IL: Insubric line; MP: Moesian Platform; PB: Provencal Basin; PaB: Pannonian Basin; RM: Rhodope Massif (from *Cavazza and Wezel*, 2003).

4.3 The Alps

The Alps are the product of continental collision along the former south-dipping subduction zone between the Adriatic promontory of the African plate to the south and the southern continental margin of the European-Iberian plate to the north. The Alpine belt extend from the Gulf of Genoa to the Vienna basin, through the French-Italian western Alpine arc and the east-west-trending central and eastern Alps. The eastward continuation of the Alps is into the Carpathians and their former connection is buried below the Neogene infill of the Pannonian basin. South of Genoa, the Alpine range disappears, because it collapsed and was fragmented during the opening of the Neogene Ligurian-Provencal-Algero basin and Late Neogene Tyrrhenian basin (e.g. *Cavazza and Wezel*, 2003; *Dal Piaz et al.*, 2003; *dal Piaz*, 2010) (Figure 4.16).

According to the sense of tectonic transport toward the foreland, the Alps are currently subdivided into two belts of differing size, internal frame, age and geological meaning: 1) the Europe-vergent belt, which is a thick collisional wedge of Cretaceous-Neogene age, consisting of continental and minor oceanic units radially displaced towards the Molasse foredeep and European foreland; and 2) the Adria-vergent Southern Alps, which is a minor, non-metamorphic, ophiolite-free and younger (Neogene) thrust-and-fold belt displaced to the south, developed inside the Alpine hinterland of the Adriatic upper plate, far from the oceanic suture (*Polino et al.*, 1990 and refs therein). These belts are juxtaposed along the Periadriatic lineament, a major fault system re-activated during the Oligo-Neogene (*Dal Piaz et al.*, 2003; *dal Piaz*, 2010). Four tectonic domains can be recognised:

1. the Austroalpine domain (yellow in Figure 4.17) derived from the Adriatic passive continental margin, which mainly developed during Cretaceous. It can be subdivided into two sectors: 1) the western Austroalpine, consisting of the Seisa-Lanzo zone and numerous external slices of the Dent Blanche nappe; these continental units either override or are tectonically interleaved with the ophiolitic units of the Penninic domain. Two units are identified (the upper Austroalpine outliers and the Sesia-Lanzo inlier), which were diachronously subducted to various depths; 2) the eastern Austroalpine, consisting in a pile of cover and basement nappes extending from the Swiss/Austrian border to the Pannonian basin. Its allocthony over the Penninic zone is marked by the ophiolitic units exposed in the Engadine, Tauern and Rechnitz windows. To the north the Austroalpine overrides the outer-Penninic Rheno-Danubian flysch belt, while to the south it is juxtaposed to the Southalpine upper continental crust along the Periadriatic lineament. In different portions of Central and Eastern Alps it is possible to recognise fragment of Variscan lower continental crust with eclogitic relics and slices of garnet-spinel peridotite (*Spalla et al.*, 2014 and refs therein);

2. the Penninic domain (blue in Figure 4.17) is limited to the north by the Penninic front; it is constituterd by the continental and oceanic nappes of the proximal European continental margin and the Mesozoic ocean. In the Western Alps five kinds of units can be distinguished: 1) the ophiolitic units, that are subdivided in eclogitic (HP/UHP) and blueschists facies (HP) units, both overprinted by a greenschist to amphibolite facies; 2) the inner-Penninic nappes of the continental basement; 3) the middle-Penninic multinappes system; 4) the lower-Penninic nappe of the Ossola-Tessin window and outer-Penninic Valais zone, including ophiolitic units and flysch décollement nappes, limited to the north by the Penninic frontal thrust; 5) klippe constituted by pre-Alpine metamorphic basement. In the Eastern Alps, the Penninic zone is exposed in the Engadine, Tauern and Rechnitz windows. The Tauern nappe consists of the ophiolitic nappe and of the underlying cover and basement nappes derived from the European passive continental margin. The conti-

nental nappes of the Penninic zone include metamorphic pre-Alpine basement and the whole domain, excluding the klippe, shows a HP Alpine metamorphism which overprints the pre-Alpine metamorphism (*Spalla et al.*, 1996; *dal Piaz*, 2010; *Lardeaux*, 2014b and refs therein);

3. the Helvetic domain (red in Figure 4.17) consists of prominent crystalline massifs, sedimentary cover units, and décollement nappes derived from the European margin. It is possible to recognise units characterised by polymetamorphic basement (with Variscan and older metamorphism) and units characterised by monometamorphic basement (only Variscan metamorphism), evolving from an Ordovician subduction, through a successive Variscan collision, to the orogenic collapse and the erosion during the Carboniferous (*Spalla et al.*, 2014 and refs therein);

4. the Southalpine domain (green in Figure 4.17) extends to the south of the Periadriatic lineament. It belongs to the continental Adriatic margin and it shows a very low-grade Alpine metamorphic imprint (chlorite, white mica and stilpnomelane) associated with the earlier Alpine fabrics (*Albini et al.*, 1994; *Carminati et al.*, 1997; *Spalla et al.*, 1999). During Alpine convergence E–W trending folds and thrusts developed and progressively propagated to the south, reactivating Mesozoic extensional faults.

By the means of deep seismic experiments two distinct Moho surfaces have been recognised: the Adriatic and the underlying European Moho, which gently bends from the Alpine foreland to the deep base of the collisional wedge (Figure 4.18). The global setting of the Alps is asymmetric and the orogeny was dominated by Europe-vergent displacements, while the antithetic Southalpine belt is only a superficial feature of the Adriatic upper plate. The Europe-vergent belt is a mantle-free crustal wedge which tapers to the north, floating over the current European lower plate and indented to the south by the current Adriatic lithosphere (Figure 4.18). The orogenic wedge groups the Austroalpine, Penninic and Helvetic domains and may be subdivided into two diachronous parts: 1) in the inner portion of the belt, between the Penninic front and the Periadriatic lineament, the older Austroalpine-Penninic part can be recognised. This is a fossil subduction complex which includes the Adria/Europe collisional zone, marked by one or more ophiolitic units and displays polyphase metamorphism evolving from blueschist or eclogite facies imprint of Cretaceous-Eocene, to a HT Barrovian overprint of late Eocene-early Oligocene age; 2) the younger Helvetic part, which is in the northern from the Penninic front. This is made up of shallower basement thrust-sheets and largely detached cover units which derived from the distal European margin, which escaped the low-T subduction regime and were accreted in front of the exhumed Austroalpine-Penninic wedge from the Oligocene (*Polino et al.*, 1990).

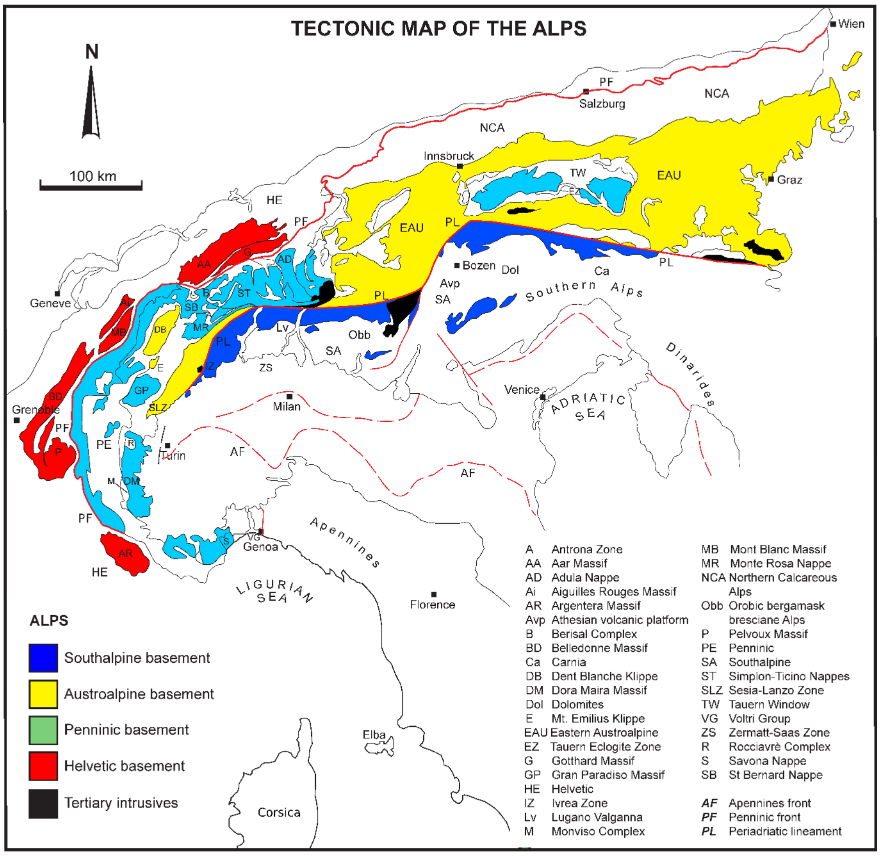

Figure 4.17: Tectonic map of the Alps (from *Spalla et al.*, 2014).

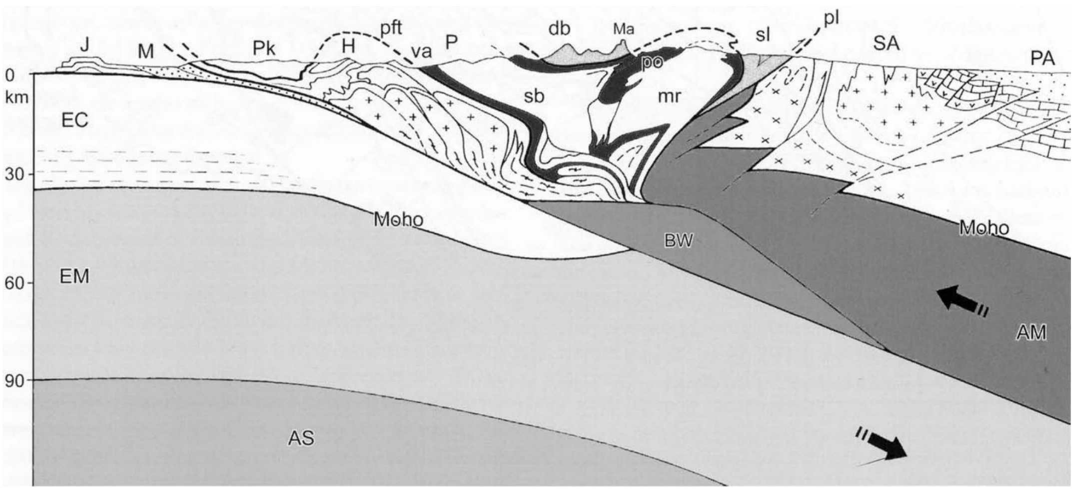

Figure 4.18: NW-SE geological section of the Alps. Austroalpine domain: Sesia-Lanzo (sl); Dent Blanche nappe (db); Matterhorn (ma). Penninic domain (P): Piedmont ophiolitic units (po); Monte Rosa (mr); Grand St. Bernard (sb) nappes; Valais zone (va); Penninic klippen (Pk); Penninic frontal thrust (pft). Helvetic domain (H); Southalpine domain (SA); periadriatic fault system (pl); molasse foredeep (M); Jura belt (J); buried wedge (BW); continental crust (EC); continental mantle (EM); asthenosphere (AS); adriatic lithospheric mantle (AM); padane-Adriatic foreland (PA) (from *dal Piaz*, 2010).

4.3.1 Variscan metamorphism in the Alps

Most of the pre-Alpine basement recycled during the Alpine subduction shows a pre-Mesozoic metamorphic evolution, compatible with the evolution that characterised the european Variscan belt (*von Raumer et al.*, 2003; *Spalla et al.*, 2014). The future Alpine domains were probably located along the southern flank of the Variscan belt (*von Raumer et al.*, 2003). The oldest zircons found in various polymetamorphic basements refer to Precambrian clastic material eroded from extra-Alpine sources. The occurrence of Proterozoic-early Cambrian ocean spreading, island-arc activity, and bimodal volcanism is documented in the European and Adriatic basement, with debated traces of Precambrian amphibolite-eclogite facies metamorphism (Aar, Silvretta) (*Maggetti and Galetti*, 1988; *Maggetti and Flisch*, 1993; *Schaltegger*, 1994). From the Middle Ordovician onward, sedimentary gaps and thermal uplift in the Alpine domain are thought to represent the general crustal extensional regime, as observed outside the Alpine domains. In many Alpine basement areas, polymetamorphic assemblages comparable to those of the contemporaneous European geological framework prevail, testifying to a polyphase metamorphic evolution accompanied by nappe stacking during different periods (*von Raumer et al.*, 2013). An early phase of subduction at about 380 Ma is characterised by transformation of metabasites into eclogites (*Stampfli*, 2002; *Liati et al.*, 2009; *von Raumer et al.*, 2013) and in some zones a subsequent recrystallisation under granulite facies conditions took place at about 340 Ma (*Ferrando et al.*, 2008; *Liati et al.*, 2009; *Rubatto et al.*, 2010). From 330 Ma onward, a general environment of exhumation and uplift is well shown in the basement outside the Alps, leading to a widespread HT overprint. These conditions induce a systematic migmatisation also observed in all the External massifs of the Helvetic domain (*von Raumer et al.*, 2013). P-T estimates of the Variscan metamorphism in the Alps are presented in Tables B.1 and B.3.

4.3.2 The Austroalpine domain

The metamorphic basement of the Austroalpine domain (data Av in Table B.1) was part of Gondwana before its involvement in the Variscan collision with Laurussia (*von Raumer*, 1998; *Desmons et al.*, 1999a). In the Austroalpine basement, relicts of HP metamorphism are preserved in lenses and elongated bodies of metabasites inside metapelites. Locally, garnet, omphacite and quartz bearing eclogites are preserved in these bodies, as result of the non-complete re-equilibration during the exhumation following the Variscan metamorphic peak (*Konzett et al.*, 2005). Eclogites have been observed in different localities of the Central and the Eastern Alps, as the Ulten zone, the Oetzal-Stubai zone, the Silvretta basement, the Languard-Campo nappe, Koralpe and Saualpe (*von Raumer*, 1998; *Spalla et al.*, 2014). All these eclogites show a polyphasic evolution with a Variscan HP metamorphism for some of them (*Miller and Thöni*, 1995; *Sassi et al.*, 2004; *Konzett et al.*, 2005).

Variscan eclogites are preserved within large bodies derived from gabbros and related ultramafic cumulates, re-equilibrated mostly under amphibolite facies conditions (*Godard et al.*, 1996; *Spalla et al.*, 2014). The Austroalpine domain of the Central and Eastern Alps is dominated by pre-Alpine basement rocks and two main types of crustal elements can be differentiated: 1) the upper Austroalpine nappes, in the external zone; and 2) the middle Austroalpine units, in the internal zone (*Neubauer*, 1988; *von Raumer*, 1998). In the external zone Ordovician to Devonian sediments with acidic volcanic rocks of Ordovician age and basic intraplate to marginal basin volcanism of Silurian and Devonian age testify to rifting along the former Gondwana passive margin. In the internal zone Gondwana-derived crustal blocks contain metabasitic series (e.g. Silvretta) which indicate a Cambrian island-arc situation. These units were the place of deep crustal thrusting since the early Variscan evolution, and synkinematic granitoids are the signs of collision during the Early Carboniferous (*von Raumer*, 1998). In the Western Alps, the Sesia zone, the Dent Blanche nappe and the klippe between them form three complexes called Lower Austroalpine (*Desmons et al.*, 1999b).

Valpelline series (Dent Blanche nappe)

The Dent Blanche nappe comprises two main units described as the structurally lower Arolla series, composed of late Paleozoic granites and granodiorites and mafic to ultramafic rocks, and the structurally higher Valpelline series, composed of high-grade paragneisses with lenses and layers of basic granulites, garnet and clinopyroxene bearing amphibolites and marbles (*Gardien et al.*, 1994; *Desmons et al.*, 1999b; *Zucali et al.*, 2011; *Manzotti and Zucali*, 2013). The dominant metamorphic imprint occurs under amphibolite to granulite facies conditions and it is of pre-Alpine age (*Gardien et al.*, 1994; *Manzotti and Zucali*, 2013) (data Av11 and Av12 in Table B.1). The Alpine imprint is localised along high-strain zones that are tens to hundreds of metres wide and occur under greenschists facies condition (*Manzotti and Zucali*, 2013). *Gardien et al.* (1994) observed a pre-Alpine polymetamorphic evolution, consisting of an early intermediate pressure granulitic stage recorded by rare relics of kyanite, rutile and alkali feldspar, follow by an intensive re-equilibration under HT amphibolite facies conditions. *Zucali et al.* (2011); *Manzotti and Zucali* (2013) observed a pre-Alpine tectonometamorphic evolution in four evolutionary stages, from pre-Permian to Alpine age and under granulite to greenschist facies conditions (Figure 4.19).

Ulten zone (Tonale nappe)

The Ulten zone is part of the upper Austroalpine domain, which consists of a metasedimentary cover and crustal slices derived from the Mesozoic passive margin of the Adria microplate (*Godard et al.*, 1996). North of the Tonale and Giudicarie lines, the Austroalpine

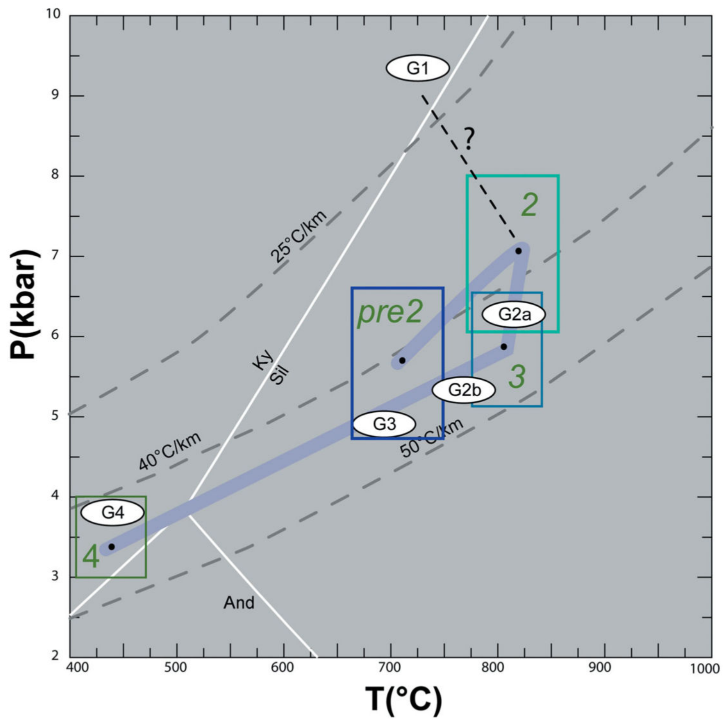

Figure 4.19: P–T–t–d paths reconstructed by *Zucali et al.* (2011); *Manzotti and Zucali* (2013) (boxes and chronology) and by *Gardien et al.* (1994) (G1, G2a, G2b, G3 and G4) (from *Manzotti and Zucali*, 2013).

system comprises a northern, cover-bearing nappe (Ortler nappe) and a southern, cover-free nappe (Tonale nappe) (*Scambelluri et al.*, 2010). The Ulten Zone belongs to the Tonale nappe that is separated from the Ortler nappe to the north by the Peio Line and from the Southalpine domain to the south by the Giudicarie line, which is a segment of the Peri-adriatic lineament. The Tonale nappe is subdivided into Tonale and Ulten Zones, which are divided by the Val Clapa and Rumo Lines. The Tonale Zone is mainly composed of sillimanite-bearing metasediments, metagranitoids with subordinated marbles, calc-silicates and mafic and ultramafic layers retrogressed during the late- or post-Variscan exhumation. In addition, an Alpine greenschist facies overprint locally affects these rocks. The crustal Ulten Zone is composed of migmatites, garnet and kyanite bearing gneisses and subordinate metagranitoids. Ultramafic lenses, ranging in composition from lherzolite to dunite, are located between the garnet-kyanite gneiss and the overlying migmatites. Boudins of mafic amphibolites and rare retrogressed eclogites also occur as lenses in the gneiss and migmatites. Differently, the Variscan HP (eclogite to granulite facies) metamorphic signatures of the Ulten zone is well-preserved (data Av4, Av5 and Av6 in Table B.1) and is only weakly overprinted by Alpine metamorphism (*Godard et al.*, 1996; *Tumiati et al.*, 2003; *Scambelluri et al.*, 2010). In the Ulten zone basement textural and/or mineralogic relicts belonging to different stages of deformation and metamorphism have been recognised and its history can be summarized as follows: 1) pre-D1

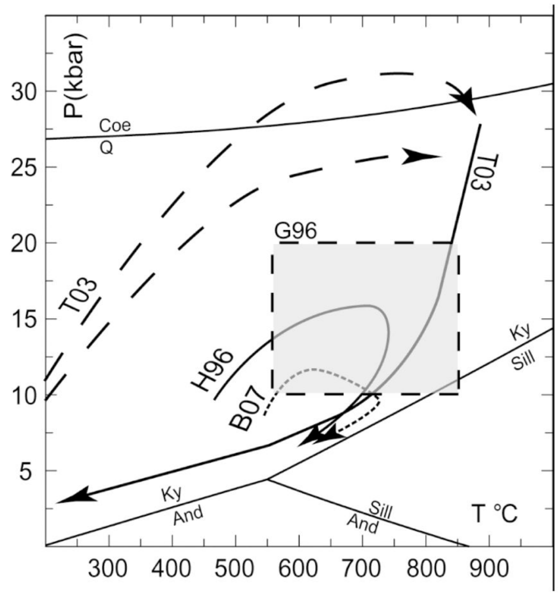

Figure 4.20: P–T paths reconstructed for the Ulten zone by *Tumiati et al.* (2003) (T03), *Godard et al.* (1996) (G96), *Hauzenberger et al.* (1996) (H96) and *Braga et al.* (2007) (B07) (from *Scambelluri et al.*, 2010).

(*Godard et al.*, 1996) (or syn-D1, *Hauzenberger et al.*, 1996), characterised by migmatisation by dehydration melting; 2) D1, characterised by mylonitic deformation at eclogite facies conditions; 3) post-D1, characterised by injection by exotic melts and further migmatisation at eclogite-granulite facies conditions during decompressional exhumation; 4) D2, characterised by shearing and retrogression. The estimates define a metamorphic evolution characterised by a clockwise P-T path, with a HP peak followed by thermal relaxation up to maximum temperature and a successive retrogression under amphibolite to greenschist facies conditions (*Scambelluri et al.*, 2010) (Figure 4.20).

Silvretta nappe

The Silvretta nappe is situated at the border zone of Switzerland and Austria and it is consituted for the large part of crystalline rocks, with the exception of the autochthonous Permo-Triassic sediments. The most common crystalline rocks are orthogneisses and metabasites, except in the northern part where metasedimentary rocks prevail. Unaltered eclogites and altered pre-Variscan eclogites occur as small subconcordant bodies in amphibolites or medium grade paragneisses (*Maggetti and Galetti*, 1988; *Maggetti and Flisch*, 1993; *Schweinehage and Massonne*, 1999). The Silvretta nappe show the highest content of metabasites compared to other basement units of the Eastern Alps and they occur as lenses of plagioclase, epidote, biotite and garnet bearing amphibolites folded around subvertical axis and intercalated in metapelites and metagreywackes (*Schweinehage and Massonne*, 1999). In the crystalline basement, ultramafic rocks have been described from the Hochnorderer to Val Sarsura, and on the western face of the Hochnorderer three ultra-

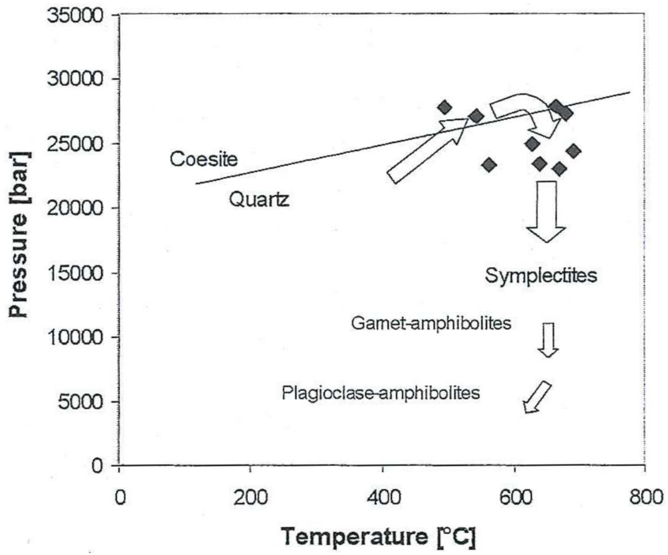

Figure 4.21: P–T paths reconstructed for the eclogites of the Silvretta nappe (from *Schweinehage and Massonne*, 1999).

mafic lenses in amphibolites have been observed (*Melcher et al.*, 2002). The polymetamorphic evolution of the Silvretta nappe begins with an Ordovician HP-HT event preserved in few orthogneisses, followed by a Variscan deformation under amphibolitic facies conditions and by a successive late-Variscan low-grade event (*Schweinehage and Massonne*, 1999) (Figure 4.21) (data Av7 and Av8 in Table B.1). The Alpine metamorphism have weakly overprined the pre-Alpine history and it is constrained to the area surrounding the Engadine window where metamorphism in greenschist facies conditions have been recorded (*Schweinehage and Massonne*, 1999; *Melcher et al.*, 2002).

Speik complex (Hochgrossen massif)

The Speik complex is a lithotectonic unit belonging to of the middle Austroalpine domain and is constituted by a package of amphibolites, gabbros, sediments and serpentinized ultramafic rocks several hundred meters thick that represent a pre-Silurian dismembered ophiolite nappe. This unit underwent metamorphism during Variscan times (data Av1 in Table B.1) and was overprinted during Eoalpine orogeny to variable degrees. The Hochgrossen massif is part of the Gaaler Schuppenzone, which contains fragments of the Speik complex with transgressing Permo-Mesozoic sediments. To the north and NE of the Hochgrossen summit, a rootless body of strongly foliated serpentinite structurally overlies a paragneiss suite with minor amphibolite. Retrogressed eclogite and amphibolite also form a concordant lens within the serpentinite close to its eastern margin (*Faryad et al.*, 2002). Differently from most eclogites to the east of the Tauren window which are related to Eoalpine metamorphic events, these eclogites show a pre-Alpine evolution as eclogites observed to the west of the Tauren window (*Miller and Thöni*, 1995; *Schweinehage* *and Massonne*, 1999; *Faryad et al.*, 2002).

Oetztal-Stubai complex

The Oetztal-Stubai polymetamorphic complex was overthrust on Pennine rock series during the late Cretaceous-Tertiary (*Miller and Thöni*, 1995). The Oetztal-Stubai complex consists predominantly of metapelitic to metapsammitic gneisses and schists with intercalated metacarbonates that recorded the Variscan metamorphic evolution under medium to high-grade conditions (data Av2 and Av3 in Table B.1) and overprinted by Eo-Alpine metamorphism, with increasing intensity from NW to SE and culminates in a zone of epidote-amphibolite to eclogite facies conditions (*Miller and Thöni*, 1995; *Konzett et al.*, 2005; *Rode et al.*, 2012). Meta-igneous rocks are present throughout the entire complex as amphibolites and granitic orthogneisses cropping out in concordant layers or lenses. The structures are dominated by a strong EW-trending schistosity and by a kilometre-scale folding around steep axes (*Konzett et al.*, 2005). Petrological and geochronological data indicate at least three major periods of metamorphism or thermal activity in the Oetztal-Stubai complex (*Miller and Thöni*, 1995; *Konzett et al.*, 2005): 1) a Cadomian to Caledonian high-grade event at 530-440 Ma that led to the formation of migmatites and the intrusion of granites and gabbros; 2) a dominant Variscan eclogite to amphibolite facies event at 390-330 Ma; 3) an Eo-Alpine event at 100–65 Ma. Rocks other than metabasites only rarely preserve evidence for a Variscan HP metamorphism. A similar Variscan metamorphic evolution can be stated for different portion of the complex and the basement can be considered to be involved in the Variscan collision as a single lithotectonic unit (*Rode et al.*, 2012) (Figure 4.22).

4.3.3 The Penninic domain

The Penninic domain (data Pv in Table B.1) is supposed to have migrated, since the Jurassic, from a more southwestern position to its actual position between the Helvetic and Austroalpine domains. (*von Raumer*, 1998). The western Penninic units consist either of Precambrian to early Palaeozoic polymetamorphic basement or monometamorphic basement (*Thélin et al.*, 1993; *Desmons and Mercier*, 1993; *von Raumer*, 1998; *Desmons et al.*, 1999a). The Grand St. Bernard nappe is commonly divided in four main tectonic units that, from the external (NW) to the internal (SE) side of the Alpine chain and from the lower to the upper structural level are: the Zone Houillere, the Pontis nappe, the Siviez-Mischabel nappe and the Mont Fort nappe. The Pontis and Siviez-Mischabel nappes comprise both poly- and mono-metamorphic basements, while the two other units apparently escaped any pre-Alpine metamorphism. Two metamorphic preserved windows allow a partial reconstitution of the pre-Alpine metamorphic history: 1) eclogites in the Siviez-Mischabel nappe, associated with banded amphibolites, that show pre-Variscan

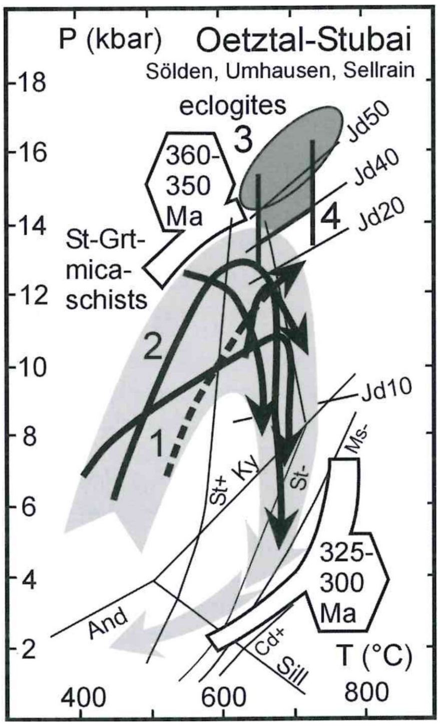

Figure 4.22: Summary of P-T paths in the central and northern Oetztal-Stubai complex (from *Rode et al.*, 2012).

HP mineral assemblages, overprinted by an amphibolite facies event; 2) the Mont Mort (Pontis nappe), composed of garnet and staurolite micaschists and aluminum silicate bearing schists (*Borghi et al.*, 1999; *Thélin et al.*, 1990; *Giorgis et al.*, 1999; *Bussy et al.*, 1996; *Thélin et al.*, 1993; *Desmons and Mercier*, 1993). The Inner Crystalline massifs (Dora Maira massif, the Monte Rosa nappe and the Gran Paradiso massif) represent basement nappe of the Inner Penninic domain, characterised by the occurrence of HP metamorphic assemblages (*Gasco et al.*, 2011a,b). To the east, the polymetamorphic basements have been recognised in the Lucomagno and Leventina areas and in the Tambo and Suretta nappes (*Thélin et al.*, 1993). The Tauern region is underlain by a metabasic series of lower Palaeozoic age which could represent a prolongation of the External massifs towards the east. The late Variscan evolution can be well compared to that of the External massifs of the Helvetic domain (*von Raumer*, 1998).

Siviez-Mischabel nappe

The Siviez-Mischabel nappe thickens progressively eastward and it is composed of polymetamorphic basement, in which eclogites can be observed, and of a mono-metamorphic cover (*Thélin et al.*, 1990, 1993). The poly-metamorphic basement is subdivided into two units: the Ergishhorn unit, composed mainly by paragneisses and amphibolites, and the Barneuza unit, which includes banded amphibolites, augen-schists and a banded com-

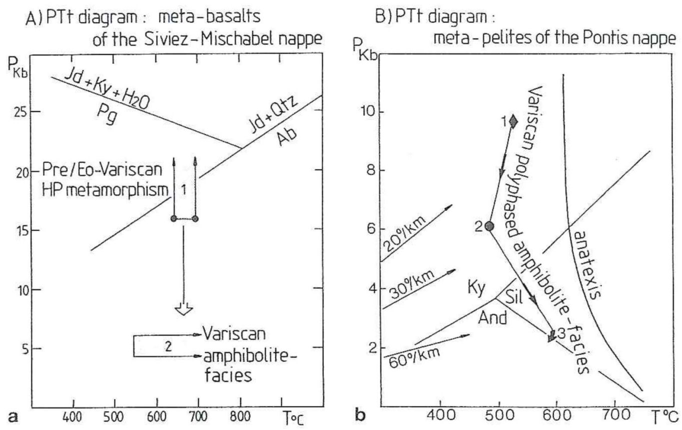

Figure 4.23: P-T-t paths related to eclogites of the Siviez-Mischabel nappe (a) and of the Pontis nappe (b) (from *Thélin et al.*, 1993).

plex made up of chlorite schists, amphibolites and garnet bearing mica schists. The eclogites and the retrogressed eclogites are associated to banded amphibolites of the Barneuza unit and they show HP mineralogical associations, sometimes overprinted by a metamorphism developed under amphibolitic facies conditions (*Thélin et al.*, 1993) (Figure 4.23a). The eclogitic imprint has been recorded only in the basement and it has been recorded in pre-Permian age, because of the presence of Permian non-eclogitised gabbro (*Thélin et al.*, 1990). The uncertain age of this HP imprint makes impossible to consider the eclogite imprint as Variscan with a good confidence (data Pv7 in Table B.1). The Alpine metamorphism developed under greenschist facies conditions has been recorded both by the basement and by the covers (*Thélin et al.*, 1993).

Pontis nappe (Mont Mort)

The Mont Mort metapelites are located in the Grand St. Bernard area, in the internal Ruitor zone of the Pontis nappe. They represent one of the best example of well preserved pre-Mesozoic metamorphic assemblages in the Penninic domain (*Bussy et al.*, 1996; *Giorgis et al.*, 1999). The Mont Mort unit is mainly composed of a thick metapelitic series overlain by garnet and staurolite bearing mica schists. Quartzites, felsic banded gneiss and amphibolitic gneisses occur sporadically within the two main lithologies (*Giorgis et al.*, 1999). Textures and mineral chemistry of the metapelites reflect a Variscan polyphase PT path, characterised by a first stage developed under amphibolitic facies (data Pv6 in Table B.1) conditions followed by an adiabatic decompression (*Thélin et al.*, 1993; *Bussy et al.*, 1996; *Giorgis et al.*, 1999) (Figure 4.23b). The Alpine metamorphism is weekly developed in the Mont Mort unit and it is characterised by greenschist facies assemblage (*Giorgis et al.*, 1999).

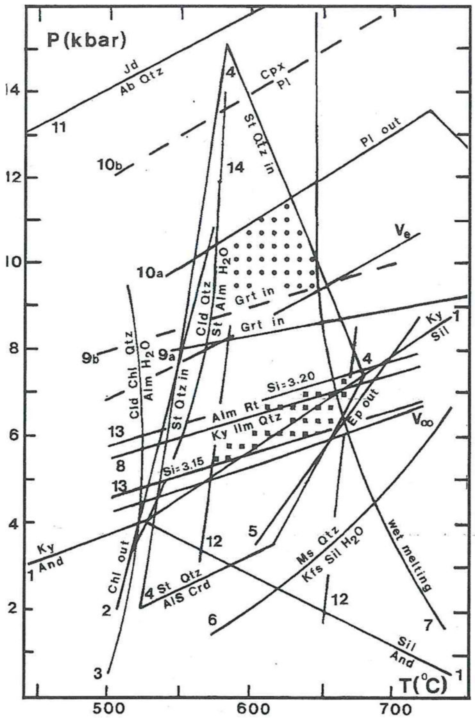

Figure 4.24: Metamorphic conditions for the first (dotted) and the second (squared) pre-Alpine events preserved in Clarea Complex (from *Borghi et al.*, 1999).

Ambin nappe

The Ambin nappe is considered a tectonic unit of continental crust belonging to the internal portion of the Grand St. Bernard nappe, showing affinities with the Pontis nappe. The Ambin nappe consists of two metamorphic complexes: the lower characterised by a pre-Alpine poly-metamorphic evolution (Clarea complex), and the upper characterised by a mono-metamorphic evolution (Ambin complex). In the lower tectonic levels, the first pre-Alpine stage occurred under IP conditions and it is defined only by mineralogical relics in the metabasites and in the metapelites (data Pv5 in Table B.1), while the second, dominant stage has been developed under epidote-amphibolitic facies conditions and it is marked by the main sub-horizontal foliation of metapelites and orthogneisses (Figure 4.24). The two complexes show the same Alpine metamorphic evolution characterised by two main events. The first event occurred under epidote-blueschist facies conditions and it is followed by adiabatic decompression and then by a second metamorphic event of Oligocene age (*Borghi et al.*, 1999).

Ligurian Alps (Savona Massif)

The Savona Massif belongs to the Variscan basement of the Ligurian Alps, which are situated within the southernmost Penninic realm, in the Brianconnais domain, a stack of pre-

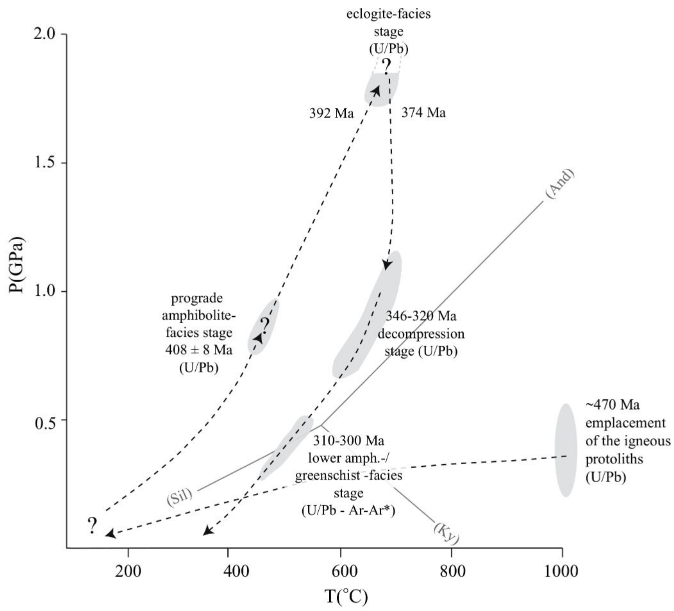

Figure 4.25: P-T-t evolution of the eclogites from the Savona Massif. U/Pb data from *Messiga et al.* (1992); *Cortesogno et al.* (1998), Ar-Ar data from *Barbieri et al.* (2003) (from *Giacomini et al.*, 2007).

Alpine sedimentary sequences and basement slices thought to represent the Mesozoic passive margin of the European continent (*Messiga et al.*, 1992; *Giacomini et al.*, 2007; *Maino et al.*, 2012). It underwent a poly-orogenic evolution, by means of which phases of Alpine deformation and metamorphism overprinted older metamorphic units of Variscan or pre-Variscan age. Despite this polyphase Alpine evolution, the Ligurian Alpine tectonic domains preserve a well-exposed post-Variscan succession (*Maino et al.*, 2012). The Savona Massif comprises a strongly deformed mafic amphibolite-paragneiss complex in tectonic contact with orthogneisses, related to pre-Alpine evolution. Locally, the amphibolites retain relics of gabbro and of eclogite facies assemblages (*Messiga et al.*, 1992; *Giacomini et al.*, 2007). Several Variscan geological events can be recognised (data Pv1 in Table B.1): 1) eclogite facies conditions during the eo-Variscan collisional stage; 2) amphibolite facies overprint and concomitant migmatisation of some protoliths; and 3) lower amphibolite-greenschist facies event related to late stages of exhumation (*Messiga et al.*, 1992; *Maino et al.*, 2012) (Figure 4.25). The Variscan basement rocks are partially covered by a Permian volcano-sedimentary succession (*Maino et al.*, 2012). The Alpine metamorphic overprint is localised along shear zones and tectonic contacts, without exceeding greenschist or blueschist facies conditions (*Messiga et al.*, 1992; *Giacomini et al.*, 2007).

Gran Paradiso massif

The Gran Paradiso massif is a large tectonic window, which consists of a subducted continental crust underlying eclogite facies oceanic units (*Le Bayon et al.*, 2006). The northern part of the Gran Paradiso massif consists of two main units, the Money unit and the overlying Gran Paradiso unit. The Money unit is a mono-metamorphic unit, mainly consists of metapelites and metaconglomeratic layers containing exclusively Alpine metamorphic minerals, while pre-Alpine relics are lacking. The Gran Paradiso unit essentially consists of augen-gneisses derived from porphyritic granitoids of late Paleozoic age (data Pv2 and Pv3 in Table B.1). The Variscan metasedimentary rocks were reworked during Alpine orogeny and transformed into a polymetamorphic complex of paragneisses and micaschists with lenses of eclogites interpreted as either pre-Alpine amphibolites or Variscan gabbros. The overprinting eclogite facies assemblages of Alpine age are identified in both the metabasic and the metasedimentary rocks of the Gran Paradiso unit (*Le Bayon et al.*, 2006; *Gasco et al.*, 2010).

Monte Rosa nappe

The Monte Rosa nappe consists of pre-Alpine basement comprising a high-grade paragneiss complex containing migmatites (data Pv4 in Table B.1), transformed to garnet-micaschists during the Alpine cycle (*Dal Piaz*, 2001; *Gasco et al.*, 2011a). The whole nappe is characterised by low-strain domains that preserve intrusive relationships between the granitoids and the high-grade pre-Alpine complex, and by high-strain domains in which the Alpine structural and metamorphic imprint is well developed. Horizons rich in mafic boudins and marbles are present at different structural levels within the metapelites (Furgg zone). The post-Variscan cover of the Monte Rosa is represented by late Carboniferous-Permian and Mesozoic sequences mainly preserved in the external parts of the nappe (Gornergrat zone) or included in the Furgg zone (*Gasco et al.*, 2011a).

Adula nappe

The original palaeogeographical position of the Adula nappe is at the distal European margin, towards the Valais ocean. The Adula nappe, including the Cima Lunga unit to the west and the Gruf Complex to the east, is the largest basement nappe in the eastern part of the Central Alps (*Liati et al.*, 2009). It consists of a basement of ortho- and paragneisses and metapelitic schists of pre-Mesozoic age, with minor amounts of metasedimentary rocks of postulated Mesozoic age occurring as thin imbricate slices in the central and northern parts. Metabasic eclogites and amphibolites occur as boudins enclosed within predominantly paragneisses. They are both Alpine and Variscan in age. The latter occurs at 306-402 Ma in the central part and at 304-354 in the northern part (data Pv8 and Pv9 in Table B.1). Ultramafic rocks are generally only present at the western and eastern margins of the nappe, but are locally dominant in the associated Cima Lunga unit to the west. Based on the mineralogy and the P-T conditions of the HP rocks, the Adula Nappe has been subdivided into northern, central and southern domains. In the northern part, metabasites are characterized by barroisite and glaucophane bearing assemblages, whereas the rock felsic gneisses are dominated by garnet, white mica and kyanite bearing assemblages. Some of the gneisses of the northern Adula nappe still preserve HP relics. The metabasites of the middle Adula nappe are generally well-preserved eclogites surrounded by HP metapelites. In the southern part, metabasic rocks are rare (*Dale and Holland*, 2003; *Liati et al.*, 2009).

Suretta nappe

The Suretta nappe forms a thin crystalline sliver covered by a thin autochthonous sedimentary cover. The crystalline basement is composed of polymetamorphic rocks, including metapelites, metagreywackes and minor mafic lenses, mainly amphibolites. The authochtonous sedimentary cover lies unconformably over the already deformed basement. Pre-Alpine structures are preserved in the core of the mafic lenses and they are associated with a schistosity oblique with respect to the Alpine schistosity. The mafic lenses show a pre-Alpine HP-HT metamorphism probably developed during the Ordovician subduction (data Pv10 in Table B.1), followed by an evolution toward HT condition developed during the continental collision. The garnet bearing amphibolitic facies observed into the lenses shows a minor retrogression under greenschist facies condition (*Nussbaum et al.*, 1998).

Tauern window (Inner Schieferhulle)

The Tauern window exposes Eastern Alpine Penninic nappes below the Austroalpine nappes. The main geological units are the Altkristallin, the Lower Schists Cover, the Upper Schists Cover and the granites (*von Quadt et al.*, 1997). The Penninic rocks of the SE Tauern window have been subdivided into a Basement Complex, consisting of a series of old poly-metamorphic schists and gneisses (the Inner Schieferhulle) and a younger series of Permian calcalkaline plutonic rocks (the Zentralgneis), and the Peripheral Schieferhulle, a structurally higher cover sequence of metamorphosed Mesozoic sedimentary and volcanic rocks. Both units have recorded Alpine metamorphism, while only the Inner Schieferhulle basement has memory of an older orogenic cycle. Two distinct phases of pre-Alpine regional metamorphism can be recognized in the Inner Schieferhulle: an eclogite facies event and a later amphibolite-facies event (Figure 4.26). They may have been part either of a single Variscan metamorphic cycle or the eclogite facies metamorphism may be older. The eclogites are exposed only in an area in the central part of a large amphibolitic body in Dosener Tal (*Droop*, 1983) (data Pv12 in Table B.1). Similar eclogitic rocks from the Penninic basement (lower Schieferhulle) have been described in the southern central portion of the Tauer window (*Zimmermann and Franz*, 1989) (data Pv11 in Table B.1).

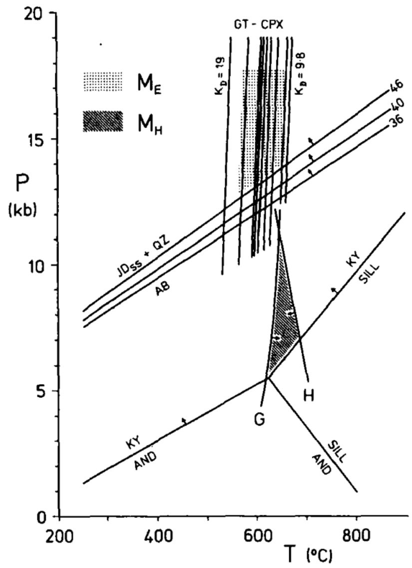

Figure 4.26: Estimates P-T conditions for pre-Alpine metamorphic events in Tauern window (from *Droop*, 1983).

4.3.4 The Helvetic domain

Wide remnants of the Variscan basement are exposed in the External Crystalline Massifs of the Helvetic domain (data Hv in Table B.1), in the Western Alps. The Paleozoic basement of the External Crystalline Massifs is composed of metamorphic rocks with ages ranging from the Cambrian to the Carboniferous and of non-metamorphic covers with ages ranging from the upper Carboniferous and the Permian (*Ferrando et al.*, 2008; *Rubatto et al.*, 2010; *von Raumer et al.*, 1999; *Guillot and Ménot*, 2009). The Permo-Carboniferous granitoids show an Alpine metamorphic imprint, limited to shear zones and developed under greenschist facies conditions, allowing the preservation of the pre-Alpine evolution (*Guillot and Ménot*, 2009; *Compagnoni and Ferrando*, 2010).The exhumation of the External Crystalline Massifs from below the Alpine sediments initiated in the Miocene, at the end of the Alpine orogeny. The External Crystalline Massifs include the Argentera massif, the Oisans massif, the Belledonne massif, the Grandes Rousses massif, the Aiguilles Rouges massif, the Mont Blanc massif, the Aar massif and the Gotthard massif (*Ferrando et al.*, 2008; *Rubatto et al.*, 2010; *von Raumer et al.*, 1999; *Guillot and Ménot*, 2009). According to *Guillot and Ménot* (2009), the External Massifs can be subdivided in three domains:

1. a western domain corresponding to the external zone of the Belledonne massif, which is composed of metasedimentary rocks with minor intercalation of mafic layers (late Proterozoic-early Paleozoic);

2. a central domain composed of the southwestern Belledonne, of the Grandes Rousses massif and of the external portion of the Oisans massif. This domain comprises the Chamrousse ophiolitic complex (Cambro-Ordovician), the plutons, the Devo-

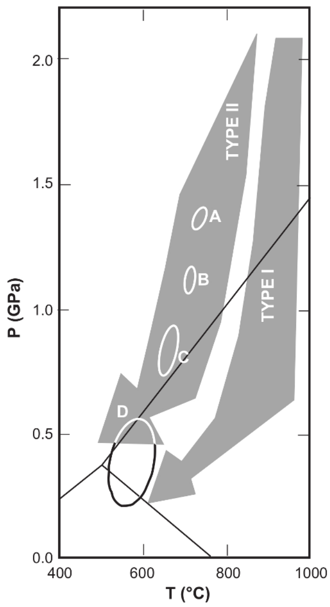

Figure 4.27: P-T path inferred for the mafic sequence of the Frisson lake of the Argentera massif (metamorphic stages A to D: white circles). P-T paths for type I and type II HP granulites are shown as broad grey arrows deduced by *O'Brien and Rötzler* (2003) (from *Ferrando et al.*, 2008).

Dinantian volcanic series and Visean metasediments;

3. an eastern domain that includes the northeastern part of Belledonne, the internal zone of the Oisans massif, the Argentera massif, the Aar massif, The Gotthard massif and the Mont Blanc massif. This domain is composed of polymetamorphic basement that includes retrogrades eclogites, mafic granulites and intrusions. The basement is covered by Visean metasediments and by Permo-Carboniferous deposits.

Argentera massif

The Argentera is the southernmost External Crystalline Massif and consists of a migmatitic basement with abundant relicts of pre-anatectic rock types, intruded by late Carboniferous to Permian granites cutting across the foliation. The massif is subdivided into two medium- to high-grade metamorphic units: the Tinée Terrain in the SW and the Gesso-Stura Terrain in the NE (data Hv1 in Table B.1), separated by the Ferriere-Molliéres shear zone (*Rubatto et al.*, 2001, 2010; *Ferrando et al.*, 2008). The two terrains are characterised by different pre-Alpine metamorphic evolutions, but both contain relics of HP and/or HT mineral assemblages, usually preserved within mafic rocks and exceptionally also in metapelites (*Ferrando et al.*, 2008; *Rubatto et al.*, 2001; *Latouche and Bogdanoff*, 1987) (Figure 4.27).

Oisans massif

The inner part of the Oisans massif is mainly composed of garnet bearing gneisses and rare kyanite and cordierite bearing metasediments. In this area the oldest structure has been identified and corresponds to the nappe emplacement of the retrogressed eclogitic unit over the paragneissic unit (data Hv6, Hv7 and Hv8 in Table B.1). The exact age and direction of thrusting is unknown, but it occurred after the eclogite formation in this unit at about 395 Ma and prior to the Devonian migmatization at less 355 Ma that affected the entire nappe pile (*di Paola*, 2001; *Guillot and Ménot*, 2009). In the south-western part of the Oisans massif, massive amphibolites with interlayered quartzites, leptynites and chlorite bearing micaschist are exposed. In the southeastern part of the Oisans Massif, amphibolic granulites record a LP-HT Late-Paleozoic metamorphism, with a P-T path marked by a strong increase in temperature during decompression (*Guillot and Ménot*, 2009; *Grandjean et al.*, 1996). A tectonic boundary can be traced between the external and internal domains of the Oisans massif, described as a major normal fault with a sinistral component (*Le Fort*, 1973; *di Paola*, 2001; *Guillot et al.*, 2009a).

Belledonne massif

The Belledonne massif is subdivided in three main tectonic domain, separated by late Paleozoic faults, which are characterized by distinct lithological, magmatic, tectonic and metamorphic features (*Menot*, 1988; *Ménot et al.*, 1987):

1. a domain exposed in the external branch, which includes a sub-vertical metapelitic series;
2. a domain exposed in the NE part of the internal branch, consisting of a gneissic and amphibolitic basement intruded by orthogneisses and granites and of green and black schists associated with acid and basic metavolcanics;
3. a domain exposed in the SW of the internal branch, built up by the tectonic superposition of four formations, the age, the geodynamic significance and the tectonometamorphic evolution of which are significantly distinct.

Eclogites in the Belledonne Massif occur as outcrops within a leptynite/amphibolite complex situated in the north-eastern part of the massif (*Paquette et al.*, 1989).

The external domain is composed of flysch slightly metamorphosed, while in the internal zone two portions divided by the Rivier-Belle Etoile fault can be distingueshed: 1) to NE the basement is composed of gneisses and amphibolic rocks intruded by Visean granits; 2) to SW the basement is constituted by three nappes, the upper Chamrousse ophiolitic complex (lower Paleozoic), the Devo-Dinantian igneous rocks and the lower Paleozoic micaschists (*Guillot and Ménot*, 2009). Within the SW domain two tectonic

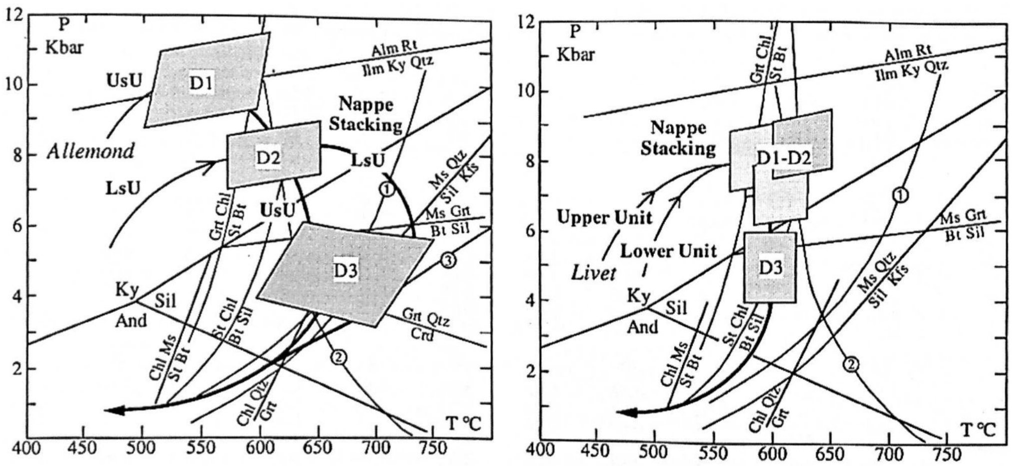

Figure 4.28: P-T conditions during the metamorphic evolution of the Allemont and Livet units. a) Upper Allemont sub-unit (UsU) and lower Allemont sub-unit (LsU) P-T evolution; b) Livet Unit P-T evolution (from *Guillot and Ménot*, 1999).

blocks have been defined, separated by the La Pra-Livet fault. The western block includes the well exposed Chamrousse ophiolite lying upside down on the Taillefer and Riouperoux-Livet formations. The eastern block displays a more complex structural pattern with successive post-nappe folds. From top to bottom, the nappe pile involves three major tectonic units: the Chamrousse ophiolitic complex; the Taillefer and Riouperoux-Livet unit and the Allemont unit. The Livet and the Allemont units (data Hv4 and Hv3 in Table B.1, respectively) recorded different initial P-T and structural evolution, followed by the same tectonometamorphic evolutions during later stages (*Guillot and Ménot*, 1999) (Figure 4.28).

Mont Blanc massif

The external Mont Blanc massif is characterised by a polymetamorphic basement composed of orthogneiss, paragneiss, carbonate lenses, mafic schists, amphibolites and pre-Alpine quartz veins (data Hv13 in Table B.1). The composition of the gneisses is generally quartzo-feldspathic, but can vary depending on the amount of deformation and/or protolith. The mafic schists tend to be associated spatially with the marbles and zones of intense deformation (*Marshall et al.*, 1997; *von Raumer et al.*, 1993). The Internal Mont Blanc massif is composed almost entirely of the Mont Blanc intrusive rock suite. The sedimentary cover of the internal massif consists of middle to upper Triassic, Jurassic and Cretaceous quartzites and calcareous rocks. The Alpine metamorphism in the Mont Blanc massif has generally overprinted the Variscan metamorphism, while the Alpine peak-metamorphic conditions in the Aiguilles Rouges massif reached lower greenschist grade, preserving the Variscan metamorphic evolution. The Mont Blanc and the Aiguilles Rouges massifs have undergone similar pre-Alpine metamorphic events, and due to similarities in the rock types and the close spatial association, data obtained from the

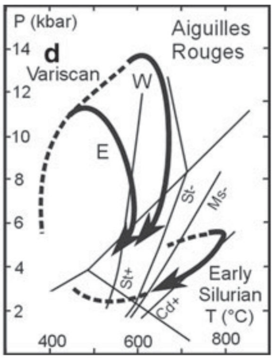

Figure 4.29: P–T path of the eastern (E) and western (W) part of the Col de Bérard region of the Aiguilles Rouges massif (from *Schulz and von Raumer*, 2011).

Aiguilles Rouges massif have been used to interpret the pre-Alpine evolution of the Mont Blanc. In Les Petoudes the Alpine deformation has been less intense and calc-silicate lenses have preserved the pre-Alpine coronitic assemblages of almandine, hornblende, quartz and plagioclase (*Marshall et al.*, 1997).

Aiguilles Rouges massif

The Aiguilles Rouges Massif consists of a complex assemblage of tectonic units with contrasting maximum P-T metamorphic conditions and it is relatively well preserved from Alpine overprint (*Schulz and von Raumer*, 2011; *Bussy et al.*, 2000) (data Hv10, Hv11 and Hv12 in Table B.1). The Alpine metamorphism increase southeasterly from anchizone to greenschist facies conditions in the nearby Mont Blanc area. The different tectonic units are separated by major, steeply dipping NE-SW faults and/or mylonitic zones (*Bussy et al.*, 2000). The massif is composed for the most part of micaschists and gneisses, often migmatitic, of various compositions (pelitic to greywacke). Subordinate amounts of graphitic schists, calcite marbles, calc-silicate gneisses, amphibole-bearing schists and amphibolites are also observed. Low-grade monometamorphic detrital sediments with interlayered volcanites filled an early Carboniferous basin at the southern end of the massif (*Schulz and von Raumer*, 2011; *Liégeois and Duchesne*, 1981). The basement in the Col de Bérard region consists of paragneisses and micaschists together with various orthogneisses and metabasites which show a polymetamorphic evolution of Variscan age, characterised by an early HP metamorphism followed by an adiabatic decompression (*Schulz and von Raumer*, 2011) (Figure 4.29).

4.3.5 The Southalpine domain

The Southalpine domain extends to the south of the Periadriatic lineament (data Sv in Table B.1). It consists of an Alpine E-W trending fold and thrust system, verging south

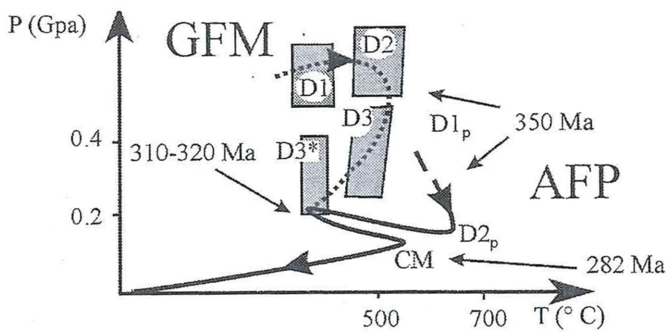

Figure 4.30: P-T-t paths of the metapelites (GFM) and of the paragneisses (AFP) of the Eisecktal area (from *Benciolini et al.*, 2006).

and is composed of pre-Alpine basement and Permian-Mesozoic volcanic and sedimentary sequences, locally displaying a very low-grade Alpine metamorphic imprint associated with the earlier Alpine fabrics (*Cassinis et al.*, 1988; *Milano et al.*, 1988; *Carminati et al.*, 1997; *Spalla and Gosso*, 1999; *Zanoni et al.*, 2010). The pre-Alpine basement comprises micaschists and gneisses, with interlayered metagranitoids, minor metabasics, marbles and quartzites. The dominant metamorphic imprints vary from epidote-amphibolite, or amphibolite, to greenschist facies conditions and generally predate the deposition of Permian-Mesozoic sequences (*Milano et al.*, 1988; *Spalla et al.*, 2009; *Zanoni et al.*, 2010).

Eastern Southalpine (Eisecktal)

The basement of the Eastern Southalpine domain represents a portion of the European Variscan belt, bounded to the north and to the west by two branches of the Periadriatic lineament, the Pustertal and the North Giudicarie faults, respectively. In the Eisecktal area the metamorphic basement is mainly composed of metapelitic and metapsammitic sequences metamorphosed under greenschist facies conditions during the early Paleozoic, in which lenses of garnet bearing paragneiss metamorphosed under HT-LP amphibolite facies conditions can be observed (data Sv11 and Sv12 in Table B.1). The metamorphism and the associated deformation, developed under amphibolite facies conditions, are compatible with crustal thickening, while metamorphism under greenschist faciers conditions indicate lower temperatures. Therefore, they represent different tectonic units, deriving from different crustal levels, coupled during the middle Carboniferous in greenschist facies conditions (*Benciolini et al.*, 2006) (Figure 4.30).

Central Southalpine

The Central Southalpine domain is composed of pre-Alpine basement (data Sv2-v4 and Sv7-Sv10 in Table B.1) and of Permo-Cenozoic covers, which locally show a low grade Alpine metamorphism. In the Orobic Alps five units belonging to the Southalpine base-

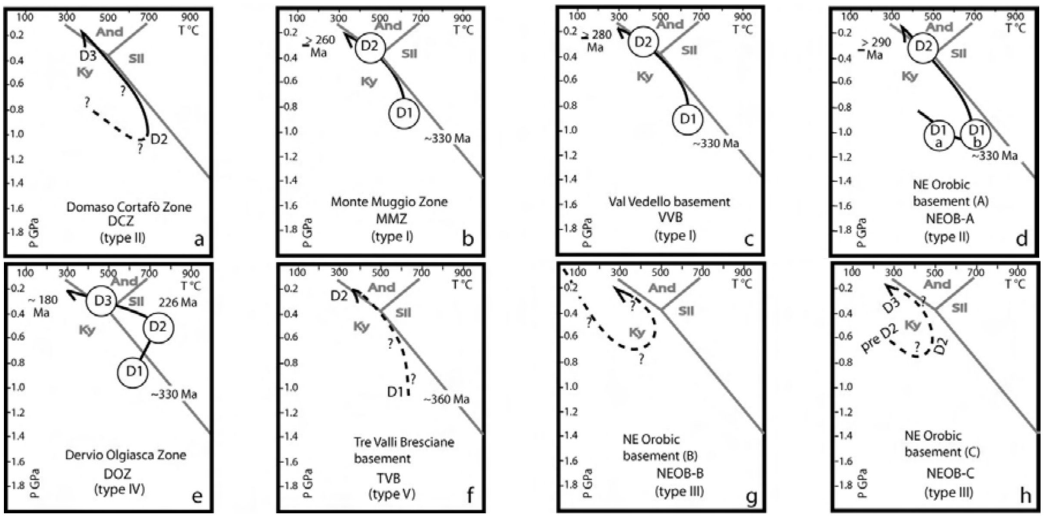

Figure 4.31: Types of metamorphic evolution recorded in the basement of the Central Southalpine domain (from *Zanoni et al.*, 2010).

ment have been identified (*Spalla and Gosso*, 1999; *Spalla et al.*, 2009; *Zanoni et al.*, 2010) (Figure 4.31): 1) units composed of continental crust exhumed after both the collision and the crustal thickening at the end of the Variscan convergence; 2) units that show a prograde P-T path, interpreted as the memory of the subduction, followed by an evolution like that of the units of the first type; 3) Variscan units of upper crust coupled with the units of the types 1 and 2 under greenschist facies conditions; 4) units characterised by a metamorphic evolution interpreted as exhumation of Variscan crust during the Permo-Mesozoic rifting; 5) units composed of continental crust that show metamorphic conditions recorded during the subduction but that do not show any sign of the Variscan collision. Four deformation stages can be distingueshed, two of them regarding only the Variscan basement and two Alpine stages recorded both by the basement and by the covers (*Spalla and Gosso*, 1999; *Spalla et al.*, 2009; *Zanoni et al.*, 2010). In the metapelites two coeval metamorphic imprints can be observed and they can be related to the initial metamorphic stage of different evolution of different tectonic units which coupled during the exhumation (*Spalla and Gosso*, 1999).

The Val Vedello basement (data Sv5 and Sv6 in Table B.1) is exposed in the central portion of the Orobic Alps, where the Morbegno gneisses are interlayered with the Edolo schists. The basement is composed primarily of micaschists and paragneisses, which prevail in Edolo schists and in the Morbegno gneisses, respectively, and secondarily of metagranitoids, marbles and metabasites. In the tectonometamorphic evolution, a metamorphism developed under amphibolite facies conditions (Variscan collision) and a successive re-equilibration under greenschist facies conditions (Variscan exhumation) can be distingueshed (*Zanoni et al.*, 2010).

Western Southalpine (Ivrea-Verbano and Strona-Ceneri zones)

The Ivrea-Verbano Zone and the Strona-Ceneri Zone (data Sv1 in Table B.1) are part of the pre-Alpine basement of the Southalpine domain, separated by the Pogallo Line and the Cossato-Mergozzo-Brissago Line and forming a SW-NE striking crustal segment exposed over 130 km length and 10-50 km width. The Ivrea-Verbano zone is bounded to the NW by the Periadriatic lineament and it represents an uptilted part of pre-Alpine lower continental crust. It displays a continuous succession through thinned lower to intermediate continental crust. The base is formed by metagabbros, ultramafic bodies, and diorites intruded into a sequence of metapelites, metapsammites, metabasites and minor marbles. The metamorphic grade increases from upper amphibolite facies in the SE to granulite facies in the NW (*Henk et al.*, 1997; *Vavra et al.*, 1999). The Strona-Ceneri zone is considered as the decoupled upper crust of the Ivrea-Verbano zone. It displays a series of interlayered metasedimentary rocks, orthogneisses and minor amphibolites intruded by late Paleozoic granites (*Henk et al.*, 1997). This association of banded ultramafic, mafic and felsic metamorphic rocks is widespread in the european Variscan basement, known as the Leptyno-Ampibolitic Complex (LAC) (*Henk et al.*, 1997; *Giobbi et al.*, 2003). The basement of the Strona-Ceneri zone is the remnant of an ophiolite belt and relics of a pre-Variscan HP event, as the garnet bearing amphibolites, could have been incorporated as clasts in turbiditic metasediments within an accretionary prism in the early stages of the Variscan cycle and successively partially re-equilibrated under amphibolite facies conditions (*Giobbi et al.*, 2003). To the east, the metamorphic basement rocks of the Strona-Ceneri zone are overlain by Permo-Carboniferous sedimentary and volcanic rocks. Both the Ivrea-Verbano zone and the Strona-Ceneri zone have been deformed during the Alpine evolution under greenschist facies conditions and the thermal peaks recorded are successive to the Variscan evolution (*Henk et al.*, 1997; *Spalla et al.*, 2014).

Chapter 5

Introduction of the free surface and comparison with natural P-T estimates

The P-T conditions recorded by each marker of the CUM-CUM models have been compared with P_{max}-T estimates related to the Variscan metamorphism inferred both from continental basement rocks of the Alpine domain and of the French Massif Central. In the polycyclic models of the Variscan orogeny, the first orogenic cycle is coeval with the early stage of the monocyclic models. It corresponds to a stage of north verging oceanic subduction, lasting between 425 and 375 Ma, and followed by a stage of collision and late orogenic collapse. In the CUM-CUM models the second evolutionary stage is represented by the phase driven only by gravitational forces, lasting 80 Ma. Therefore, the stage of collision and orogenic collapse has been considered to last between 375 and 295 Ma. Since the duration of the ocenic subduction phase has to last 50 Ma, only the CUM-CUM.5 model has been taken into account for the comparison with the natural P-T estimates.

Table B.1 and Table B.2 show the P_{max} and T_{Pmax} estimates from the Alps (Figure 5.1) and from the French Massif Central (Figure 5.6), respectively, recorded during their Variscan P-T paths. To have a complete agreement between natural estimates and model predictions, three conditions must be satisfied contemporaneously:

1. same lithotype (in terms of oceanic crust, continental crust and mantle);
2. same ages;
3. same P-T values.

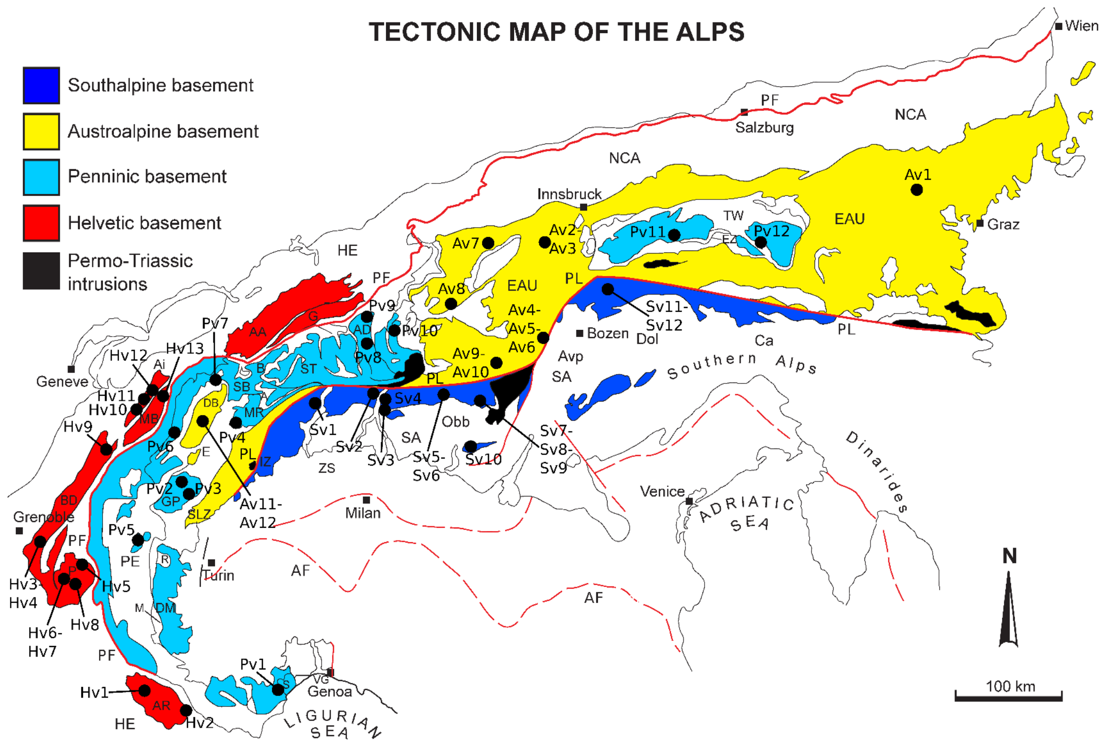

Figure 5.1: Tectonic map of the Alps with the localisation of the data in Table B.1.

5.1 Comparison with the CUM-CUM.5 model

5.1.1 Alps

Helvetic domain

Data from the Helvetic domain that fit with the model predictions during the active subduction phase (data Hv3, Hv4, Hv6, Hv7, Hv11 and Hv12 in Figure 5.2a) recorded pressures over 0.8 GPa in a wide range of temperatures (between 800 K and 1200 K), and lithological affinities only with continental markers (brown and red points in Figure 5.3a). During the early stages of evolution, natural P_{max}-T_{Pmax} estimates fit both with subducted markers eroded by the upper plate (data Hv6, Hv7, Hv11 and Hv12 in Figure 5.4a) and with markers at the bottom of the crust of the upper plate (datum Hv12 in Figure 5.4a), depending on the estimated pressure. Differently, no oceanic markers show an agreement, because their thermal conditions are too cold (below 800 k) for all data (for example datum Hv1 has an estimate temperature of about 1000 K). Proceeding with the evolution, the upper plate warms up and markers in the deep portion of the crust begin to fit with datum Hv4 (Figure 5.4c-f), while datum Hv12 continues to fit only in the colder internal and shallow portion of the wedge (Figure 5.4b-f). Differently, the slab cools down and continental markers show an agreement only with data characterised by temperatures under 1000 K (Figure 5.3a). In particular, Hv3 shows a fitting with markers in the internal portion of the wedge (Figure 5.4b-f), while datum Hv11 does not fit with continuity because it is characterised by higher temperatures and the fitting occurs only with continental markers that are recycled in the warmer external portion of the wedge (Figure 5.4d and e). During the last stages of the active subduction phase data Hv3, Hv4, Hv6, Hv11 and Hv12 show an agreement also with the subducted portion of the lower plate (Figure 5.4f).

During the active subduction phase, data characterised by intermediate P/T ratios and data characterised by high P/T ratios fit with the model in different portion of the subduction complex. Markers at the bottom of the upper plate crust fit with data characterised by intermediate P/T ratios, such as data Hv4 and Hv12, while data with higher P/T ratios show agreement with subducted markers in different portions of the wedge. In particular, the higher the ratio, the more external the portion (data Hv3 and Hv11).

Data characterised by high P/T ratios (data Hv3 and Hv11 in Figure 5.3a) show agreement with the model after the collision only in the early stages (Figure 5.2a), when the thermal conditions are similar to the active subduction phase. Datum Hv4 fits with continental markers placed in portions of both the upper and the lower plate characterised by temperatures above 800 K (Figure 5.5a-e). Data Hv5 and Hv8 are characterised by intermediate-to-low P/T ratios (Figure 5.3a) and they show an agreement with both oceanic and continental markers in the thickened crust (above 30 km of depth) during the second half of the pure gravitational evolution, after the thermal re-equilibration and the warming of the subduction complex (Figure 5.5d-f). Oceanic and continental markers in the deeper portions of the thickened crust fit with datum Hv6 (Figure 5.5a-f), which is characterised by high temperature and intermediate pressure (Figure 5.3a). Generally, with the proceeding of the post-collisional evolution there is a decreasing of P/T ratios characterising the data that fit the model.

Pennidic domain

In the early stage of the the oceanic subduction phase there is correspondence between data Pv3, Pv10, Pv11 and Pv12 (Figure 5.2a) and model predictions. Datum Pv3 is characterised by intermediate P/T ratio and show the agreement with markers in the external and shallow portion of the wedge, while data Pv10, Pv11 and Pv12 are characterised by high P/T ratio and fit with markers either in the internal and shallow portion of the wedge (datum Pv11) or in the deeper portion (data Pv10 and Pv12) (Figure 5.3b and Figure 5.4a). Proceeding with the evolution two groups of data characterised by clear contrasting P/T ratios and fitting with the model can be recognised: a first group composed by data characterised by intermediate P/T ratio, pressures below 0.8 GPa and temperatures between 800 K and 900K (data Pv2, Pv3, Pv4 and Pv7 in Figure 5.3b); and a second group characterised by high P/T ratio, pressures above 1.8 GPa and temperature over

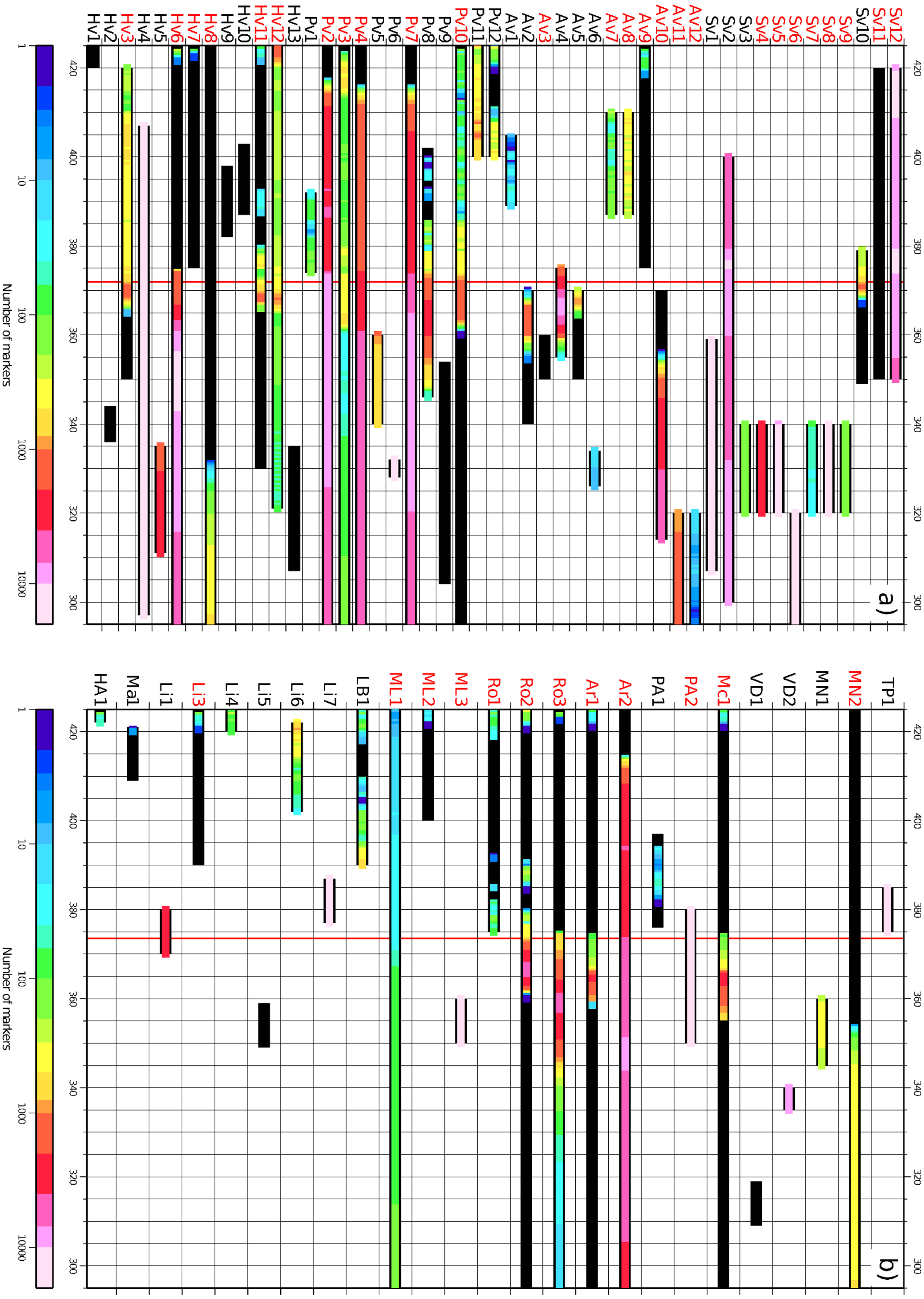

Figure 5.2: Fitting of natural P_{max}-$T_{P_{max}}$ estimates of the Alps (panel a) and of the French Massif Central (panel b) with the CUM-CUM.5 model. Black bars represent the age of the natural P-T estimates, while colour bars represent the fitting with the markers of the model. Different colours represent the number of markers showing the agreement. Red vertical line identifies the collision occurrence. Keys are the same of Table B.1 and Table B.2. Red keys represent geological ages, black keys represent radiometric age.

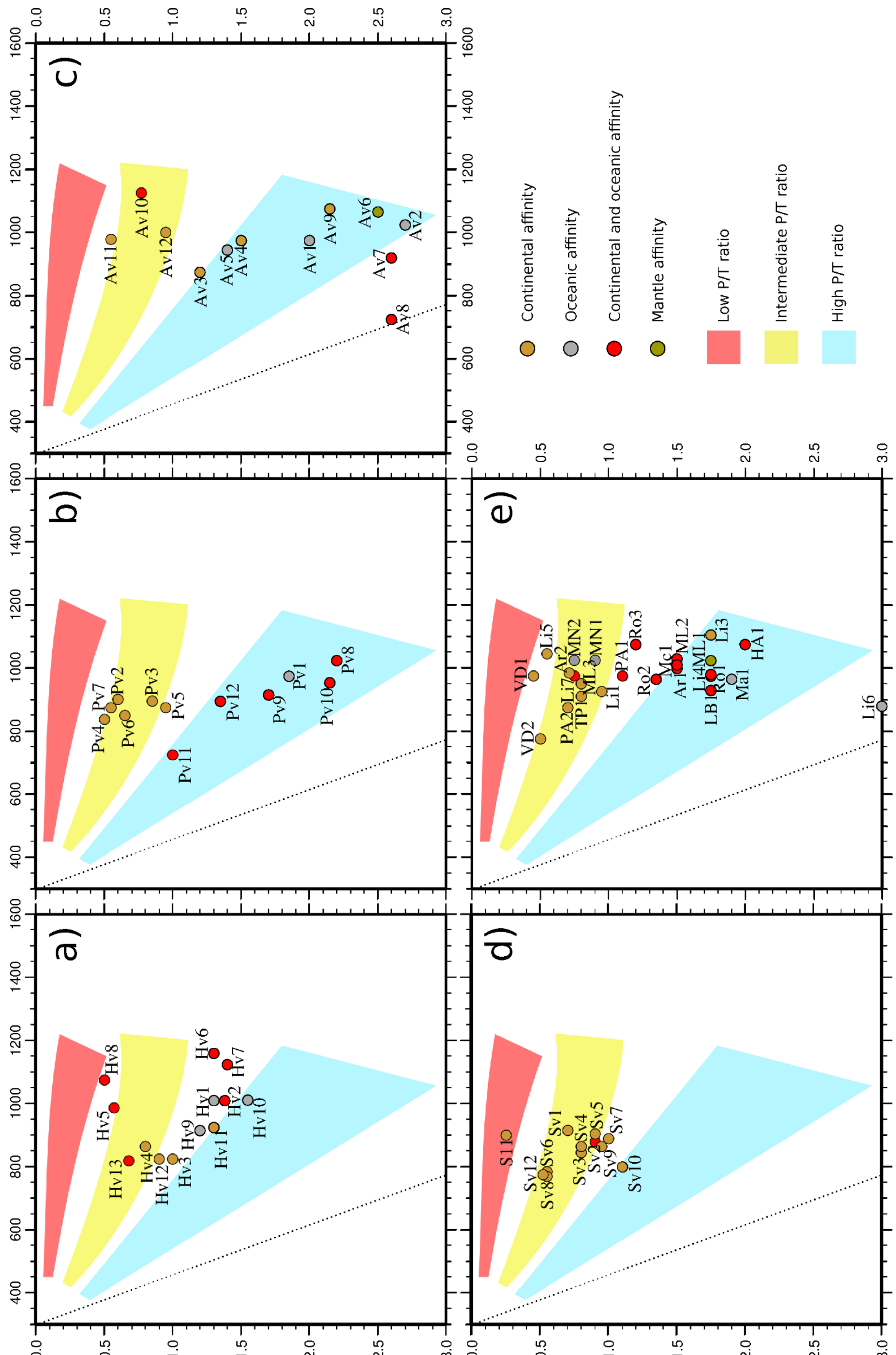

Figure 5.3: P_{max}-T_{Pmax} estimates of data from the Helvetic domain (panel a), the Penninic domain (panel b), the Austroalpine domain (panel c), the Southalpine domain (panel d) and from the French Massif Central (panel e). Different colours of the data indicate different lithological affinities, as described in figure. Red, yellow and light blue areas indicate low, intermediate and high P/T ratios, respectively.

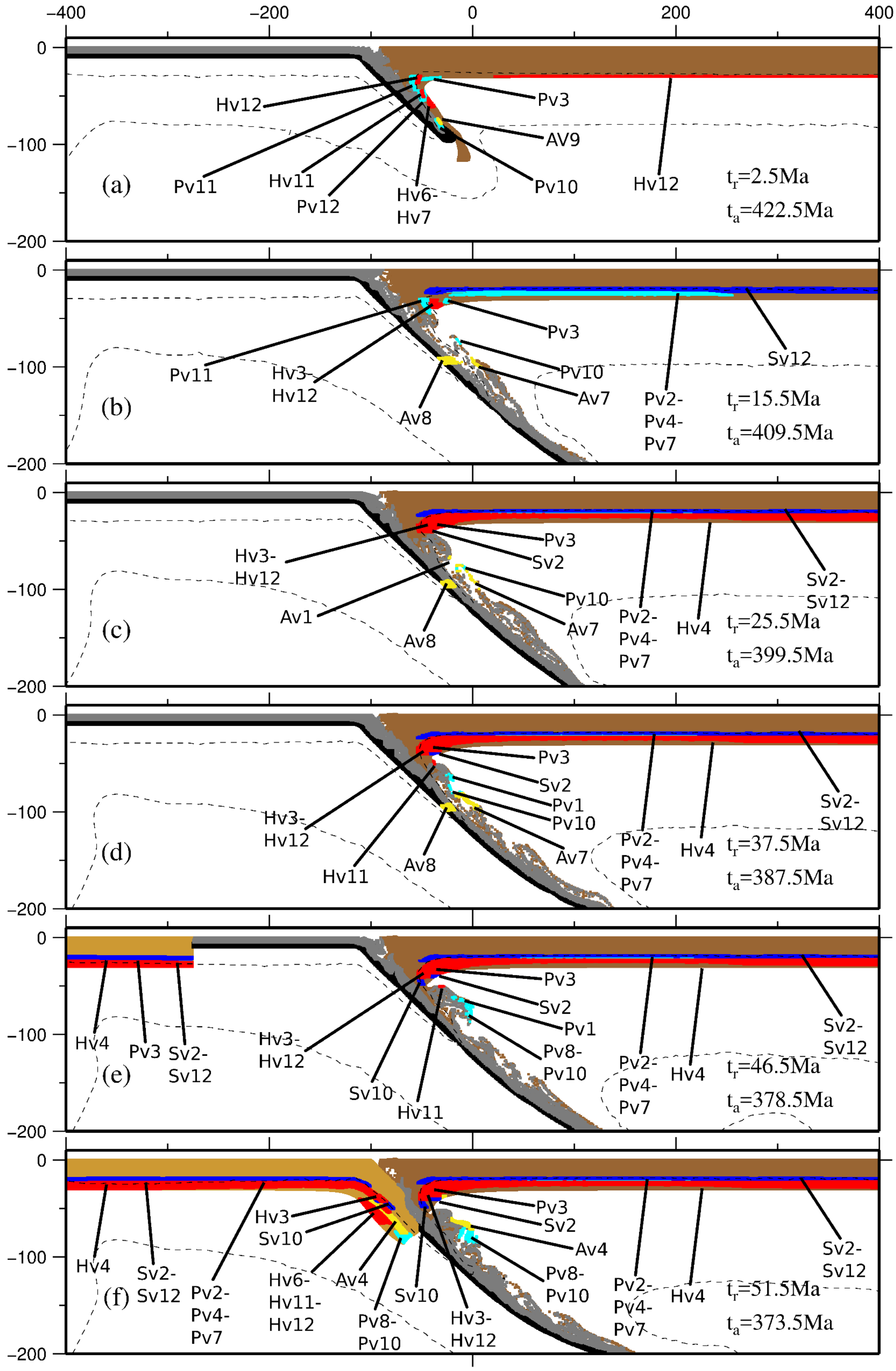

Figure 5.4: Comparison between CUM-CUM.5 model and P_{max}-T_{Pmax} estimates from the Alps for different times during the oceanic subduction phase. Dotted lines indicate 800 K and 1500 K isotherms. Red dots indicate fitting with data from the Helvetic domain, light blue dots fitting with data from the Pennidic domain, yellow dots fitting with data from Austroalpine domain and blue dots indicate fitting with Southalpine domain.

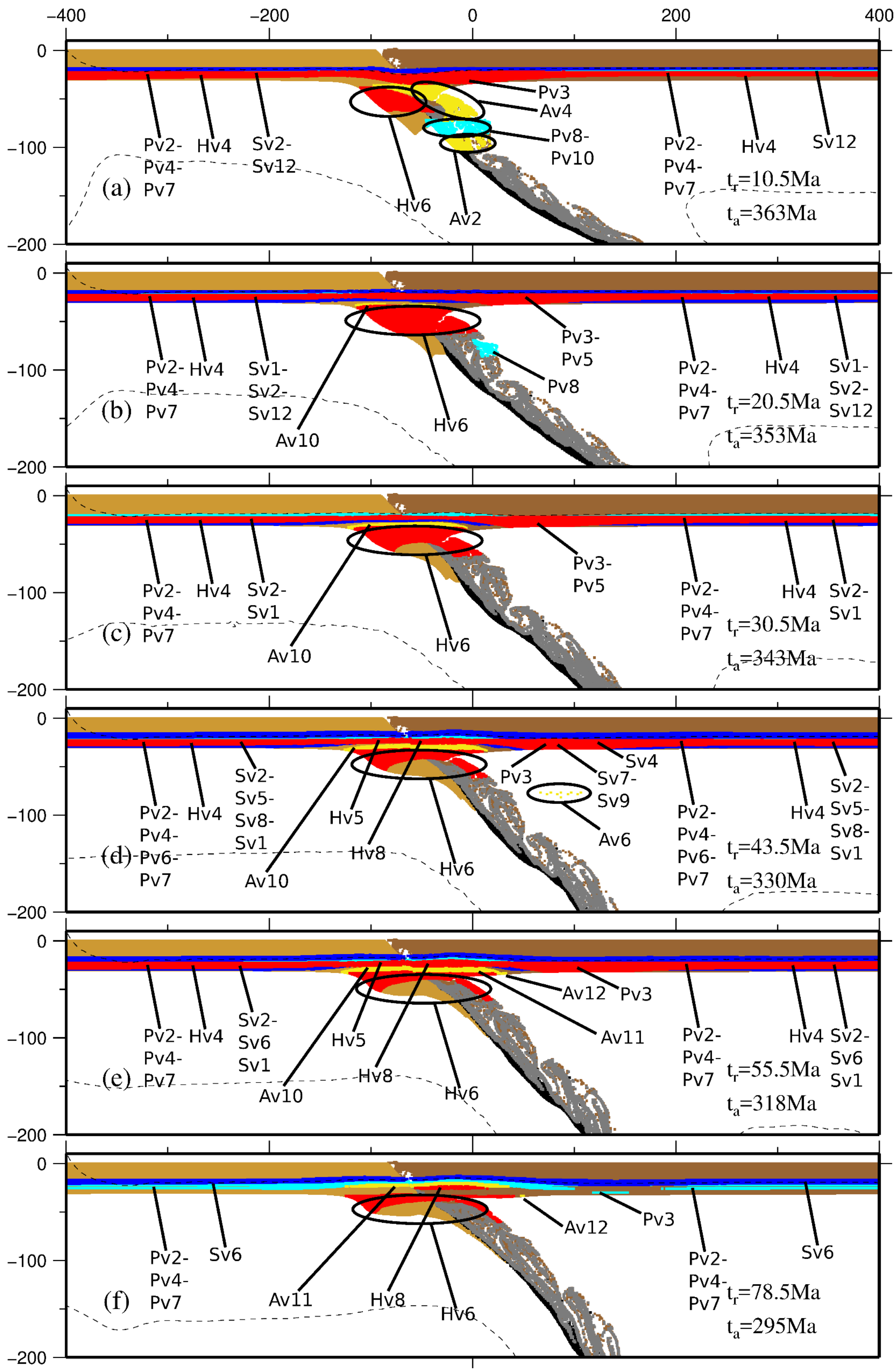

Figure 5.5: Comparison between CUM-CUM.5 model and P_{max}-T_{Pmax} estimates from the Alps for different times during the post-collisional phase. Dotted lines indicate 800 K and 1500 K isotherms. Red dots indicate fitting with data from the Helvetic domain, light blue dots fitting with data from the Pennidic domain, yellow dots fitting with data from Austroalpine domain and blue dots indicate fitting with Southalpine domain.

900 K (data Pv1, Pv8 and Pv10 in Figure 5.3b). The first group show correspondences with continental markers in the shallow and external portion of the wedge (datum Pv3 in Figure 5.4b-f) or at the bottom of the crust of the upper plate (data Pv2, Pv4 and Pv7 in Figure 5.4b-f), while the second group show an agreement with recycled oceanic and continental markers on the deep and external portion of the wedge (data Pv1, Pv8 and Pv10 in Figure 5.4b-f). The contemporary appearance of these two contrasted metamorphic gradients and their location inside the subduction complex is comparable to the metamorphic gradient described by *Miyashiro* (1973) for the paired metamorphic belts, even if the distribution at the surface after the exhumation is difficult to restore, due to subduction-related Alpine reworking.

Data Pv8 and Pv10 fit with the model also during the early stages of the post-collisional phase (Figure 5.2a), also if they are characterised by high P/T ratios (Figure 5.3b). They show the agreement with oceanic and continental markers recycled during the oceanic subduction phase and localised at a depth of about 70 km (Figure 5.5a and b). In time, the slab warms up, as consequence of the thermal re-equilibration of the subduction complex, and no data characterised by high P/T ratios fit with the model, as data Pv9 and Pv10 (Figure 5.2a and Figure 5.3b). Differently, data characterised by intermediate P/T ratios (Pv2, Pv3, Pv4, Pv5, Pv6 and Pv7 in Figure 5.3b) show correspondences with the model during the whole duration of this phase. These data fit with continental markers at the bottom of both the upper and the lower plate, at different distances from the trench (Figure 5.5a-f). As for the data of the Helvetic domain, the model show an agreement with data of the Pennidic domain characterised by lower P/T ratios with the proceeding of the evolution.

Austroalpine domain

All the data of the Austroalpine domain that have the peak of the Variscan metamorphism dated between 375 and 425 Ma (data Av1, Av4, Av7, Av8 and Av9 in Figure 5.2a) are characterised by high P/T ratios (Figure 5.3c). All these data fit with deep oceanic and continental markers. In particular, datum Av8 shows the agreement with the oceanic markers of the most internal and coldest portion of the slab, while data Av1 and Av7 have correspondences with oceanic and continental markers in the external portion of the wedge, during their recycling (Figure 5.4b-d). Therefore, the lower the P/T ratios of the data, the more the external portion of the wedge shows the agreement with them. In addition, datum Av4 has a fit both with the subducted portion of the lower plate and with recycled markers in the external portion of the wedge (Figure 5.4f).

Data Av2, Av4 and Av5 show correspondences with the model in the first 15-20 Ma of post-collisional evolution (Figure 5.2a) and are characterised by high P/T ratios (Figure 5.3c). They show the agreement with subducted oceanic and continental markers placed at different depths, in relation to their estimated pressures (Figure 5.5a). Proceeding with the evolution, the model show correspondences with data characterised by intermediate P/T ratios (data Av10, Av11 and Av12 in Figure 5.3c). These data have the agreement with markers of both the upper and the lower plate at a depth of about 30 km, in correspondence of the thickened crust (Figure 5.5b-f). As for the data of the Helvetic domain, with the proceeding of the post-collisional evolution there is a decreasing of P/T ratios characterising the data that fit the model. An exception is represented by datum Av6 which is characterised by high P/T ratios (Figure 5.3c) and fit the model at about 40 Ma of evolution after the collision (Figure 5.2a). It shows an agreement with a portion of mantle at a depth of about 70 km, far from the subducted slab and from the recycled markers in the wedge (Figure 5.5d).

Southalpine domain

Only three estimates of P_{max}-T_{Pmax} from the Southalpine domain are dated between 375 and 425 Ma (data Sv2, Sv10 and Sv12 in Figure 5.2a) and all of them show a correspondence with the model. Sv2 and Sv12 are characterised by intermediate P/T ratios while datum Sv10 is characterised by high P/T ratio (Figure 5.3d). Among these data, Sv12 has the lowest P/T ratio and it fits with markers in the deep portion of the crust of the upper plate (Figure 5.4b-f). Differently, datum Sv10 has the highest P/T ratio and it shows agreement with the model in the external portion of the wedge, at a depth of about 45 km (Figure 5.4e and f). Datum Sv2 has a P/T ratio between Sv10 and Sv12 and it has correspondences with markers at the bottom of the crust of the upper plate (deeper than datum Sv12) and in the wedge, in a shallower area than datum Sv10 (Figure 5.4c-f). All of these data have an agreement also with the lower plate: data Sv2 and Sv12 with continental markers in the deep portion of the non-subducted plate, while Sv10 with continental markers in the subducted portion of the lower plate. (Figure 5.4e and f).

Datum Sv10, which is the only data of the Southalpine domain characterised by high P/T ratio, has an agreement also in the early stage after the collision, for about 5 Ma (Figure 5.2a). All the others, with the exception of datum Sv11, have intermediate P/T ratios (Figure 5.3d). They fit with continental markers of both the upper and lower plate at a depth between 25 and 30 km and at different distances from the subduction system and the thickened crust (Figure 5.5a-f).

5.1.2 French Central Massif

In the early stage of the evolution, the model has correspondences with data HA1, Li3, Li4, LB1, ML1, ML2, Ro1, Ro2, Ro3, Ar1 and Mc1 (Figure 5.2b). All of them are characterised by high P/T ratios, with pressures above 0.7 GPa and temperatures over 900 K (Figure 5.3e). With the exception of datum ML1 which has mantle affinities, all the data

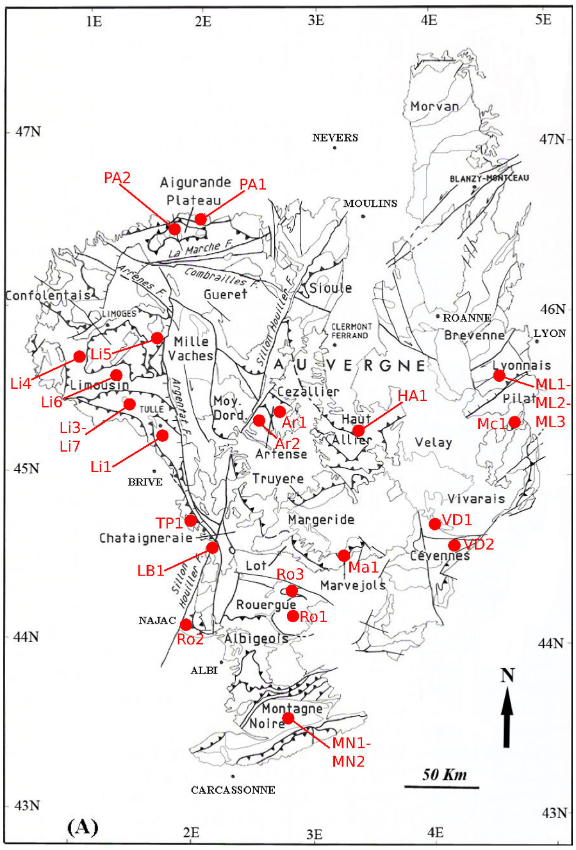

Figure 5.6: Tectonic map of the French Central Massif with the localisation of the data in Table B.2.

fit with continental subducted markers, previously eroded by the base of the crust of the upper plate (Figure 5.7a). Data Ro3, Ar1 and Mc1 also have an agreement in the last stages of this phase with continental markers in the subducted portion of the lower plate (Figure 5.4f). Proceeding with the evolution, also data with intermediate P/T ratios (data Li1, Li7, Ar2, PA2 and TP1) show agreement with the model. Among these data, Li1 has the highest P/T ratio and all of them have correspondences with continental markers at the bottom of both the upper and lower plate (Figure 5.7b-f). datum Ar2 begins to fit after 10 Ma of evolution, as consequence of the increase of temperature in the upper plate due to the mantle flow. datum PA1 has a P/T ratios slightly higher than Li1 (Figure 5.3e) and it fits with the shallowest and hottest subducted continental markers, in the external and shallow portion of the wedge (Figure 5.7d). Data Li6, LB1, Ro1 and Ro2 are characterised by high P/T ratios (Figure 5.3e) and their correspondences are with deep oceanic and continental subducted markers (Figure 5.4b-e). As observed for the data of the Pennidic domain of the Alps, different data characterised by contrasting P/T ratios show agreement with the model at the same time in different portion of the subduction complex. In particular data characterised by intermediate P/T ratios have correspondences with markers at the bottom of the plates (for example datum Ar2), while data with high

P/T ratios fit with subducted markers at different depths, depending on the estimated pressures (for example data LB1 and Li6).

In the first 20 Ma after the continental collision, data Ro2, Ar1 and Mc1 (Figure 5.2b) have agreements with continental and oceanic markers at a depth between 40 and 60 km, in correspondence of the thickened crust (Figure 5.8a). These data are characterised by high P/T ratios (Figure 5.3b). Differently, data ML3, Ro3, Ar2, PA2, MN1 and MN2 are characterised by intermediate P/T ratios (Figure 5.3e) and they fit for the whole duration of the post-collisional phase with continental and oceanic markers at a depth between 25 and 35 km both in the upper and in the lower plate, not only in correspondence of the thickened crust (Figure 5.8a-f). An exception is datum ML1, which is characterised by high P/T ratio (Figure 5.3e) and fit with the model during the entire phase (Figure 5.2b). This datum has the agreement with a portion of the mantle at a depth of about 60 km, which increase its extension in time (Figure 5.8a-f). Therefore, during this phase there is an agreement with different data characterised by contrasted metamorphic gradient only at the beginning, while in the last stages only data characterised by intermediate P/T ratios fit with the model.

5.2 Introduction of the free surface

5.2.1 Model setup

Both the SIN-CUM and the CUM-CUM models show the activation of short-wavelength convective cells related to the hydration and the serpentinisation of the mantle wedge, with the consequent recycling of oceanic and continental subducted material (Chapter 3.3). These convective cells are limited below a depth of about 30-35 km and the recycled materials are never exhumed to the surface but they rise up to the bottom of the continental crust of the upper plate. This dynamics can be due to the lack of a layer of atmosphere above the upper and the lower plate, which are limited in their upper boundary.

To verify that the recycling of markers in the shallow portion of the wedge is not an artificial consequence of the lack of the atmosphere, a 10 km thick layer has been introduced in the CUM-CUM model above both plates, in order to simulate a free topographic surface. Over the lower plate the layer is divided in a 3 km thick lower layer of water and a 7 km thick upper layer of air. Differently, the crust of the upper plate has been thickened by 3 km, having a 7 km thick layer of air above. Erosion and sedimentation processes have been implemented as described by *Roda et al.* (2010b). The boundary conditions are the same of the CUM-CUM models. The erosion-sedimentation mechanism has been introduced only in the model with a velocity of 5 cm/yr (ED.5 model), in order to compare its P-T predictions to natural P-T estimates of the Variscan metamorphism.

A new distribution of markers has been used in order to have a transition between the

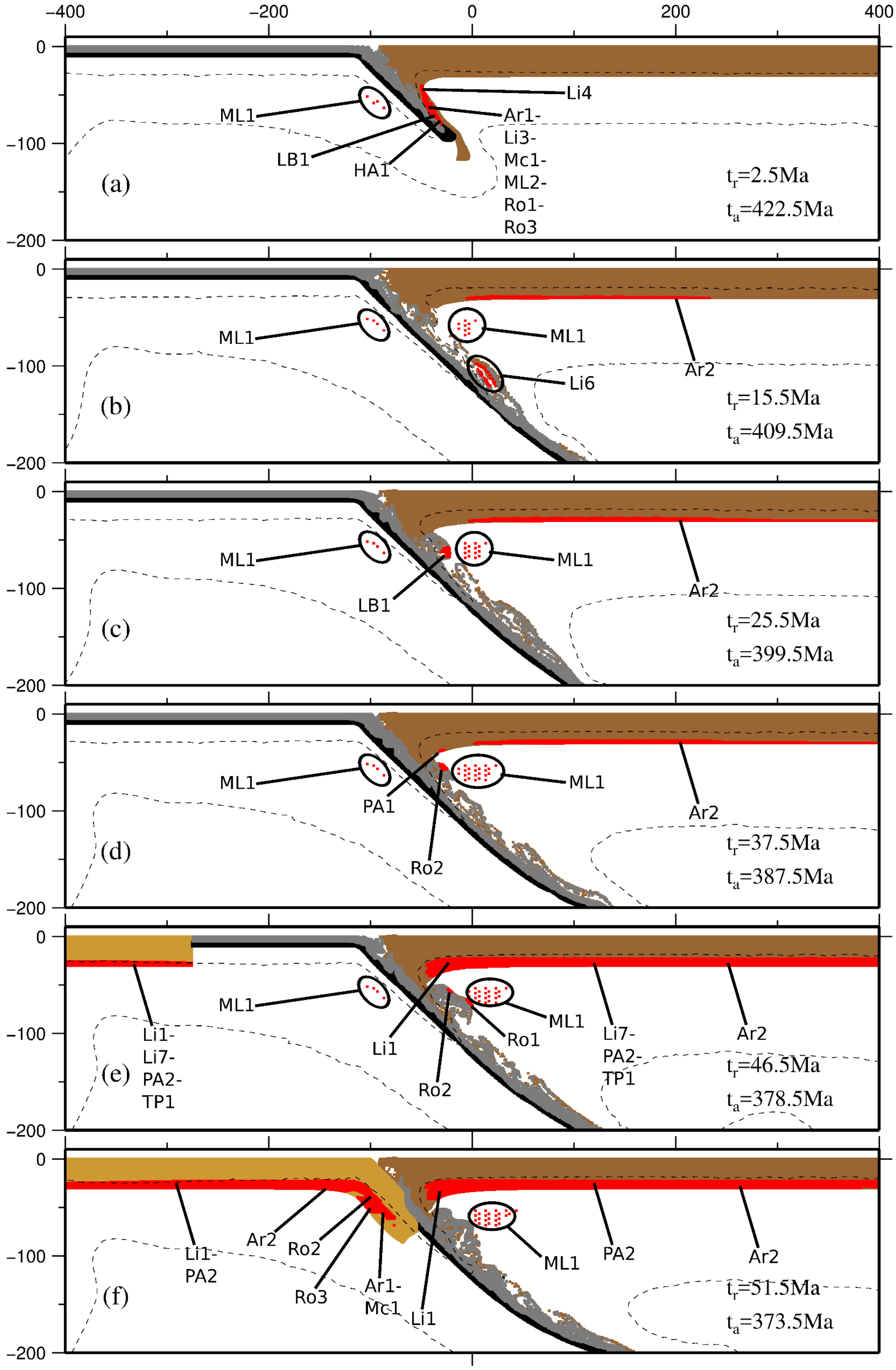

Figure 5.7: Comparison between CUM-CUM.5 model and P_{max}-T_{Pmax} estimates from the French Central Massif for different times during the oceanic subduction phase. Dotted lines indicate 800 K and 1500 K isotherms. Red dots indicate fitting with data.

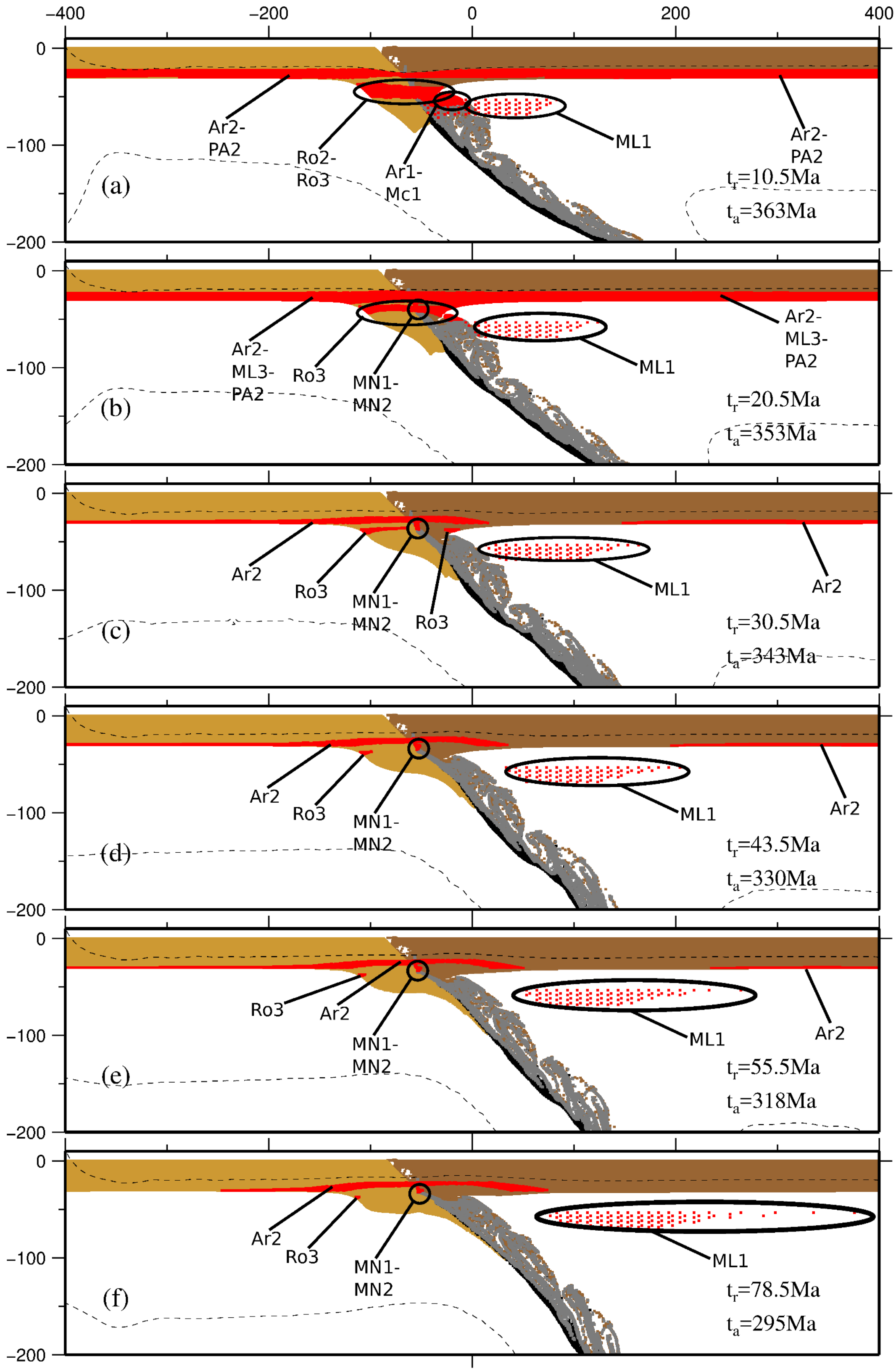

Figure 5.8: Comparison between CUM-CUM.5 model and P_{max}-T_{Pmax} estimates from the French Central Massif for different times during the post-collisional phase. Dotted lines indicate 800 K and 1500 K isotherms. Red dots indicate fitting with data.

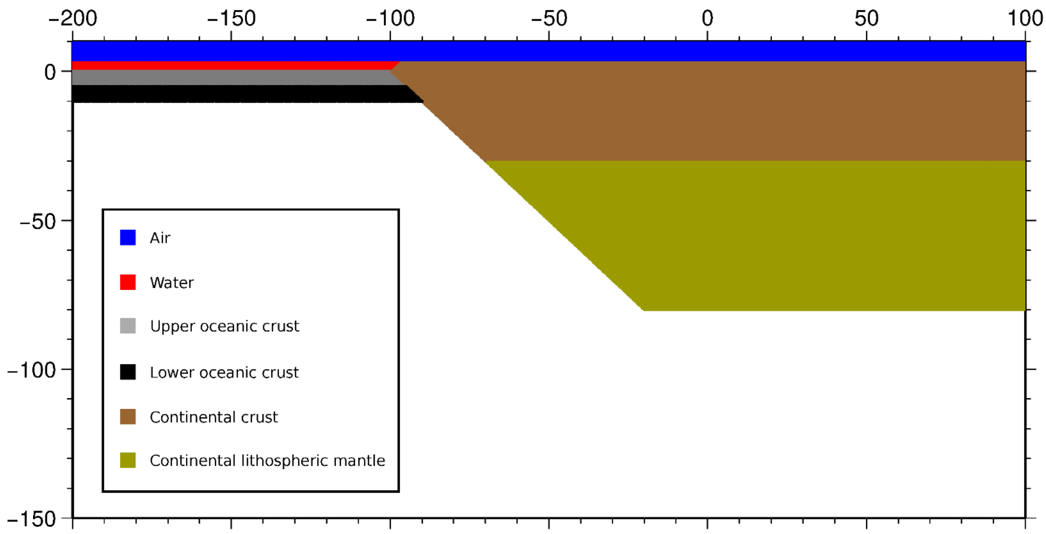

Figure 5.9: Setup of the subduction zone for the model with free surfaces and the introduction of the erosion-sedimentation mechanism (ED.5 model).

oceanic crust of the lower plate and the continental crust of the upper plate characterised by a 45° dip contact. A 50 km thick layer composed by mantle markers of the continental lithosphere has been introduced, to verify that also mantle can be exhumed and to follow their paths in the wedge. A detail of the initial distribution of the markers for this model is shown in Figure 5.9.

5.2.2 Results

As observed in CUM-CUM and in SIN-CUM models, also in this case there is the activation of small convective cells in the mantle wedge, which favour the recycling of subducted material. The first convective cell develops after 5.5 Ma and is located at a depth of about 25 km (Figure 5.10a), in a shallower position with respect to the previous models. The recycling of subducted continental crust and sediments is shown by the presence of some orange and dark green markers, which are respectively continental markers and sediments subducted below 35 km and then exhumed above 30 km (Figure 5.10a). At the same time, markers of the lithospheric mantle are carried to shallower depths toward the trench. With the evolution of the model the convective cell slightly expands in depth, favouring the recycling also of subducted oceanic crust at about 15.5 Ma after the beginning of the subduction (light grey in Figure 5.10b). Further in the evolution, at about 35.5 Ma, others two small cells develop at higher depth, favouring the recycling also of deeper material (Figure 5.10c). At the collision only one bigger convective cell is active (Figure 5.10d). After an initial increase, the hydrated area seems to maintain its dimensions during the whole oceanic subduction phase. This is due to the regularity of the thermal conditions inside the slab and in the mantle wedge, which are underlined by the regularity of the isotherm 800 K (Figure 5.10a-c). The shallower position of the isotherm 800 K in the upper plate at the collision with respect to its initial depth, is related to the large scale mantle flow described in all the previous models (Chapter 3.3). Comparing the thermal state of this model with the CUM-CUM.5 model, an increase of temperature in the mantle wedge can be observed, as consequence of a more intense mantle flow in the most internal portion of the wedge.

A warming of the system can be observed starting from the collision, highlighted by the rising of the isotherm 800 K, which produces the disappearing of the hydrated area and the consequent deactivation of the convective cells in the mantle wedge. As observed in the previous model, the thermal re-equilibration of the system is associated with a gradual rising of all the subducted material until the last stages of evolution (Figure 5.10e and f). At the end of the evolution, the thermal state in the thickened crust is slightly colder than that observed at the end of the CUM-CUM.5 model. This is due to the larger amount of mantle and oceanic crust in the shallow and internal portion of the wedge, which causes a decrease of the energy produced by radioactive decay.

5.3 Comparison with the ED.5 model

An improvement in the duration of the agreement of the natural P-T estimates with ED.5 model (Figure 5.11) with respect to CUM-CUM.5 model (Figure 5.2) can be observed. This improvement concerns all data that does not show an agreement with CUM-CUM.5 model during the whole duration of the oceanic subduction phase, both from the Alps and from the French Central Massif (for example data Hv6, Pv7, Av9, Li3 and Ar1). Differently, during the post-collisional phase some data show an improvement in the fitting (for example data Hv11, Pv9, Av3, Sv10 and Mc1), while some others worsen their fitting (for example data Hv5, Av11 and MN2).

5.3.1 Alps

Helvetic domain

During the oceanic subduction phase, all data from the Helvetic domain have correspondences with ED.5 model. As for the CUM-CUM.5 model, data characterised by intermediate P/T ratios (data Hv4 and Hv12 in Figure 5.3a) show an agreement with the model at the bottom of the continental crust of the upper plate (Figure 5.12a-f). Datum Hv12 is characterised by a lower estimated temperature with respect to Hv4, and it does not fit with the bottom of the crust after 15 Ma, because of the increase of the temperature of the upper plate (Figure 5.12c-f). Differently from CUM-CUM.5 model, datum Hv4 fits also with recycling markers in the internal portion of the wedge. This is due to the higher temperatures characterising the wedge of the ED.5 model. Consequently

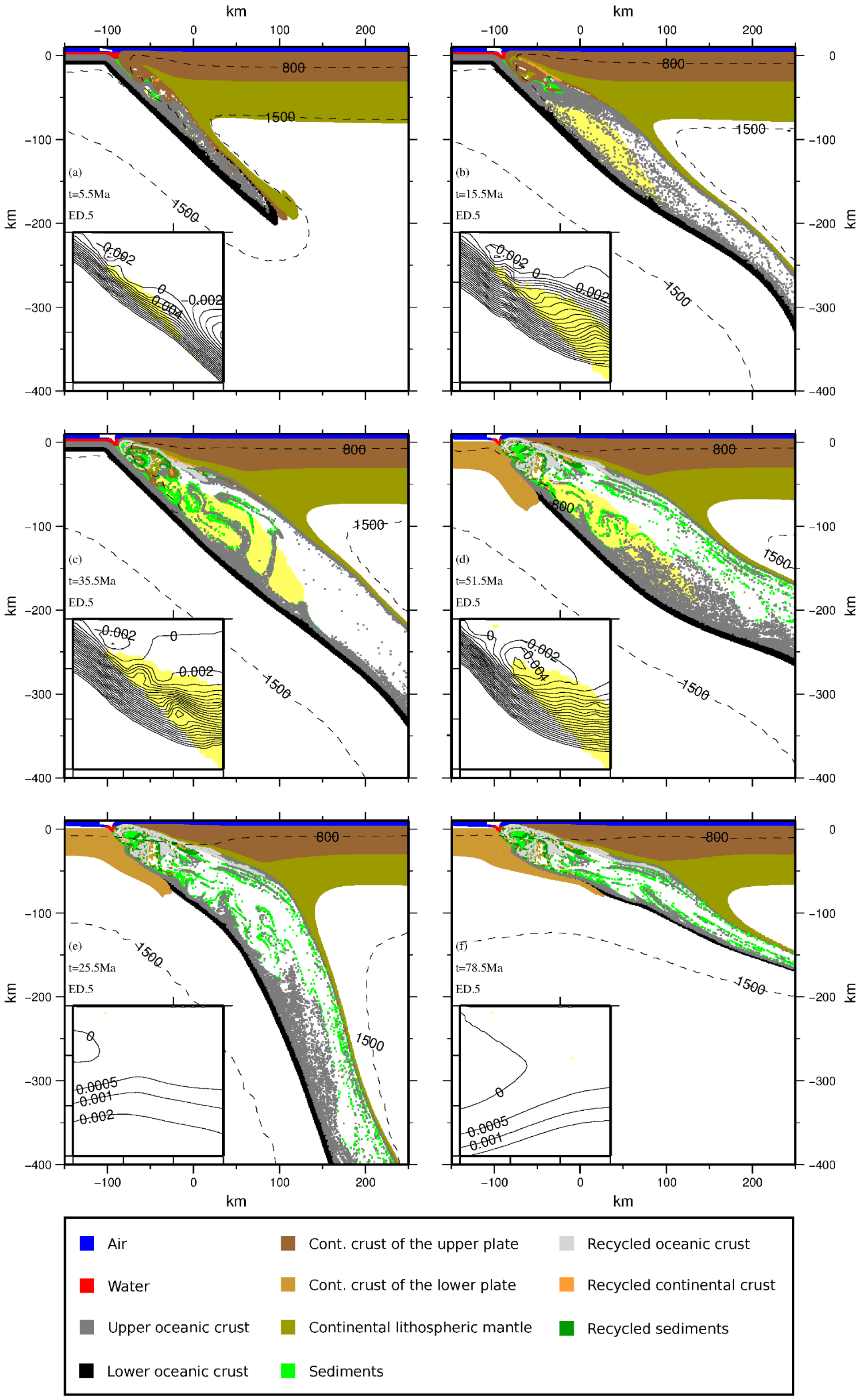

Figure 5.10: Temperature field in terms of the 800 K and the 1500 K isotherms (dashed lines) and streamline patterns (black solid lines in the insets) surrounding the wedge area for the ED.5 model at different times: 5.5 Ma (panel a), at 15.5 Ma (panel b), at 35.5 Ma (panel c) and at 51.5 Ma (panel d) after the beginning of the active convergence, and at 25.5 Ma (panel e) and at 78.5 Ma (panel f) after the continental collision. The yellow areas represent the hydrated wedge domains.

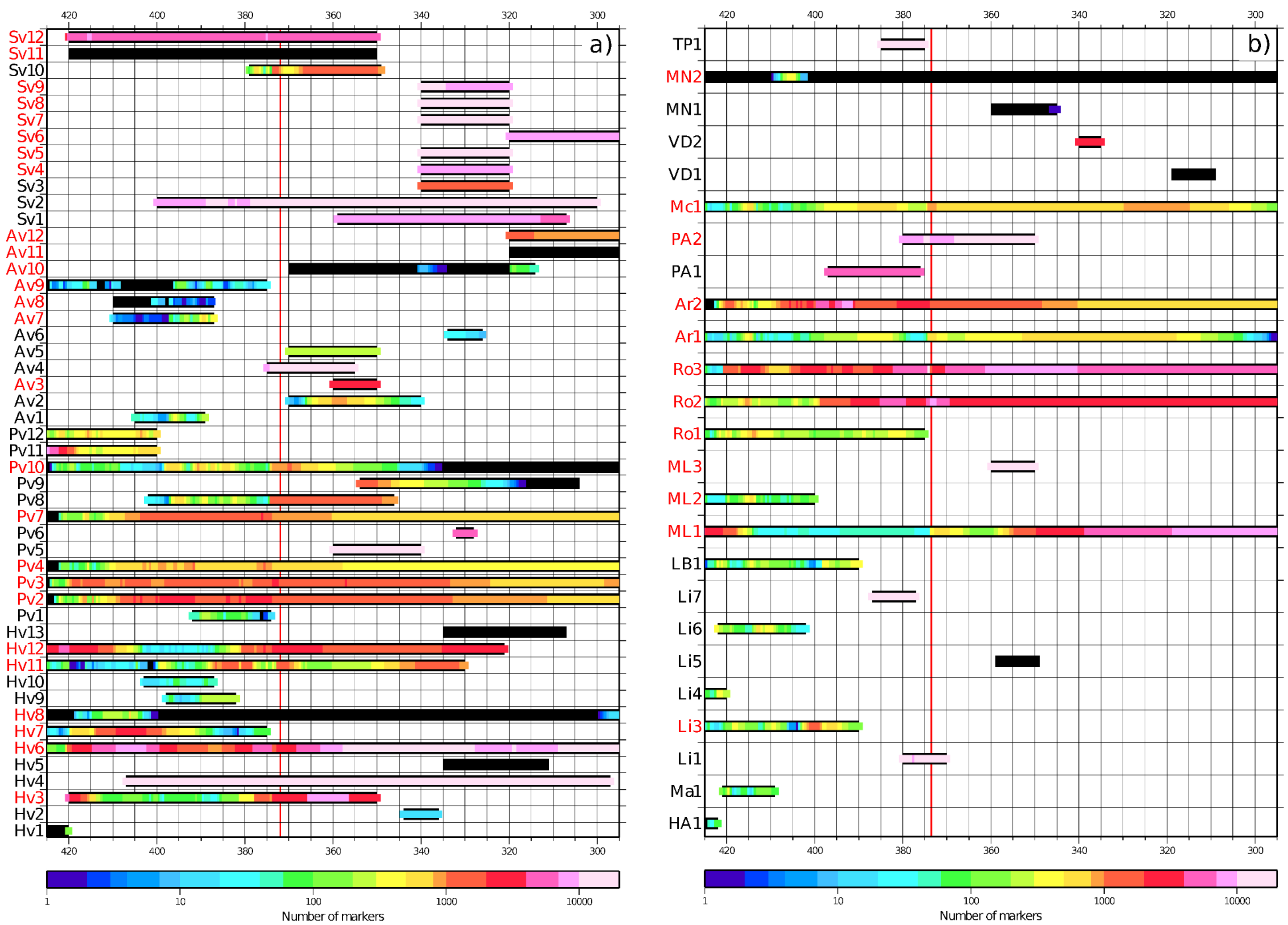

Figure 5.11: Fitting of natural P_{max}-T_{Pmax} estimates of the Alps (panel a) and of the French Massif Central (panel b) with the ED.5 model. Black bars represent the age of the natural P-T estimates, while colour bars represent the fitting with the markers of the model. Different colours represent the number of markers showing the agreement. Red vertical line identifies the collision occurrence. Keys are the same of Table B.1 and Table B.2. Red keys represent geological ages, black keys represent radiometric age.

to the increase of temperature in the wedge, also datum Hv8, which is characterised by the lowest P/T ratio, fits with the model in the shallowest portion of the wedge (Figure 5.12b). The increase of temperature does not concern only the internal and shallow portion of the wedge, but also the external areas that, in this model, show agreement with data Hv6, Hv7 and Hv10 (Figure 5.12b-f). Given that the temperature increase moving toward the external portions of the wedge, the data fit with markers in different positions of the wedge depending on their estimated temperatures: the higher the temperature of the data, the more external the areas in which they show the agreement.

With respect to the CUM-CUM.5 model, data Hv5 and Hv8 worsen their agreement, while data Hv2 and Hv11 improve it (Figure 5.11a), as consequence of the colder thermal state of the system. In fact, all these data have temperatures between 1000 and 1100 K, but they are characterised by very different pressures: data Hv2 and Hv11 have an estimated pressure of about 1.3-1.4 GPa, while data Hv5 and Hv8 have an estimated pressure of about 0.5 GPa, with a consequent lower P/T ratio. As with model CUM-CUM.5, datum Hv4 shows correspondences with the bottom of the continental crust of both the upper and lower plate, and datum Hv6 fits with the deeper portion of the thickened crust (Figure 5.13a-f).

Pennidic domain

Data of the Pennidic domain show an improvement in the agreement with respect to CUM-CUM.5 model, in particular during the early stages of evolution. In fact, the bottom of the crust of the upper plate have correspondences with data Pv2, Pv4 and Pv7 from the beginning (Figure 5.11a). This could be the consequence of a faster warming of the crust due to a more intense mantle flow that in this model is not limited at the top of the plate. Moreover, these data show an agreement also with recycled markers in the internal and shallow portion of the wedge, as already observed in data characterised by intermediate P/T ratio of the Helvetic domain (Figure 5.3a and b). Datum Pv3 is characterised by intermediate P/T ratio (Figure 5.11b) and fits with an area at the bottom of the crust of the upper plate that widens in time further from the trench, in relation with the gradual increase of temperature (Figure 5.12a-f). On the other hand, the warming of the crust determines a migration of the area that have P-T conditions compatible with datum Pv11, from the bottom of the crust of the upper plate, to the most internal portion of the wedge (Figure 5.12a and b). All the other data of the Pennidic domain, which metamorphism is dated between 375 and 425 Ma, are characterised by high P/T ratios (data Pv1, Pv8, Pv10 and Pv12 in Figure 5.3b) and they show agreements with subducted and recycled markers in the wedge (Figure 5.12a-f). So, as observed during the comparison with CUM-CUM.5 model, different data characterised by contrasted metamorphic gradients fit with the model at the same time in different portion of the subduction system. In par-

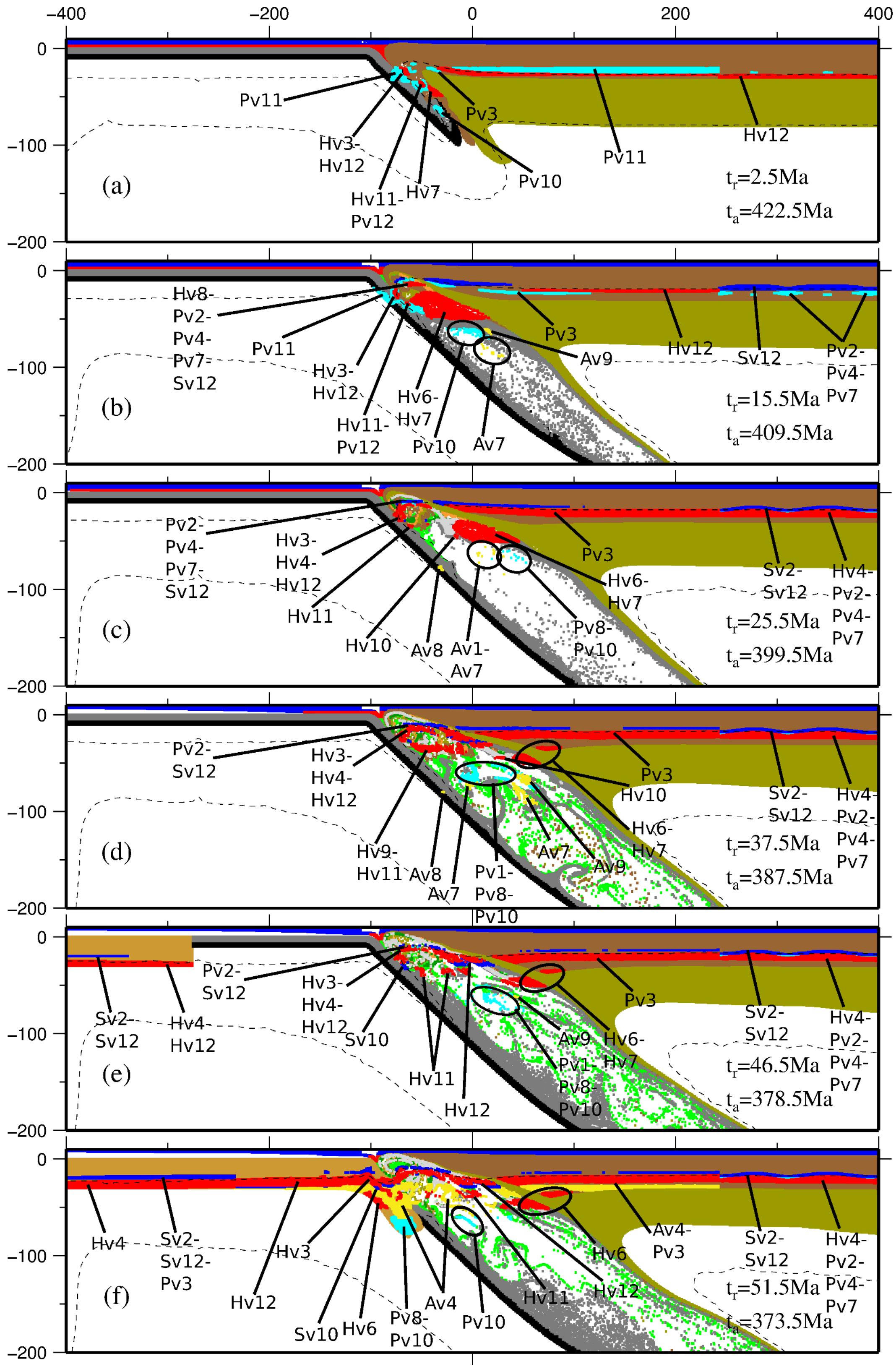

Figure 5.12: Comparison between ED.5 model and P_{max}-T_{Pmax} estimates from the Alps for different times during the oceanic subduction phase. Dotted lines indicate 800 K and 1500 K isotherms. Red dots indicate fitting with data from the Helvetic domain, light blue dots fitting with data from the Pennidic domain, yellow dots fitting with data from Austroalpine domain and blue dots indicate fitting with Southalpine domain.

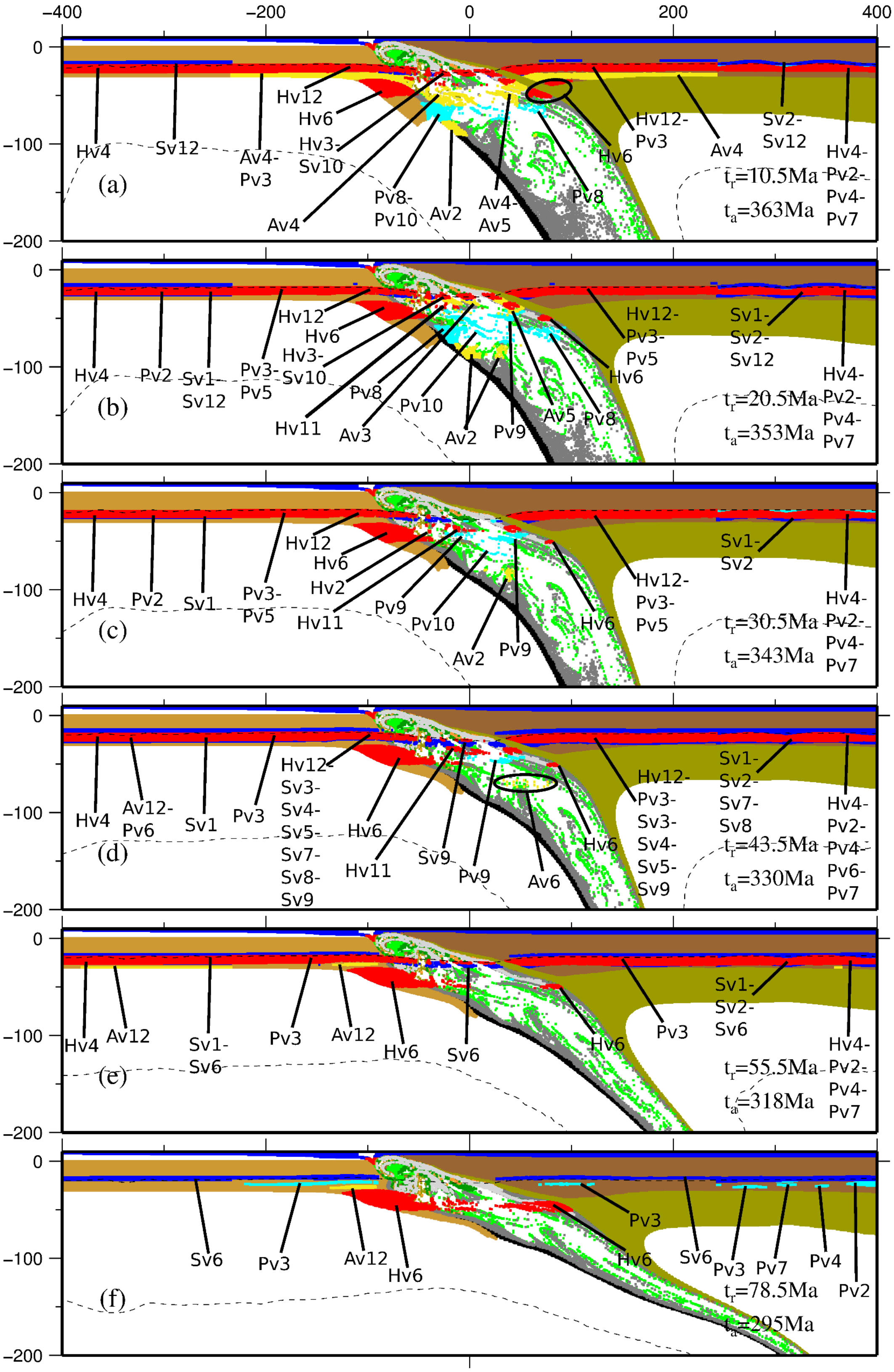

Figure 5.13: Comparison between ED.5 model and P_{max}-T_{Pmax} estimates from the Alps for different times during the post-collisional phase. Dotted lines indicate 800 K and 1500 K isotherms. Red dots indicate fitting with data from the Helvetic domain, light blue dots fitting with data from the Pennidic domain, yellow dots fitting with data from Austroalpine domain and blue dots indicate fitting with Southalpine domain.

ticular data with intermediate P/T ratios fit at the bottom of the continental crust of the upper plate and data with high P/T ratios fit with the subducted markers, highlighting one more time the occurrence of different gradients in different parts of the subduction system. However, this model shows that P-T conditions compatible with some data characterised by intermediate P/T ratios can be found also in the shallow and internal portion of the wedge.

During the post-collisional phase, data Pv2, Pv3, Pv4, Pv5, Pv6 and Pv7 have a complete correspondence with the model (Figure 5.11a), as observed also with the CUM-CUM.5 model (Figure 5.2a). They are characterised by intermediate P/T ratios (Figure 5.3b) and fit with the model at the bottom of the continental crust. In particular, data Pv2, Pv4 and Pv7 fit with the base of the continental crust of the upper plate further than 300 km from the trench, datum Pv6 shows agreement at the bottom of the continental crust of both the plates at a slightly less distance, and data Pv3 and Pv5 have correspondence with the bottom of the crust of both plates within 200 km from the trench (Figure 5.13a-f). Therefore, the lower the P/T ratio, the further the distance from the trench. With respect to CUM-CUM.5 model, the crust of the lower plate is slightly colder and it does not fit with data Pv2, Pv4 and Pv7. Inside the wedge, the model have a fitting with data Pv8, Pv9 and Pv10 (Figure 5.13a-d), which are characterised by high P/T ratios (Figure 5.3b), showing an improvement with respect to CUM-CUM.5 model. However, none of these data have correspondences with the model until the last stages of the evolution.

Austroalpine domain

During the oceanic subduction phase, data Av1, Av7, Av8 and Av9 have a good agreement with the model in the deep and internal portion of the wedge, at different distances from the slab (Figure 5.12c). Av8 is the only datum that worsens its agreement with respect to CUM-CUM.5 model, considering the duration of the fitting with the model (Figure 5.11a). This because the increase of temperature in the wedge affects also the slab, with a consequent decrease in the extension of the area characterised by very high P/T ratio, compatible with data Av8 and Av7 (Figure 5.3c). In fact, also datum Av7 worsens its agreement, not as duration of the fitting, but as number of markers that show the agreement (Figure 5.11a). Differently, data Av1 and Av9, characterised by lower P/T ratios with respect to Av7 and Av8 (Figure 5.3c), improve their agreement with the model, both in the duration of the fitting and in the number of markers that show the agreement (Figure 5.11a). At the collision, datum Av4 fits at the bottom of the crust of the upper plate, in the shallow and internal portion of the wedge and with continental markers in the subducted portion of the lower plate (Figure 5.12f).

Av10 and Av11 are the data of the Austroalpine domain characterised by the lowest P/T ratio (Figure 5.3c) and, as for data Hv5 and Hv8 of the Helvetic domain, they worsen its agreement with respect to CUM-CUM.5 model, showing almost no agreement with model predictions (Figure 5.11a). On the other hand, data Av2, Av3, Av4, Av5 improve their agreements, showing correspondences with recycled markers in the wedge (Figure 5.13a-c). Datum Av2 has a very high P/T ratios (Figure 5.3c) and it fits with deep markers very close to the slab, while data Av3, Av4 and Av5 have lower P/T ratios (Figure 5.3c) and they have correspondences with recycled markers in a shallower and more external portion of the wedge. Datum Av6 shows agreement with portions of mantle in the internal and deep area of the wedge, while datum Av12 fits continental markers of the lower plate near the trench at a depth of about 25-30 km (Figure 5.13d-f).

Southalpine domain

Data Sv2, Sv10 and Sv12 do not show differences in the duration of the agreement with the model with respect to CUM-CUM.5 model (Figure 5.11a and Figure 5.2a). Sv2 and Sv12 are characterised by intermediate P/T ratios (Figure 5.3d) and they have correspondence at the bottom of the crust of both the upper plate (Figure 5.12a-f) and the lower plate (Figure 5.12e and f). Moreover, datum Sv12 has a fitting also inside the wedge, in its shallow portion. Differently, datum Sv10 (high P/T ratio in Figure 5.3d) has P-T conditions compatible with an area in the wedge close to the slab, at a depth of about 30 km. As CUM-CUM.5 model, there is no correspondence with datum Sv11, characterised by low P/T ratio (Figure 5.3d).

During the post-collisional phase, all data of the Southalpine domain, with the exception of Sv10, have correspondences with the bottom of the continental crust of both the plates (Figure 5.13a-f). They are characterised by intermediate P/T ratios (Figure 5.3d) and the fitting is very similar to that observed for CUM-CUM.5 model. The only difference is that datum Sv2 does not fit with the crust of the lower plate, but only with the upper plate. Differently, datum Sv10, characterised by high P/T ratio (Figure 5.3d), improve its agreement with the model with markers at a depth of about 25-30 km inside the wedge (Figure 5.13a and b).

5.3.2 French Central Massif

With the exception of data HA1 and Li4 that have the same agreement with CUM-CUM.5 and ED.5 models, all data characterised by high P/T ratios (data Ma1, Li3, LB1, ML2, Ro1, Ro2, Ro3, Ar1, PA1 and Mc1 in Figure 5.3e) improve the correspondences with model predictions (Figure 5.11b). They fit with recycling markers in the wedge, at different depths and distances from the slab (Figure 5.14a-f), depending on their estimated pressures and temperatures. Data Ro3 and PA1, which are characterised by lower P/T ratios, fit also with the portion of the non-subducted continental crust of the upper plate closest to the trench (Figure 5.14c-f). Moreover, also data Ar2 and MN2, characterised by intermediate

P/T ratios (Figure 5.3e), improve their fitting with the model (Figure 5.11b). They have correspondences with both the shallow and internal portion of the wedge and the bottom of the continental crust of the upper plate, further than the area that have an agreement with data Ro3 and PA1 (Figure 5.14b-f). Therefore, as observed for the data of the Pennidic domain, different portions of the model that show contrasted metamorphic gradient have correspondence with data characterised by high and by intermediate P/T ratios at the same time (for example data Ro1 and Ar2). Also in this case, there are correspondences with data with intermediate P/T ratios not only in the continental crust far from the trench, but also inside the wedge at shallow depths.

Data Ro2, Ar1 and Mc1 are the only having a metamorphism dated between 375 and 295 Ma characterised by a high P/T ratio (Figure 5.3e). All these data improve their fitting with model predictions, having correspondences with subducted and recycled markers in the wedge (Figure 5.15a-f). Datum Ro3 has an intermediate-to-high P/T ratio (Figure 5.3e) and it has correspondence with a larger amount of markers with respect to CUM-CUM.5 model (Figure 5.11b), fitting with continental markers in the upper and in the lower plates near the trench, at about 30 km deep (Figure 5.15a-f). Among the data characterised by intermediate P/T ratio, MN1 and MN2 have the highest temperatures and they worsen their fitting, with almost no correspondences with ED.5 model (Figure 5.11b). Data ML3, Ar2 and PA2 which have intermediate P/T ratios, do not show differences in the agreement with respect to CUM-CUM.5 model, and they have correspondences at the bottom of the continental crust. In particular, data ML3 and PA2 have correspondences with both the plates, while datum Ar2 only with the continental crust of the upper plate (Figure 5.15a-f).

5.3.3 P-T paths

For model ED.5 it has been observed that convective cells in the hydrated wedge are active for the whole duration of the oceanic subduction phase, favouring the recycling of oceanic and continental markers and their exhumation up to the shallower structural levels of the crust. On the other hand, during the post-collisional phase deep subducted material of the slab slowly rises up, but material already exhumed at "crustal levels" does not show a further exhumation.

The paths of subducted and exhumed markers, in terms of pressure and temperature, have been compared with inferred P-T-t paths of rocks from the Alps and from the French Central Massif. Data chosen for the comparison satisfy three conditions:

1. their P_{max}-T_{Pmax} stages (Tables B.1 and B.2) have correspondences with the model during the oceanic subduction and/or the post-collisional phase (Figure 5.11);
2. the correspondences are with markers that reside above a depth of 100 km at the end of the post-collisional phase;

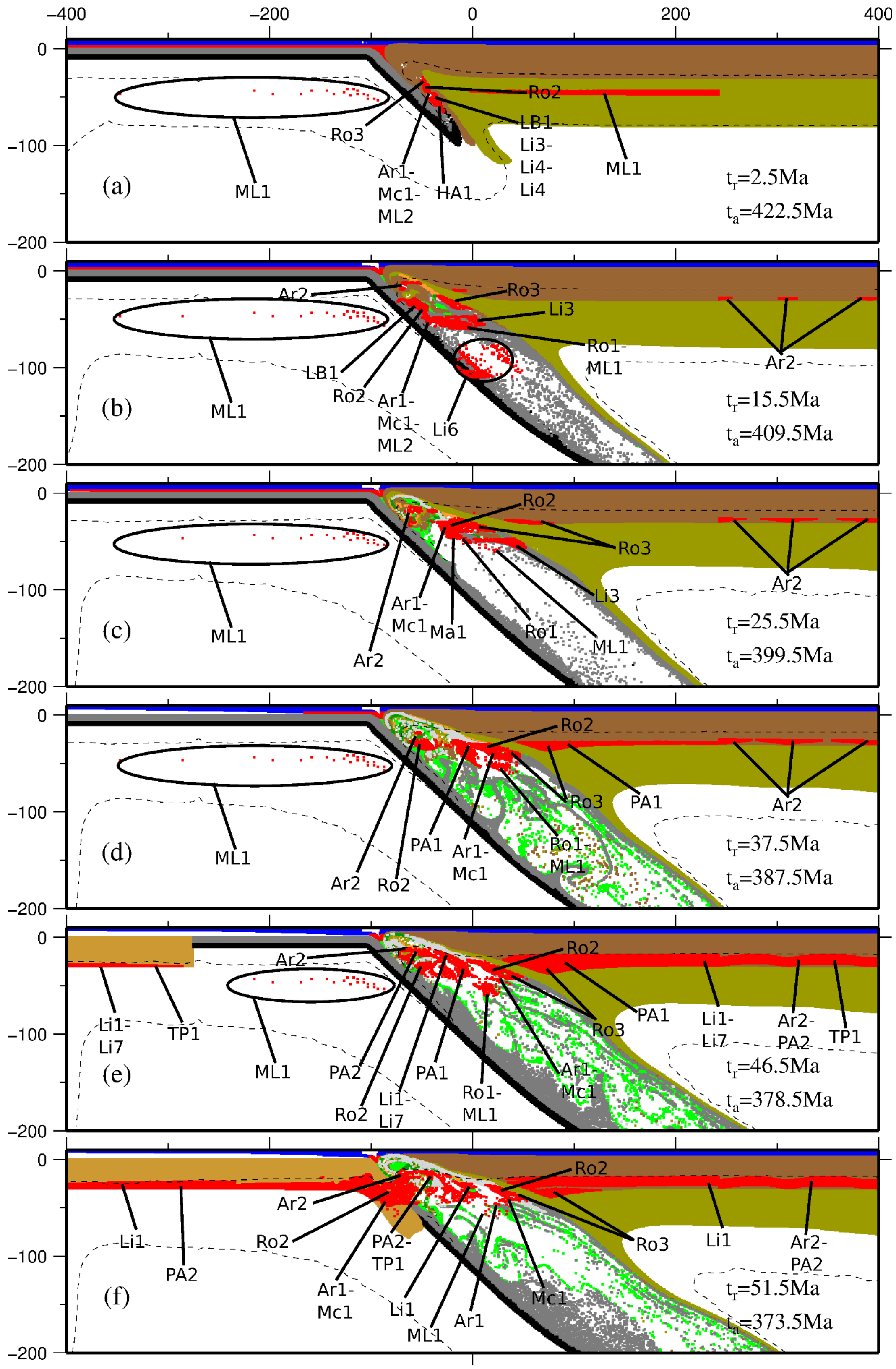

Figure 5.14: Comparison between ED.5 model and P_{max}-T_{Pmax} estimates from the French Central Massif for different times during the oceanic subduction phase. Dotted lines indicate 800 K and 1500 K isotherms. Red dots indicate fitting with data.

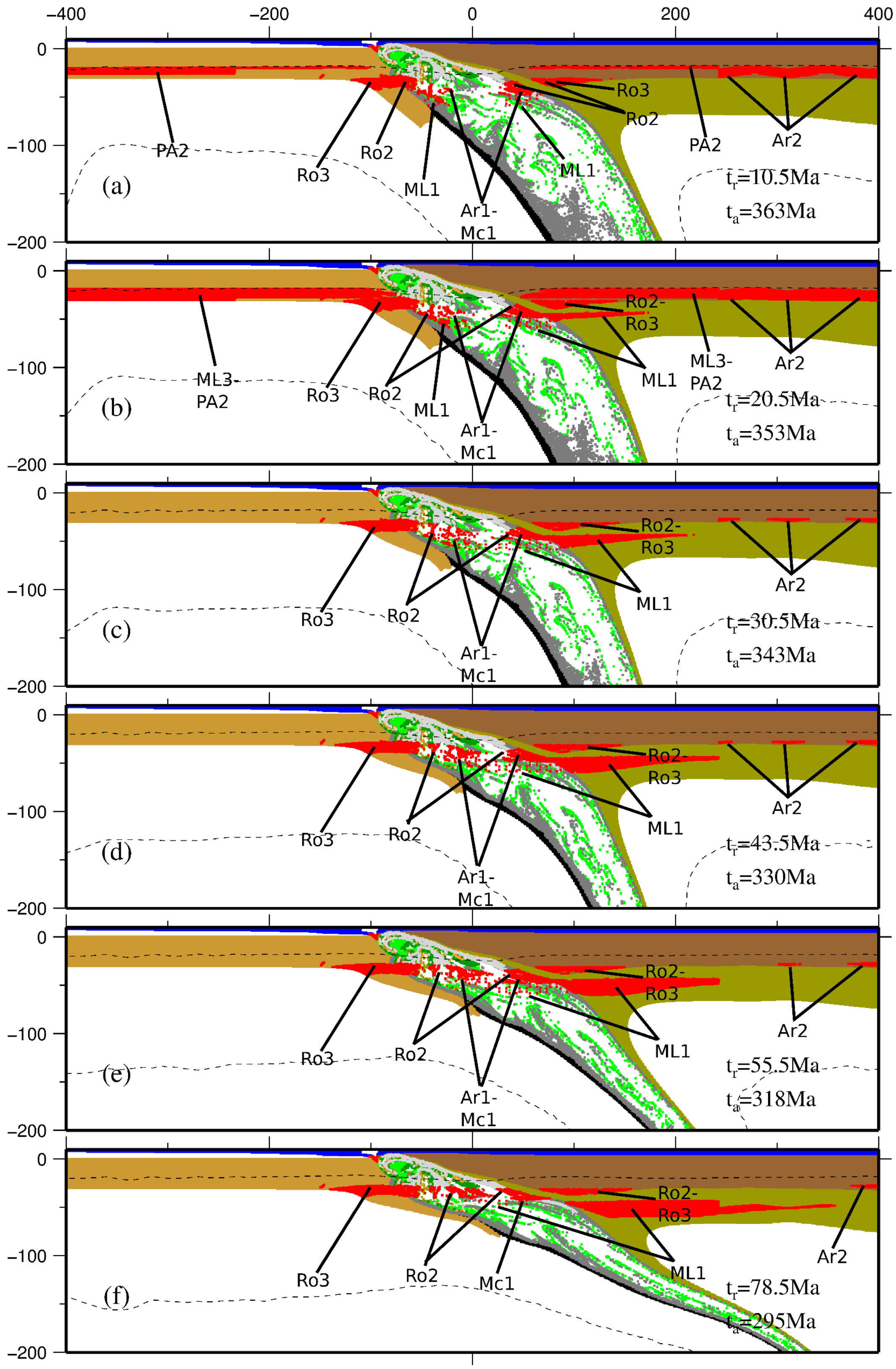

Figure 5.15: Comparison between ED.5 model and P_{max}-T_{Pmax} estimates from the French Central Massif for different times during the post-collisional phase. Dotted lines indicate 800 K and 1500 K isotherms. Red dots indicate fitting with data.

3. they have recorded and preserved at least two stages during their metamorphic evolution;

The data used for the discussion of the P-T paths are presented in Tables B.3 and B.4. The simulated P-T paths used for the comparison have been chosen to show different type of possible paths that had correspondences with the metamorphic evolution, in agreement with the lithologic affinities of the data.

Helvetic domain

Datum Hv2 is characterised by high P/T ratio and an intermediate maximum pressure recorded during its evolution. Its peak pressure is dated 336-344 Ma (*Ferrando et al.*, 2008; *Rubatto et al.*, 2010), corresponding to the post-collisional phase in ED.5 model. Figure 5.16 shows that markers with correspondences with datum Hv2 between 336 and 344 Ma reach the correct pressure only at the end of the oceanic subduction phase and after that they warm up slowly, fitting the P-T conditions estimated for the stage I during the post-collisional phase. Though, none of these markers are exhumed and they do not fit stages II, III and IV after stage I.

However, a lot of markers that fit with datum Hv2 shows one cycle of subduction and exhumation before the final sinking. During the first stage of exhumation, prior to the correspondence with stage I, they show a paths in agreement with the natural inferred P-T path. So, the metamorphic evolution of datum Hv2 has been compared with paths predicted during the oceanic subduction phase, in order to verify that some markers could reproduce a P-T path compatible with the natural P-T path. In this case, only continental markers have correspondences with the stage I of datum Hv2 and they show 2 cycles of subduction and exhumation (Figure 5.17). Stage I corresponds to the peak pressure reached by the markers during their first cycle and it is followed by the thermal peak, which is recorded at slightly less pressures. After the thermal peak, the markers show an isothermal exhumation up to about 1 GPa, and then some markers cool down during the rise (yellow, green and light blue paths in Figure 5.17), while others cool down rapidly, with no changes in pressure, up to a temperature of about 1000 K (red and blue paths in Figure 5.17). The latter group fit with stage III and IV during the exhumation. After the first exhumation, all markers are subducted and exhumed again, fitting stage III and IV (some of them record P-T conditions similar to that of the stage II, but they do not fit).

During the first cycle, the time between the stage I and the stage IV is about 23-33 Ma, which correspond to the time span between the natural ages of the two stages (336-344 Ma for stage I and 310-315 Ma for stage IV). Considering that stage I is reached by the markers after about 3-8 Ma, the beginning of the subduction could be at approximately 340-350 Ma, so long after the subduction occurred between 375 and 425 Ma. This means

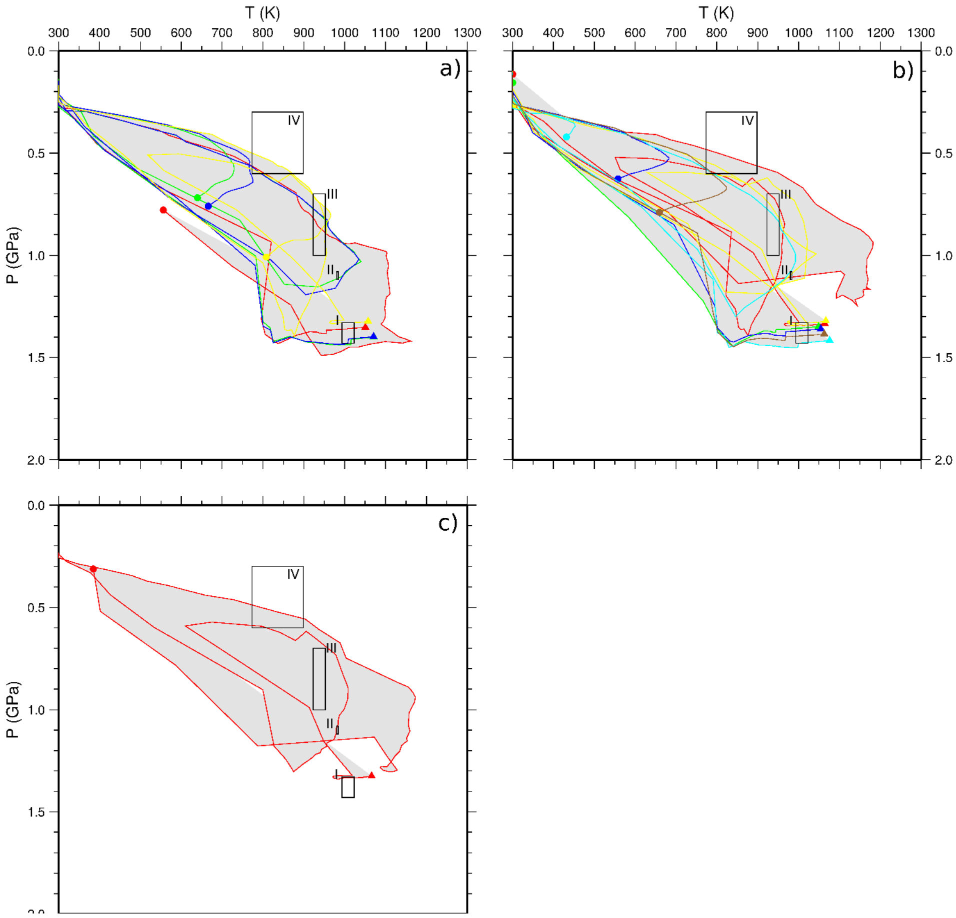

Figure 5.16: P-T paths of the markers fitting with datum Hv2 between 336 and 344 Ma. Panel a) represents simulated paths of continental markers; panel b) represents simulated paths of sediments; panel c) represents simulated paths of oceanic markers. Different colours represent paths of different markers. Circles represents the starting point of the markers and triangles represent the ending points. Natural P-T stages are represented with black rectangles.

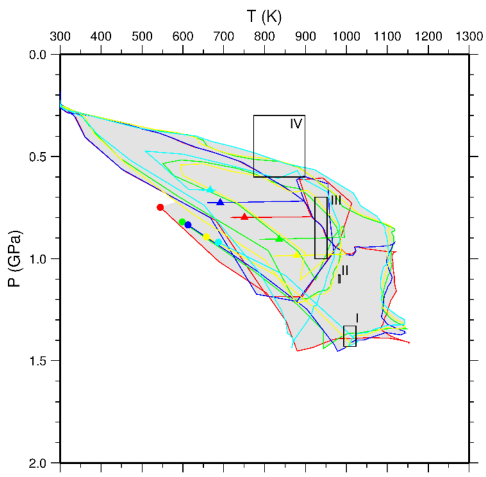

Figure 5.17: P-T simulated paths of the continental markers fitting with datum Hv2 during the oceanic subduction phase. Different colours represent paths of different markers. Circles represents the starting point of the markers and triangles represent the ending points. Natural P-T stages are represented with black rectangles.

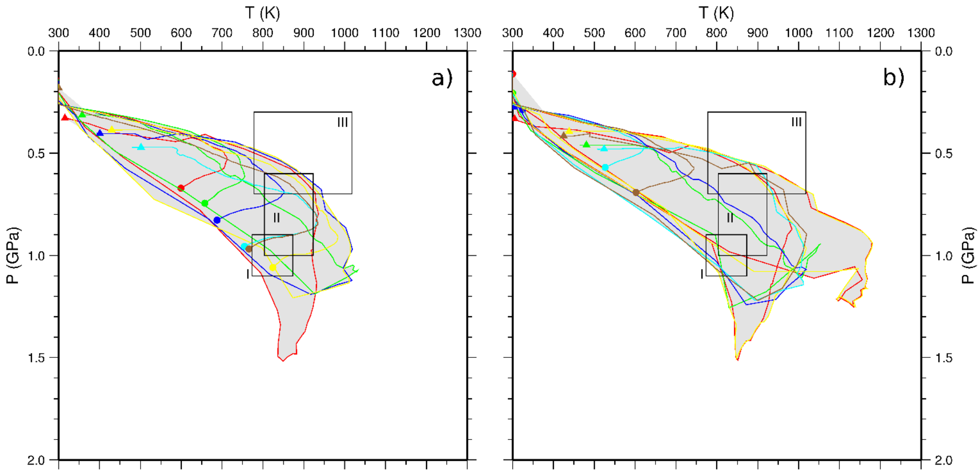

Figure 5.18: P-T simulated paths of the continental markers (panel a) and sediments (panel b) fitting with datum Hv3 during the oceanic subduction phase. Different colours represent paths of different markers. Circles represents the starting point of the markers and triangles represent the ending points. Natural P-T stages are represented with black rectangles.

that the metamorphic stages recorded by datum Hv2 could be related to an exhumation happened during a phase characterised by oceanic subduction, while P-T paths of exhumation predicted during the post-collisional phase do not fit with the metamorphic evolution of datum Hv2.

Continental markers that record P-T conditions in agreement with datum Hv3 shows two types of paths, some of them are exhumed from their initial position and then subducted and exhumed again (red, blue, green and yellow lines in Figure 5.18a), while others show only an exhumation from their initial position (light blue and brown lines in Figure 5.18a). Continental markers with an initial pressure below 1 GPa (red, green and blue lines in Figure 5.18a) have P-T conditions compatible with the early metamorphic imprint recorded by rocks Hv3 during their subduction, before to reach their peak pressure. After the re-equilibration at the peak pressure, some of them (red line in Figure 5.18a) have an isothermal exhumation, fitting stage II, and at about 0.7 GPa they begin to cool down, fitting stage III; some others (yellow, blue and green lines in Figure 5.18a), have a lower peak pressure and they warm up before to be exhumed and fit stage II and III. These markers fit with stage I after 25-40 Ma from the beginning of the subduction. Continental markers with an initial pressure of about 1 GPa (light blue and brown lines in Figure 5.18a) show only exhumation, characterised by an initial warming, up to the thermal peak, during which they fit stage I and II, and followed by cooling, during which they fit stage III. In these cases the agreement with stage I is before 5 Ma of evolution. A finale case is represented by some deep markers (yellow line in Figure 5.18a) that show correspondences both during the initial exhumation and during the following cycle of subduction and exhumation.

Markers of sediments can be divided in two groups: one group that completes only one cycle of subduction and exhumation (blue, green, light blue and brown lines in Figure 5.18b), and another group that completes two cycles (red and yellow lines in Figure 5.18b). Markers belonging to the first group fit with stage I during subduction, then they reach their pressure peak and the successive thermal peak, before to be exhumed and fit stage II and III. The time of the correspondence with stage I is between 20 and 45 Ma. Markers belonging to the second group fit with stage I and II during their first subduction, then they reach their thermal peak (about 1200 K) before the exhumation, during which they fit stage III; during the second cycle they fit stage I during subduction, then they reach their pressure peak (about 1.5 GPa) and during the exhumation they have correspondences with stage II and III. During the first subduction they reach stage I after about 5 Ma, while during the second subduction they reach it after about 30 Ma.

Stage I has a geological Devonian age (350-420 Ma) and markers show the agreement with it in a wide range of time (0-45 Ma). Therefore, the period during which the subduction could begin is very wide (350-465 Ma, *Guillot and Ménot*, 1999; *Guillot et al.*, 2009a), in agreement both with the subduction occurred between 425 and 375 Ma and with a possible successive subduction between 340-350 Ma deduced by datum Hv2. So, radiometric dating need to better constrain this metamorphic evolution.

Datum Hv4 has correspondences with continental markers and sediments that complete one or two cycles of subduction and exhumation (Figure 5.19). Markers that complete one cycle fit with stages I, II and III during the exhumation, while markers that complete two cycles have correspondences with stage III during the first exhumation, and with stages I, II and III during the second exhumation. However, the largest amount of markers cool down during their exhumation, while the three metamorphic stages of datum Hv4 are characterised by different pressures but very similar temperatures, suggesting an isothermal exhumation. This kind of path is in agreement with some markers that complete only one cyle, showing an isothermal exhumation after the peak pressure at about 1.5 GPa (brown line in Figure 5.19a and blue line in Figure 5.19b). These markers fit with stage I (dated 297-407 Ma, *Ménot et al.*, 1987; *Guillot and Ménot*, 1999; *Guillot et al.*, 2009a) after about 40 Ma, identifying the beginning of the subduction between 340 and 450 Ma, as observed for datum Hv3.

Both continental markers from different crustal depth and sediments fit with the first stage of datum Hv11 after the pressure peak, that is at about 1.2-1.5 GPa (Figure 5.20). Some of them have an isothermal exhumation, while others warm up reaching their thermal peak after their fit with stage I. However, all of them have correspondences with stage II during the exumation. Stage I can be reached both during the oceanic subduction phase and the post-collisional phase, but in the latter case they are not exhumed and they have no correspondences with stage II. In the other case, P-T conditions compatible with stage II can be recorded between and 35 and 45 Ma of oceanic subduction, so before continental collision. Being the stage II dated at 300-330 Ma (*Schulz and von Raumer*, 2011),

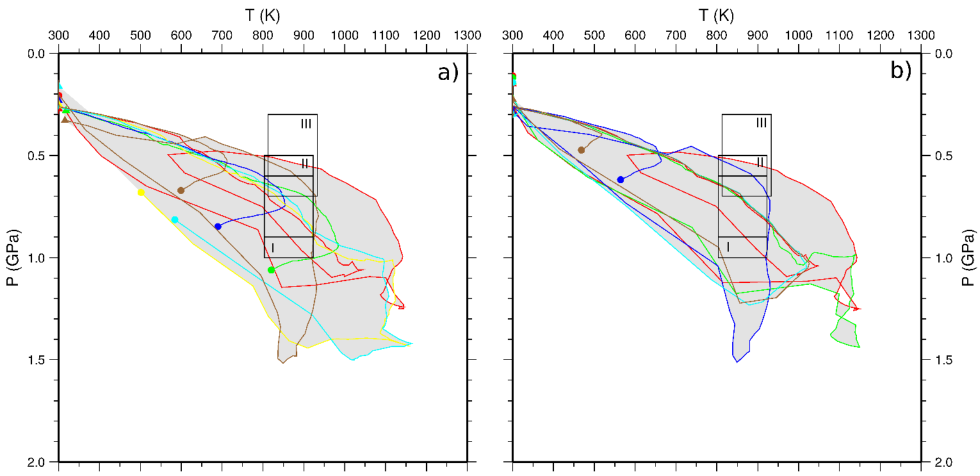

Figure 5.19: P-T simulated paths of the continental markers (panel a) and sediments (panel b) fitting with datum Hv4 during the oceanic subduction phase. Different colours represent paths of different markers. Circles represents the starting point of the markers and triangles represent the ending points. Natural P-T stages are represented with black rectangles.

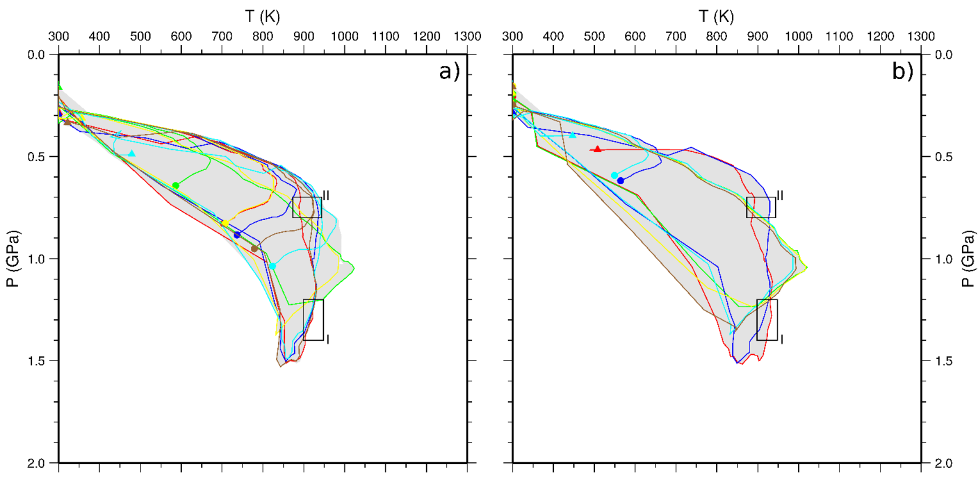

Figure 5.20: P-T simulated paths of the continental markers (panel a) and sediments (panel b) fitting with datum Hv11 during the oceanic subduction phase. Different colours represent paths of different markers. Circles represents the starting point of the markers and triangles represent the ending points. Natural P-T stages are represented with black rectangles.

subduction should begin between 335 and 375 Ma, in agreement with the observation from datum Hv2.

The largest amount of markers that have an agreement with stage I of datum Hv12 show two cycles of subduction and exhumation (Figure 5.21). All of them fit with stage I during the subduction of both cycles but P-T conditions compatible with stage II can be recorded only during the first exhumation, after 20-25 Ma from the beginning of the subduction. Moreover, few continental markers with an initial pressure of about 1 GPa (red line in Figure 5.21a) are characterised by an initial exhumation followed by a cycle of subduction and exhumation. These markers fit with stage I at the beginning of the evolution, while they show correspondences with stage II during the second exhumation. For these markers stage II is reached at about 45 Ma of evolution. As for datum Hv11,

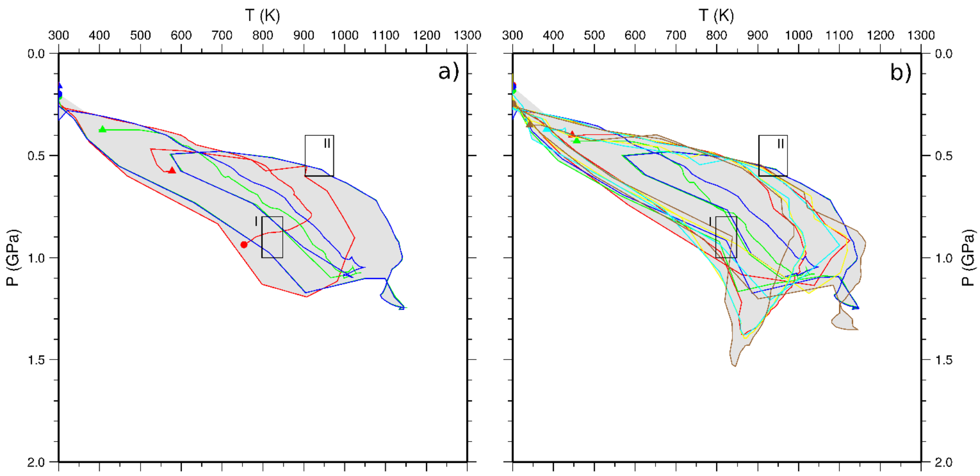

Figure 5.21: P-T simulated paths of the continental markers (panel a) and sediments (panel b) fitting with datum Hv12 during the oceanic subduction phase. Different colours represent paths of different markers. Circles represents the starting point of the markers and triangles represent the ending points. Natural P-T stages are represented with black rectangles.

stage I can be reached also during the post-collisional phase, but in this case there is not a successive exhumation with fitting with stage II. Considering that stage II is dated at 319-321 Ma (*Genier et al.*, 2008; *Bussy et al.*, 2000) and that it can be recorded by the markers after 20-45 Ma, the beginning of the subduction could be at about 340-365 Ma, in according with the previous data. It is clear that the lack of radiometric ages for successive re-equilibration stages negatively influences the quality of the comparison between natural data and model predictions.

Pennidic domain

Datum Pv1 has correspondences with oceanic markers that reach high pressures, over 2 GPa. The agreement with stage I is after the pressure peak, during an exhumation characterised by warming (Figure 5.22). Markers that record the higher pressures, up to 3 GPa, are exhumed at about 1.5 GPa, while markers subducted up to 2.5 GPa are exhumed up to shallower depths, approximately at 1.2 GPa, fitting also with stage II. The exhumation after the pressure peak is very fast, of approximately 3 mm/yr. After stage I, the exhumation of the deepest markers is characterised by a period of cooling with no changes in pressures, followed by a slight rising associated to warming. This last phase of exhumation takes place during the post-collisional phase and it is not shown by any other shallower markers. This is due to the dynamics characterising the wedge after the collision, that show rising of the deep portion of the slab only, while it does not occur at crustal depths. This means that material in the crust can be exhumed during the post-collisional phase either by the mean of other kind of mechanisms, such as faults and fractures, or a different tectonic setting, such as extension. This is in agreement with data from Mont du Lyonnais, showing an initial phase of fast exhumation up to

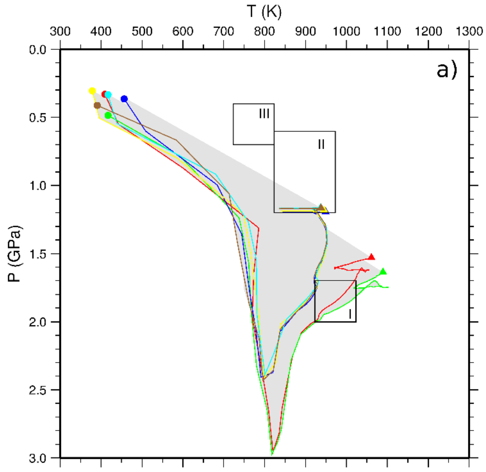

Figure 5.22: P-T simulated paths of the oceanic markers fitting with datum Pv1 during the oceanic subduction phase. Different colours represent paths of different markers. Circles represents the starting point of the markers and triangles represent the ending points. Natural P-T stages are represented with black rectangles.

approximately 20 km depth (> 1.5 mm/yr) associated with active subduction, followed by a phase of exhumation with velocity lower than one order of magnitude associated to a transpressive regime (*Lardeaux et al.*, 2001). Stage I is dated 374-392 Ma (*Messiga et al.*, 1992; *Giacomini et al.*, 2007; *Maino et al.*, 2012) and it is reached by the markers after about 35-40 Ma of subduction, suggesting the beginning of the subduction between 410 and 430 Ma. The hypothesis that a further exhumation could be related to other mechanisms is supported by the ages of stages II and III, indicating lower velocities of exhumation (less than 0.5 mm/yr).

Markers that have correspondences with stage I of datum Pv5, show an agreement also with stage I of datum Pv6 (Figure 5.23). All these markers, both of continents and sediments, complete two cycles of subduction and exhumation, the first characterised by their thermal peak, while during the second they record the pressure peak. During the first cycle, they fit with stage I of datum Pv5 during the subduction, before maximum temperature, and with stage I of Pv6 and stage II of Pv5 during the exhumation. Differently, during the second cycle, they have correspondences with stage I and II of Pv5 and stage I of Pv6 after the pressure peak. An exception is represented by deep continental markers (yellow and brown lines in Figure 5.23a), which paths are characterised by a single cycle after an initial exhumation. Some of these markers (brown line in Figure 5.23a) fit only with stage I of Pv6 during their first exhumation. Therefore, stage I of datum Pv6 can be considered either as a metamorphic stage recorded by deep continental rocks never subducted to high depths, or as a metamorphic stage successive to a non-preserved HP stage (as stage I of datum Pv5). However, the latter case is supported by the ages of stage I of Pv5 and stage I of Pv6. In fact, markers have correspondences with stage I of Pv6 5-15 Ma after the fitting with the stage I of Pv5, in agreement with ages of 340-360

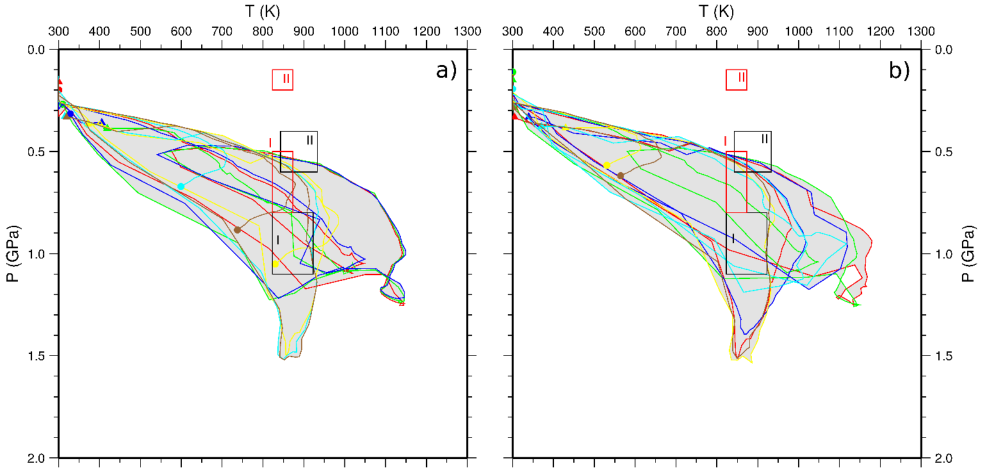

Figure 5.23: P-T simulated paths of the continental markers (panel a) and sediments (panel b) fitting with data Pv5 and Pv6 during the oceanic subduction phase. Different colours represent paths of different markers. Circles represents the starting point of the markers and triangles represent the ending points. Natural P-T stages are represented with black (datum Pv5) and red (datum Pv6) rectangles.

Ma for Pv5 (*Monie*, 1990; *Borghi et al.*, 1999) and of 328-332 Ma for Pv6 (*Bussy et al.*, 1996; *Giorgis et al.*, 1999). Moreover, stage I of datum Pv5 is reached by the markers after 10-20 Ma, suggesting the beginning of the subduction between 345 and 380 Ma. The lacking of correspondences with stage II of Pv6 can be related to the absence of exhumation during the post-collisional phase of the model, suggesting, as for datum Pv1, the requirement of a different tectonic setting.

Oceanic markers that show an agreement with stage I of datum Pv12 (Figure 5.24c) complete only one cycle of subduction and exhumation, while sediments and continental markers (Figure 5.24a and b, respectively) complete either one or two cycles. Oceanic markers and sediments with paths characterised by one cycle reach their peak pressure in correspondence of stage I, then they show a first phase of exhumation characterised by warming, up to approximately 1 GPa, followed by exhumation associated to cooling, during which they fit with stage II (blue, yellow, light blue and brown lines in Figure 5.24b and Figure 5.24c). For what concern continental markers, only the deepest ones complete one cycle (yellow, green, light blue and brown lines Figure 5.24a). This cycle is characterised by an increase of temperature after the peak pressure without changes of depth, followed by an exhumation that in a first stage is isothermal. Continental markers and sediments with paths characterised by two cycles fit with stage I only during the first subduction, while stage II has correspondences during both exhumations. In this case, the peak pressure corresponds with stage I and it is followed by the thermal peak, before the agreement with stage II. Stage I is dated at 400-437 Ma (*Droop*, 1983; *von Quadt et al.*, 1997) and markers fit with it after 5-20 Ma of evolution, so the beginning of the subduction has to be between 405 and 460 Ma.

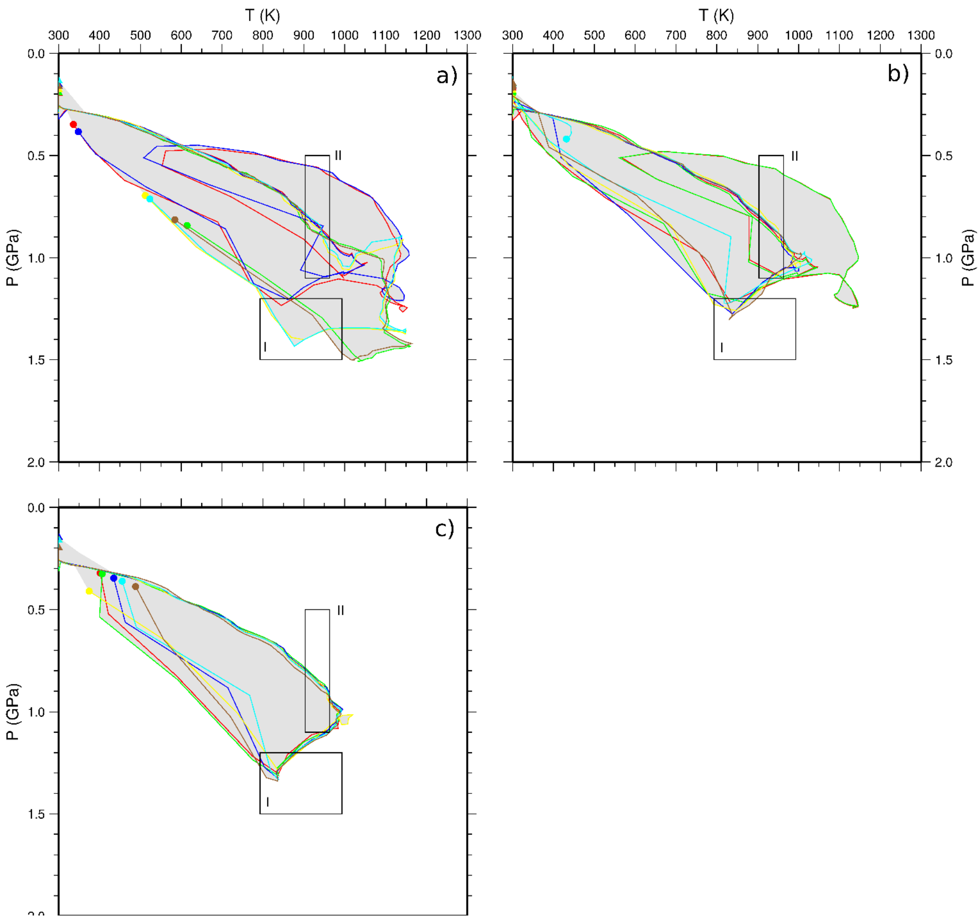

Figure 5.24: P-T simulated paths of the continental markers (panel a), sediments (panel b) and oceanic markers (panel c) fitting with datum Pv12 during the oceanic subduction phase. Different colours represent paths of different markers. Circles represents the starting point of the markers and triangles represent the ending points. Natural P-T stages are represented with black rectangles.

Austroalpine domain

The paths of the markers with correspondences with datum Av3 are characterised by two cycles of subduction and exhumation (Figure 5.25). However, they have a fitting both with stage I and with stage II only during the first cycle, while during the second cycle they do not reach pressures high enough to fit stage I and the exhumation occurs at temperatures too low to fit with stage II. P-T conditions compatible with stage I are reached at the end of the subduction, at pressure of approximately 1.2 GPa, then there is a significant warming, reaching the thermal peak (approximately 1200 K) before to start the exhumation and to fit with stage II. Stage I has a geological age of 350-360 Ma (*Rode et al.*, 2012) and stage II has a radiometric age of 304-330 Ma. This time interval is in agreement with the paths of the markers that record P-T conditions compatible with stage II approximately 20 Ma after the fitting with stage I. Considering that markers reach stage I after 5-10 Ma of evolution, the beginning of the subduction should be set between

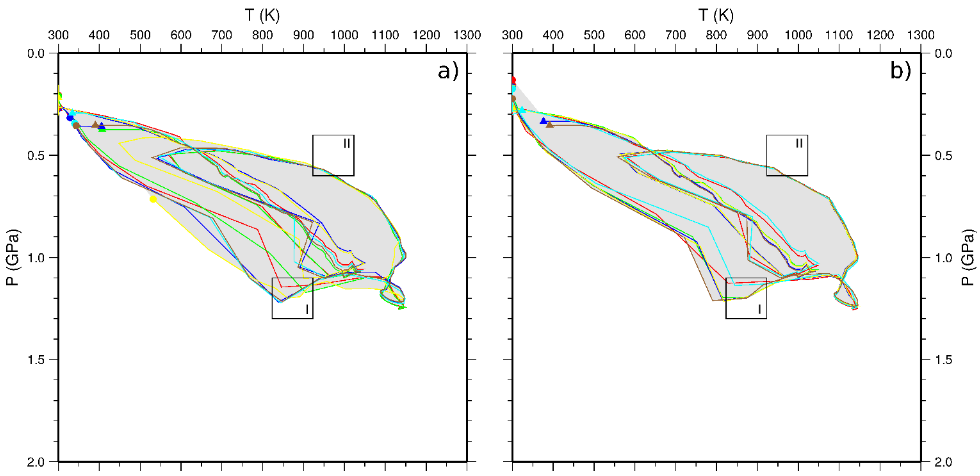

Figure 5.25: P-T simulated paths of the continental markers (panel a) and sediments (panel b) fitting with datum Av3 during the oceanic subduction phase. Different colours represent paths of different markers. Circles represents the starting point of the markers and triangles represent the ending points. Natural P-T stages are represented with black rectangles.

330 and 360 Ma, according with data from the Helvetic domain and with data Pv5 and Pv6 from the Pennidic domain.

Stage I of datum Av4 has correspondences both with markers that complete two cycles of sinking and exhumation (red, blue and green lines in Figure 5.26a, and light blue and brown lines in Figure 5.26b), and with markers that complete only one cycle (yellow, light blue and brown lines in Figure 5.26a, and red, blue, green and yellow lines in Figure 5.26b). For what concerns markers with paths characterised by two cycles, the fitting with stage I occurs during the sinking of both cycles, while there is correspondence with stage II only during the second and final exhumation. In fact, the first cycle is characterised by an increase of temperature after the fitting with stage I, which determines an exhumation too hot to fit with stage II. Markers characterised by paths with a single cycle fit with stage II during the exhumation that occurs at temperature comparable to that of the second cycle. Stage I has an age of 365 Ma (*Godard et al.*, 1996; *Hauzenberger et al.*, 1996) and if fits with markers after 5-40 Ma, positioning the beginning of the subduction between 370 and 405 Ma.

Same conclusions can be deduced by datum Av5. In fact, stage I and stage II are compatible with the metamorphic conditions observed in datum Av4 and the oceanic markers show the same kind of paths: some of them (yellow and brown lines in Figure 5.27) complete two cycles, fitting with both stages I and II only during the second cycle; others (red, blue, green and light blue lines in Figure 5.27) complete one cycle, fitting with both stages during their exhumation. Stage I has an age similar to that of datum Av4 (360 Ma, *Godard et al.*, 1996) and has correspondences with oceanic markers after 9-35 Ma of evolution, positioning the beginning of the subduction between 370 and 395 Ma.

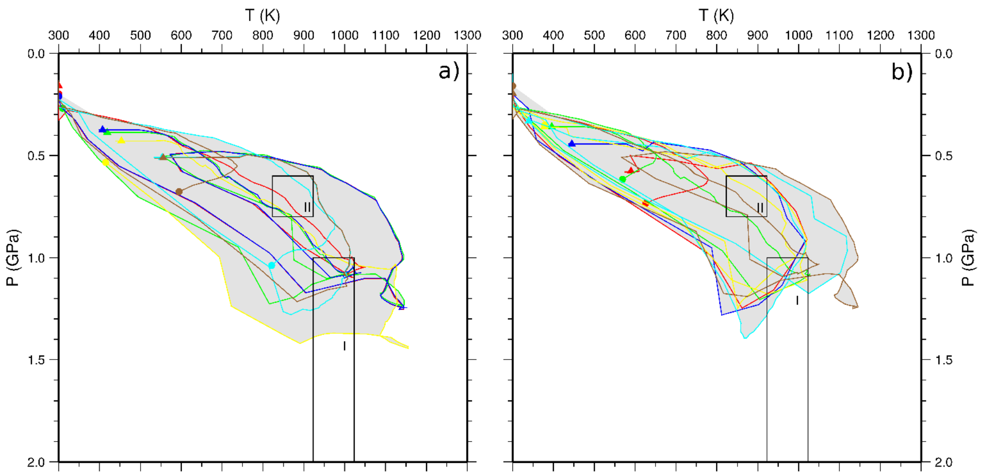

Figure 5.26: P-T simulated paths of the continental markers (panel a) and sediments (panel b) fitting with datum Av4 during the oceanic subduction phase. Different colours represent paths of different markers. Circles represents the starting point of the markers and triangles represent the ending points. Natural P-T stages are represented with black rectangles.

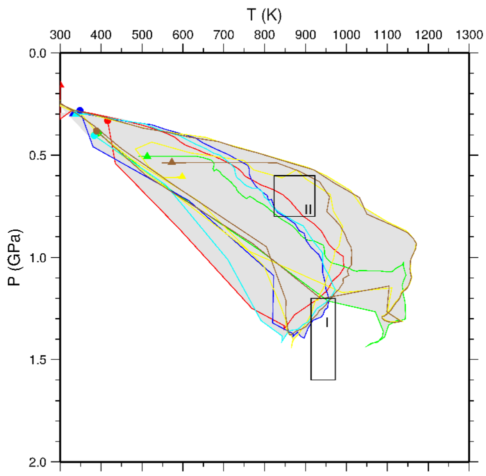

Figure 5.27: P-T simulated paths of the oceanic markers fitting with datum Av5 during the oceanic subduction phase. Different colours represent paths of different markers. Circles represents the starting point of the markers and triangles represent the ending points. Natural P-T stages are represented with black rectangles.

Southalpine domain

Stage I of data Sv4 and Sv5 has been recorded at P-T conditions comparable with P-T conditions recorded by data Sv7 and Sv9 during stage II. However, stage II of datum Sv4, stage II of datum Sv5 and stage II of data Sv7 and Sv9 have been developed at different P-T conditions, suggesting a retrograde path. Moreover, data Sv7 and Sv9 show relicts of a stage I developed at lower pressure and temperature than stage II, showing also a previous prograde path. Paths of the same markers have been used for the comparison with all data of the Southalpine domain, to verify if different paths can be related to different initial P-T conditions.

For the continental markers (Figures 5.28a and 5.29a) three group of markers can be

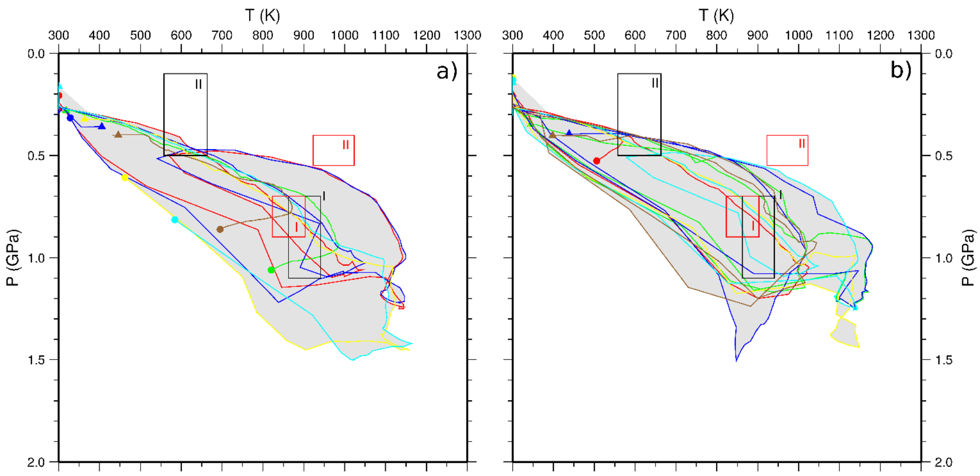

Figure 5.28: P-T simulated paths of the continental markers (panel a) and sediments (panel b) fitting with data Sv4 and Sv5 during the oceanic subduction phase. Different colours represent paths of different markers. Circles represents the starting point of the markers and triangles represent the ending points. Natural P-T stages are represented with black (datum Sv5) and red (datum Sv4) rectangles.

identified: a first group of markers coming from shallow depths (red and blue lines in Figures 5.28a and 5.29a), a second group of intermediate markers (yellow and light blue lines in Figures 5.28a and 5.29a), and a third group of deep markers (green and brown lines in Figures 5.28a and 5.29a). Markers of the first group complete two cycles of subduction and exhumation, and they fit with stage I and stage II (in the right order) of datum Sv5 only during the exhumation of the second cycle. Differently, P-T conditions compatible with stage I of datum Sv4 are recorded during the sinking and the exhumation of the second cycle. Intermediate markers of the second group complete only one cycle of subduction and exhumation, and they fit with stage I of data Sv4 and Sv5 and with stage II of datum Sv5 during the exhumation. The third group of markers have initial pressures above 0.8 GPa and they show only exhumation, characterised by an initial warming of about 200 K. They fit with stage I of data Sv4 and Sv5 and with stage II of datum Sv5. None of these markers fit with stage II because the exhumation occurs always at not high enough temperatures (Figures 5.28a). The prograde path deduced by stage I and stage II of data Sv7 and Sv9 fit only with shallow markers (red line Figures 5.29a), both during the first and the second cycle, while stage III never fit.

For what concerns the sediments (Figures 5.28b and 5.29b), two groups of paths can be recognised: a first group of markers that complete one cycle of subduction and exhumation (red and yellow lines in Figures 5.28b and 5.29b), and a second group of markers that complete two cycles (gree, blue, light blue and brown lines in Figures 5.28b and 5.29b). Markers of the second group fit with stage I and II of data Sv7 and Sv9 during their subduction, while they have correspondence with stage I of data Sv4 and Sv5 and with stage II of datum Sv5 during the exhumation. Differently, markers of the second group fit with stage I and II of data Sv7 and Sv9 during the first sinking, while correspond with stage I

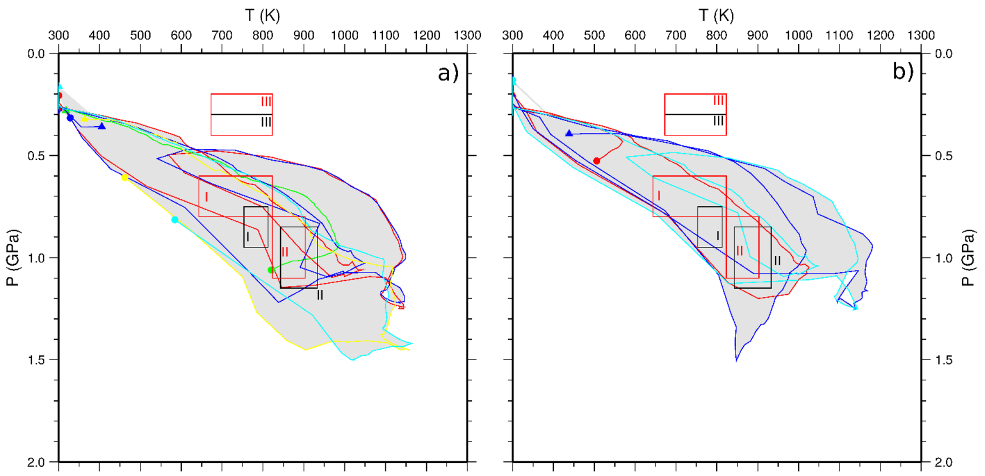

Figure 5.29: P-T simulated paths of the continental markers (panel a) and sediments (panel b) fitting with data Sv7 and Sv9 during the oceanic subduction phase. Different colours represent paths of different markers. Circles represents the starting point of the markers and triangles represent the ending points. Natural P-T stages are represented with black (datum Sv7) and red (datum Sv9) rectangles.

of data Sv4 and SV5 and with stage II of datum Sv5 during the second exhumation. As for the continental markers, there are no sediments that during their paths fit with stage II of datum Sv4 and with stage III of data Sv7 and Sv9.

Only markers deriving from shallow portions of the crust, both continent and sediments, have prograde paths compatible with stage I and II of data Sv7 and Sv9, while continental markers from intermediate depths are subducted at thermal conditions too cold to have correspondences, and deep continental markers do not show paths characterised by a prograde stage. Differently, markers deriving from any portion of the crust fit with the retrograde path deduced by stage I and II of datum Sv5, and with stage I of datum Sv4. Therefore, there could be two explanations for the lacking of relicts metamorphic stage prior to stage I of data Sv4 and Sv5: either they are recorded by rocks deriving from high depths (above 0.8 GPa) that do not show a prograde path but only an exhumation from their initial position; or previous stages are not preserved. As observed for data Pv1 and Pv6, there are no markers with a path of exhumation compatible with the path suggested by the last stage of data Sv4, Sv7 and Sv9, which could be characterised by higher temperatures. This could be related to an exhumation occurred in a different tectonic setting.

Markers have correspondences with stage I (dated 320-340 Ma, *Diella et al.*, 1992; *Zanoni et al.*, 2010) of data Sv4 and Sv5 after 10-30 Ma of evolution (it depends if they fit during the first or the second cycle), so the subduction should begin between 330 and 370 Ma. Stage II of data Sv7 and Sv9 have the same age of stage I of data Sv4 and Sv5 (*Spalla et al.*, 1999, 2006) and there are correspondences with markers after 5-20 Ma, positioning the beginning of the subduction beteween 325 and 360 Ma.

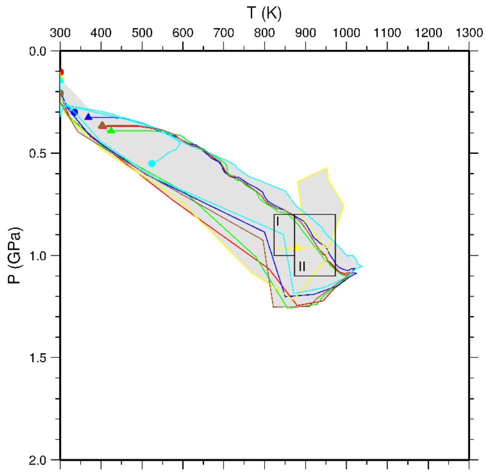

Figure 5.30: P-T simulated paths of the sediments fitting with datum Li1 during the oceanic subduction phase. Different colours represent paths of different markers. Circles represents the starting point of the markers and triangles represent the ending points. Natural P-T stages are represented with black rectangles.

French Central Massif

Datum Li1 has been determined for rock from the Lower Gneiss Unit and they show a slight decrease of temperature (from about 920 K to about 850 K) at approximately 0.8-1.0 GPa from stage I to stage II. No continental markers show a decrease of temperature in that range of pressures, while a lot of sediments have paths characterised by a single cycle of subduction and exhumation (with a maximum pressure recorded at approximately 1.2 GPa), with a cooling observed at about 0.8 GPa (red, green, blue and brown lines in Figure 5.30). They fit with stage I and then with stage II during the exhumation, right after the thermal peak. However, the interval of time between when markers begin to have P-T conditions compatible with stage I and when they fit with stage II is about 5-6 Ma, so lesser than the difference of ages between the stages (370-380 Ma for stage I and 350-360 Ma for stage II, *Faure et al.*, 2008, 2009). However, some markers have P-T conditions compatible with stage I at the collision, at approximately 50 Ma, and after that their paths are characterised by cooling, showing an agreement with stage II (yellow line in Figure 5.30). In this case, the interval of the correspondences between stage I and stage II is approximately 15-25 Ma, comparable with the natural ages. Considering these markers, the beginning of the subduction range between 420 and 430 Ma.

Continental markers show correspondence with stage I of datum Li4 when they reach the maximum pressure of their paths, approximately 1.6 GPa. After that they undergo a warming up to approximately 1200 K associated to a slight decrease of pressure, then they are isothermally exhumed at different depths, from 1.2 GPa (yellow line in Figure 5.31) to 1.0 GPa (green and blue lines in Figure 5.31). The last stage of the retrograde path is characterised by exhumation associated to cooling, during which markers fit stage II or stage III. The paths described by the markers fitting with stage I are different from

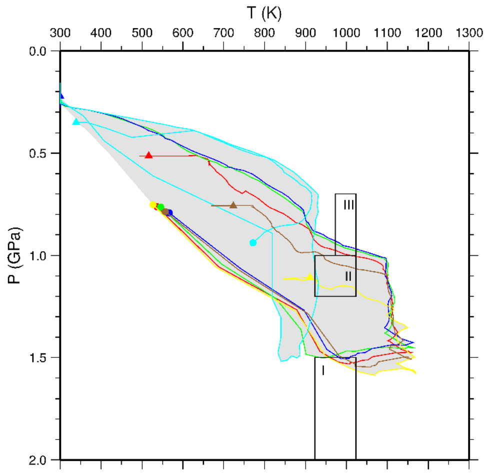

Figure 5.31: P-T simulated paths of the continental markers fitting with datum Li4 during the oceanic subduction phase. Different colours represent paths of different markers. Circles represents the starting point of the markers and triangles represent the ending points. Natural P-T stages are represented with black rectangles.

the path deduced by the natural stages, that seems to be characterised by a isothermal exhumation from stage I to stage III. This path is similar to the path accomplished by some markers (light blue line in Figure 5.31), but it occurs at lower temperatures and there is not a fitting with stage I and stage III. Stage I (dated at 420-440 Ma, *Pin and Sills*, 1986; *Mercier et al.*, 1991a) is reached by markers before 5 Ma of evolution, so the subduction should begin between 425 and 445 Ma, in accordance with the subduction taken into account for the comparison with the model.

Datum Li7 derives from rocks of the Upper Gneiss Unit. As for rocks of datum Li1, they show a decrease of the thermal conditions at approximately 0.8-1.0 GPa from stage I to stage II, but at higher temperatures (from approximately 970 K to approximately 920 K). Differently from datum Li1, both oceanic and continental markers, coming from different depths, and sediments show a cooling between 0.7 and 0.8 GPa, fitting with stage I and with stage II. Continental markers with an initial position at about 1 GPa, fit with stage I and II both during the initial exhumation and during the exhumation of the following cycle (red, yellow and light blue lines in Figure 5.32a). Shallower continental markers fit with both stages only during their cycle of subduction and exhumation (green and blue lines in Figure 5.32a). Oceanic markers and sediments (Figure 5.32c and Figure 5.32b, respectively) have paths characterised bu one or two cycles of sinking and rising. In case of one cycle, they fit with both stages during the exhumation, while in case of two cycles, they fit during the second exhumation, because the first rising is too hot. With respect to datum Li1, for which markers are never subducted below 1.2 GPa, some markers fitting with Li7 have reached higher pressures during the subduction, up to approximately 1.5-1.6 GPa. Stage I has a radiometric age of 377-387 Ma and markers reach compatible P-T conditions after 27-47 Ma. Therefore, the beginning of the subduction

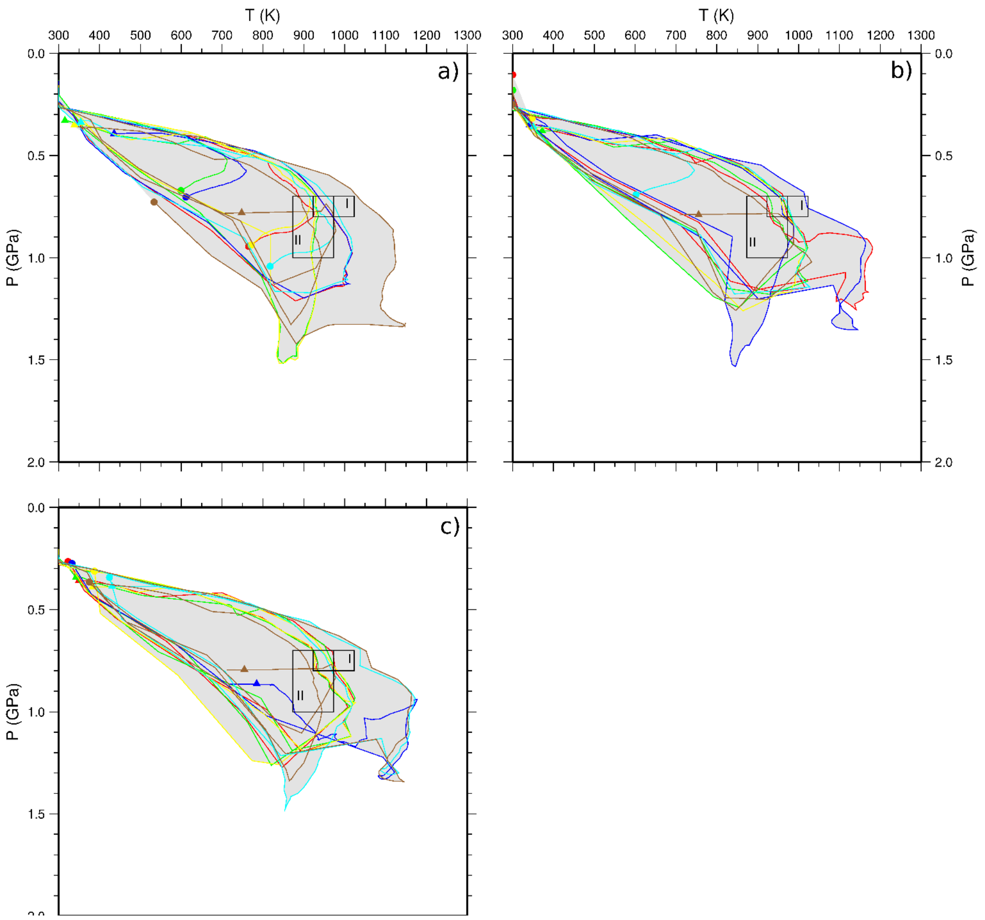

Figure 5.32: P-T simulated paths of the continental markers (panel a), sediments (panel b) and oceanic markers (panel c) with datum Li7 during the oceanic subduction phase. Different colours represent paths of different markers. Circles represents the starting point of the markers and triangles represent the ending points. Natural P-T stages are represented with black rectangles.

can be positioned between 405 and 435 Ma. Thermal conditions compatible with stage I followed by a cooling at same pressures can be observed also at the end of the oceanic subduction. In this case, markers complete three cycles, but P-T conditions compatible with stage I are reached only during the last exhumation, after approximately 50 Ma (brown lines in Figure 5.32). After that, during the post-collisional phase, markers cool down, showing correspondences with stage II. Both in case of cooling during the last stages of the oceanic subduction and in the case of cooling right after the collision, the time interval of the correspondence stages I and II is about 2 Ma, so much lesser than that deduced by the natural ages of approximately 25 Ma.

Natural estimates of successive metamorphic stages recorded and preserved by datum ML1 shows a prograde path, up to about 2.5 GPa and 1250 K, followed by a retrograde path, with the exhumation characterised by a gradual decrease of temperature, up to pressures lower than 0.6 GPa and 750 K. Some markers of continental lithospheric mantle have initial P-T conditions compatible with stage I, but none of them show an

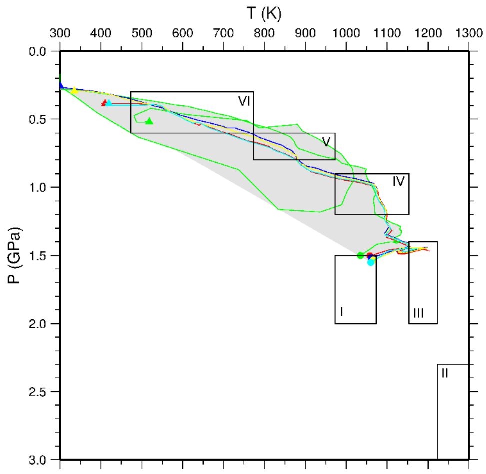

Figure 5.33: P-T simulated paths of markers of the continental lithospheric mantle fitting with datum ML1 during the oceanic subduction phase. Different colours represent paths of different markers. Circles represents the starting point of the markers and triangles represent the ending points. Natural P-T stages are represented with black rectangles.

initial prograde path characterised by an increase of pressure. In fact, all these markers warm up with no changes in pressure, reaching the thermal peak in correspondence of stage III. After that, the retrograde paths described by the markers fit clearly with a path inferred by the natural estimates of the different metamorphic stages and all markers have correspondences with stage IV, V and VI. Moreover, some markers (Green line in Figure 5.33) show a second cycle of subduction and exhumation, during which they fit with stages IV, V and VI.

Continental markers that record their maximum pressure under P-T conditions compatible with the stage I of datum ML2, complete two (red, blue, green, yellow and brown lines in Figure 5.34a) or three cycles (light blue line in Figure 5.34a) of subduction and exhumation. All of them reach stage I only at the end of the subduction of the first cycle, while they show correspondences with stages II and III during the exhumation of all cycles. However, the conditions under which the first exhumation occur are not always the same for all markers. In fact, after a general increase of temperature after stage I and a successive adiabatic exhumation up to approximately 0.9 GPa, two paths can be described: a first group of markers (red, blue and green lines in Figure 5.34a) show a decrease of temperature with no changes in pressure reaching P-T conditions compatible with stage II, and then there is a phase of exhumation associate to cooling, during which they fit with stage III; and a second group of markers that show a uniform exhumation associated to cooling, fitting with stage II and III.

Differently, there are no sediments or oceanic markers that fit with stage II and III during the exhumation. In fact, after the correspondence with stage I, there is an increase of temperature during a rising up to approximately 1.1 GPa, followed by a fast cooling associated to exhumation, which result too cold to fit with stages II and III (Figure 5.34a

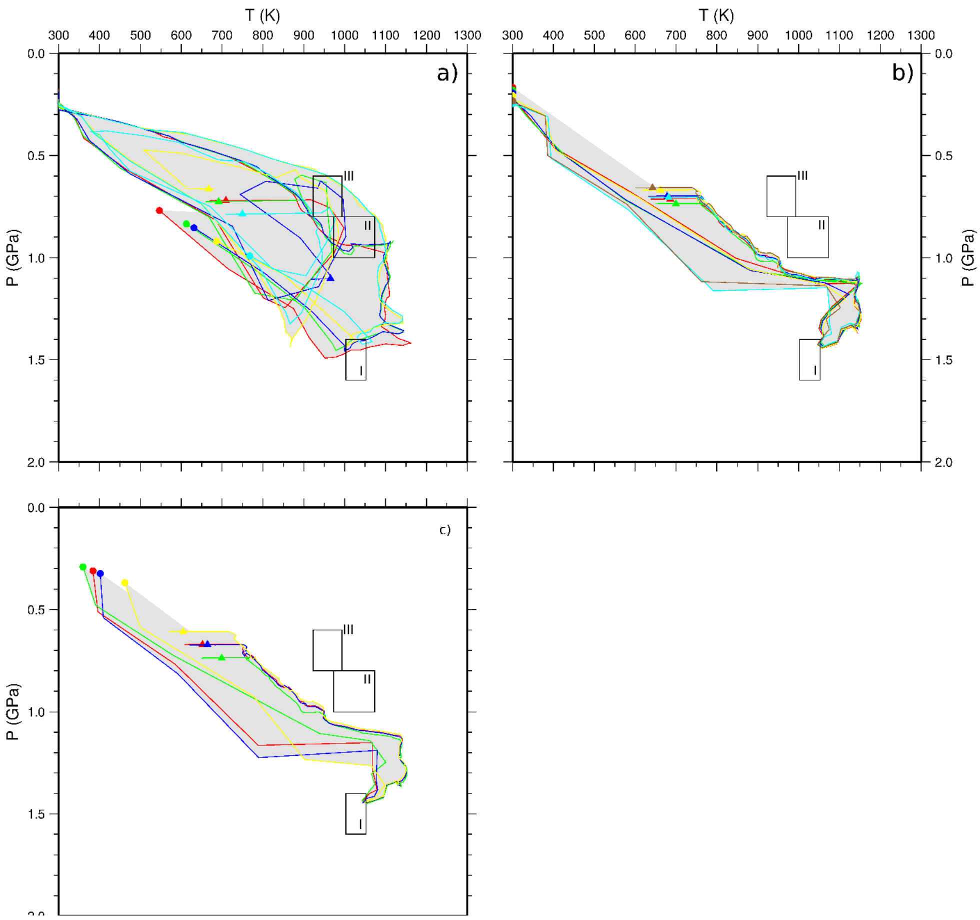

Figure 5.34: P-T simulated paths of the continental markers (panel a), sediments (panel b) and oceanic markers (panel c) fitting with datum ML2 during the oceanic subduction phase. Different colours represent paths of different markers. Circles represents the starting point of the markers and triangles represent the ending points. Natural P-T stages are represented with black rectangles.

and b).

Stage II has an age of 368-400 Ma (*Lardeaux et al.*, 2001; *Lardeaux and Dufour*, 1987; *Dufour et al.*, 1985; *Feybesse et al.*, 1988; *Lardeaux et al.*, 1989; *Mercier et al.*, 1991a; *Costa et al.*, 1993; *Pin and Lancelot*, 1982) and have an agreement with markers after 20-25 Ma of evolution. This indicates that the subduction should begin between 390 and 425 Ma, in agreement with the beginning of subduction in the model.

Stage I of datum Ro1 has correspondences with oceanic and continental markers and with sediments at the end of their prograde paths, at about 1.5-1.6 GPa. After the fitting with stage I, some continental markers show an increase of temperature associated to a slight decrease of pressure, up to approximately 1200 K, followed by a faster rising, charaterised by an initial isothermal exhumation and by a final exhumation associated to cooling (red, green, yellow, light blue and brown lines in Figure 5.35a). During the exhumation these markers fit either with stage II or with stage III, but they never fit with both of them. Other continental markers (blue line in Figure 5.35a) have a retrograde

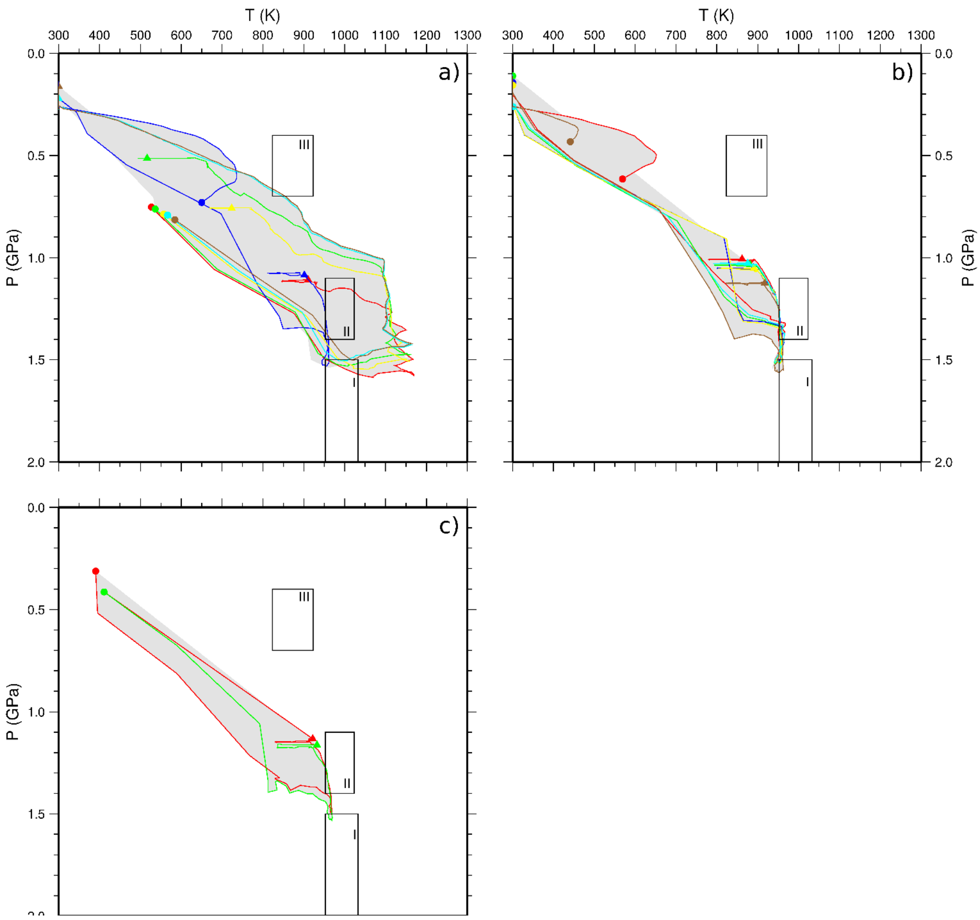

Figure 5.35: P-T simulated paths of the continental markers (panel a), sediments (panel b) and oceanic markers (panel c) fitting with datum Ro1 during the oceanic subduction phase. Different colours represent paths of different markers. Circles represents the starting point of the markers and triangles represent the ending points. Natural P-T stages are represented with black rectangles.

path compatible with the path of the oceanic markers (Figure 5.35c) and of the sediments (Figure 5.35b). Their paths are characterised by a isothermal exhumation after the fitting with stage I, avoiding the phase of warming. All these markers fit with stage II, but they are not exhumed enough to reach pressures compatible with stage III. This could be due to a final stage of exhumation developed under a different tectonic setting, as observed for some data of the Pennidic domain and of the Southalpine domain. In this case, the age of stage III (345-355 Ma, *Mercier et al.*, 1991a) would be compatible with the end of the oceanic subduction at approximately 375 Ma.

Stages I, II and III of datum Ro2, described a retrograde path characterised by exhumation associated to cooling. Some sediments and continental markers complete two cycles of sinking and exhumation, while others, as all the oceanic markers complete only one cycle. Markers with paths characterised by two cycles (red and yellow lines in Figure 5.36a and red line in Figure 5.36b) fit with stage I during the first subduction, before their P-T peak, while they fit with stages II and III during the exhumation of both cycles. Dif-

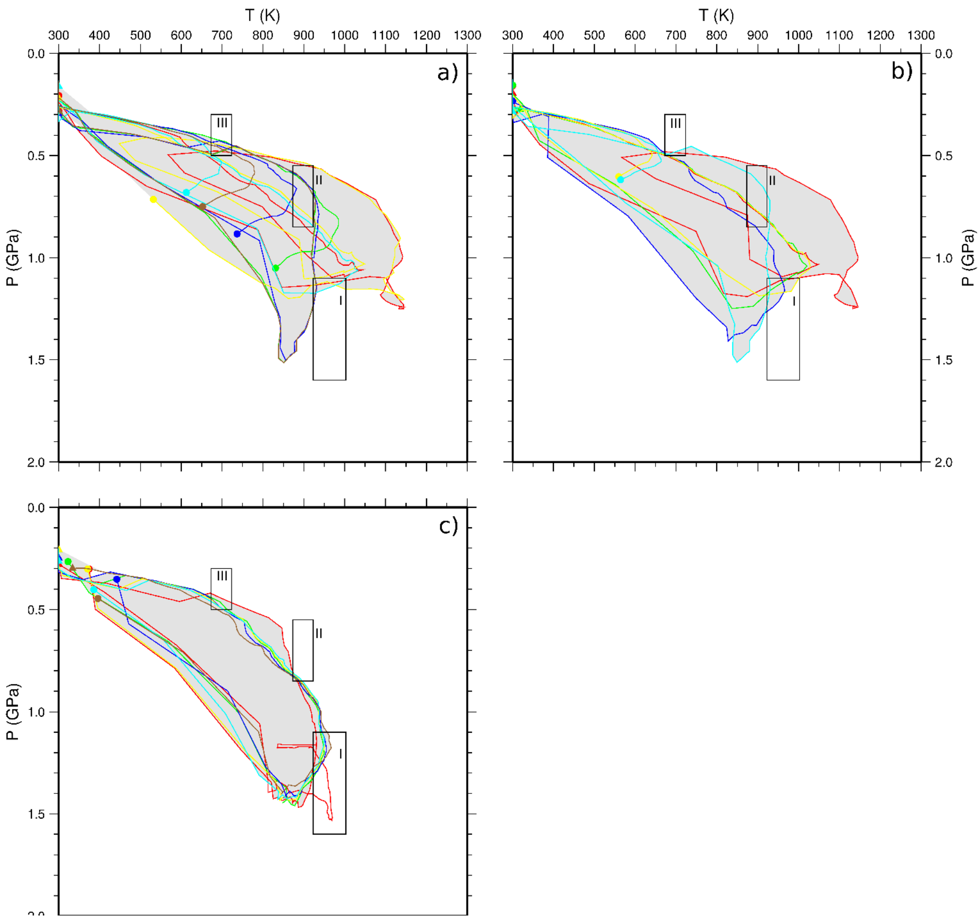

Figure 5.36: P-T simulated paths of the continental markers (panel a), sediments (panel b) and oceanic markers (panel c) fitting with datum Ro2 during the oceanic subduction phase. Different colours represent paths of different markers. Circles represents the starting point of the markers and triangles represent the ending points. Natural P-T stages are represented with black rectangles.

ferently, markers with paths characterised by only one cycle, reach their pressure peak, at approximately 1.5 GPa and 850 K, before the agreement with stage I, and they have correspondences with all stages during the exhumation.

Differently from datum Ro2, the metamorphic stages recorded by datum Ro3 indicate an initial adiabatic exhumation, followed by cooling. Shallow and intermediate continental markers complete two cycles of subduction and exhumation, fitting with stages I and II only during the first cycle. This because during the second cycle of subduction, markers reach lower temperatures, being exhumed in a thermal state colder than that necessary to fit with stage II. During the first cycle, reach approximately 1150 K and 1.3 GPa in correspondence of stage I, and after that they show a isothermal exhumation, fitting with stage II, before to conclude their exhumation that in the successive phase is characterised by cooling (red, blue, green and brown lines in Figure 5.37a). Deep continental markers complete only one cycle of sinking and exhumation and they reach higher maximum pressures, approximately 1.5 GPa, at P-T conditions higher than those of stage I. These

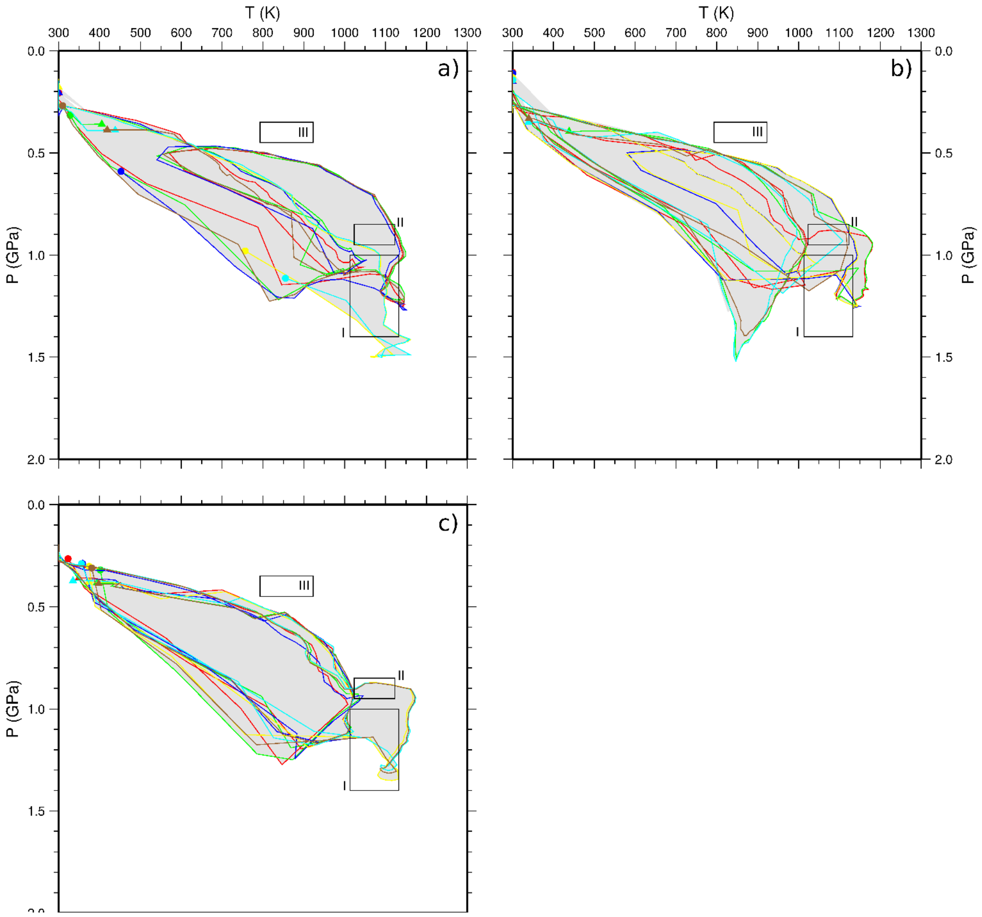

Figure 5.37: P-T simulated paths of the continental markers (panel a), sediments (panel b) and oceanic markers (panel c) fitting with datum Ro3 during the oceanic subduction phase. Different colours represent paths of different markers. Circles represents the starting point of the markers and triangles represent the ending points. Natural P-T stages are represented with black rectangles.

markers fit with stage I both during the subduction and a phase of adiabatic exhumation, and they fit with stage II right after the beginning of the cooling (yellow and light blue lines in Figure 5.37a). Both sediments and oceanic markers (Figure 5.37b and c) always complete two cycles, having correspondences with stages I and II only during the first cycle. Although the paths of these markers during the first cycle is similar to those of the continental markers, some of them show an increase of temperature after the fit with stage I, and the correspondence with stage II occurs during a phase of cooling with no changes in pressure. Stage III do not have correspondences with any kind of markers because the exhumation occurs always in a thermal state too cold. The increase of temperatures essential to fit with stage III could be related to an exhumation associated to other mechanisms or occurring in other tectonic settings.

Metamorphic stages I and II of data Ar1 and Mc1 have been developed under very similar P-T conditions, while stage III of datum Mc1 shows lower pressures and temperatures. However, the natural path deduced by these metamorphic stage is comparable. All

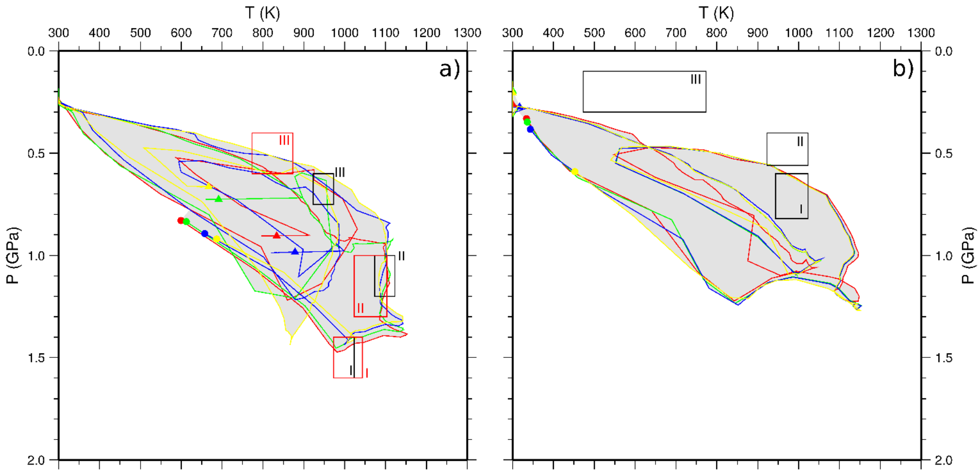

Figure 5.38: P-T simulated paths of the continental markers fitting with data Ar1 and Mc1 (panel a) and of the continental markers fitting with datum Ar2 (panel b) during the oceanic subduction phase. Different colours represent paths of different markers. Circles represents the starting point of the markers and triangles represent the ending points. Natural P-T stages are represented with black (data Ar1 and Ar2) and red (datum Mc1) rectangles.

metamorphic stages of data Ar1 and Mc1 have correspondences with continental markers that complete two cycle of sinking and rising during the oceanic subduction (Figure 5.38a). Stage I of both data show agreement with markers in correspondence of the maximum pressure recorded during their paths, at approximately 1.5 GPa. The successive retrograde path is characterised by an initial phase with an increase of temperature of about 100 K associated to a rising up to 0.8-0.9 GPa, during which the markers fit with stage II. After that, the exhumation is characterised by cooling and markers show correspondences with stage III. The second cycle of sinking and exhumation is characterised by lower temperatures and all markers fit only with stage III. Therefore, stage II of data Ar1 and Mc1 can be recorded at different times of the same path.

Differently, datum Ar2 does not preserve traces of high pressures and stages I and II have correspondences with continental markers, which path is characterised by two cycles, during their first phase of exhumation (Figure 5.38b). These markers record their peak pressure during the first cycle of subcudtion and it is lower (approximately 1.2 GPa) than that recorded by markers fitting with datum Ar1. Stage III is characterised by a P/T ratio too low to have correspondences with any markers during their exhumation.

Stage II of datum PA1 and stage I of datum PA2 have been developed under the same P-T conditions, and similar P-T conditions are recorded also during stage III of datum PA1 and stage II of datum PA2. Moreover, datum PA1 shows relicts of a previous metamorphic stage characterised by higher pressures and temperatures. Shallow continental markers complete two cycles of sinking and exhumation (red, green and blue lines in Figure 5.39a), fitting with stage I of datum PA1 during both cycles, while they have correspondences with stage II of datum PA1 and stage I of datum PA2 only during the second exhumation. In fact, the first cycle is characterised by a great increase of temper-

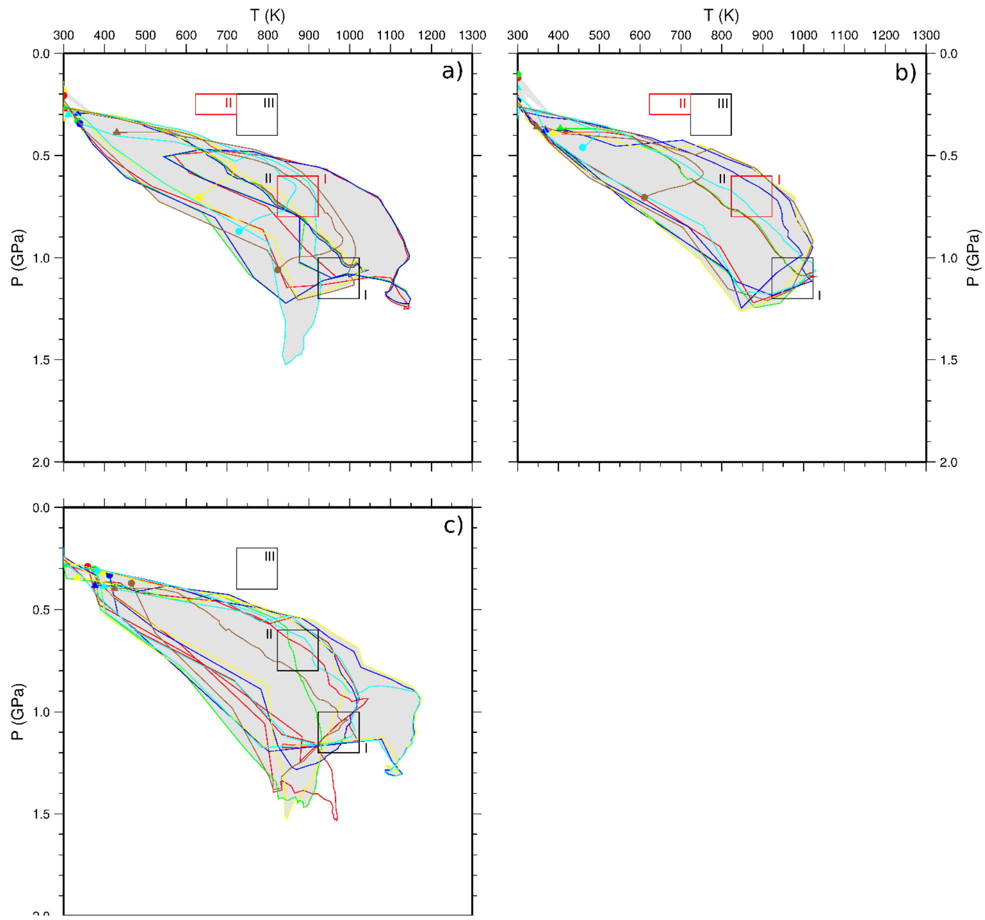

Figure 5.39: P-T simulated paths of the continental markers (panel a), sediments (panel b) and oceanic markers (panel c) fitting with data PA1 and PA2 during the oceanic subduction phase. Different colours represent paths of different markers. Circles represents the starting point of the markers and triangles represent the ending points. Natural P-T stages are represented with black (datum PA1) and red (datum PA2) rectangles.

ature after stage I of datum PA1, with a consequent exhumation under too hot thermal conditions. Intermediate and deep continental markers (yellow, light blue and brown lines in Figure 5.39a) undergo an initial exhumation, followed by one cycle of sinking and rising. They fit with stages I and II of datum PA1 and with stage I of datum PA2 during the final exhumation. Oceanic markers show paths similar to those completed by continental markers, but, during the first cycle, they cool rapidly, fitting with stage II of datum PA1 and with stage I of datum PA2 also during the first exhumation. Sediments complete either one or two cycles, but the thermal conditions of the cycles is very similar and they fit with stages I and II of datum PA1 and with stage I of datum PA2 during both cycles. Stage III of datum PA1 and stage II of datum PA2 never show an agreement with markers, as observed for the last metamorphic stage of datum Ar2. Stage I of datum PA1 has a radiometric age of 376-397 Ma and compatible P-T conditions are recorded by the markers after 25-40 Ma, positioning the beginning of the subduction between 400 and 440 Ma.

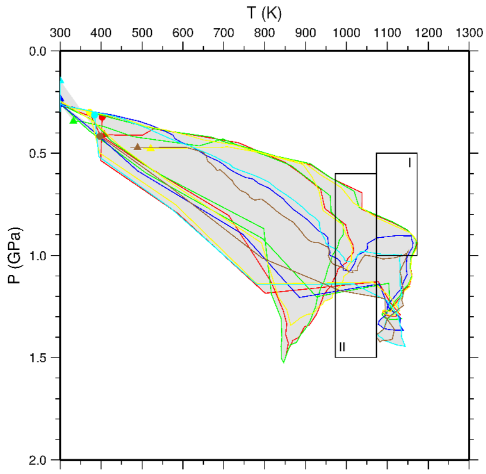

Figure 5.40: P-T simulated paths of the oceanic markers fitting with datum MN2 during the oceanic subduction phase. Different colours represent paths of different markers. Circles represents the starting point of the markers and triangles represent the ending points. Natural P-T stages are represented with black rectangles.

Stages I and II of datum MN2 shows a decrease of temperature characterised by none or slightly changes in pressure. All oceanic markers that fit with stage I complete two cycles of subduction and exhumation and they show a decrease of temperature according to stages I and II right after a phase of adiabatic exhumation. In fact, at approximately 0.9-1.0 GPa there is a clear decrease of temperature associated to slight variations of pressure. In particular, some of them (red, yellow and green lines in Figures 5.40) show an increase of pressure from stage I to stage II, while others (blue, brown and light blue lines in Figure 5.40) show a decrease of pressure.

Continental markers that have correspondences with datum TP1 have paths characterised by an initial exhumation followed by a cycle of subduction and exhumation. Markers with an initial pressure above 1.0 GPa (yellow, light blue and brown lines in Figure 5.41a) fit with stage I and II both during the first exhumation and during the following cycle, while shallower continental markers (red, blue and green lines in Figure 5.41a) fit with both stages only during the second exhumation. Some markers record a maximum pressure at approximately 1.5 GPa and their retrograde path is characterised by an isothermal exhumation up to the fitting with stage I (red, green and light blue lines in Figure 5.41a); other markers record lower maximum pressure (approximately 1.2 GPa) and the exhumation path is characterised by a gradual cooling (blue, yellow and brown lines in Figure 5.41a). Deep markers have correspondence with stage I after approximately 5 Ma, while all continental markers fit with stage I after the subduction at about 45 Ma. Sediments can be divided in two groups: a first group of markers that complete two cycles of sinking and exhumation (red, blue and green lines in Figure 5.41b), and a second group that complete only one cycle (yellow, light blue and brown lines in Figure 5.41b). Markers of the first group record their thermal peak during the first cycle, while

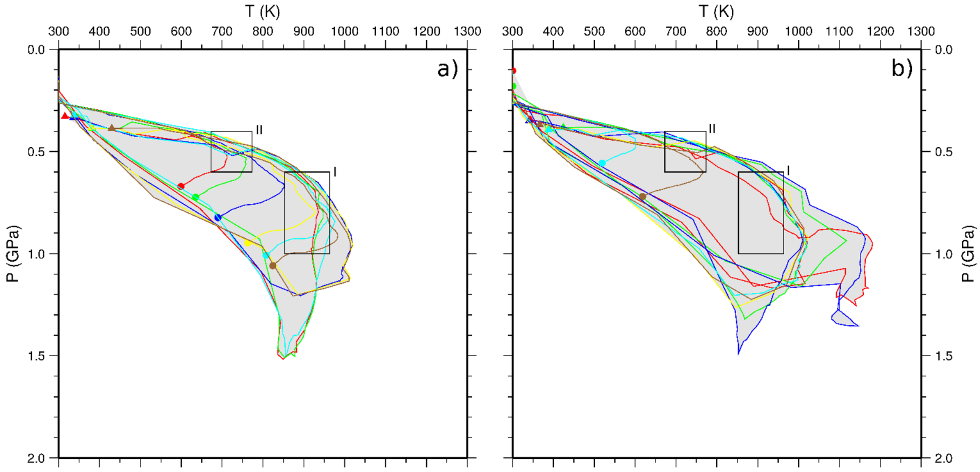

Figure 5.41: P-T simulated paths of the continental markers (panel a) and sediments (panel b) fitting with datum TP1 during the oceanic subduction phase. Different colours represent paths of different markers. Circles represents the starting point of the markers and triangles represent the ending points. Natural P-T stages are represented with black rectangles.

the peak of pressure is reached during the second cycle. In both cycles they have correspondence with stages I and II during the exhumation. Markers of the second group record both the pressure and the thermal peak before the fitting with both stages. Sediments fit with stage I between 25 and 45 Ma from the beginning of the subduction. So, considering the age of the stage I (375-385 Ma), the subduction should begin between 400 and 430 Ma. Time range compatible with the time between stage I and stage II (approximately 15-30 Ma) are recorded only during the first exhumation of the deep continental markers (estimated between 10 and 20 Ma), while the time range during the second exhumation is of approximately 5 Ma.

5.4 Discussion

The comparison between Figure 5.2 and Figure 5.3 shows that natural P_{max}-T_{Pmax} estimates that are characterised by both intermediate P/T ratios (for example data Hv3, Pv4, Sv12 and Ar2) and high P/T ratios (for example data Hv11, Pv10, Av9, Sv10 and LB1) are in agreement with CUM-CUM.5 model predictions during the oceanic subduction phase. This can be observed for data with different lithological affinities (oceanic, continental and mantle), both coming from different domains of the Alps and coming from the French Massif Central. The data with intermediate P/T ratio show agreement with CUM-CUM.5 model predictions at the bottom of the crust of the upper plate after approximately 10 Ma of evolution (for example data Ar2 and Pv7), as consequence of the activation of the large scale mantle flow that determines an increase of temperatures at the base of the crust (for details see Chapter 3.3). Differently, data characterised by high P/T ratios fit with subducted markers, oceanic or continental, in different portions of the wedge, depending on the estimated temperatures and pressures. In particular, the higher the P/T ratios of the data, the more the internal portion of the wedge shows the agreement with them (for example datum Av10 with respect to data Av8, Pv10 and LB1). Consequently, two situations in which data characterised by different P-T conditions fit with CUM-CUM.5 model predictions can be recognised: 1) the first is related to the contemporaneous fitting of the natural data with subducted markers, characterised by high P/T ratios, and with non-subducted continental markers at the bottom of the crust, characterised by intermediate P/T ratios. This situation remember the occurrence of contrasted thermal regime. Contrasted thermal regime have been invoked in the past by *Miyashiro* (1973) to justify the juxtaposition of belt characterised by HP and LT (Sanbagawa) with belt characterised by LP and HT (Abukuma). We do not observe a such homogeneous distribution in the actual chains; 2) the second is related to the different conditions that can be developed in the wedge. In this case, data with higher P/T ratios fit with markers in the internal and deep portion of the wedge, while data with lower P/T ratios show agreement with data in the external and shallow portion. For example, datum Hv11 has P-T estimate compatible with Kyanite-Granulite facies conditions and it fits with CUM-CUM.5 model predictions at the same time of data Pv10 and LB1, which show conditions compatible with Amphibole-Eclogite facies, and with datum Av7, that is compatible with Epidote-Eclogite facies conditions. Differently, during the post-collisional phase, the coeval fitting with data characterised by intermediate P/T ratios and with data characterised by high P/T ratios is observed only for few Ma after the collision, so before the thermal re-equilibration of the system, when the thermal conditions are similar to the oceanic subduction phase. In fact, data characterised by intermediate P/T ratios have an agreement with the model for the whole duration of the post-collisional phase (for example data Hv6, Pv7, Av10, Sv2 and Ar2), while crustal data characterised by high P/T ratios show an agreement only during the early stages (for example data Hv11, Pv10, Av2, Sv10 and Ar1).

ED.5 model is characterised by the introduction of the atmosphere and the implementation of the erosion-sedimentation mechanisms. As consequence of the introduction of the air layer, in the ED.5 model the upper plate is characterised by a free surface. The new setup does not limit anymore vertical movements of the upper plate, with consequences on the mantle flow at the lithospheric depth. In fact, the mantle flow is more intense close to the slab and the increase of temperature at the bottom of the continental crust is faster. However, the thermal conditions in the perturbed crust are comparable to that CUM-CUM.5 model. Moreover, the increase of mantle flow determines an increase of temperatures also in the internal and shallow portion of the wedge. In the hydrated area shallower small convective cells favour the recycling and the exumation of subducted material up to very shallow crustal level, not only at the bottom of the continental crust, as observed in SIN-CUM and in CUM-CUM models. During the post-collisional phase, the dynamics is still characterised by a general rising of the subducted slab, but the temperatures in the thickened crust are lower. This is due to the larger amount of recycled oceanic and lithospheric mantle markers, characterised by a lesser radiogenic decay with respect to the continental crust.

These variations on the thermal state of the subduction complex determines a different fitting of model predictions with natural P_{max}-T_{Pmax} estimates of the Variscan metamorphism. The increase of temperature during the oceanic subduction phase deteremines a general improvement of the agreement, especially for data with HT, both characterised by intermediate P/T ratios, such as data Hv6, Hv7, Ar2, MN2, and characterised by high P/T ratios, such as data Pv8, Av9, Ma1, Li3. The improvement of correspondences with data characterised by intermediate P/T ratios is localised mainly in the shallower portions of the wedge. In fact, P-T conditions compatible with data characterised by Barrovian-type metamorphism can be recorded not only at the bottom of the continental crust, as observed for CUM-CUM.5 model, but also in the wedge. Therefore, intermediate and high P/T ratios can be recorded at the same time, not only in areas of the subduction complex that are distant from each other (the continental crust and the wedge) as described in the paired metamorphic belts, but also at different levels of the wedge. Differently, during the post-collisional phase, the slight decrease of temperatures recorded in the thickened crust determines an improvement of fitting with some data and a worsen with others. Data that show an improvement are characterised by intermediate temperatures and high P/T ratios, such as data Pv9, Sv10 and Ar1, while data that worsen their correspondence are characterised by low-to-intermediate P/T ratios, such as data Hv5, Av11, MN1 and MN2.

Simulated P-T paths of markers of ED.5 model, show a wide variety of possible paths, and they do not depend only by the initial position of the markers. In fact, some markers that are close at the beginning of the simulation can accomplish different retrograde and/or prograde paths and also complete a different number of cycles of sinking and exhumation. On the other hand, markers coming from different portions of the subduction system can be coupled during their evolution and be exhumed together. In particular, the coupling of units deriving from different areas and having recorded different P-T conditions during their paths is often observed in the orogenic belts, for example at the Plateau d'Aigurande, in the French Massif Central (*Faure et al.*, 1990), and in the Belledonne Massif, in the Helvetic domain of the Alps (*Guillot and Ménot*, 1999). In general, three groups of maximum pressure recorded by the markers before the exhumation can be identified: a first group of sediments and of oceanic and continental markers that reach a maximum pressure of about 1.2 GPa; a second group of of oceanic and continental markers and sediments with a maximum pressure of about 1.6 GPa; and a group of oceanic markers subducted to a maximum pressure between 2 and 3 GPa and exhumed at about 1 GPa (for example markers that have correspondences with datum Pv1).

The largest amount of data characterised by polymetamorphic evolution, find correspondences with simulated paths of the markers for all the metamorphic stages, both prograde and retrograde. The metamorphic stages that do not fit with any markers are characterised by very low pressures and high temperatures. An example is the last stage of data Sv4, Sv7 and Sv9 that never have correspondences, in contrast with the last stage of datum Sv5, although the previous stages are very similar and have a lot of correspondences. This can be due to the development of those P-T conditions during the exhumation under a different tectonic settings, characterised by higher thermal conditions. However, final stages of exhumation under greenschist facies are constrained worse than other metamorphic stages, because of the lack of thermobarometers.

Natural ages of the P_{max}-T_{Pmax} estimates for the Variscan metamorphism in the Alps range from approximately 330 Ma to 437 Ma. In particular, data from the Helvetic and Penninic domains (Hv and Pv, respectively) are characterised by ages older than 390 Ma (as data Hv1, Hv3, Hv4, Hv9, Hv10, Pv1, Pv8, Pv11 and Pv12), while data from the Austroalpine and Southalpine domains and data Pv5 and Pv9 from the Penninic domain are characterised by younger ages. The comparison with simulated paths can be useful to infer the age of the subduction of data characterised by geological ages. By the comparison between the age of the metamorphic stages of the data and the time necessary to models to develop compatible P-T conditions, two time ranges for the beginning of the subduction can be identified. By the data of the French Central Massif and by data from the Helvetic and Pennidic domains can be inferred that the subduction begins between 400 and 450 Ma; differently, data from Austroalpine and Southalpine domains, data Hv11 and Hv12 from the Helvetic domain (characterised by geological ages) and datum Pv5 from the Penninic domain indicate a possible younger subduction, starting approximately between 330 and 380 Ma. The contrasted ages inferred by the data could be related to two different periods of subduction spaced out by a brief period characterised by continental collision. This hypothesis would be in agreement with the idea of two cycles of subduction/collision with opposite polarities proposed by many authors for the evolution of the Variscan orogeny (*Matte*, 2001; *Faure et al.*, 2005, 2009; *Guillot et al.*, 2009a; *Spiess et al.*, 2010; *Lardeaux*, 2014a).

Chapter 6

Model of double subduction

As discussed in the previous chapter, the P-T paths predicted by the model show a really good agreement with natural P-T paths inferred by the metamorphic stages recorded and preserved during the Variscan orogeny by rocks from both the Alps and the French Central Massif. By the way, the modelled paths opened the possibility to have two cycles of subduction and collision involved in the evolution of the Variscan belt. The hypothesis of two successive subduction systems is supported also by petrologic and geochronologic data and, nowadays, it is widely accepted. For the French Central Massif, *Lardeaux* (2014a) proposed a Silurian north-dipping subduction of Medio-European ocean and north margin of Gondwana underneath either the southern margin of Armorica or an unknown continent, followed by a late Devonian south-dipping subduction of the Saxothuringian ocean. A similar model has been supposed by *Matte* (2001), who suggested a north-dipping subduction that closed the Galician-Southern Brittany ocean during the Devonian, with the collision between Armorica and Gondwana, followed by a south-dipping subduction that led the closure of the Rheic ocean and the collision between Armorica and Avalonia at the end of the Devonian. The evolution inferred from data of the French Central Massif is compatible also with the evolution of the External Crystalline Massifs of the the Western Alps (*Guillot et al.*, 2009a). The Medio-European (or Galician-Southern Brittany) domain is under debate, because of discrepancies between metamorphic and paleo-geographic data. In fact, on the one hand the presence of HP/UHP metamorphism is evidence of its existence for at least 30 Ma, on the other hand the lack of biostratigraphic and paleomagnetic data suggest a narrow oceanic domain, smaller than 500-1000km (*Matte*, 2001; *Faure et al.*, 2009; *Lardeaux*, 2014a). The ages of the subductions deduced by the comparison between the simulated P-T paths of the model and the natural ages of different metamorphic stages of the data (Chapter 5) agrees with the timing of subduction inferred by geodynamic reconstructions (*Matte*, 2001; *Guillot et al.*, 2009a; *Spiess et al.*, 2010; *Lardeaux*, 2014a), positioning the beginning of the first subduction between 400 and 450 Ma and the beginning of the second subduction between

330 and 380 Ma.

A model of double subduction, characterised by two opposite subduction systems, has been developed to verify that it could well-represent the evolution of the Variscan belt. Therefore, P-T data predicted by the new model has been compared to data of Variscan metamorphism from the Alps and from the French Central Massif.

6.1 Model setup

The model characterised by a double opposite subduction has been developed with the configuration of the CUM-CUM models. Therefore, same boundary conditions, same grid and same density of the markers have been used (Chapter 3.1). Three models characterised by different velocities of the first oceanic subduction have been developed, to verify the impact on the thermal state and on the dynamics related to the second oceanic subduction. Velocities of 1, 2.5 and of 5 cm/yr have been used for the first subduction (in DS.1, DS.2.5 and DS.5 models, respectively), while the second subduction is characterised by a velocity of 5 cm/yr. Differently from the CUM-CUM models that were characterised by two evolutionary phases over a period of 130 Ma, four phases that covers the same period have been now considered:

1. a first phase of active oceanic subduction that lasts 51.5 Ma, until the first continental collision;
2. a second phase of 10 Ma characterised by a pure gravitational evolution;
3. a third phase of active oceanic subduction that lasts 26.5 Ma, until the second continental collision;
4. a fourth phase of pure gravitational evolution that lasts 42 Ma.

Being assumed the duration of the first phase the same for DS.1, DS.2.5 and DS.5 models, the width of the oceanic domain involved in the first subduction, representing the Medio-European ocean, is different for the three models with different subduction velocitites. The oceanic domain is 500 km, 1250 km and 2500 km wide in DS.1, DS.2.5 and DS.5 models, respectively. Therefore, the dimension of the ocean for DS.1 and for DS.2.5 models is compatible also with paleo-geographic reconstructions. Differently, the continent located between the two oceanic domains, which represent either Armorica or another micro-continent, and the oceanic domain involved in the second subduction, representing the Saxothuringian ocean, have the same size in both models. The continent is 400 km wide, while the ocean is 1250 km wide. The width of the continent is compatible with the dimension of Armorica inferred by cross-sections of the Variscan belts in France (*Matte*, 2001). The initial distribution of the markers for all models is shown in Figure 6.1.

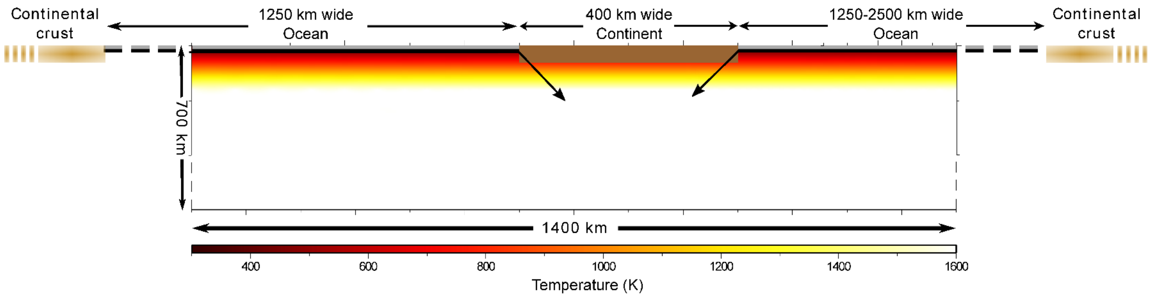

Figure 6.1: Setup and initial thermal configuration of the double subduction model. Brown, grey and black colours indicate the continental crust, the upper oceanic crust and the lower oceanic crust, respectively. The distances are not to scale.

6.2 Results

In Chapter 3.3 it has been already enlightened how changes in the velocity of subduction can influence the thermo-mechanics of the system. In particular, the lower the velocity of subduction, the higher the temperature in the slab and in the mantle wedge. This is due to the larger amount of cold material subducted for higher velocities, while the large-scale mantle flow contributes on the thermal state in the same way for all models. The consequence of lower temperatures for higher velocities is that the area in which the P-T conditions are compatible with the stability field of the serpentine is wider. Therefore, for low velocities the hydrated area is smaller and the convective cells in the mantle wedge are less efficient to recycle subducted material. This general behaviour characterises the first subduction of the presents model. In particular, the slab of DS.1 model is characterised by temperatures too high to have hydration of the mantle wedge and, therefore, to recycle subducted crust (Figure 6.2). Furthermore, as observed for CUM-CUM models, the higher the subduction velocity, the lower the dip angle of the slab (Figure 6.2).

Below, the discussion of the thermal state and of the dynamics of the models characterised by two opposite subduction will focus from the beginning of the second oceanic subduction, being the thermo-mechanics related to the first subduction widely described in Chapter 3.3. In particular, differences in the dynamics and in the thermal state between the models with different velocity of the first subduction will be enlightened, and the thermal states will be compared to the thermal state of a subduction started in a non-perturbed system.

The sinking of the slab determines a gradual backward bending of the first slab, associated to a thinning below a depth of approximately 150 km (Figure 6.3). Differently from the large-scale dynamics observed in the SIN-CUM and in the CUM-CUM models (Figures 3.3 and 3.7, respectively), the mantle flow above the slab is very weak, with the exception of the DS.5 model, in which it intensifies at about 15.5 Ma (Figures 6.3c3). The lack of an intense large-scale mantle flow could be related to the presence of the first slab that prevent the activation of the convective flow. Its enhancing in DS.5 model after

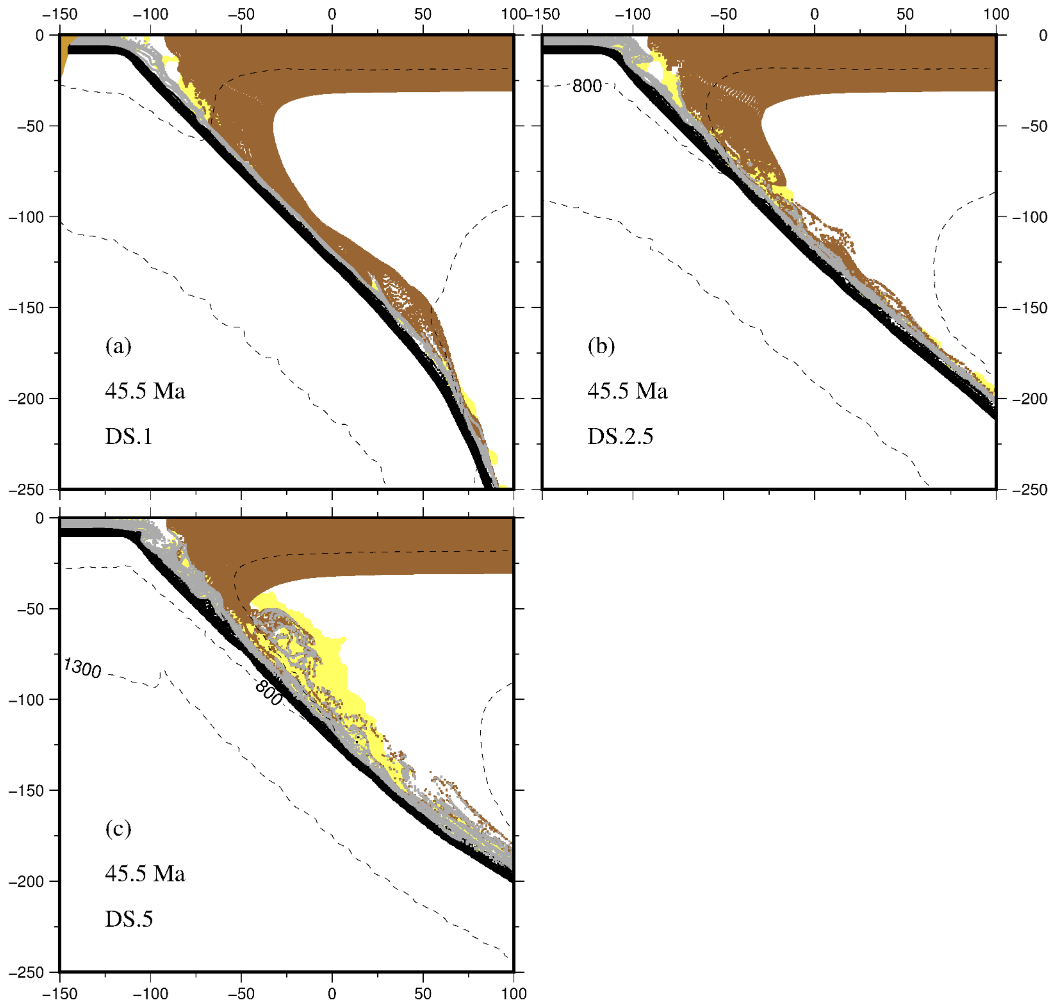

Figure 6.2: Temperature field in terms of the 800 K and 1300 K isotherms (dashed black lines) surrounding the wedge area for the DS.1 model (panel a), DS.2.5 model (panel b) and for the DS.5 model (panel c) at 26.5 Ma of evolution of the first subduction. The yellow areas represent the hydrated wedge domains. Black, grey, dark brown and light brown points represent the lower oceanic crust, upper oceanic crust, continental crust of the upper plate, and continental crust of the lower plate, respectively.

15.5 Ma is due to the higher dip angle of the slab with a consequent larger area above it. The presence of the short-lived convective flow in the DS.5 model determines an increase of temperature at the bottom of the first slab (Figures 6.3c3 and d3) with respect to DS.1 and DS.2.5 models (Figures 6.3c1, d1 and c2, d2, respectively) and a decrease of the dip angle toward the new subduction. However, the large-scale mantle flow is limited above the second slab and below the new one. As consequence, in the internal portion of the subduction complex, between the slabs, there is no thermal contribution of mantle flow from external and hotter portions of the domain, as observed in CUM-CUM models. Differently, the large-scale convective cell below the second slab is of the same order of magnitude for all models and comparable with the flow of CUM-CUM.5 model.

Figure 6.4 show the differences in the thermal state between DS.1 (black lines), DS.2.5

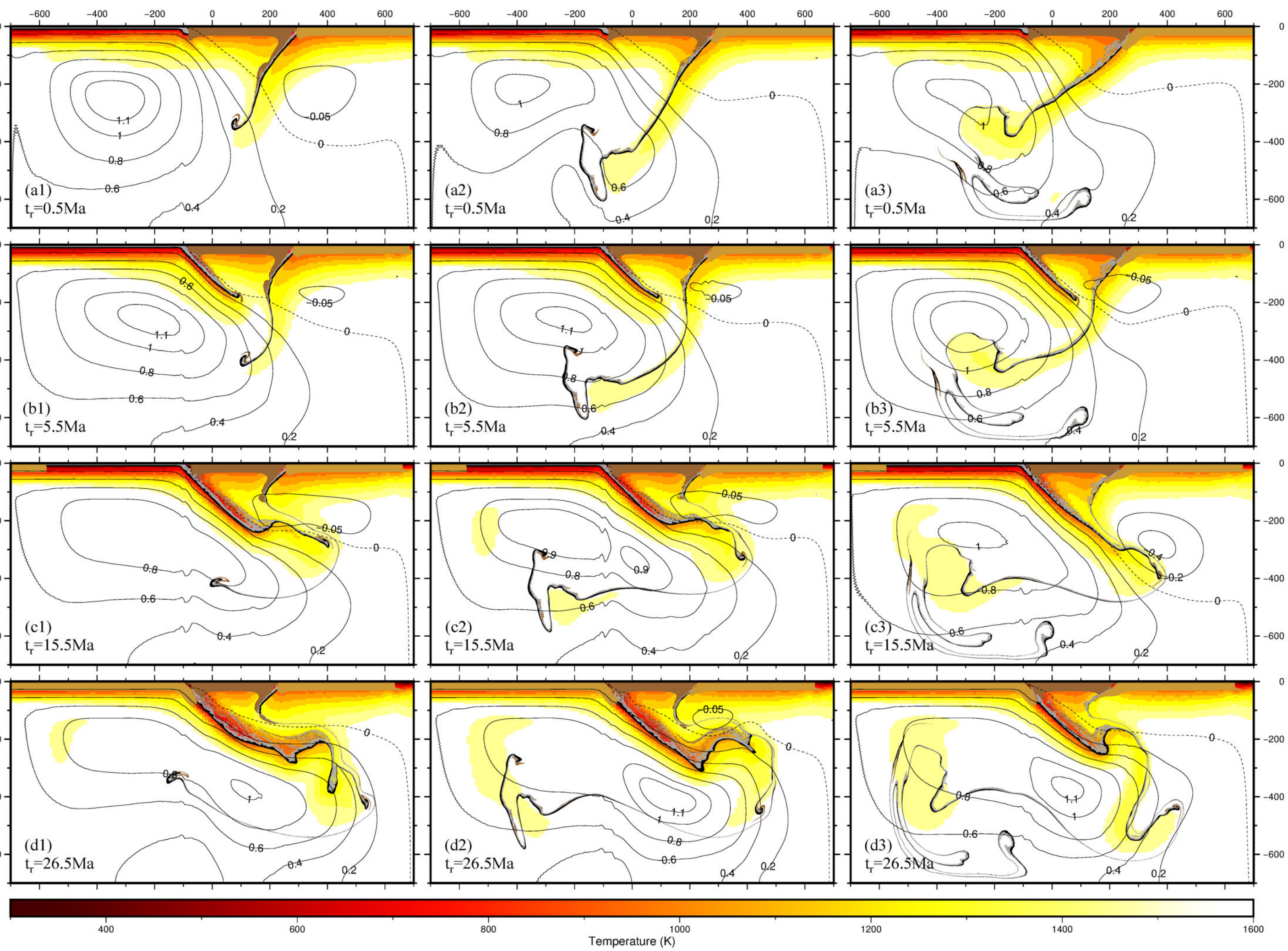

Figure 6.3: Large-scale temperature field (colours) and streamline patterns (solid black lines) for DS.1 (panels a1-d1), DS.2.5 (panels a2-d2) and DS.5 (panels a3-d3) models at 0.5 Ma (panels a_i), at 5.5 Ma (panels b_i), at 15.5 Ma (panels c_i) and at 26.5 Ma (panels d_i) after the beginning of the second active convergence. Black, grey, dark brown and light brown points represent the lower oceanic crust, upper oceanic crust, continental crust of the upper plate, and continental crust of the lower plate, respectively.

(red lines), DS.5 (blue lines) and CUM-CUM.5 models (green lines) in terms of isotherms 800, 1100 and 1300 K. At the beginning of the second subduction the upper plate is still thermally perturbed. In particular, in the micro-continent isotherms 800 K are shallower than in an unperturbed system (continues green line of CUM-CUM.5 model) and there are no differences between DS.1, DS.2.5 and DS.5 models (continues black, red and blue lines, respectively). On the other hand, the first slab is not yet thermally re-equilibrated, as shown by the depression of isotherms 1100 and 1300 K (dotted and dashed lines in Figures 6.4a and b). Comparing the isotherm 1100 K of DS.1, DS.2.5 and of DS.5 model, one can see that in the early stages DS.5 model is the coldest, while DS.1 is the warmest. This is the consequence of the thermal state at the end of the first subduction, which is colder for higher velocities, as described in Chapter 3.3.

Despite of the colder thermal state in correspondence of the first slab, the isotherms 800 and 1100 K are very similar in the slab and in the internal portion of the wedge for all models during the early stages of evolution. In fact, differences in the thermal states of the models are enlightened only by isotherm 1300 K, that show a colder thermal state for DS.1, DS.2.5 and DS.5 models with respect to CUM-CUM.5 model (dotted lines in Figure 6.4b). Isotherm 800 K shows only a slight difference inside the slab after 5.5 Ma, when it is slightly deeper in model DS.1 with respect to DS.2.5 and DS.5 models (continues black line in Figure 6.4b). However, it begins to clearly differentiate inside the slab after 15.5 Ma of evolution (continues lines in Figure 6.4c), when isotherm 800 K is the deepest in model DS.1 and the shallowest in DS.5 and CUM-CUM.5 models. Further differences can be observed at the collision (continues lines in Figure 6.4d), when DS.5 model is colder than CUM-CUM.5 model but warmer than DS.1 and DS.2.5 models, and DS.2.5 model is the coldest. In the same way, 1100 K isotherm begins to show differences in the portion of the wedge close to the new subduction at approximately 15.5 Ma (dashed lines in Figure 6.4c), with a colder thermal state for DS.1, DS.2.5 and DS.5 models. The colder thermal state in the wedge observed in DS.1, DS.2.5 and DS.5 models with respect to CUM-CUM.5 model could be related to the lack of heat supply due to the mantle flow, which in case of double subductions does not reach the portion of the wedge close to the second slab. In correspondence of the doubled crust related to the first continental collision, isotherm 1100 K is shallower in model DS.1, DS.2.5 and DS.5 models with respect to the isotherm in a non-thickened crust, because of the higher energy produced by radioactive decay (dashed lines in Figures 6.4c and d).

The dynamics in the wedge is comparable to the dynamics observed for CUM-CUM models (Figure 3.8), with slightly differences due to the lower temperatures inside the slab predicted in DS.1, DS.2.5 and in DS.5 models (Figure 6.5). In fact, the hydrated area is more extended in DS.1 and in DS.2.5 models with respect to DS.5 model (yellow area in Figure 6.5), because of the colder thermal state and the consequent larger portion of mantle wedge in which the serpentine in stable. Differences in the extension of the

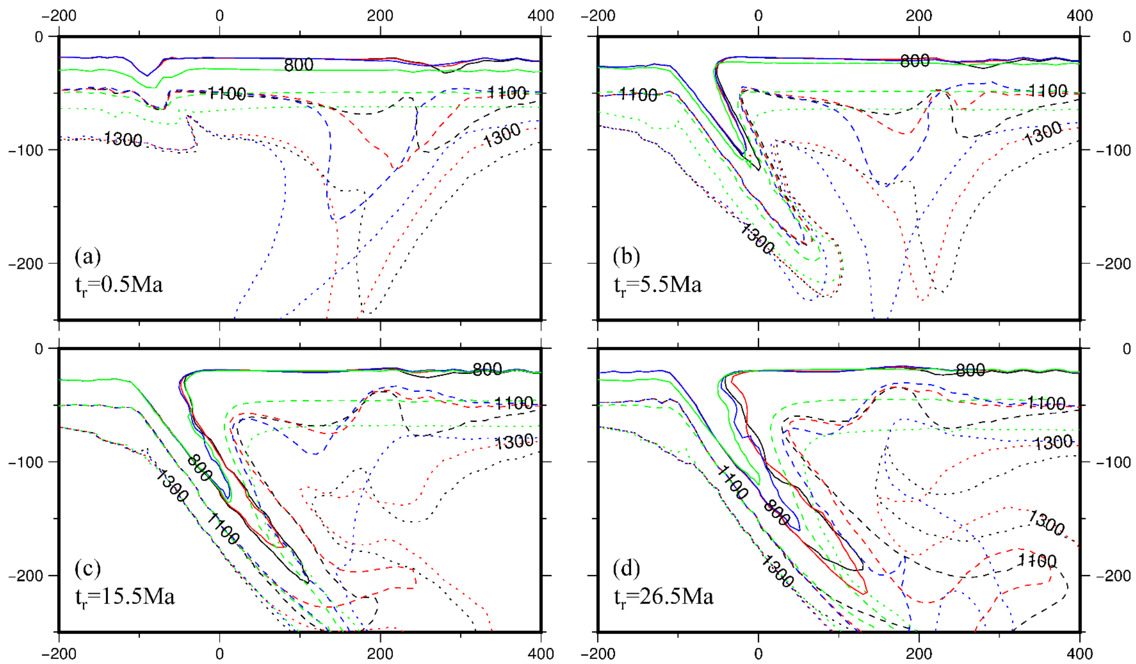

Figure 6.4: Thermal configurations predicted by the DS.1 (black lines), DS.2.5 (red lines), DS.5 (blue lines) and CUM-CUM.5 models (green lines) in terms of isotherms 800 K (continues lines), 1100 K (dashed lines) and 1300 K (dotted lines) at different time steps during the oceanic subduction phase: at 0.5 Ma (panel a), at 5.5 Ma (panel b), at 15.5 Ma (panel c) and at 26.5 Ma (panel d).

hydrated area are more evident at the end of the subduction, when differences of the thermal conditions in the slab are more pronounced (Figures 6.5b, d and f).

After the collision, the large-scale dynamics shows a decrease in the intensity of the convective flow, below the second subducted slab, of approximately two order of magnitude (Figure 6.6), for all models. On the other hand, above the slab the activation of a feeble convective cell occurs, of the same order of magnitude, that decrease its intensity during the post-collisional evolution. The combined action of these two large-scale convective cells determines the increase of the dip angle of the deep portion of both the slabs (Figures 6.6b, d and f). At the same time, both the subducted portion of the continental crust of the lower plate and the recycled material in the wedge rise to shallower depths, because of the lower density of the continental crust with respect to the mantle.

During the post-collisional phase, the portion of the slab characterised by temperatures below 800 K thermally re-equilibrates by the first 10 Ma, as shown by the isotherms 800 K that do not have differences between DS.1, DS.2.5, DS.5 and CUM-CUM.5 models (continues lines in Figure 6.7a). Differently, isotherms 1100 K have different maximum depths for the models until the last stages of the evolution. In particular, isotherm 1100 K reach a depth of approximately 150 km in DS.1 model, more than 150 km in DS.2.5 model, of approximately 100 km in DS.5 model and of less than 100 km in CUM-CUM.5 model (black, red, blue and green dashed lines in Figure 6.7b, respectively). The slower re-equilibration and the final colder thermal state of DS.2.5 model and, to a lesser extent,

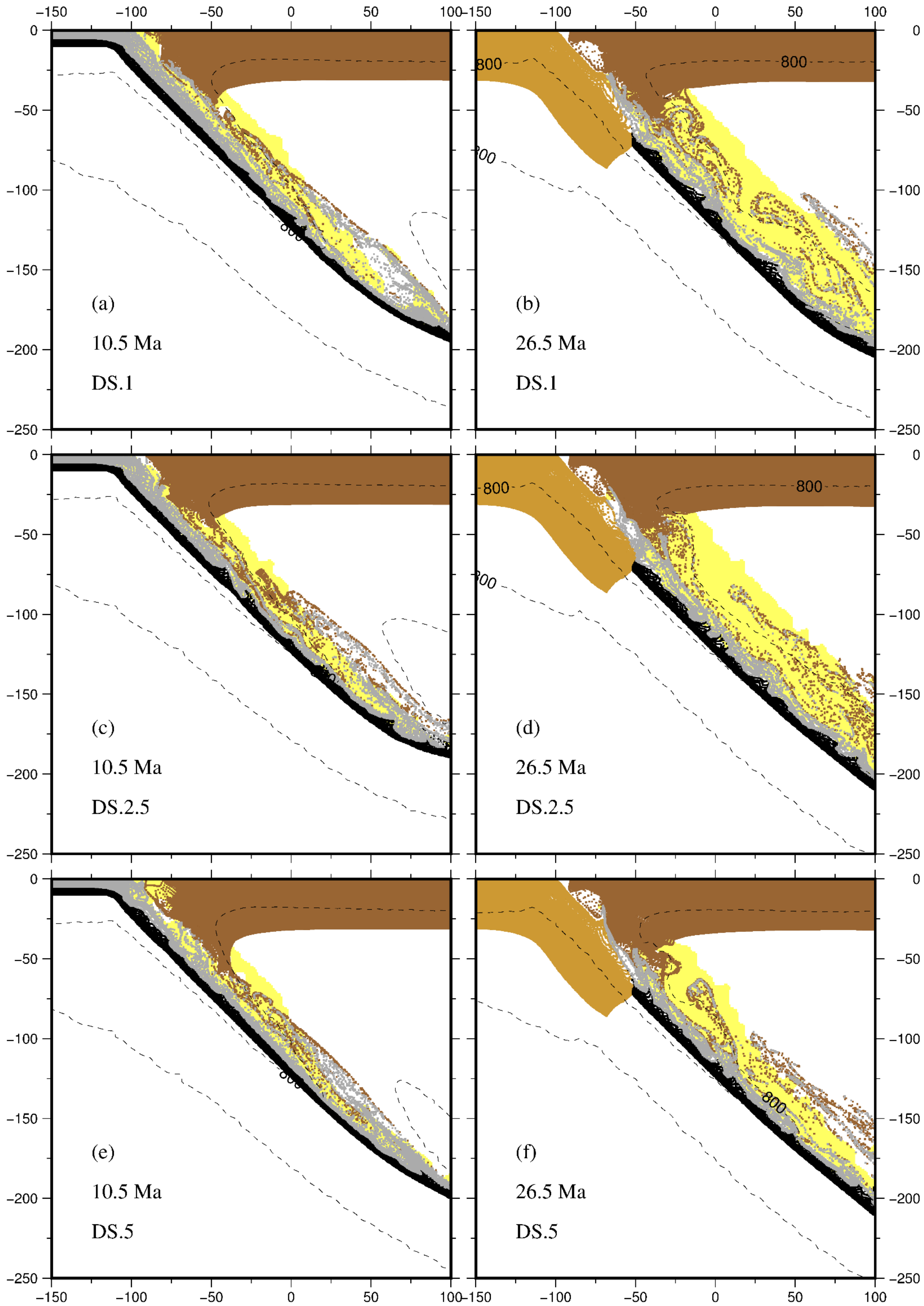

Figure 6.5: Temperature field in terms of the 800 K and 1300 K isotherms (dashed black lines) surrounding the wedge area for the DS.1 model (panels a and b), DS.2.5 model (panels c and d) and for the DS.5 model (panels e and f) at different times. Panels a, c and e show models at 10.5 Ma after the beginning of active convergence; panels b, d and f show models at 26.5 Ma after the beginning of active convergence. The yellow areas represent the hydrated wedge domains. Black, grey, dark brown and light brown points represent the lower oceanic crust, upper oceanic crust, continental crust of the upper plate, and continental crust of the lower plate, respectively.

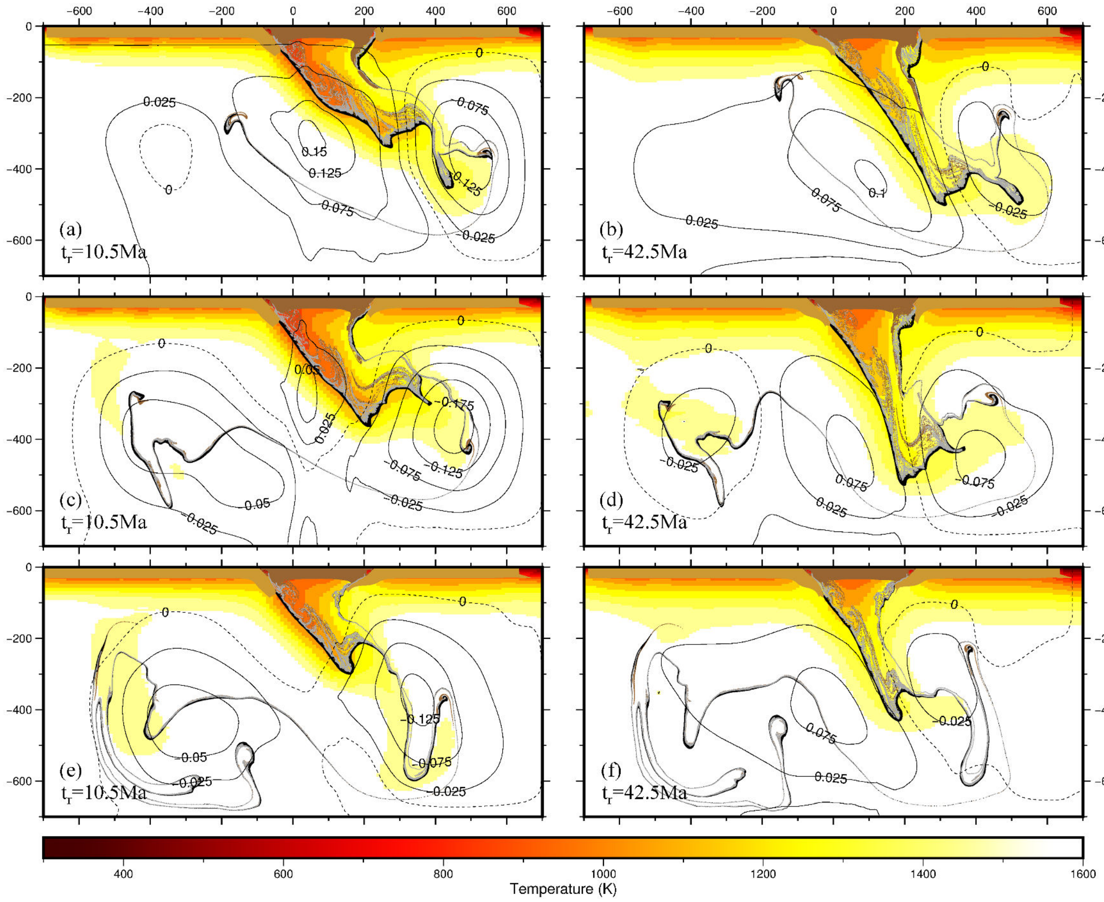

Figure 6.6: Large-scale temperature field (colours) and streamline patterns (solid black lines) for DS.1, (panels a and b), DS.2.5 (panels c and d) and DS.5 (panels e and f) models at 10.5 Ma (panels a, c and e) and at 42.5 Ma (panels b, d and f) after the second continental collision. Black, grey, dark brown and light brown points represent the lower oceanic crust, upper oceanic crust, continental crust of the upper plate, and continental crust of the lower plate, respectively.

of DS.1 and DS.5 models are related to the lower temperatures predicted at the end of the oceanic subduction.

6.3 Comparison with natural P-T estimates

The western Alps (considering the Alpine convergence) represent a clear example of a metamorphic belt related to a cold subduction zone, while the French Central Massif is an example of a Silurian metamorphic evolution in relation with hotter subduction system (*Lardeaux*, 2014a). This is in agreement with the thermal states predicted by DS.1, DS.2.5 and DS.5 models with respect to CUM-CUM.5 model. In fact, the second subduction is always colder than the first subduction, irrespective of the velocity of subduction. In particular, DS.1 and DS.2.5 models are characterised by colder second subductions, while the first subduction is the hottest for DS.1 model, as consequence of the lowest velocity. However, DS.1 model does not show recycling of subducted crust during the

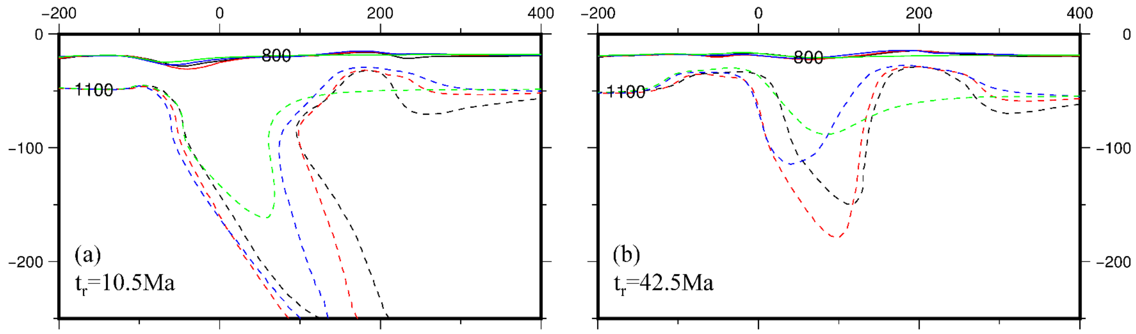

Figure 6.7: Thermal configurations predicted by the DS.1 (black lines), DS.2.5 (red lines), DS.5 (blue lines) and CUM-CUM.5 models (green lines) in terms of isotherms 800 K (continues lines) and 1100 K (dashed lines) at different time steps during the post-collisional phase: at 10.5 Ma (panel a and at 42.5 Ma (panel b).

first subduction, as consequence of the higher temperatures. Differently, DS.5 model has ocean related to the first subduction more wide to that proposed by paleo-geographic reconstructions. Therefore, DS.2.5 model results to be the most adequate to make a comparison with natural P-T estimates of the Variscan metamorphism.

6.3.1 First subduction-collision cycle

In DS.2.5 model the first oceanic subduction corresponds to a north verging oceanic subduction, spanning between 425 and 373.5 Ma, and followed by a stage of collision lasting 10 Ma, before the beginning of the second subduction. This intermediate post-collisional stage span between 373.5 and 363.5 Ma.

Alps

A general improvement in the agreement with natural P_{max}-T_{Pmax} of the Alps can be observed during the first subduction of DS.2.5 model (Figure 6.8a) with respect to the oceanic subduction phase of the CUM-CUM.5 model (Figure 5.2a). In particular, DS.2.5 model shows an increase in the correspondence with data Hv6, Hv7, Hv11, Pv12 and Av9, while a worsening is observed only for datum Av8. In models DS.2.5, at the collision, datum Hv11 fits both with continental markers in the wedge and with continental markers in the subducted portion of the lower plate (Figure 6.9f1), while in model CUM-CUM.5 it fitted only with continental subducted markers of the lower plate (Figure 5.4f). Figures 6.9a1-f1 show that all the data that improve their fit have correspondence with markers in the portion of the wedge characterised by temperatures higher than 800 K. Therefore, the improvement of the fit is due to the higher temperatures characterising slow subductions, both in the slab and in the mantle wedge. In the same way, datum Av8 worsens its fit because it is characterised by low temperature and high pressure and none of the markers of the slab record appropriate P-T conditions. On the other hand, none of the data with correspondence at the bottom of the continental crust of the upper plate show differences in the fitting between the models. So, the velocity of subduction does not influence the thermal state in the upper plate but only in the slab and in the mantle wedge.

French Central Massif

An improvement occurs also by the comparison of natural P_{max}-T_{Pmax} estimates with the first subduction of DS.2.5 model (Figure 6.8b), with respect to the comparison with the subduction phase of CUM-CUM.5 model (Figure 5.2b). In fact, data Li3, LB1, Ro1, Ro2, Ro3, Ar1, Mc1, PA1 and ML2 have correspondences with DS.2.5 model for longer period and datum Li6 shows an increase in the number of markers that show the agreement. In particular, datum Li6 improves its correspondences because larger portion of the slab are characterised by temperatures above 800 K at high pressure. In fact, there is a change of position of the area with P-T conditions compatible with datum Li6, from the external portion of the wedge in CUM-CUM.5 model (Figure 5.7b), to the internal portion of the slab (Figure 6.9b2). As observed for the data of the Alps, all the data of the French Central Massif that improve their fit with the model are characterised by high or intermediate-to-high P/T ratios and show correspondences with oceanic and continental subducted markers. So, none of the markers that fit at the bottom of the continental crust of the upper plate, which are characterised by intermediate P/T ratios, improve their agreement. With the exception of data LB1 and Ro2 that are characterised by the lowest temperatures (Figure 5.3e), all the other data fit with CUM-CUM.5 model only at the beginning of the subduction (Figure 5.7a), then the system cool and it does not show compatible P-T conditions anymore. Differently, a slower subduction, characterised by higher temperatures, shows correspondences with these data for longer periods with subducted and recycled markers in the wedge (Figure 6.9a2-f2). At the collision, data Ar1, Mc1, Ro2 and Ro3 have correspondences with subducted markers of the lower plate and continues to fit also with markers in the wedge (Figure 6.9f2), differently from correspondences only with the lower plate shown in model CUM-CUM.5 (Figure 5.7f). No differences in the correspondences can be observed between the first gravitational phase of DS.2.5 model and the early stages of the post-collisional phase of CUM-CUM.5 model, both for data of the Alps and for data of the French Central Massif.

6.3.2 Second subduction-collision cycle

The second oceanic subduction phase lasts 26.5 Ma and it corresponds to a south verging subduction running between 363.5 and 337 Ma. It is followed by a final post-collisional phase lasting 42 Ma, between 337 and 295 Ma.

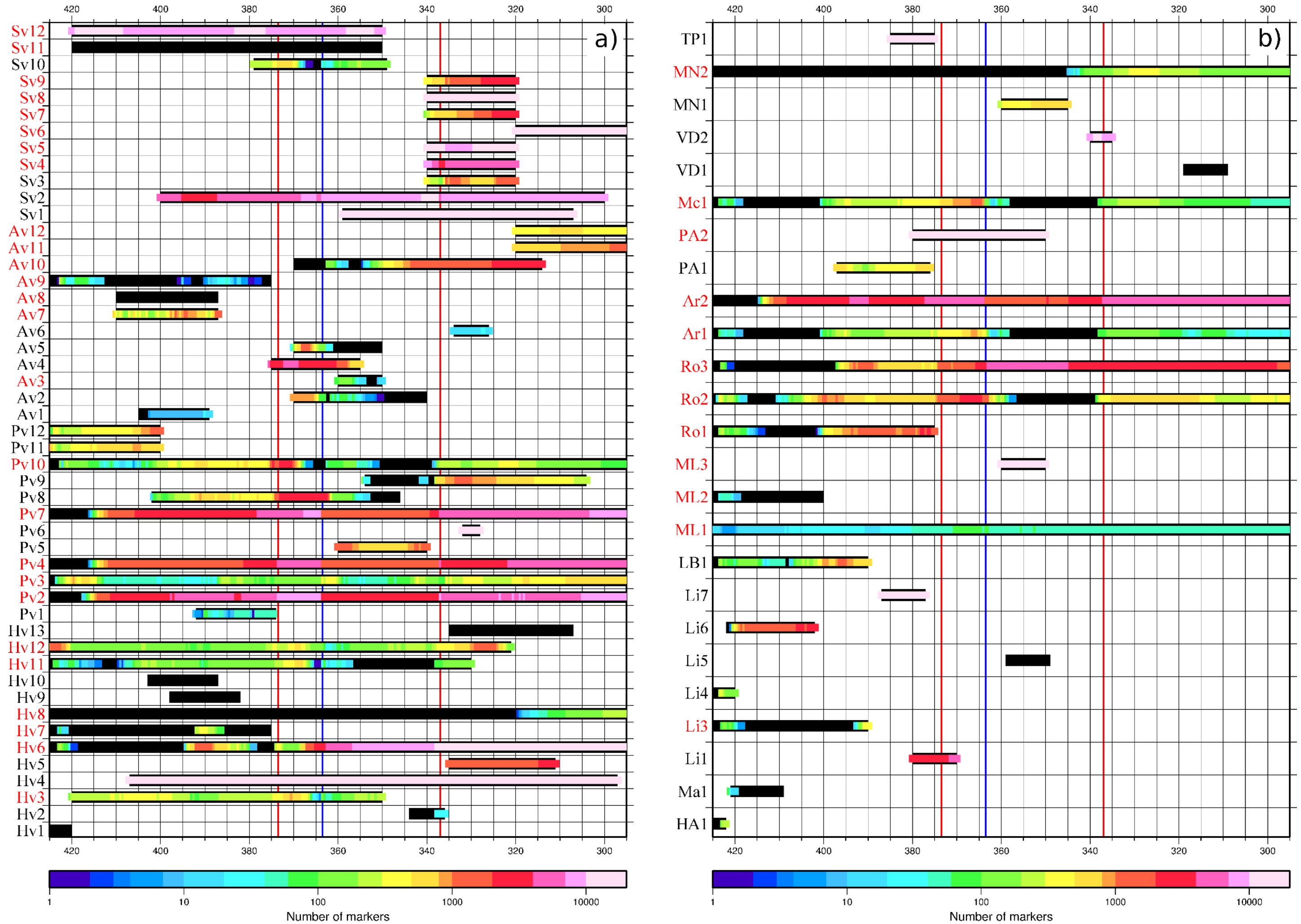

Figure 6.8: Fitting of natural P_{max}-$T_{P_{max}}$ estimates of the Alps (panel a) and of the French Massif Central (panel b) with the DS.2.5 model. Black bars represent the age of the natural P-T estimates, while colour bars represent the fitting with the markers of the model. Different colours represent the number of markers showing the agreement. Red vertical lines identify the occurrence of collisions and blue vertical line identifies the beginning of the second subduction. Keys are the same of Table B.1 and Table B.2. Red keys represent geological ages, black keys represent radiometric age.

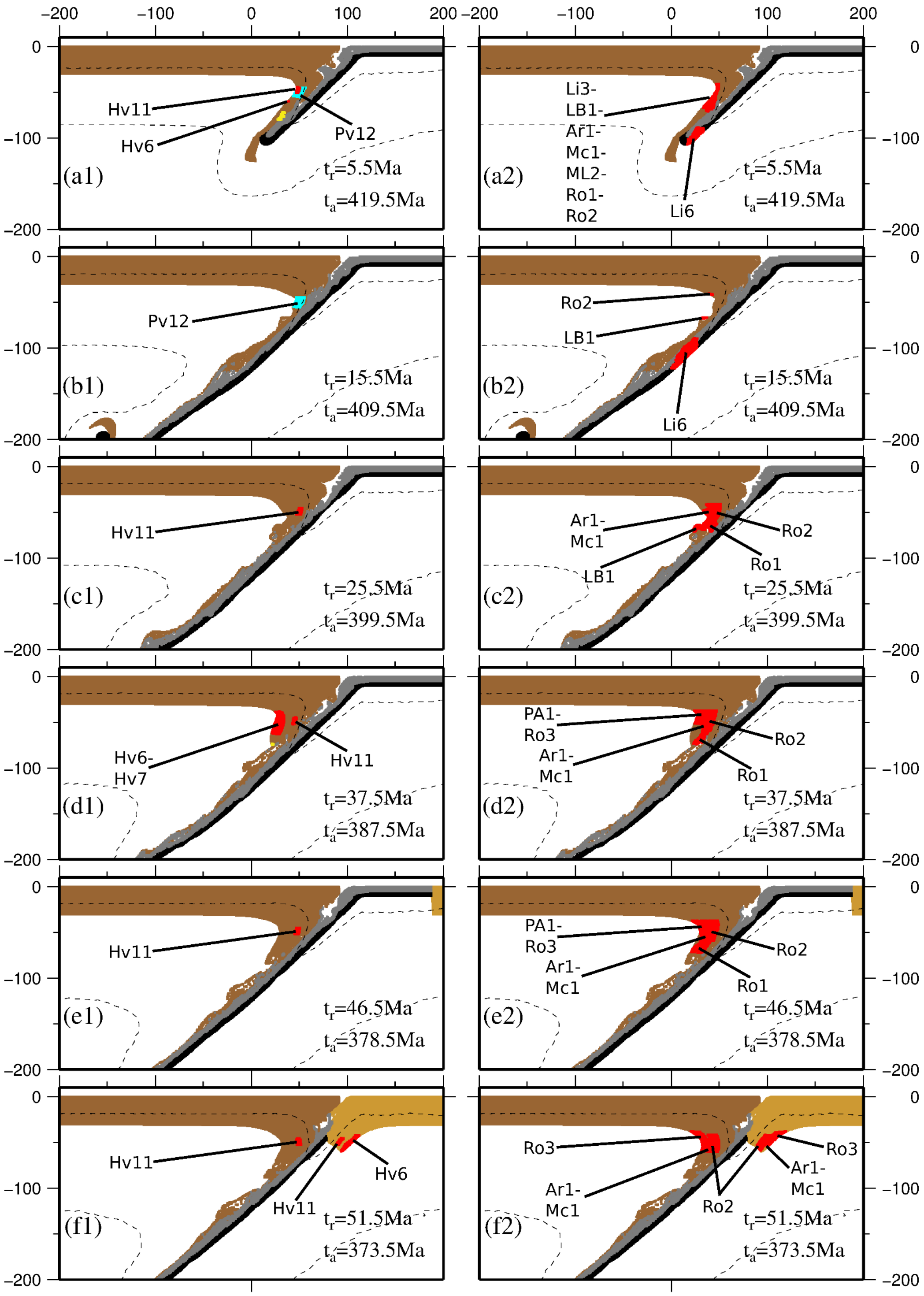

Figure 6.9: Comparison between DS.2.5 model and P_{max}-T_{Pmax} estimates from the Alps (panels a1-f1) and from the French Central Massif (panels a2-f2) for different times during the first oceanic subduction phase. Dotted lines indicate 800 K and 1500 K isotherms. In panels a1-f1, red dots indicate fitting with data from the Helvetic domain, light blue dots fitting with data from the Pennidic domain, yellow dots fitting with data from Austroalpine domain and blue dots indicate fitting with Southalpine domain; in panels a2-f2, red dots indicate fitting with data from the French Central Massif.

Alps

Comparing the correspondences of data from the Alps during the second oceanic subduction of DS.2.5 model (Figure 6.8a) with the correspondences during the equivalent period of post-collisional phase of CUM-CUM.5 model (between 363.5 and 337 Ma in Figure 5.2a) an improvement in the agreement can be observed. In particular data Hv2, Hv3, Hv11, Pv9, Pv10, Av3, Av10 and Sv10 have a better agreement with the model, while only datum Pv8 slightly worsens its agreement, being characterised by a high P/T ratio with a temperature over 1000 K. The worsening of the fit of datum Pv8 is due to the colder thermal state predicted by the model in the slab during the second oceanic subduction, with respect to the thermal conditions recorded in the external and deep portion of the wedge in CUM-CUM.5 model, both during the oceanic subduction and during the post-collisional phase. However, datum Pv8 shows an agreement with subducted markers during the early stages of the second subduction of DS.2.5 model (Figure 6.10a1). Amongst the data that improve their fit, the only one characterised by an intermediate P/T ratio is Av10. It begins to fit with the model approximately 10 Ma earlier than in CUM-CUM.5 model (Figures 6.10b1-c2), but it fits only in the shallower portions of the thickened crust of the first subduction (as in CUM-CUM.5 model), while it has no correspondences with markers involved in the second subduction. In CUM-CUM.5 model, datum Pv10 ceased to fit after few Ma of the beginning of the post-collisional phase, after the thermal re-equilibration of the slab. Differently, in DS.2.5 model, datum Pv10 has correspondences with subducted and recycled markers in the external portion of the wedge until 10 Ma from the beginning of the second subduction (Figures 6.10a1 and b1). Furthermore, it fits again starting from the second continental collision, at the beginning with continental markers in the subducted portion of the lower plate (Figures 6.10e1 and a2), and later also with continental markers in the wedge, until the end of the post-collisional evolution (Figures 6.10b2-e2). In the same way, datum Pv9 fits with model DS.2.5 from the beginning of the collision to the end of the evolution (Figures 6.10e1-d2), while datum Pv9 has not correspondences with CUM-CUM.5 model. Data Av3, Hv2, Hv3 and Hv11 display correspondences with simulated P-T paths compatible with the beginning of the subduction between 340 and 380 Ma, in agreement with the second subduction simulated in the DS.2.5 model, and all of them improve their fit. In fact, they are characterised by high P-T ratios and they fit with markers involved in the second subduction. In particular, Av3 and Hv3 and Hv11 have correspondences with subducted markers in the shallow portion of the wedge during the early stages (Figures 6.10a1 and b1), while Hv2 fits with continental markers in the subducted portion of the lower plate at the collision (Figure 6.10e1). In additon, datum Hv11 shows correspondences also with continental markers of the lower plate in the early stages of the post-collisional phase (Figures 6.10e1 and a2). Datum Sv10 has some correspondences with the model in the shallow portion of the wedge during the early stages, improving its fit (Figures 6.10a1 and b1).

Datum Av4 shows a slight improvement in the number of markers that show an agreement because there are two areas characterised by compatible P-T conditions. In fact, in CUM-CUM.5 model Av4 fitted only with continental markers in the wedge at the beginning of the post-collisional phase, while in DS.2.5 model it fits both with continental markers in the subducted portion of the lower plate, related to the first subduction, and with continental subducted markers in the wedge of the second subduction (Figure 6.10a1). With respect to datum Av4, characterised by a high P/T ratio, data Av2 and Pv8 have an higher P/T ratio, and they only fit with deep subducted markers in the wedge related to the second subduction (Figures 6.10a1 and b1) but they do not fit anymore with the first subduction, as occurred in CUM-CUM.5 model. During the oceanic subduction, datum Hv6 shows the same correspondence observed in CUM-CUM.5 model, in the deep portion of the doubled crust of the first subduction (Figures 6.10a1-e1), while after the collision it fits with markers in the thickened crust of both the subductions (Figures 6.10a2-e2). Datum Hv5 shows the same correspondences than in CUM-CUM.5 model, in the shallow portion of the thickened crust (Figures 6.10a2-c2). Data Hv4, Pv2, Pv4, Pv7 and all data from the Southalpine domain, with the exception of Sv10, are characterised by intermediate P/T ratios and fit at the entire bottom of the non-subducted continental crust, both of the upper and of the lower plates (Figures 6.10a1-e2).

French Central Massif

Data from the French Central Massif do not have differences in the correspondences during the second oceanic subduction with DS.2.5 model with respect to CUM-CUM.5 model. In fact, there are no data that fit with the second slab during subduction, with the exception of datum Ro2 during the early stages of the evolution, with markers in the external portion of the wedge (Figure 6.11a1). However, it does not fit with subducted markers belonging to the first slab, conversely to what occurred in CUM-CUM.5 model. On the other hand, data Ro2, Ar1 and Mc1, all characterised by high P/T ratios, fit with the second slab starting from the second continental collision, showing an improvement in the correspondences with respect to CUM-CUM.5 model. These data fit only with continental markers of the subducted portion of the wedge until 10 Ma of post-collisional evolution (Figures 6.11e1-b2), then they have correspondence also with recycled markers in the wedge (Figures 6.11c2-d2).

Differently, data characterised by intermediate P/T ratios (ML3, PA2, Ro3, MN1, MN2, Ar2) do not show differences in the correspondences both during the second oceanic subduction and during the second post-collisional phase. In particular, data ML3 and PA2 continues to fit at the bottom of the continental crust of the upper plate and at the bottom of the crust of the lower plate related to the first subduction (Figures 6.11a1 and

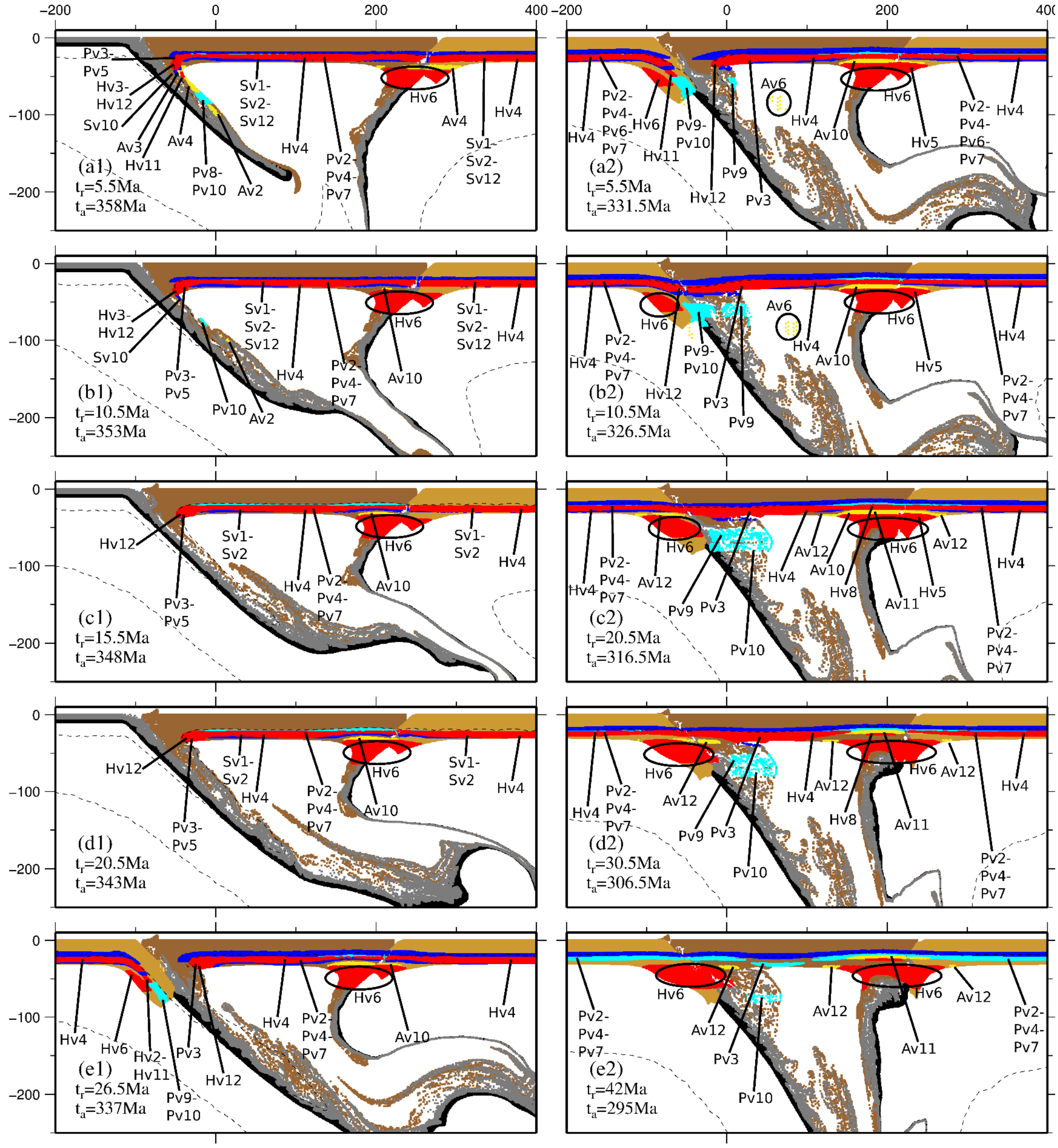

Figure 6.10: Comparison between DS.2.5 model and P_{max}-T_{Pmax} estimates from the Alps for different times during the second oceanic subduction phase (panels a1-f1) and during the second post-collisional evolution (panels a2-f2). Dotted lines indicate 800 K and 1500 K isotherms. Red dots indicate fitting with data from the Helvetic domain, light blue dots fitting with data from the Pennidic domain, yellow dots fitting with data from Austroalpine domain and blue dots indicate fitting with Southalpine domain.

b1). In addition, data Ro3, MN1 and MN2 have correspondences only in the portion of the thickened crust related to the first subduction below a depth of 30 km, as occurred in CUM-CUM.5 model (Figures 6.11a1-e2). Datum Ar2 had correspondences with CUM-CUM.5 model at the bottom of the crust during the first half of the post-collision phase and nearby the doubled crust during the second half of evolution. In the comparison with DS.2.5 model, it shows the same correspondences in relation of the first slab (Figures 6.11a1-e1) and, during the second post-collisional phase, also with the thickened crust due to the second slab (Figures 6.11a2-e2).

In general, data of the French Central Massif show a worsening in the fit during the second subduction with respect to the first subduction. This means that a hot subduction is necessary to develop P-T conditions compatible with these data, or that a refinement and an amount improvement of radiometric dating could sensibly refine the comparison between natural data and model predictions.

6.4 Discussion

Three models of double subduction, characterised by different velocities of the first subduction, have been developed, to analyse the impact of a perturbed system on the activation and evolution of an oceanic subduction. Differences of the thermal state inside the slab for different velocities of the first subduction confirm the conclusion inferred in Chapter 3. In fact, a decrease of velocity determines an increase of temperatures because of lesser amount of cold material subducted for same time periods. In particular, temperatures in the slab and in the mantle wedge for a velocity of 1 cm/yr are too high to have P-T conditions compatible with the stability field of serpentine and the mantle wedge can not be hydrated. As a consequence, there are not activation of small-scale convective cells and recycling of subducted material.

In all models, at large scale, there is an intense mantle flow above the second slab, as observed in CUM-CUM models. This is due to the presence of the first subduction, which prevent the activation of the large-scale convective cell. The lack of the mantle flow up to the external boundaries of the hydrated area, and the consequent absence of its heat supply, determines a decrease of temperatures in the mantle wedge, in the portion between the slabs of the two successive subductions. Moreover, also the temperature inside the second slab is lower than in CUM-CUM.5 model. In particular, DS.1 and DS.2.5 models are characterised by a thermal state colder than DS.5 model. During the second post-collisional phase there is an increase of dip angle of both the slabs.

Considering both paleo-geographic reconstructions of the Variscan orogeny and metamorphic evidences, the more appropriate model to compare the predicted P-T with natural P-T estimates is DS.2.5 model. In fact, DS.5 model is characterised by a wide ocean involved in the first subduction (2500 km), while paleo-geographic reconstructions suggest

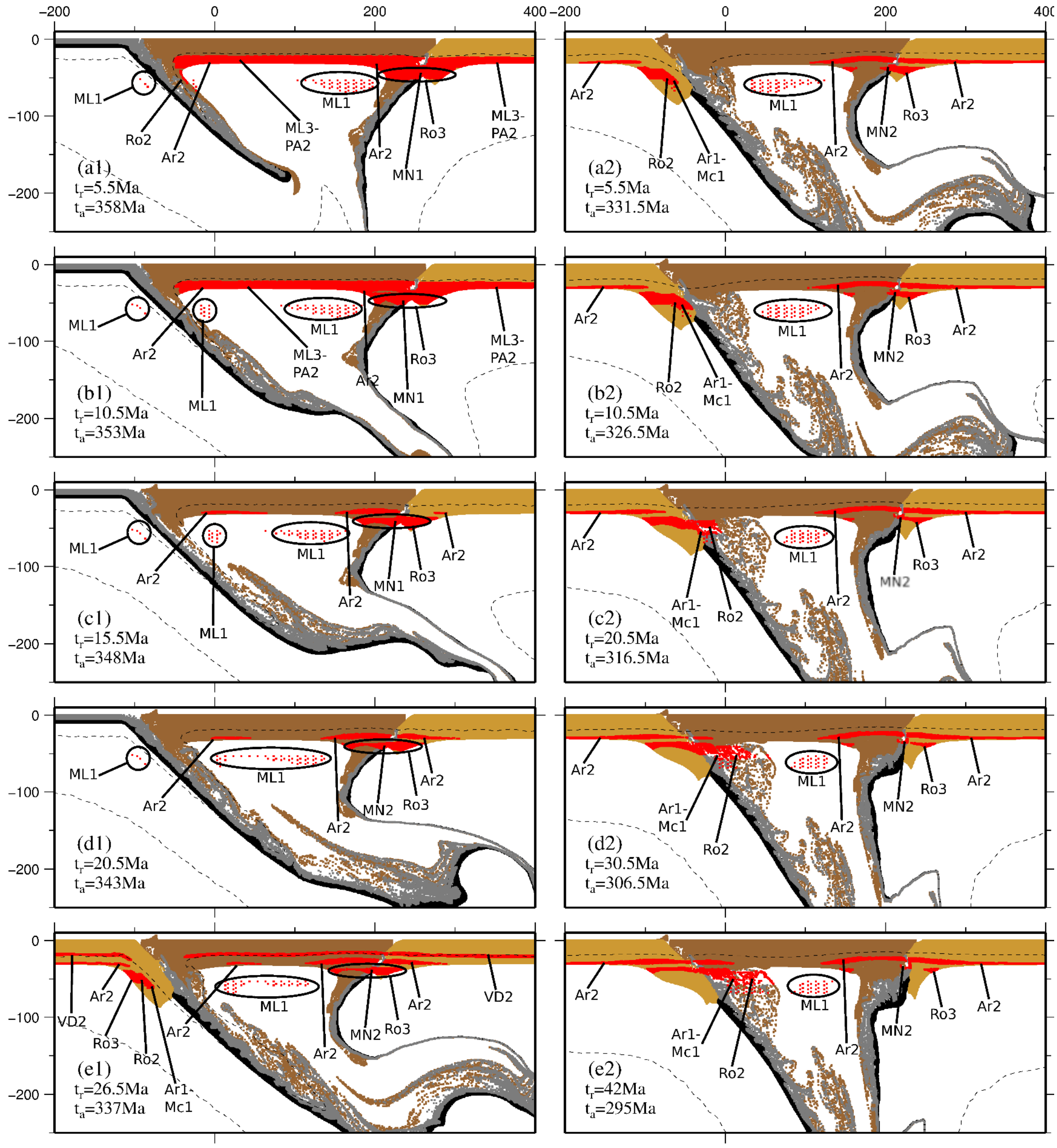

Figure 6.11: Comparison between DS.2.5 model and P_{max}-T_{Pmax} estimates from the French Central Massif for different times during the second oceanic subduction phase (panels a1-f1) and during the second post-collisional evolution (panels a2-f2). Dotted lines indicate 800 K and 1500 K isotherms. Red dots indicate fitting with data.

a dimension of max 1000 km. On the other hand, DS.1 model does not show recycling of subducted material related to the first subduction.

DS.2.5 model shows a general improvement in the agreement with natural data, both from the Alps and from the French Central Massif. All the data that improve their fit during the first subduction of the model have an estimated temperature above 800 K and have correspondences with subducted and recycled markers in the external and warmer portion of the mantle wedge. This because of the higher thermal state predicted in the slab for lower velocities. In particular, almost all data from the French Central Massif show better correspondences with the model, while an improvement for only few data of the Alps can be observed. On the other hand, during the second subduction a lot of data from the Alps, all of them characterised by high P/T ratios, improve their fit, while none of the data from the French Central Massif show differences in the correspondences with respect to CUM-CUM.5 model. Therefore, a slow and hot subduction is needed to develop P-T conditions in the wedge compatible with data from the French Central Massif. Differently, data from the Alps are characterised by different metamorphic gradients and some of them have better correspondences with a hot subduction (for example datum Pv12), while others with a cold subduction (for example data Hv2 and Av3).

The fit of data from the Alps with the first and the second subduction is in agreement with results obtained by the comparison with natural P-T paths. In fact, paths of markers compatible with Alpine data show that two time ranges for the beginning of the subduction can be identify: one between 350 and 380 Ma and another between 400 and 450 Ma, in agreement with the available radiometric dating distribution, with the ages > 390 Ma concentrated in Helvetic and Penninic domains, as already evinced by *Spalla et al.* (2014). Differently, modelled paths compatible with data from the French Central Massif suggest only one subduction beginning at approximately 400-450 Ma and their lack of fit with the second subduction support this result. For example, data Hv2 and Av3 show better correspondences with the second subduction and their paths agreed suggesting a more recent subduction, while data Pv12 and PA1 have a better fit with a hot subduction and its paths suggested an older subduction.

Chapter 7

Conclusions

In a first phase, this work focuses on the effects of the hydration of mantle wedge and of shear heating on the thermo-mechanics of a subduction complex. The introduction of the hydration determines the activation of small convective cells during the early stages of active subduction, because of the low viscosities associated to the serpentinisation of the wedge, favouring the recycling and the partial exhumation of subducted oceanic and continental crust. Differently, the introduction of shear heating slightly affects the thermal state in the hydrated area, while it is more effective in the slab and in the non-hydrated mantle. In fact, in the hydrated wedge the decrease of the viscosity is greater than the increase of the strain rates, with a consequent low production of energy by shear heating. In the models characterised by both the hydration of the wedge and the shear heating there is a correlation between the velocity of subduction and the dimension of the hydrated area. In fact, the higher the velocity, the larger the hydrated domain. This is due to the lower temperatures that characterise the internal portion of the slab and the resulting thermal depression at the bottom of the hydrated area. Lower temperatures related to higher velocities of subduction are due to the larger amount of cold lithosphere subducted in the same time.

During the pure gravitational phase, the slab progressively warms as consequence of the thermal re-equilibration of the system. Moreover, the recycling of large amount of continental crust during the oceanic subduction determines the doubling of the crust, with a consequent increase of energy due to radiogenic decay. This additional heat supply produces a thermal state warmer than in a non-perturbed system. The progressive warming of the system generates a thermal environment in which the markers record P-T conditions compatible with a Barrovian metamorphism. In all models, the highest T_{maxC} values are reached at the end of the evolution.

The P-T conditions predicted by the models show that contrasting P-T conditions can exist simultaneously in different portions of the same subduction systerm. In general, intermediate P/T ratios can be developed at the bottom of the continental crust of the upper plate and in the shallow and most external portion of the hydreated wedge. On the other hand, high P/T ratios can be recorded by the markers during their cycles of subduction and exhumation, in the internal portion of the wedge at different depths. Differences of temperature predicted in various portions of the wedge determine different thermal gradients recorded by the markers during the evolution. The coexistence of metamorphic facies characterised by contrasted P-T gradients can be observed also during the early stages of the pure gravitational evolution. In fact, the warming of the subduction complex does not occur suddenly, and some Ma are necessary to thermally re-equilibrate the slab and the wedge with the surrounding warmer mantle.

The coeval existence of domain characterised by different P-T conditions is underlined also by the comparison with natural P-T estimates. In fact, data characterised by intermediate P/T ratios and data characterised by high P/T ratios show correspondences in different areas of the model at the same time. In particular, model predictions agree with data with intermediate P/T ratio at the bottom of the crust of the upper plate, while data characterised by high P/T ratios fit with subducted oceanic and continental markers in different portions of the wedge. However, different conditions can be developed also in the wedge. In fact, data with higher P/T ratios are compatible with P-T conditions in the more internal and deeper portion of the wedge.

The introduction of an upper layer of air, allowing free movements of the upper plate, produces an increase in the intensity of the mantle flow. The consequence is an increase of temperature of the system. Furthermore, the activation of shallower small convective cells is observed, favouring the exhumation of subducted material up to very shallow crustal level. The variations induced on the thermal state determine a variation in the comparison between model predictions and natural P_{max}-T_{Pmax} estimates. The increase of temperature during the oceanic subduction phase determines a general improvement of the agreement, especially for data with HT, both characterised by intermediate P/T ratios and characterised by high P/T ratios. In this model P-T conditions compatible with data characterised by Barrovian-type metamorphism can be recorded not only at the bottom of the continental crust but also in the wedge.

The comparison between the simulated P-T paths and successive metamorphic stages preserved by rocks from the Alps and from the French Central Massif supports the possibility to have an evolution of the Variscan orogeny characterised by two opposite subduction. In fact, two periods during which the subduction could begin can be recognised: based on the data from the French Central Massif and on some data from the Helvetic and Pennidic domains, it can be inferred that the subduction begins between 400 and 450 Ma; differently, data from Austroalpine and Southalpine domains of the Alps indicate a possible younger subduction starting approximately between 330 and 380 Ma. These results agree with the hypothesis of two cycles of subduction/collision characterised by opposite polarities, as already proposed by many authors for the evolution of the Variscan orogeny

(*Matte*, 2001; *Faure et al.*, 2005, 2009; *Guillot et al.*, 2009a; *Spiess et al.*, 2010; *Lardeaux*, 2014a).

Three models of double subduction characterised by different velocities of the first subduction have been developed, to analyse the impact of a perturbed system on the activation and evolution of an oceanic subduction. The second slab results to be always colder than the first subduction and models with a lower first subduction have a second slab characterised by lower temperatures. In addition, also the portion of mantle between the two slabs is colder, because the first subduction prevent the mantle flow to reach the hydrated area. The model used for the comparison with natural P-T estimates of the Variscan metamorphism is DS.2.5 model, with a velocity of the first subduction of 2.5 cm/yr. This choice has been made to make the width of the first ocean involved in the subduction compatible with paleo-geographic reconstruction, differently from DS.5 model. During the first subduction the slab is characterised by temperatures compatible with the develop of the hydrated area with the possibility to recycle subducted material, differently from DS.1 model.

As observed for the model with an upper layer of air, the increase of temperature during the first subduction determines an increase in the agreement between model predictions and natural data. In particular all data from the French Central Massif improve their correspondences. On the other hand, during the second colder subduction no data of the French Central Massif fit with model predictions, while data from the Alps sensibly improve their fit. This is in agreement with metamorphic evidences that suggest a hot subduction as cause for the metamorphism of the French Central Massif (*Lardeaux*, 2014a).

Appendix A

Benchmarks

A.1 Benchmark on Runge-Kutta

The implementation of the Runge-Kutta scheme has been tested by means of the classical Zalesak disc test (*Zalesak*, 1979; *Thieulot*, 2014). For this experiment, a disc of radius $R = 0.15$ is centered at location $(x_0, y_0) = (0.5, 0.75)$ of a square domain of size $L_x = L_y = 1$ (Figure A.1a). A grid of 50×50 linear triangular elements has been used to discretised the domain. The markers in the disc area are 50 per element. The velocity field in the domain is prescribed as follows:

- $u(x, y) = 2\pi(y - \frac{L}{2})$
- $v(x, y) = -2\pi(y - \frac{L}{2})$

After a 2π rotation, markers should be back to their initial location. In spite of its simplicity, the Runge-Kutta scheme at first order shows a great accuracy in the determination of the position of the markers during different stages of the rotation (Figures A.1b-e).

A.2 Benchmark on Rayleigh–Taylor instability

The Rayleigh-Taylor instability test consists of two fluids that are placed on each other, with a compositionally lighter layer ($\rho_1 = 1000$) under a thicker denser layer ($\rho_2 = 1010$) (*van Keken et al.*, 1997; *Thieulot*, 2014). The viscosity is $\mu_1 = \mu_2 = 100$. The experiment has been performed in a isothermal 2D domain of $L_x = 0.9142$ and $L_y = 1$, discretised with a grid composed of 40×40 quadratic triangular elements. All parameters are normalised. The markers characterising the fluids are 229458, 1 every 0.002 both in x and in y. The thickness of the lower layer is $y = 0.2$ and the initial deflection of the interface between the layers is $w(x) = 0.02\cos(\frac{\pi x}{L_x})$ (Figure A.2a). No-slip boundary conditions are applied at the top and at the bottom, while free-slip boundary conditions are applied on the

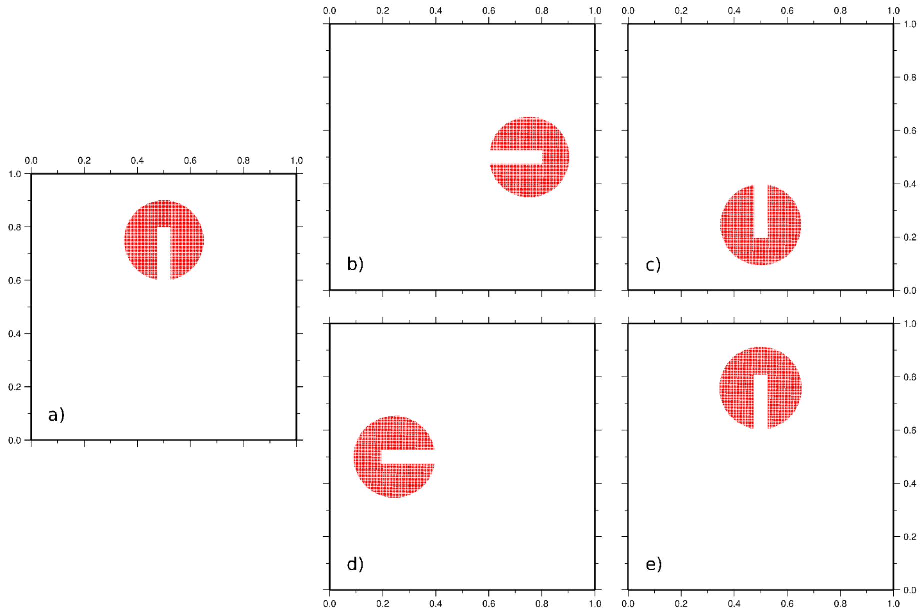

Figure A.1: Initial setup (panel a, $t = 0$) and evolution of the Zalesak disc test at different times. Panel b: $t = \frac{\pi}{2}$; panel c: $t = \pi$; panel d: $t = \frac{3}{2}\pi$; panel e: $t = 2\pi$.

lateral sides. The thermal and compositional Rayleigh number are $R_a = 0$ and $R_c = 1$, respectively. The gravity acceleration is chosen to be 10 m/s^2. The long-wavelength shape of the initial interface determines the rise of the first plume along the left edge of the domain (Figure A.2b) and a second plume follows, rising along the right edge (Figure A.2c). The evolution does not show any artificial mixing at the interface between the layers and the final stage (Figure A.2e) is comparable to that obtained by *van Keken et al.* (1997) (Figure A.2f).

A.3 Benchmark on shear and adiabatic heating

The benchmark test described by *Gerya* (2011) for the shear and the adiabating heating has been carried out to verify the results predicted by the *SubMar* code. In this experiment the continuity and momentum equations have been solved for a buoyancy-driven flow in a purely vertical gravity field characterised by two vertical layers with different density and viscosity: the left layer is characterised by a density of 3200 kg/m^3 and a viscosity of 10^{20} Pa·s, while the right layer is characterised by a density of 3300 kg/m^3 and a viscosity of 10^{22} Pa·s. The model domain is 1000×1500 km with a regular grid characterised by 1200 triangular elements. Free slip conditions are applied along all boundaries; a constant temperature of 1300 K is fixed in the whole domain and the thermal expansion is assumed equals to $3 \cdot 10^{-5}$ 1/K. The gravity acceleration is chosen to be 10 m/s^2.

The difference in viscosities characterising the two layers generates a viscous flow

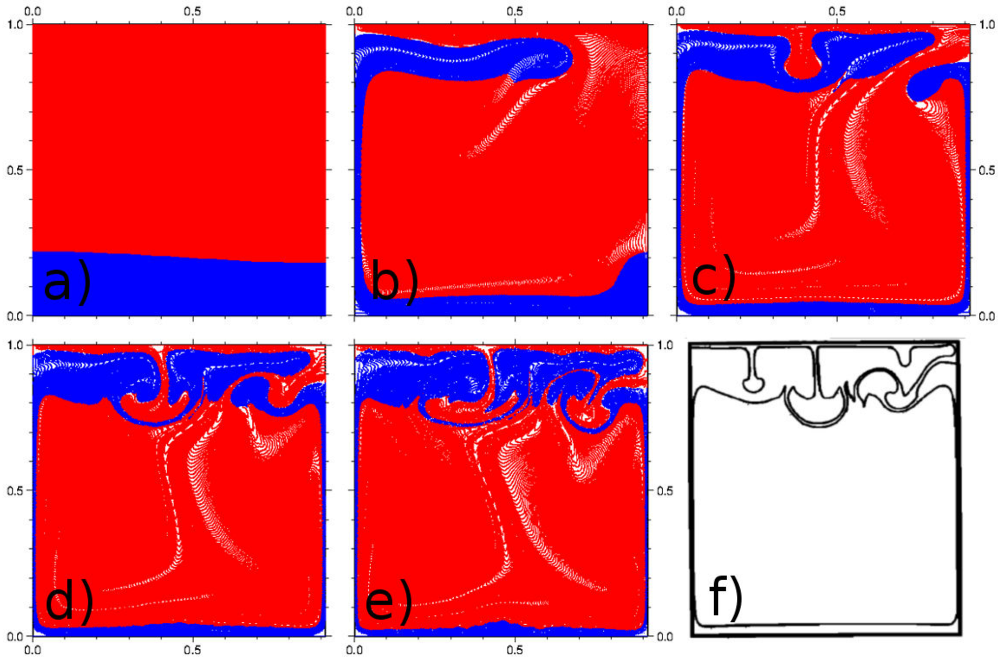

Figure A.2: Evolution of the Rayleigh-Taylor instability experiment. Panel a: $t = 0$; panel b: $t = 500$; panel c: $t = 1000$; panel d: $t = 1500$; panel e: $t = 2000$; panel f: fluids interface at the end of the evolution from *van Keken et al.* (1997).

resulting in shear and adiabatic heating. Figure A.3 shows the energy due to shear and adiabatic heating predicted by the *SubMar* code (panels a and b), compared to that obtained by Gerya's code (panels c and d, from *Gerya*, 2011). The two simulations are very similar in all the domain in terms of values and pattern for both the shear and the adiabatic heating, differing each other by less than 5%.

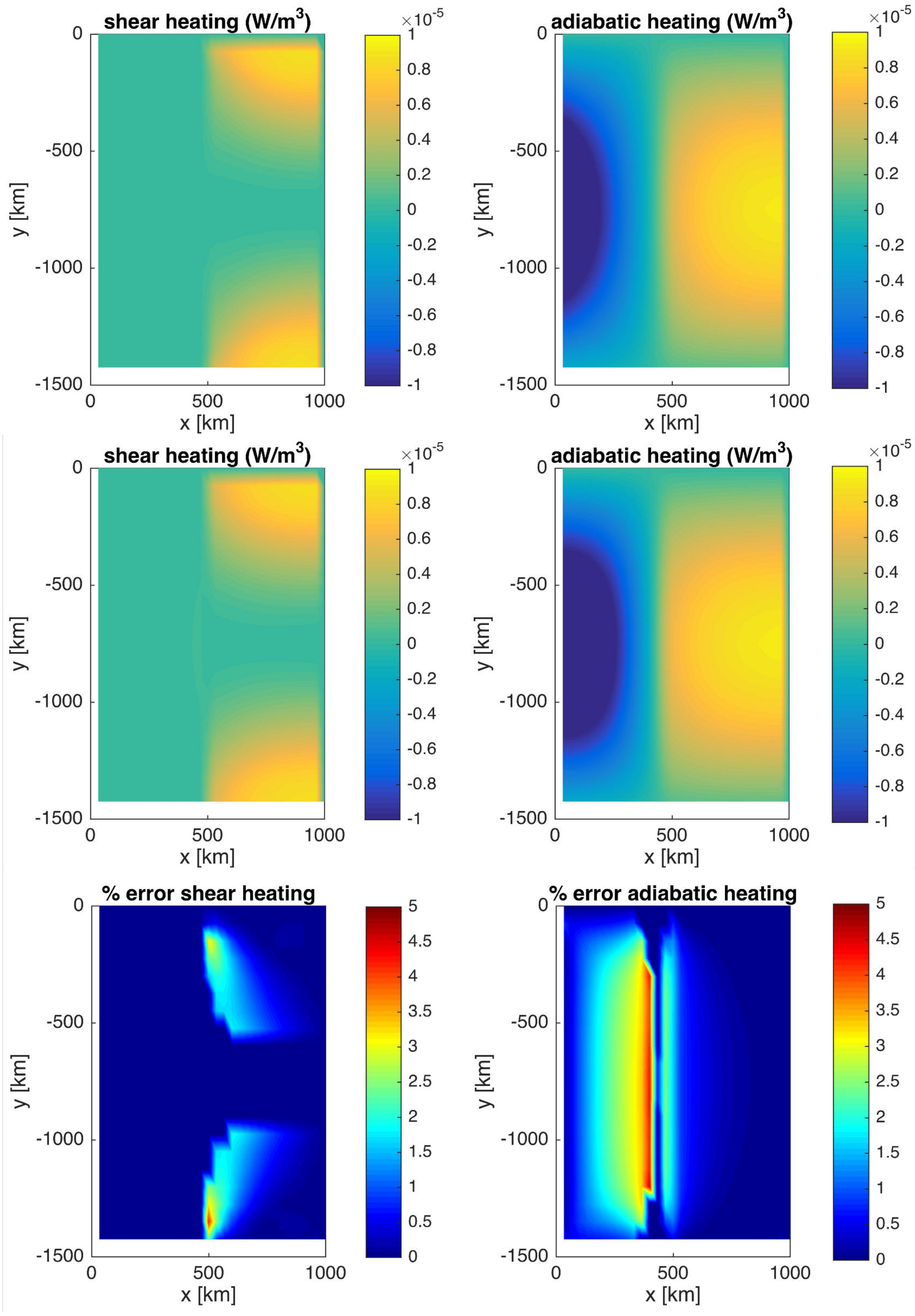

Figure A.3: Results of the benchmark for shear (panels a, c and e) and adiabatic (panels b, d and f) heating. Panels a and b show the results for the *SubMar* code; panels c and d show the results for the Gerya's code (*Gerya*, 2011); panels e and f show the percentage error of the *SubMar* in respect to the Gerya's code of shear and adiabatic heating, respectively.

Appendix B

P-T estimates of the Variscan metamorphism

B.1 P_{max}-T estimates

Table B.1: P_{max}-T estimates recorded in the crustal and mantle rocks of the Alps

Key	Location	Lithology	T (K)	P (GPa)	Age (Ma)	References
Hv1	AR: Tinèe; Gesso-Stura-Vésubie	Metabasite	983-1033	1.2-1.4	420-428 (U/Pb)	1, 2
Hv2	AR: Frisson	Eclogitic gneiss	993-1023	1.33-1.43	336-344 (U/Pb)	3, 4
Hv3	BD: Allemont	Metapelite	773-873	0.9-1.1	Devonian (350-420)	5, 6
Hv4	BD: Livet	Metapelite	803-923	0.6-1.0	297-407 (K/Ar)	5, 6, 7
Hv5	P: Romanche valley	Metabasite	923-1058	0.45-0.7	311-335 (Ar/Ar)	8
Hv6	P: Oisan	Metabasite	1048-1267	0.9-1.7	Variscan (295-425)	8
Hv7	P: La Lavey	Metabasite	1073-1173	1.3-1.5	Early Variscan (375-425)	9, 10
Hv8	P: Peyre Arguet	Metabasite	1023-1123	0.3-0.7	Variscan (295-425)	9, 10, 11
Hv9	BD: Lac de la Croix; Beaufortin	Metabasite	883-943	1.1-1.3	382-398 (U/Pb)	2, 10
Hv10	Ai: Lac Cornu	Metabasite	998-1023	1.5-1.6	387-403 (U/Pb)	2, 12, 13
Hv11	Ai: Lac Cornu; Col de Bérard	Metapelite	898-948	1.2-1.4	> 330	14
Hv12	Ai: Emosson lake	Metapelite	798-948	0.8-1.0	> 320	15
Hv13	MB: Mont Blanc	Amphibolite Skarn	772-863	0.61-0.76	307-335 (Ar/Ar)	16
Pv1	LB: Savona Massif	Eclogite	923-1023	> 1.7	374-392 (U/Pb)	17, 18, 19
Pv2	GP: Gran Paradiso	Metapelite	873-923	0.5-0.7	Variscan (295-425)	20
Pv3	GP: Orco valley	Metapelite	883-903	0.8-0.9	Variscan (295-425)	21
Pv4	MR: Monte Rosa	Metapelite	823-848	0.4-0.6	Variscan (295-425)	22
Pv5	GS: Ambin nappe (Clarea Complex)	Metapelite	823-923	0.8-1.1	340-360 (Ar/Ar)	23, 24
Pv6	GS: Mont Mort	Metapelite	823-873	0.5-0.8	328-332 (U/Pb)	25, 26
Pv7	GS: Siviez-Mischabel	Metabasite	823-923	0.5-0.6	Variscan (295-425)	27
Pv8	Ad: Central part	Metabasite	948-1098	1.95-2.45	346-402 (U/Pb)	28, 29

Continues in the next page

Continues from the previous page

Pv9	Ad: Northern part	Metabasite	838-988	1.45-1.95	304-354 (U/Pb)	28, 29
Pv10	Su: Suretta	Metabasite	890-1023	> 2.0	Variscan (295-425)	30
Pv11	TW: Frosnitztal	Metabasite	673-773	0.8-1.2	400-437 (U/Pb)	31, 32
Pv12	TW: Doesenertal	Metabasite	793-993	> 1.2	400-437 (U/Pb)	32, 33
Av1	SC: Hochgrossen Massif	Metabasite	923-1023	1.0-2.2	389-405 (Ar/Ar)	34, 35
Av2	Oe: Central Oetztal Stubai	Metabasite	973-1073	2.5-2.9	340-370 (Rb/Sr)	36, 37, 38
Av3	Oe: Oetztal Stubai	Metapelite	823-923	1.1-1.3	350-360	39
Av4	TZ: Ultental	Metapelite	923-1023	1.0-2.0	365 (Pb/Pb)	40, 41
Av5	TZ: Ultental	Metabasite	913-9733	1.2-1.6	360 (Ar/Ar)	42
Av6	TZ: Ultental	Ultramafite	1043-1083	2.2-2.8	326-334 (Sm/Nd)	42, 43, 44
Av7	Sil: Ischgl	Metabasite	893-943	2.3-2.9	> 387	45
Av8	Sil: Val Puntota	Metabasite	673-773	2.5-2.7	> 387	45
Av9	LCN: Mortirolo	Metapelite	1023-1123	> 2.0	Early Variscan (375-425)	46
Av10	LCN: Mortirolo	Metabasite	1023-1223	0.65-0.9	314-370	47, 48
Av11	DB: Valpelline	Metapelite	934-1018	0.45-0.65	< 320	49, 50
Av12	DB: Valpelline	Metabasite	973-1023	0.9-1.0	< 320	50, 51
Sv1	Strona Ceneri Zone	Metapelite	863-963	0.6-0.8	307-359 (Ar/Ar)	52, 53
Sv2	DCZ: Upper Como lake	Metapelite	833-923	0.7-1.1	300-400 (K/Ar)	54, 55, 56
Sv3	Monte Muggio Zone	Metapelite	833-853	0.7-0.9	320-340 (K/Ar)	55, 57, 58
Sv4	VVB: Dervio Olgiasca	Metapelite	823-903	0.7-0.9	320-340	59, 60
Sv5	Val Vedello	Metapelite	863-941	0.7-1.1	320-340	60
Sv6	Val Vedello	Metapelite	743-823	0.35-0.75	< 320	60
Sv7	Valtellina NEOB Type (A)	Metapelite	843-933	0.85-1.15	320-340	61
Sv8	Valtellina NEOB Type (B)	Metapelite	713-823	0.35-0.75	320-340	60, 62
Sv9	Val Camonica NEOB Type (A)	Metapelite	823-903	0.8-1.1	320-340	63, 64
Sv10	TVB: Val Trompia	Metapelite	773-823	0.9-1.3	349-379 (Rb/Sr)	65, 66, 67
Sv11	Ei: Eisecktal	Paragneiss	873-923	0.2-0.3	Devonian (350-420)	68
Sv12	Ei: Eisecktal	Metapelite	723-823	0.5-0.65	Devonian (350-420)	68

Helvetic domain (Hv): AR: Argentera; BD: Belledonne; P: Pelvoux; Ai: Aiguilles Rouges; MB: Mont Blanc. Penninic domain (Pv): LB: Ligurian Brianconnais; GP: Gran Paradiso; MR: Monte Rosa; GS: Grand ST. Bernardo; Ad: Adula; SU: Suretta; TW: Tauern window. Austroalpine domain (Av): SC: Speik Complex; Oe: Oetztal; TZ: Ulten Zone; Sil: Silvretta; LCN: Languard-Campo nappe; DB: Dent Blanche. Southapline domain (Sv): DCZ: Domaso-Cortafò Zone; VVB: Val Vedello basement; NEOB: NE Orobic basement; TVB: Tre Valli Bresciane; Ei: Eisecktal. References: 1 = *Latouche and Bogdanoff* (1987); 2 = *Paquette et al.* (1989); 3 = *Ferrando et al.* (2008); 4 = *Rubatto et al.* (2010); 5 = *Guillot and Ménot* (1999); 6= *Guillot et al.* (2009a); 7 = *Ménot et al.* (1987); 8 = *di Paola* (2001); 9 = *Le Fort* (1973); 10 = *Guillot et al.* (1998); 11 = *Grandjean et al.* (1996); 12 = *Liégeois and Duchesne* (1981); 13 = *von Raumer et al.* (1999); 14 = *Schulz and von Raumer* (2011); 15 = *Genier et al.* (2008); 16 = *Marshall et al.* (1997); 17 = *Messiga et al.* (1992); 18 = *Giacomini et al.* (2007); 19 = *Maino et al.* (2012); 20 = *Le Bayon et al.* (2006); 21 = *Gasco et al.* (2010); 22 = *Gasco et al.* (2011a); 23 = *Monie* (1990); 24 = *Borghi et al.* (1999); 25 = *Bussy et al.* (1996); 26 = *Giorgis et al.* (1999); 27 = *Thélin et al.* (1993); 28 = *Dale and Holland* (2003); 29 = *Liati et al.* (2009); 30 = *Nussbaum et al.* (1998); 31 = *Zimmermann and Franz* (1989); 32 = *von Quadt et al.* (1997); 33 = *Droop* (1983); 34 = *Faryad et al.* (2002); 35 = *Melcher et al.* (2002); 36 = *Miller and Thöni* (1995); 37 = *Thoeni* (2002); 38 = *Konzett et al.* (2005); 39 = *Rode et al.* (2012); 40 = *Godard et al.* (1996); 41 = *Hauzenberger et al.* (1996); 42 = *Herzberg et al.* (1977); 43 = *Tumiati et al.* (2003); 44 = *Morten et al.* (2004); 45 = *Schweinehage and Massonne* (1999); 46 = *Gosso et al.* (1995); 47 = *Thoeni* (1981); 48 = *Zucali* (2001); 49 = *Zucali and Spalla* (2011); 50 = *Manzotti and Zucali* (2013); 51 = *Gardien et al.* (1994); 52 = *Boriani and Villa* (1997); 53 = *Giobbi et al.* (2003); 54 = *Fumasoli* (1974); 55 = *Mottana et al.* (1985); 56 = *di Paola and Spalla* (2000); 57 = *Bertotti et al.* (1993); 58 = *Siletto et al.* (1993); 59 = *Diella et al.* (1992); 60 = *Zanoni et al.* (2010); 61 = *Spalla et al.* (1999); 62 = *Spalla and Gosso* (1999); 63 = *Pigazzini* (2003); 64 = *Spalla et al.* (2006); 65 = *Riklin* (1983); 66 = *Giobbi and Gregnanin* (1983); 67 = *Spalla et al.* (2009); 68 = *Benciolini et al.* (2006).

Table B.2: P_{max}-T estimates recorded in the crustal and mantle rocks of the French Central Massif

Key	Location	Lithology	T (K)	P (GPa)	Age (Ma)	References
HA1	Haut Allier	Eclogite (UGU)	1023-1123	1.8-2.2	422-452 (U/Pb)	1, 2, 3, 4, 5, 6, 7
Ma1	Marvejols	Eclogite (LAC)	923-1003	1.8-2.0	409-421 (U/Pb)	1, 2, 3, 4, 5, 8, 9
Li1	Limousine	Paragneiss (LGU)	873-973	0.8-1.1	370-380 (U/Th/Pb)	4, 10
Li3	Limousine	Metapelite (UGU)	1103	1.6-1.9	390-430	11
Li4	Limousine	Eclogite (LGU)	23-1023	1.5-2.0	420-440 (Pb/Pb)	1, 8
Li5	Limousine	Migmatite (LGU)	1033-1053	0.5-0.6	349-359 (U/Th/Pb)	12, 13
Li6	Limousine	Eclogite	853-1003	2.5-3.5	402-422 (U/Pb)	14
Li7	Limousine	Migmatite (UGU)	923-1023	0.7-0.8	377-387 (U/Pb)	3, 4, 15
LB1	La Bessenoits	Eclogite (UGU)	873-983	1.6-1.9	390-436 (Pb/Pb)	4, 5, 16
ML1	Mont du Lyonnais	Peridotite	973-1073	< 2.0	Variscan (295-425)	17
ML2	Mont du Lyonnais	Eclogite (UGU)	1003-1053	1.5	Early Variscan (400-425)	6, 8, 9, 18, 19 20, 21, 22
ML3	Mont du Lyonnais	Migmatite	873-1023	0.6-1.0	350-360	4, 5, 10
Ro1	Lévézou	Eclogite (UGU)	953-1033	1.5-2.0	Early Variscan (375-425)	8, 23
Ro2	Najac	Eclogite (UGU)	923-1003	1.1-1.6	Variscan (295-425)	8, 23
Ro3	Le Vibal	Eclogite (UGU)	1013-1133	1.0-1.4	Variscan (295-425)	23
Ar1	Artense	Eclogite (UGU)	973-1023	1.4-1.6	Variscan (295-425)	8, 24
Ar2	Artense	Amphibolite (LGU)	943-1023	0.6-0.82	Variscan (295-425)	25
PA1	Plateau d'Aiguran	Metapelite (LAC)	923-1023	1.0-1.2	376-397 (Ar/Ar)	4, 26, 27
PA2	Plateau d'Aiguran	Micaschist	823-923	0.6-0.8	350-380	26
Mc1	Maclas	Eclogite (UGU)	973-1043	1.4-1.6	Variscan (295-425)	28, 29
VD1	Velay Dome	Migmatite (LGU)	948-998	0.4-0.5	309-319 (U/Pb)	29, 30
VD2	Velay Dome (Cévennes)	Metapelite	748-798	0.4-0.6	335-340 (Ar/Ar)	29
MN1	Montagne Noire	Metabasite	973-1073	0.7-1.1	345-360 (U/Th/Pb)	31, 32
MN2	Montagne Noire	Ultramafite	1073-1173	0.5-1.0	Early Variscan (375-425)	32
TP1	Quercy	Metapelite (TPU)	853-963	0.6-1.0	375-385 (Rb/Sr)	33

UGU: Upper Gneiss Unit; LGU: Lower Gneiss Unit; LAC: Leptyno-amphibolitic Complex; TPU: Thiviers-Payzac Unit. References: 1 = *Pin and Sills* (1986); 2 = *Ledru et al.* (1989); 3 = *Faure et al.* (2005); 4 = *Faure et al.* (2008); 5 = *Lardeaux* (2014a); 6 = *Costa et al.* (1993); 7 = *Ducrot et al.* (1983); 8 = *Mercier et al.* (1991a); 9 = *Pin and Lancelot* (1982); 10 = *Faure et al.* (2009); 11 = *Bellot and Roig* (2007); 12 = *Gebelin et al.* (2004); 13 = *Gébelin et al.* (2009); 14 = *Berger et al.* (2010); 15 = *Lafon* (1986); 16 = *Paquette et al.* (1995); 17 = *Gardien et al.* (1988); 18 = *Lardeaux et al.* (2001); 19 = *Dufour et al.* (1985); 20 = *Lardeaux and Dufour* (1987); 21 = *Feybesse et al.* (1988); 22 = *Lardeaux et al.* (1989); 23 = *Burg et al.* (1989); 24 = *Mercier et al.* (1989); 25 = *Mercier et al.* (1992); 26 = *Boutin and Montigny* (1993); 27 = *Faure et al.* (1990); 28 = *Gardien and Lardeaux* (1991); 29 = *Ledru et al.* (2001); 30 = *Barbey et al.* (2015); 31 = *Demange* (1985); 32 = *Faure et al.* (2014); 33 = *Duguet et al.* (2007).

B.2 P-T paths

Table B.3: P-T paths of the crustal and mantle rocks of the Alps

Key	Metamorphic stage	T (K)	P (GPa)	Age (Ma)	References
Hv2	Stage I	993-1023	1.33-1.43	336-344 (U/Pb)	1, 2
	Stage II	980-984	1.08-1.12	330-335	1, 3, 4
	Stage III	923-953	0.7-1.0	315-330	1, 3, 4
	Stage IV	773-998	< 0.59	310-315 (Ar/Ar)	1, 4
Hv3	Stage I	773-873	0.9-1.1	Devonian (350-420)	5, 6
	Stage II	803-963	0.6-1.0	Post-Devonian I	5
	Stage III	778-1018	0.3-0.7	Post-Devonian II	5
Hv4	Stage I	803-923	0.6-1.0	297-407 (K/Ar)	5, 6, 7
	Stage II	803-923	0.5-0.9	Post-Carboniferous I	5
	Stage III	813-933	0.3-0.7	Post-Carboniferous II	5
Hv11	Stage I	898-948	1.2-1.4	> 330	8
	Stage II	873-943	0.7-0.8	300-330 (U/Pb)	8
Hv12	Stage I	798-848	0.8-1.0	> 320	9
	Stage II	903-973	0.4-0.6	319-321 (U/Pb)	9, 10
Pv1	Stage I	923-1023	> 1.7	374-392 (U/Pb)	11, 12, 13
	Stage II	823-973	0.6-1.2	320-346 (U/Pb)	11, 12, 13, 14
	Stage III	723-823	0.4-0.7	300-310 (U/Pb)	11, 12, 13, 14
Pv5	Stage I	823-923	0.8-1.1	340-360 (Ar/Ar)	15, 16
	Stage II	843-933	0.4-0.6	Post-middle Mississippian	16
Pv6	Stage I	823-873	0.5-0.8	328-332 (U/Pb)	17, 18
	Stage II	823-873	0.1-0.2	Post-late Mississippian	18
Pv12	Stage I	793-993	> 1.2	400-437 (U/Pb))	19, 20
	Stage II	903-963	0.5-1.1	Post-early Devonian	20
Av3	Stage I	823-923	1.1-1.3	350-360	21
	Stage II	923-1023	0.4-0.6	304-330 (U/Th/Pb)	21
Av4	Stage I	923-1023	1.0-2.0	365 (Pb/Pb)	22, 23
	Stage II	823-923	0.6-0.8	Post-Devonian	22, 23
Av5	Stage I	913-973	1.2-1.6	360 (Ar/Ar)	22
	Stage II	823-923	0.6-0.8	Post-Devonian	22
Sv4	Stage I	823-903	0.7-0.9	320-340	24, 25
	Stage II	923-1023	0.4-0.55	Post-Mississippian	26
Sv5	Stage I	863-941	0.7-1.1	320-340	25
	Stage II	558-663	0.1-0.5	Early Permian	25
Sv7	Stage I	753-813	0.75-0.95	> 340	27
	Stage II	843-933	0.85-1.15	320-340	27
	Stage III	673-823	0.3-0.4	Post-Mississippian	27
Sv9	Stage I	643-823	0.6-0.8	350-380	28, 29
	Stage II	823-903	0.8-1.1	320-340 I	28, 29
	Stage III	673-823	0.2-0.4	Post-Mississippian	28

References: 1 = *Ferrando et al.* (2008); 2 = *Rubatto et al.* (2010); 3 = *Rubatto et al.* (2001); 4 = *Corsini et al.* (2004); 5 = *Guillot and Ménot* (1999); 6= *Guillot et al.* (2009a); 7 = *Ménot et al.* (1987); 8 = *Schulz and von Raumer* (2011); 9 = *Genier et al.* (2008); 10 = *Bussy et al.* (2000); 11 = *Messiga et al.* (1992); 12 = *Giacomini et al.* (2007); 13 = *Maino et al.* (2012); 14 = *Barbieri et al.* (2003); 15 = *Monie* (1990); 16 = *Borghi et al.* (1999); 17 = *Bussy et al.* (1996); 18 = *Giorgis et al.* (1999); 19 = *von Quadt et al.* (1997); 20 = *Droop* (1983); 21 = *Rode et al.* (2012); 22 = *Godard et al.* (1996); 23 = *Hauzenberger et al.* (1996); 24 = *Diella et al.* (1992); 25 = *Zanoni et al.* (2010); 26 = *Siletto et al.* (1993); 27 = *Spalla et al.* (1999); 28 = *Pigazzini* (2003); 29 = *Spalla et al.* (2006).

Table B.4: P-T paths of the crustal and mantle rocks of the French Central Massif

Key	Metamorphic stage	T (K)	P (GPa)	Age (Ma)	References
Li1	Stage I	873-973	0.8-1.1	370-380 (U/Th/Pb)	1, 2
	Stage II	823-873	0.8-1.0	350-360 (Ar/Ar)	2
Li4	Stage I	923-1023	1.5-2.0	420-440 (Pb/Pb)	3, 4
	Stage II	923-1023	1.0-1.2	Early Devonian	4
	Stage III	983-1023	0.85	Middle-Devonian	4
Li7	Stage I	8923-1023	0.7-0.8	377-387 (U/Pb)	1, 5, 6
	Stage II	873-973	0.7-1.0	350-360 (Ar/Ar)	2, 6
ML1	Stage I	973-1073	< 2.0		7
	Stage II	1223-1323	2.3-3.0		7, 8
	Stage III	1153-1223	< 2.0		7
	Stage IV	973-1153	< 1.2		7, 8
	Stage V	< 973	0.6-0.8		7
	Stage VI	< 773	< 0.6		7
ML2	Stage I	1003-1053	1.5	> 400	9, 10
	Stage II	1023	0.8-1.0	368-400 (Rb/Sr)	4, 8, 11, 12, 13, 14
	Stage III	923-993	0.6-0.8	340-350 (Ar/Ar)	4, 8, 11, 12, 13, 14
Ro1	Stage I	953-1033	1.5-2.0	Early Variscan (375-425)	4, 15
	Stage II	953-1023	1.1-1.4	Late Devonian	4
	Stage III	823-923	0.4-0.7	345-355 (Rb/Sr)	4
Ro2	Stage I	923-1003	1.1-1.6		4, 15
	Stage II	873-923	0.7		4, 15
	Stage III	673-723	0.3-0.5		15
Ro3	Stage I	1013-1133	1.0-1.4		15
	Stage II	1023-1123	0.85-0.95		15
	Stage III	793-923	0.35-0.45		15
Ar1	Stage I	973-1023	1.4-1.6		4, 16
	Stage II	1073-1123	1.0-1.2		4, 16
	Stage III	923-973	0.6-0.75		4, 16
Ar2	Stage I	943-1023	0.6-0.82		17
	Stage II	923-1023	0.4-0.56		17
	Stage III	< 773	< 0.3		17
PA1	Stage I	923-1023	1.0-1.2	376-397 (Ar/Ar)	1, 18, 19
	Stage II	823-923	0.6-0.8	350-380	19
	Stage III	723-823	0.2-0.4	300-320	19
PA2	Stage I	823-923	0.6-0.8	350-380	19
	Stage II	623-723	0.2-0.3	300-320	19
Mc1	Stage I	973-1043	1.4-1.6		20, 21
	Stage II	1023-1103	1.0-1.3		21
	Stage III	773-873	0.5		21
MN2	Stage I	1073-1173	0.5-1.0		22
	Stage II	973-1073	0.6-1.5		22
TP1	Stage I	853-963	0.6-1.0	375-385 (Rb/Sr)	23
	Stage II	673-773	0.4-0.6	350-360 (Ar/Ar)	2, 23

References: 1 = *Faure et al.* (2008); 2 = *Faure et al.* (2009); 3 = *Pin and Sills* (1986); 4 = *Mercier et al.* (1991a); 5 = *Lafon* (1986); 6 = *Faure et al.* (2005); 7 = *Gardien et al.* (1988); 8 = *Costa et al.* (1993); 9 = *Lardeaux et al.* (2001); 10 = *Dufour et al.* (1985); 11 = *Lardeaux and Dufour* (1987); 12 = *Feybesse et al.* (1988); 13 = *Lardeaux et al.* (1989); 14 = *Pin and Lancelot* (1982); 15 = *Burg et al.* (1989); 16 = *Mercier et al.* (1989); 17 = *Mercier et al.* (1992); 18 = *Boutin and Montigny* (1993); 19 = *Faure et al.* (1990); 20 = *Gardien and Lardeaux* (1991); 21 = *Ledru et al.* (2001); 22 = *Demange* (1985); 23 = *Duguet et al.* (2007).

Appendix C

Publications and abstracts realised during the PhD

C.1 Paper on the PhD subject

A 2D NUMERICAL STUDY OF HYDRATED WEDGE DYNAMICS

Alessandro Regorda*, Manuel Roda, Anna Maria Marotta and M. Iole Spalla

Dipartimento di Scienze della Terra 'A. Desio',

Università degli Studi di Milano, via Mangiagalli 34, I-20133 Milano, Italy

* corresponding author: alessandro.regorda@unimi.it

ABSTRACT

We developed a 2D finite element model to investigate the effect of shear heating and mantle hydration on the dynamics of the mantle wedge area. The model considers an initial phase of active oceanic subduction with three different prescribed velocities that is followed by pure gravitational evolution after the collision. The dynamics that allow the recycling and exhumation of subducted material in the wedge area is strictly correlated with the thermal state at the external boundaries of the mantle wedge, and the size of the hydrated area depends on the subduction velocity when mantle hydration and shear heating are considered simultaneously. During the pure gravitational phase, the hydrated portion of the mantle wedge increases in models with high subduction velocities.

The predicted P-T configuration indicates that contrasting P-T conditions, such as Barrovian- to Franciscan-type metamorphic gradients, can contemporaneously characterise different portions of the subduction system during both the active and gravitational phases instead of being indicative of collisional or subduction, respectively.

KEY WORDS: Numerical modelling, Continental margins: convergent, Heat generation and transport.

INTRODUCTION

1

Accepted after major revision after editor decision on 14/11/2016 by the Geophysical Journal International. This subject has been treated in the thesis in Chapter 3.

C.2 Short notes

GIGS Annual Meeting 2013

Rend. Online Soc. Geol. It., Vol. 29 (2013), pp. 142-145, 3 figs.

Numerical model of an ocean/continent subduction and comparison with Variscan orogeny natural data

Alessandro Regorda ([a]), Anna Maria Marotta ([a, b]) & M. Iole Spalla ([a, b])

([a]) Department of Earth Sciences "Ardito Desio", University of Milan, via Mangiagalli 34, 20133, Milan, Italy. E-mail: alessandro.regorda@gmail.com
([b]) CNR-IDPA, via Mangiagalli 34, 20133, Milan, Italy.

Document type: Short note.
Manuscript history: received 23 September 2013; accepted 6 October 2013; editorial responsibility and handling by Davide Zanoni.

ABSTRACT

The effects of the viscous heating and the hydration of the mantle wedge on the continental crust recycling during the evolution of an ocean/continent subduction system are analysed by using a 2D finite element thermo-mechanical model. The dehydration of the oceanic slab, and the consequent hydration of the mantle wedge, is accomplished by lawsonite breakdown (Roda et al., 2010; 2011). The model shows the activation of convective cells in the mantle wedge that determine the recycling of subducted continental material. Moreover, with respect to Marotta and Spalla (2007), in which the hydration of the mantle wedge was not taken into account, much more correspondences between P-T predictions and the natural P-T estimates of the Alpine Variscan metamorphism are obtained.

KEY WORDS: Mantle wedge hydration, Numerical modelling, Ocean/continent subduction.

INTRODUCTION

To analyze the geodynamic evolution of the active ocean/continent convergence stage that characterized the Variscan orogeny of the Alps and induced the subduction of oceanic lithosphere until continental collision, a 2D finite-element thermo-mechanical model was developed. It is based on Marotta and Spalla (2007)'s model and modified to include the effects of viscous heating and hydration of the mantle wedge. Both mechanisms could induce the development of short wavelength convective cells in the wedge area that would favor the exhumation of subducted crustal material since the early stages of the subduction.

Model predictions, in terms of pressure, temperature, lithology and age, have been compared with the P-T estimates for the convergence stage that precedes the Variscan collision signatures in the Alps, within a time span between 425 and 370 Ma.

NUMERICAL MODELLING

The model is based on the assumption that a 2500 km wide ocean is consumed during 50 Ma of active convergence.

The physics of the crust-mantle system during subduction is described by the equations of continuity, of conservation of momentum and of conservation of energy, expressed by:

$$\nabla \cdot \vec{u} = 0$$

$$\frac{\partial \tau_{ij}}{\partial x_j} = \frac{\partial p}{\partial x_i} - \rho \vec{g}$$

$$\rho c_p \left(\frac{\partial T}{\partial t} + \bar{u} \cdot \nabla T \right) = -\nabla \cdot \left(-K \nabla T \right) + \rho H ,$$

respectively (Marotta & Spalla, 2007), where ρ is the density, τ_{ij} is the deviatoric stress, c_p is the specific heat at constant pressure, p is the pressure, T is the temperature, K is the thermal conductivity, H is the heat production rate per unit mass, $\vec{u}$ is the velocity and $\vec{g}$ is the gravity acceleration. A Newtonian rheology is assumed for the whole system.

The numerical model uses the penalty function formulation to integrate the conservation of momentum equation and the Petrov-Galerkin method to integrate the conservation of energy equation.

Numerical integration has been performed in a 2D rectangular domain 1400 km wide and 700 km deep, discretized by 3580 quadratic triangular elements, with a total amount of 7315 nodes, with a denser nodal distribution near the contact region between the two interacting plates, where the most significant gradients in the temperature and velocity fields are expected.

In order to compositionally differentiate the crust (both oceanic and continental) from the mantle, 288061 markers have been distributed through the 2D domain, with a density of 1 marker per 0.25 km^2. The base of the crust is defined compositionally while the base of the lithosphere is defined thermally by the 1600 K isotherm.

Thermal boundary conditions correspond to fixed temperatures at the top and the bottom of model domain, at 300 K and 1600 K respectively, and to zero thermal flux imposed at the vertical sidewalls. The velocity boundary conditions correspond to a subduction velocity fixed to 5 cm/yr and to a velocity fixed to zero along the other sides of the model.

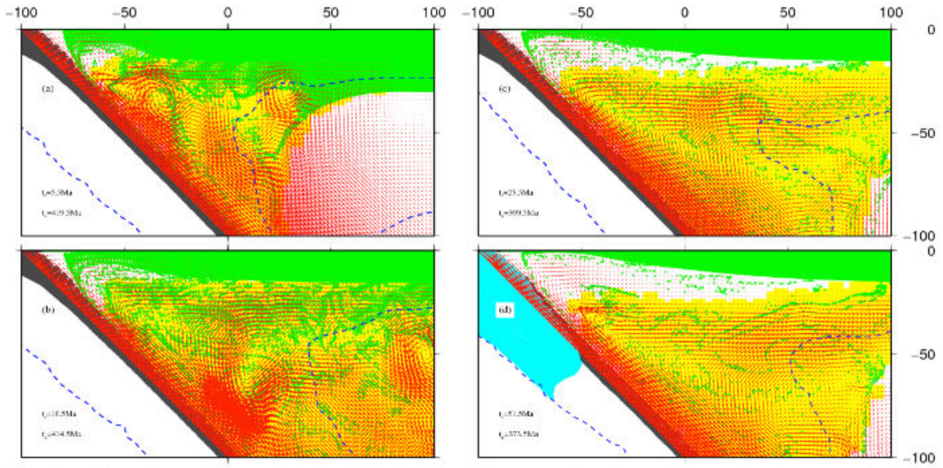

Fig. 1 - Zoom of the wedge area. Different colors indicate: Red – Velocity vectors, green – continental crust of the upper plate, dark grey – oceanic crust and cyan – continental crust of the lower plate. The hydrated area of the mantle wedge is colored in yellow (see discussion in the text).

To define the dynamic geometry of the hydrated portion of the wedge area we followed Roda et al. (2010) and Roda et al. (2011) and assumed that the maximum depth where dehydration takes place is identifiable by that of the deepest oceanic marker in the stability field of lawsonite, up to 300 km deep, beyond which the water budget in the hydrated phases of the basaltic system could be considered negligible (Schmidt & Poli, 1998). The progressive hydration of the mantle wedge is defined by the stability field of the serpentine (Schmidt & Poli, 1998).

In the area in which the hydration occurs, a viscosity of 10^{19} Pa·s (Gerya e Stockhert, 2005; Roda et al., 2010; 2011) and a density of 3000 kg/m^3 (Schmidt & Poli, 1998; Roda et al., 2010; 2011) are assumed.

The bottom of the hydrated zone is defined at each time by the envelope of the crustal markers located at the base of the oceanic crust belonging to the subducting plate.

RESULTS AND DISCUSSION OF THE MODEL

Accounting for both viscous heating and hydration of the mantle wedge favours the development of short wavelength convective motions in the wedge area, which remain active until continental collision (Fig.1). In particular, it is possible to recognise two convective cells during the first 10.5 Ma, which increase their dimensions while they move to the external portion of the hydrated wedge (Figs.1a and 1b). After 25.5 Ma, until continental collision, only one convective cell remains active with dimensions greater than those of the cells active during the earlier stages of the subduction (Figs.1c and 1d).

The formation of the convective cells induces the recycling and the exhumation of a huge amount of continental crust scraped off the upper plate and carried to depth (Fig.1).

In the hydrated area the energy produced by viscous heating remains very low, up to 1 to 3 orders of magnitude lower than the radiogenic contribution (Fig.2), due to both the huge amount of recycled continental material (Figs. $2a_3$ to $2d_3$) and to the considerable reduction of mantle viscosity caused by the hydration (Figs. $2a_1$ to $2d_1$). Outside the hydrated zone and below the subducted crust, the energy produced in the mantle by viscous heating is much higher because of the high viscosity due to the low temperatures.

The comparison between model predictions and natural P-T estimates (Fig. 3) shows that accounting for viscous heating and mantle hydration in the wedge area promotes, with respect to Marotta and Spalla (2007)'s model, an increase of the agreement for the early-Variscan rocks of the Alps in terms of both duration of the agreement and amount of markers that show compatibility. The P-T estimates result from rocks that preserve pre-Alpine metamorphic imprint and at present occurring as non re-equilibrated relicts in the Helvetic (red), Pennidic (cyan), Austroalpine (yellow) and Sudalpine (green) domains.

The location, the P-T estimate values and the radiometric ages are summarised in Marotta and Spalla (2007) and in Spalla and Marotta (2007).

The P-T estimates for which the improvement of compatibility with respect to Marotta and Spalla (2007)'s model is greater are those with higher P-T ratio, which show

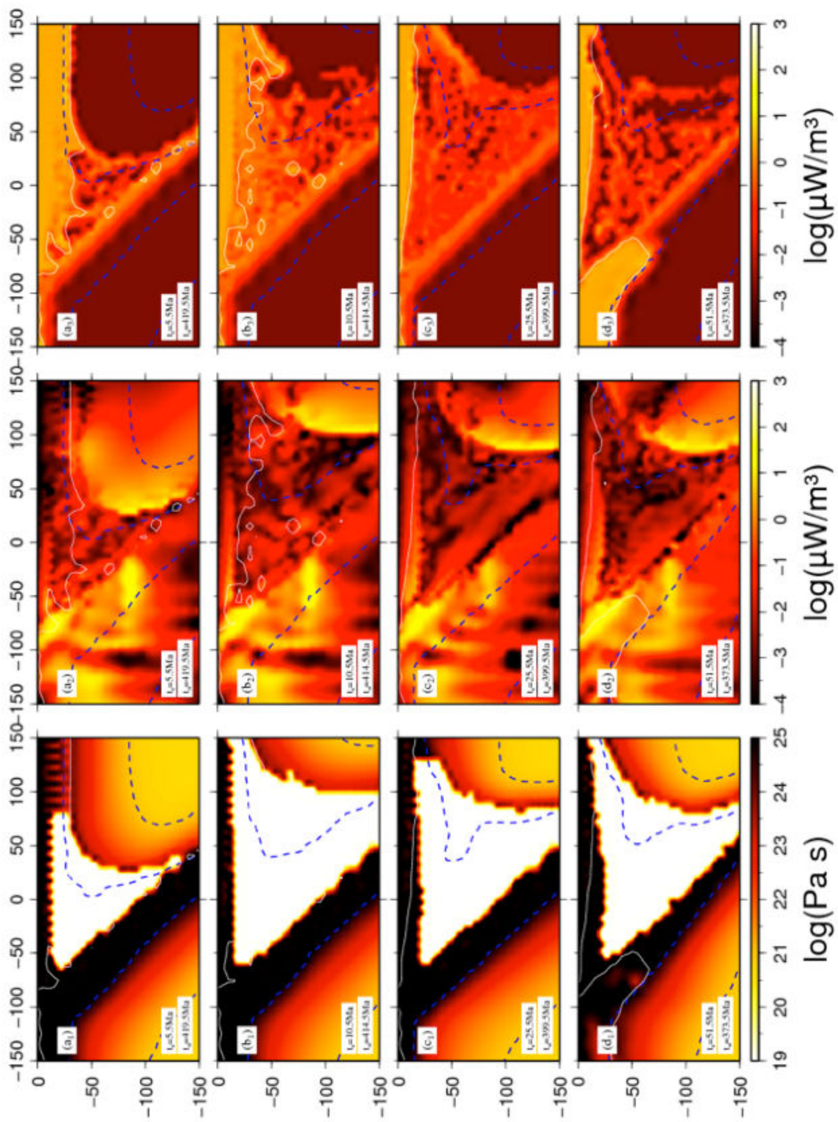

Fig. 2 - Representation of the viscosity (a1-d1), of the energy produced by viscous heating (a2-d2) and of the radiogenic energy (a3-d3).

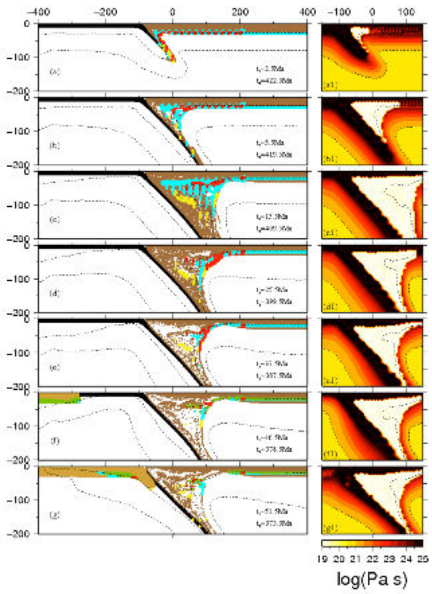

Fig. 3 - Results of the comparison between the estimated P-T conditions and the numerical modelling predictions. The dashed lines show 800 and 1500 K isotherms. Colored dots represent the correspondences with data from Helvetic (red), Pennidic (cyan), Austroalpine (yellow) and Sudalpine (green) domains. The images on the right represent the viscosity.

their correspondences with the continental markers that have been recycled in the mantle wedge. For data with intermediate P-T ratio the improvement with respect to Marotta and Spalla (2007)'s model is less evident because the agreement occurs with the markers located at the bottom of continental crust, also far from the subduction zone where the effects of hydration and viscous heating mechanisms are negligible. During the development of subduction there is an increase of markers which record a thermal state compatible with P-T estimates, caused by thermal erosion at the bottom of continental crust of the upper plate.

The compatibility between the predicted thermal state and the P-T estimates, referred to the pressure peak of the natural rocks, suggests that the Barrovian metamorphism can occur also during active subduction, instead of well before the continental collision as commonly envisaged by mono-dimensional models. This metamorphic imprint is compatible with that predicted by our model at the base of the continental crust and in the external portions of the hydrated mantle wedge, suggesting that during the subduction phase high temperature can be reached also in the mantle wedge.

REFERENCES

Gerya T. & Stöckhert B. (2005) - Two dimensional numerical modeling of tectonic and metamorphic histories at active continental margins. Int. J. Earth Sci., 95, 250-274, doi: 10.1007/s00531-005-0035-9.

Marotta A.M. & Spalla M.I. (2007) - Permian-Triassic high thermal regime in the Alps: Result of late Variscan collapse or continental rifting? Validation by numerical modeling. Tectonics, 26, doi: 10.1029/2006TC002047

Roda M., Marotta A.M. & Spalla M.I. (2010) - Numerical simulation of an ocean-continent convergent system: Influence of subduction geometry and mantle wedge hydration on crustal recycling. Geochem. Geophys. Geosyst., 11, Q05008, doi: 10.1029/2009GC003015

Roda M., Marotta A.M. & Spalla M.I. (2011) - The effects of the overriding plate thermal state on the slab dip in an ocean-continent subduction system. Com. Ren. Geosci., 343, 323-330.

Schmidt M.W. & Poli S. (1998) - Experimentally based water budget for dehydrating slabs and consequences for arc magma generation. Earth Plan. Sci. Lett., 163, 361-379.

Spalla M.I. & Marotta A.M. (2007) - P-T evolutions vs. Numerical modelling; a key to unravel the Paleozoic to early-Mesozoic tectonic evolution of the Alpine area. Per. Miner., 76, 267-308.

GNGTS 2016

active. These transfer zones were affected by uplifts and inversion structures.

In the Late Middle Pleistocene to Present extensional basins and transfer zone formed. Intense volcanism and eastwards migration of the extension was recorded in the northern Campania Margin. NNE-trending normal faults developed in the ETM and Apennines and this extensional pattern is coherent with the migration of the Calabrian accretionary prism toward E-SE. During this tectonic stage, a NW-SE transfer zone, featuring restraining and releasing bends, formed at the SW border of the ETM.

The deformation features of the upper plate in correspondance of the ETM are not consistent with the current rifting models. We hypothesize a link between the evolution of upper plate and subducting slab. The proposed geodynamic scenario is characterized by the formation of extensional basins in the upper plate and onset and development of a STEP (Subduction-Transform-Edge-Propagator) fault along the northern margin of the Ionian slab.

References

Catalano, S., Monaco, C., Tortorici, L., 2004. Neogene-Quaternary tectonic evolution of the southern Apennines. Tectonics 23, TC2003, doi:10.1029/2003TC001512.

Koulakov, I., Kaban, M.K., Tesauro M., Cloetingh, S.A.P.L., 2009. P and S velocity anomalies in the upper mantle beneath Europe from tomographic inversion of ISC data. Geophysical Journal International 179, 345-366.

Govers, R., Wortel, M.J.R., 2005. Lithosphere tearing at STEP faults: response to edges of subduction zones. Earth Planet. Scie. Lett. 236, 505–523.

Marani, M., Gamberi, G., Bortoluzzi, G., Carrarra, G., Ligi, M., Penitenti, D., 2004. Seafloor morphology of the Tyrrhenian Sea. Scale 1:1,000,000. Included to: Mem. Descr. Carta Geol. Ital., LXIV. Rome. Martin, A.K., 2006. Oppositely directed pairs of propagating rifts in back arc basins: double saloon door seafloor spreading during subduction rollback. Tectonics 25, TC3008. http://dx.doi.org/10.1029/2005TC001885.

Mattei, M., Petrocelli, V., Lacava, D., Schiattarella, M., 2004. Geodynamic implication of Pleistocene ultrarapid vertical – axis rotation in the Southern Apennines, Italy. Geology,789-792, doi:10.1130/G20552.1.

Milia, A., Torrente, M.M., Massa, B., Iannace, P., 2013. Progressive changes in rifting directions in the Campania margin (Italy): new constrains for the Tyrrhenian Sea opening. Glob. Planet. Change 109, 3-17, http://dx.doi.org/10.1016/j.gloplacha.2013.07.003.

Milia, A., Torrente, M.M., 2015. Tectono-stratigraphic signature of a rapid multistage subsiding rift basin in the Tyrrhenian-Apennine hinge zone (Italy): A possible interaction of upper plate with subducting slab. J. Geodyn. 86, 42–60, http://dx.doi.org/10.1016/j.jog.2015.02.005.

Milia, A., Iannace, P., Tesauro, M., Torrente, M.M., 2016. Upper plate deformation as marker for the Northern STEP fault of the Ionian slab (Tyrrhenian Sea, central Mediterranean). Tectonophysics, in press, http://dx.doi.org/10.1016/j.tecto.2016.08.017

Patacca, E., Sartori, R., Scandone, P., 1990. Tyrrhenian basin and Apenninic arcs: kinematic relations since late Tortonian times. Memorie Società Geologica Italiana 45, 425–451.

Schiatterella, M., Beneduce, P., Di Leo, P., Giano, S.I., Giannandrea, P., Principe, P., 2005. Assetto strutturale ed evoluzione morfotettonica quaternaria del vulcano del Monte Vulture (Appennino lucano). Boll. Soc. Geol. Ital. 124, 543-562.

Wortel, M.J.R., Spakman, W., 2000. Subduction and slab detachment in the Mediterranean-Carpathian Region. Science 290, 1910–1917, http://dx.doi.org/10.1126/science.290.5498.1910.

WHAT DRIVES ALPINE TETHYS OPENING: SUGGESTIONS FROM NUMERICAL MODELLING

M. Roda, A. Regorda, A. M. Marotta, M. I. Spalla
Dipartimento di Scienze della Terra "A. Desio", Università degli Studi di Milano, Italy

Introduction. Continental crustal slices, preserving pre-Alpine metamorphism, are widely described in Alps and Apennine realms (Fig. 1). Variscan-age eclogites (430-326 Ma) generated from continental, oceanic and mantle rocks occur within these slices and suggest

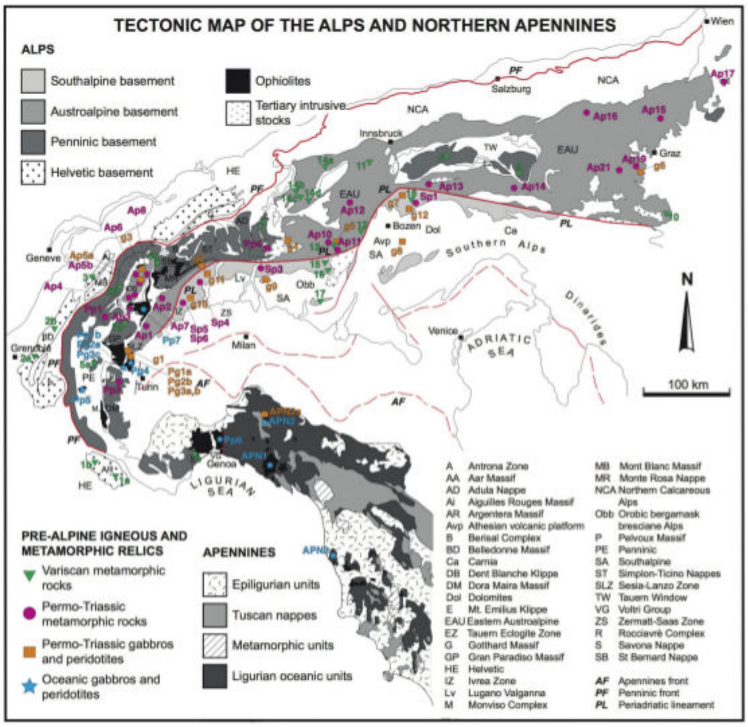

Fig. 1 – Tectonic outline of the Alps and northern Apennines with the locations of igneous and metamorphic pre-Alpine relicts as labeled in Spalla *et al.* (2014) and Marotta *et al.* (2016).

a pre-Alpine burial of continental crust at convergent plate margins, in a context of oceanic lithosphere subduction underneath continental upper plate, characterized by a low thermal regime, and followed by continental collision (e.g. Marotta and Spalla, 2007; von Raumer *et al.*, 2013; Spalla *et al.*, 2014). Permian-Triassic remnants (300-220 Ma) of high-temperature metamorphism, mainly occurring within Austroalpine and Southalpine domains (belonging to Adria plate) and associated with widespread basic to acidic igneous activity testified by large gabbro bodies (Fig. 1), indicate an increase of the lithospheric thermal regime (e.g. Lardeaux and Spalla, 1991; Schuster and Stüwe, 2008; Marotta *et al.*, 2009; Spalla *et al.*, 2014) related to asthenospheric upwelling and lithospheric thinning (e.g. Thompson, 1981; Sandiford and Powell, 1986; Beardsmore and Cull, 2001). During Late Triassic-Early Jurassic an important extensional stage leads to the break-up of the Pangaea continental lithosphere and the opening of the Alpine Tethys Ocean, accounted by the occurrence of ophiolitic sequences in the western Alps and Apennines (Fig. 1). The geodynamic significance of the Permian-Triassic high temperature and low pressure metamorphic event has been widely debated and recent numerical models suggest an origin consequent to successive lithospheric extension and thinning events leading to the Mesozoic continental rifting (e.g. Marotta and Spalla, 2007; Marotta *et al*., 2009; Spalla *et al*., 2014), whereas on the basis of recent paleogeographic reconstructions it has also been interpreted as engaged by the neo-Variscan late-orogenic collapse (e.g. Spiess *et al*., 2010; von Raumer *et al*., 2013). In the northern Atlantic region for instance, a sequence of rift basins from Permian to Cretaceous has been described occurring before the opening of the ocean (e.g. Doré and Steward, 2002) making the rifting of the North Atlantic Ocean a long lasting process with several extensional events associated with a migration of eulerian poles as testified by the anticlockwise and successive clockwise rotation of superposed rift axes.

Based on this idea, we test whether the lithospheric extension can lead the rifting of the Alpine Tethys by comparing numerical modelling of post-collisional extension and successive rifting and oceanization with Permian-Triassic to Jurassic natural data from the Alps and northern Apennines (Fig. 1). In particular, we focus our attention on the thermal state of the pre-rifting (Permian-Triassic in age) lithosphere in order to explore if the opening of the Alpine Tethys started on a stable continental lithosphere or rather developed on a thermally perturbed one.

Results. We here discuss the results obtained for two subsequent numerical models that simulate the evolution of the European lithosphere from the late collision of the Variscan chain to the Jurassic opening of the Alpine Tethys. The first model accounts for the evolution of the crustal lithosphere after the Variscan subduction and collision (300 Ma) up to 220 Ma (Marotta *et al*., 2009). The second model accounts for the rifting of the continental lithosphere from 220 Ma up to reach the crustal breakup and the formation of the oceanic crust (Marotta *et al*., 2016). For both models different initial geodynamic configurations have been tested and we compare the results with natural data of Permian-Triassic metamorphic rocks and Jurassic gabbros and peridotites (Fig. 1), in order to evaluate which configuration best matches the observations. Natural data belong to different structural Alpine domains. Continental rocks are collected from Helvetic and Penninic domains (European paleomargin) and from Austroalpine and Southalpine domains (Adriatic paleomargin) and oceanic rocks are collected from Alpine and Apennine ophiolites (Fig. 1). The comparison is made in terms of contemporaneous agreement to lithology, pressure and temperature values, and ages. The differences between model predictions and natural P-T-age data are synthesized in Fig. 2, where the ages estimate for the rocks are shown using light grey bars for radiometric ages and dark grey for geologically determined ages.

For the first model we compare the results of two different configurations. The first one is characterized by a purely gravitational evolution of the lithosphere in order to simulate a late-orogenic collapse. The second configuration instead, is characterized by a forced extension of the lithosphere of 2 cm/yr. With respect to the purely gravitational simulation, for which the fit between predictions and observations is obtained for few data only (Fig. 2), the forced extension simulation agrees well with all collected natural data (Fig. 2). The most peculiar character of the Permian–Triassic igneous activity is the widespread emplacement of gabbro stocks at the base of the crust and the occurrence of basaltic products in the volcanics. Therefore, we verify whether the P-T conditions predicted for the lithospheric and asthenospheric mantle by different configurations cross the solidus of peridotite. Although predictions from all configurations satisfy the thermal state for mantle partial melting, the latter is attained at 75 km depth for the purely gravitational configuration and at 50 km depth for the simulation with forced extension. Basaltic melt production is thus compatible with all the simulated tectonic settings but, to allow the partial melting of the continental crust, the thermal state must be similar to that suggested by simulation with forced extension. The final thermo-mechanical setting is very different between the two configurations. In the purely gravitational simulation both the crustal thickness and the lithospheric thermal state are similar to the initial conditions, while in the forced extension simulation a strong lithospheric thinning occurs together with a hot thermal state.

The second model simulates the extension of the continental lithosphere up to reach the

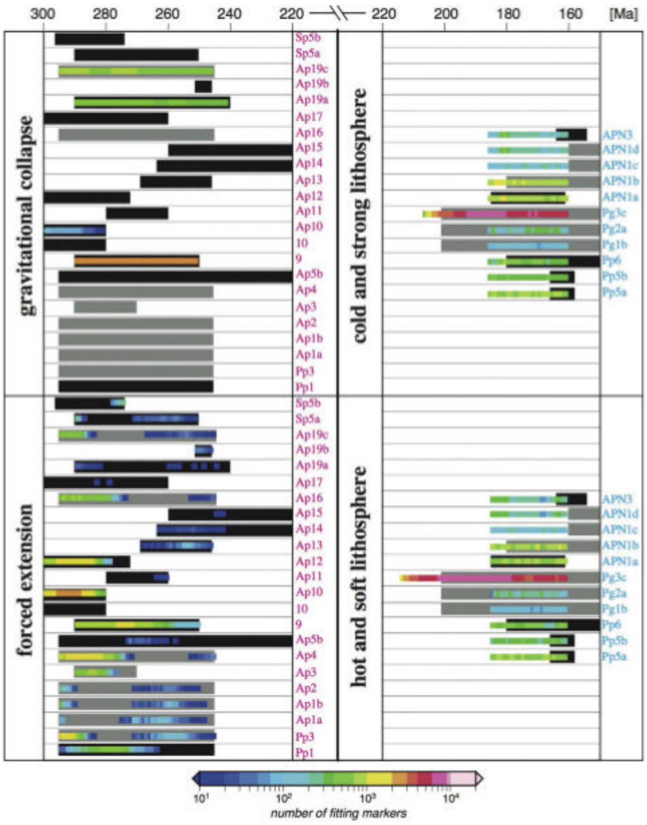

Fig. 2 – Duration of the agreement between the predictions and the natural data as well as number of fitting markers (colors) in terms of lithological affinity and coincident P–T values compared to the radiometric (black thick segments) and geologic (grey thick segments) ages of the natural data. Panel (a) refers to the hot simulations, whereas panel (b) refers to the cold one. The labels are defined in Fig. 1.

crustal breakup and the formation of the oceanic crust. The model also includes the hydration of the uprising mantle peridotite and the extension rate is constant and fixed to 1.25 cm/yr on the both sides of the domain (total extension rate of 2.5 cm/yr). Accounting for two different thermal configurations of the lithosphere allows to constrain two different pre-rifting settings of the Alpine lithosphere (hot and cold simulations with 1600 K isotherm at 80 and 220 km depth respectively). The model results in a symmetric rifting of the continental lithosphere and shows the exhumation of a serpentinized lithospheric mantle (ocean-continent transition zone – OCTZ). The onset of the lithospheric thinning strongly depends on the initial lithospheric

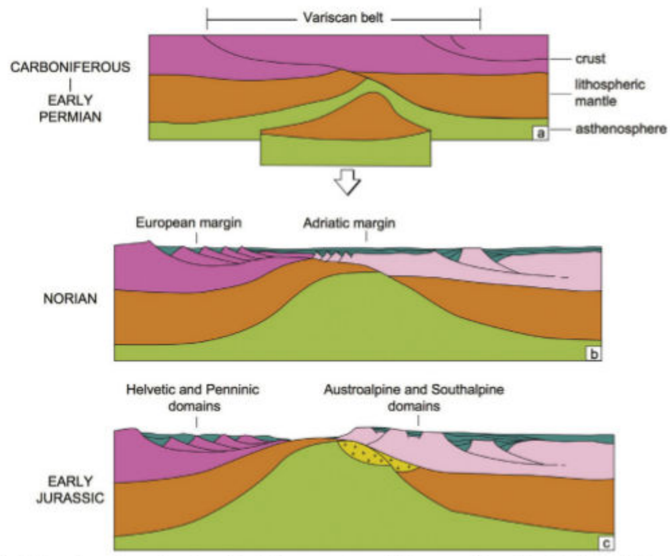

Fig. 3 – Schematic geodynamic cartoon illustrating some stages of the proposed transition from late collisional slab breakoff after the Variscan subduction to Jurassic ocean opening. Legend: pink = Variscan continental crust (dark = European; light = Adriatic); orange = lithospheric mantle; light green = asthenosphere; yellow = area of mantle partial melting generating oceanic gabbros; dark green = Permian-Jurassic sediments.

thermal state: for a cold and strong lithosphere, the thinning is very rapid (4.4 Ma) with respect to a hot and weak lithosphere (15.4 Ma). Similarly, the occurrence of the crustal breakup is shorter for a cold lithosphere (7.4 Ma) than for a hot lithosphere (approximately 31.4 Ma). For both the chosen initial thermal configurations of the lithosphere, the exhumation of the serpentinized mantle starts before the oceanic spreading and the mantle partial melting, making the model compatible with a magma-poor rifting, as suggested for the Alpine case (e.g., Manatschal *et al*., 2015). In the hot configuration the continental crust thickness sensibly decreases during the extension from 30 km to approximately 5 km close to the OCTZ. In the cold model instead, the crustal thickness decreases from 30 km to approximately 20 km. The comparison between the natural data and the model predictions shows a good agreement with all of the oceanic data for both hot and cold configurations. Taking into account that a hyperextended system has been proposed for the Alpine Tethys rifting (e.g. Manatschal *et al*., 2015) and a time span of approximately 30-40 Ma is considered between the first extensional structures related to the rifting (200 Ma, Mohn *et al*., 2012) and the oceanic gabbros emplacement (170-160 Ma, see review in Marotta *et al*., 2009, 2016), a rifting developed on thermally perturbed lithosphere better agrees the natural data available in ophiolites.

Discussion and conclusion. The comparison between Permian-Triassic to Jurassic natural data from the Alps and the northern Apennines and two subsequent numerical models simulating the evolution of the lithosphere from the late collision of the Variscan chain to the Jurassic opening of the Alpine Tethys suggests that: i) a forced extension of the lithosphere results in a thermal state that better agrees the Permian-Triassic high temperature event(s) than a solely late-orogenic collapse; ii) a rifting developed on a thermally perturbed lithosphere agrees with a hyperextended configuration of the Alpine Tethys rifting and with the duration of the extension up to the oceanization. These results suggest that the Alpine Tethys rifting and oceanization developed on a lithosphere characterized by a thermo-mechanical configuration consequent to a post-Variscan extension affecting the European realm during Permian and Triassic. Therefore, a long lasting period of continuous active extension can be envisaged for the breaking of Pangea supercontinent, starting from the unrooting of the Variscan belts (300 Ma, Fig. 3a), followed by the Permian-Triassic thermal peak highlighted by HT-LP metamorphism and gabbros emplacement (Fig. 3b), and ending with the crustal breakup and the formation of the Alpine Tethys ocean (170-160 Ma, Fig. 3c). This process could be characterized by alternated period of active extension and stasis, as proposed for the Northern Atlantic rifting or as envisaged for the Ivrea-Verbano Zone on the basis of three metamorphic ages (Permian, Triassic and Jurassic; Langone and Tiepolo, 2015). In order to explore this issue a continuous and polycyclic numerical model is necessary to record the thermo-mechanical inheritance of different events during the entire extensional process, and use ages and P-T-t paths of natural data as constraints.

References

Beardsmore, G. R. and Cull, J. P.; 2001: *Crustal Heat Flow: a guide to measurement and modelling.* Cambridge University Press, 321 pp.

Doré, A. G. and Stewart, I. C.; 2002: *Similarities and differences in the tectonics of two passive margins: the Northeast Atlantic Margin and the Australian North West Shelf*, in: Keep, M., Moss, S.J. (Eds.), The Sedimentary Basins of Western Australia 3. Petroleum Exploration Society of Australia (PESA), pp. 89-117.

Langone, A. and Tiepolo, M.; 2015: *U-Th-Pb "multi-phase" approach to the study of crystalline basement: application to the northernmost sector of the Ivrea-Verbano Zone (Alps).* Periodico di Mineralogia, **84**, 633-655.

Lardeaux, J. M. and Spalla, M. I.; 1991: *From granulites to eclogites in the Sesia zone (Italian Western Alps): a record of the opening and closure of the Piedmont ocean*. J. Metamorph. Geol, **9**, 35-59.

Manatschal, G., Lavier, L. and Chenin, P.; 2015: *The role of inheritance in structuring hyperextended rift systems: Some considerations based on observations and numerical modeling*. Gondwana Research, **27**, 140-164.

Marotta, A. M., Roda, M., Conte, K. and Spalla, M. I.; 2016: *Thermo-mechanical numerical model of the transition from continental rifting to oceanic spreading: the case study of the Alpine Tethys.* Geological Magazine, 1-30.

Marotta, A. M. and Spalla, M. I.; 2007: *Permian-Triassic high thermal regime in the Alps: Result of late Variscan collapse or continental rifting? Validation by numerical modeling*. Tectonics, **26**, 1-27.

Marotta, A. M., Spalla, M. I. and Gosso, G.; 2009: *Upper and lower crustal evolution during lithospheric extension: numerical modelling and natural footprints from the European Alps*, in: Ring, U., Wernicke, B. (Eds.), Extending a Continent: Architecture, Rheology and Heat Budget. The Geological Society, London, Special Publications, pp. 33-72.

Mohn, G., Manatschal, G., Beltrando, M., Masini, E. and Kusznir, N.; 2012: *Necking of continental crust in magma-poor rifted margins: Evidence from the fossil Alpine Tethys margins.* Tectonics, **31**, 1-28.

Sandiford, M. and Powell, R.; 1986. *Deep crustal metamorphism during crustal extension: modern and ancient examples*. Earth Planet. Sci. Lett., **79**, 151-158.

Schuster, R. and Stüwe, K.; 2008: *Permian metamorphic event in the Alps*. Geology, **36**, 603-606.

Spalla, M. I., Zanoni, D., Marotta, A. M., Rebay, G., Roda, M., Zucali, M. and Gosso, G.; 2014: *The transition from Variscan collision to continental break-up in the Alps: insights from the comparison between natural data and numerical model predictions*. Geol. Soc. London, Spec. Publ., **405**, 363-400.

Spiess, R., Cesare, B., Mazzoli, C., Sassi, R. and Sassi, F.P.; 2010: *The crystalline basement of the Adria microplate in the eastern Alps: a review of the palaeostructural evolution from the Neoproterozoic to the Cenozoic*. Rend. Lincei Sci. Fis. Nat., **21**, 31-50.

Thompson, A.B.; 1981: *The pressure–temperature (P,T) plane viewed by geophysicists and petrologists.* Terra Cogn., **1**, 11-20.

von Raumer, J. F., Bussy, F., Schaltegger, U., Schulz, B. and Stampfli, G. M.; 2013: *Pre-Mesozoic Alpine basements - Their place in the European Paleozoic framework.* Geol. Soc. Am. Bull., **125**, 89-108.

C.3 Abstract

EGU General Assembly 2014

Geophysical Research Abstracts
Vol. 16, EGU2014-7105, 2014
EGU General Assembly 2014

Numerical modelling of an ocean/continent subduction and comparison with Variscan orogeny real data

Anna Maria Marotta (1), Alessandro Regorda (1), M. Iole Spalla (2), Manuel Roda (3), and Gisella Rebay (4)
(1) University of Milan, Department Earth Sciences - Geophysics, Milano, Italy (anna.maria.marotta@unimi.it), (2) University of Milan, Department of Earth Sciences - Geology, Milano, Italy (iole.spalla@unimi.it), (3) Universiteit Utrecht, Fac. of Geosciences, Utrecht, The Netherlands (m.roda@uu.nl), (4) University of Pavia, Department of Earth Science and Environment, Pavia, Italy (gisella.rebay@unipv.it)

The effects of the viscous heating and the hydration of the mantle wedge on the continental crust recycling during the evolution of an ocean/continent subduction system are analysed by using a 2D finite element thermo-mechanical model. The dehydration of the oceanic slab, and the consequent hydration of the mantle wedge, is accomplished by lawsonite breakdown (Roda et al., 2010; Roda et al., 2011). The model shows the activation of convective cells in the mantle wedge that determine the recycling of subducted continental crust. Moreover, with respect to Marotta and Spalla (2007), in which the hydration of the mantle wedge was not taken into account, much more correspondences between P-T predictions and the natural P-T estimates of the Alpine Variscan metamorphism are obtained.

SGI-SIMP Annual Congress

Rend. Online Soc. Geol. It., Suppl. n. 1 al Vol. 31 (2014) CONGRESSO SGI-SIMP 2014

2D numerical study of the effects of mantle hydration and viscous heating on the dynamics of the wedge area within an ocean/continent subduction complex: the case study of Variscan crust in the Alpine domain

Regorda A.*[1], Marotta A.M.[1], Spalla M.I.[1], Roda M.[2] & Rebay G.[3]

1. Dipartimento di Scienze della Terra, Università degli Studi di Milano. 2. Faculty of Geosciences - Universiteit Utrecht. 3. Dipartimento di Scienze della Terra e dell'Ambiente, Università di Pavia.

Corresponding email: alessandro.regorda@unimi.it

Keywords: Mantle hydration and viscous heating, Numerical modeling, ocean/continent subduction.

The geodynamics of a convergent ocean/continent margin, evolving from subduction to continental collision, was analyzed by means of a 2D finite element thermo-mechanical model, in which the physics of the crust-mantle system is described by the equations for continuity, conservation of momentum and conservation of energy. A viscous behavior for the whole system and density and viscosity depending from both temperature and composition are assumed. Different values of convergence velocities, 3, 5 and 8 cm/yr, have been used, as representative of slow, medium and fast subductions.

Our analysis is particularly focused on the effects of viscous heating and mantle hydration on the dynamics in the wedge area. The results support that both mechanisms induce the development of short wavelength convective cells in the wedge area that favor the exhumation of subducted crustal material since the early stages of the subduction. Model predictions, in terms of pressure, temperature, lithology and age, have been compared with the structural, petrological and age natural data from the Variscan crust of the Alpine domain.

Variscan2015

Effects of mantle hydration and viscous heating on the dynamics of mantle wedge in a subduction system: differences and similarities of 2D model predictions with examples from the Variscan crust.

Alessandro Regorda*, Anna Maria Marotta*, Manuel Roda*, Jean Marc Lardeaux** and M. Iole Spalla*

(*) Università degli Studi di Milano, Dipartimento di Scienze della Terra, Milan, Italy
(**) Géoazur, Université de Nice-Sophia Antipolis, France

Mechanisms that favor the exhumation of subducted crustal material, both continental and oceanic, have been explored by mean of several models and 2D numerical studies. Petrological and numerical models (e.g. Ernst and Liou, 2008; Roda et al., 2010; Regorda et al., 2013 and refs. therein) reveal that the dehydration process of the oceanic slab, with a consequent hydration of the mantle wedge, have a primary role for developing a convective dynamics in the area between the slab and the upper plate, since the beginning of the subduction.
The geodynamics of a convergent ocean/continent margin, evolving from subduction to continental collision, was analyzed by means of a 2D finite element thermo-mechanical model, in which the physics of the crust-mantle system is described by the equations for continuity, conservation of momentum and conservation of energy. A viscous behavior for the whole system is assumed, with both density and viscosity depending on temperature and composition. Different values of convergence velocities, 3, 5 and 8 cm/yr, have been used, as representative of slow, medium and fast subduction systems, respectively.
Our analysis is particularly focused on the effects of viscous heating and mantle hydration on the dynamics in the wedge area. The results support that these mechanisms, differently from our reference model without hydration and viscous heating (Marotta and Spalla, 2007), induce the development of short wavelength convective cells in the wedge area, that favor the exhumation of buried crustal material since the early stages of the subduction (Figure 1).
Model predictions, in terms of pressure, temperature, lithology and time, will be compared with structural, petrological and age natural data from the European Variscan crust to check and interactively improve 2D numerical models of the explored ocean/continent subduction system.

REFERENCES

Ernst W.G. and Liou J.G. (2008), High- and ultrahigh-pressure metamorphism: Past results and future prospects, *American Mineralogist*, 93, 1771–1786, doi: 10.2138/am.2008.2940.

Marotta A.M. and Spalla M.I. (2007), Permian-Triassic high thermal regime in the Alps: Result of late Variscan collapse or continental rifting? Validation by numerical modeling, *Tectonics,* 26, TC4016, doi: 10.1029/2006TC002047.

Regorda A., Marotta A.M. and Spalla M.I. (2013), Numerical model of an ocean/continent subduction and comparison with Variscan orogeny natural data, *Rend. Online Soc. Geol. It.* 01/2013, 29, 142-145.

Roda M., Marotta A.M. and Spalla M.I. (2010), Numerical simulation of an ocean-continent convergent system: Influence of subduction geometry and mantle wedge hydration on crustal recycling, *Geochem. Geophys. Geosyst*., 11, Q05008, doi: 10.1029/2009GC003015.

GIGS Annual Meeting 2015

2D numerical model of an ocean/continent subduction system: examples from the Variscan crust

Regorda A.*[1], Marotta A.M.[1], Roda M.[1], Lardeaux J.M.[2] & Spalla M.I.[1]

1. Università degli Studi di Milano, Dipartimento di Scienze della Terra, Milan, Italy
2. Géoazur, Université de Nice-Sophia Antipolis, France

Corresponding email: alessandro.regorda@unimi.it

Keywords: ocean/continent subduction, numerical model, Variscan

Mechanisms that favor the exhumation of subducted crustal material, both continental and oceanic, have been explored by mean of several models and 2D numerical studies. Petrological and numerical models (e.g. Ernst and Liou, 2008; Roda et al., 2010 and refs. therein) reveal that the dehydration process of the oceanic slab, with a consequent hydration of the mantle wedge, have a primary role for developing a convective dynamics in the area between the slab and the upper plate, since the beginning of the subduction.
The geodynamics of a convergent ocean/continent margin, evolving from subduction to continental collision, was analyzed by means of a 2D finite element thermo-mechanical model, in which the physics of the crust-mantle system is described by the equations for continuity, conservation of momentum and conservation of energy. A viscous behavior for the whole system is assumed, with both density and viscosity depending on temperature and composition. Different values of convergence velocities, 3, 5 and 8 cm/yr, have been used, as representative of slow, medium and fast subduction systems, respectively.
Our analysis is particularly focused on the effects of viscous heating and mantle hydration on the dynamics in the wedge area. The results support that these mechanisms, differently from our reference model without hydration and viscous heating (Marotta and Spalla, 2007), induce the development of short wavelength convective cells in the wedge area, that favor the exhumation of buried crustal material since the early stages of the subduction.
Model predictions, in terms of pressure, temperature, lithology and time, will be compared with structural, petrological and age natural data from the European Variscan crust to check and interactively improve 2D numerical models of the explored ocean/continent subduction system.

Ernst W.G. & Liou J.G. (2008) - High- and ultrahigh-pressure metamorphism: Past results and future prospects. American Mineralogist, 93, 1771–1786.
Marotta A.M. & Spalla M.I. (2007) - Permian-Triassic high thermal regime in the Alps: Result of late Variscan collapse or continental rifting? Validation by numerical modeling. Tectonics, 26, TC4016.
Roda M., Marotta A.M. & Spalla M.I. (2010) - Numerical simulation of an ocean-continent convergent system: Influence of subduction geometry and mantle wedge hydration on crustal recycling. Geochem. Geophys. Geosyst., 11, Q05008.

AGU Fall Meeting 2015

NEW INSIGHTS INTO THE DYNAMICS OF WEDGE AREAS FROM A 2D NUMERICAL STUDY OF THE EFFECTS OF SHEAR HEATING AND MANTLE HYDRATION ON AN OCEAN-CONTINENT SUBDUCTION SYSTEM

Manuel Roda, Alessandro Regorda, Anna Maria Marotta, M. Iole Spalla

Abstract

To obtain new insights regarding the mechanisms that favor the exhumation of buried crustal material during ocean-continent subduction, we have developed a 2D finite element model that investigates the effects of shear heating and mantle hydration on the dynamics of wedge areas. The development of the model consists of an initial phase of active oceanic subduction and a second phase, after collision, of pure gravitational evolution; in addition, it considers 3 different velocities of active subduction. Our results show that accounting for mantle hydration is essential to produce small-scale convective flows in a wedge area with the consequent recycling and exhumation of subducted material. In addition, the dynamics of hydrated areas are strictly correlated to the thermal state at the external boundaries of the mantle wedge, and the extension of hydrated areas is independent from the subduction velocities when mantle hydration and shear heating are simultaneously considered during the active subduction phase. During the pure gravitational phase, the hydrated portion of the wedge undergoes a progressive enlargement for models with a high subduction velocity during the previous active phase. Finally, a comparison between the predicted P/T ratios and the P-T conditions recorded by markers during subduction, which show metamorphic gradients that are traditionally considered to be distinctive examples of different phases of evolution in an ocean/continent subduction complex, supports the notion that contrasting P-T conditions can contemporaneously characterize different portions of the subduction system during successive phases of modeled subduction-collision.

Bibliography

Abers, G. A. (2005), Seismic low-velocity layer at the top of subducting slabs: observations, predictions, and systematics, *Earth and Planetary Science Letters*, *149*, 7–29, doi: 10.1016/j.pepi.2004.10.002.

Afonso, J. C., and G. Ranalli (2004), Crustal and mantle strengths in continental lithosphere: is the jelly sandwich model obsolete?, *Tectonophysics*, *394*, 221–232, doi: 10.1016/j.tecto.2004.08.006.

Agard, P., P. Yamato, L. Jolivet, and E. Burov (2009), Exhumation of oceanic blueschists and eclogites in subduction zones: Timing and mechanisms, *Earth-Science Reviews*, *92*, 53–79, doi:10.1016/j.earscirev.2008.11.002.

Albini, S., et al. (1994), Alpine deformations and pre-Alpine remnants in the north-eastern Orobic Alps, Southalpine Belt, *Proceedings of the symposium "CROP - Alpi Centrali".*, *2*(January), 25–39.

Alejano, L. R., and A. Bobet (2012), Drucker-Prager criterion, *Rock Mechanics and Rock Engineering*, *45*(6), 995–999, doi:10.1007/s00603-012-0278-2.

Arcay, D., E. Tric, and M.-P. Doin (2005), Numerical simulation of subduction zones.Effect of slab dehydration on the mantle wedge dynamics., *Physics of the Earth and Planetary Interiors*, *149*(1-2), 133–153, doi:10.1016/j.pepi.2004.08.020.

Bally, A. W. (1981), Thoughts on the tectonics of folded belts, *Geological Society, London, Special Publications*, *9*(1), 13–32, doi:10.1144/GSL.SP.1981.009.01.03.

Banno, S. (1970), Classification of eclogites in terms of physical conditions of their origin, *Physics of the Earth and planetary Interiors*, (1965), 405–421.

Barbey, P., A. Villaros, C. Marignac, and J.-M. Montel (2015), Multiphase melting , magma emplacement and P-T-time path in late-collisional context : the Velay example (Massif Central , France), *Bulletin de la Societe Géologique de France*, *186*(2-3), 93–116.

Barbieri, C., B. Carrapa, A. Di Giulio, J. Wijbrans, and G. R. Murrell (2003), Provenance of Oligocene synorogenic sediments of the Ligurian Alps (NW Italy): Inferences on belt age and cooling history, *International Journal of Earth Sciences*, *92*(5), 758–778, doi: 10.1007/s00531-003-0351-x.

Bellot, J. P., and J. Y. Roig (2007), Episodic exhumation of HP rocks inferred from structural data and P-T paths from the southwestern Massif Central (Variscan belt, France), *Journal of Structural Geology*, *29*(9), 1538–1557, doi:10.1016/j.jsg.2007.04.001.

Benciolini, L., M. M. E. Poli, D. Visonà, and A. Zanferrari (2006), Looking inside late Variscan tectonics: structural and metamorphic heterogeneity of the Eastern Southalpine basement (NE Italy), *Geodinamica Acta*, *19*(1), 17–32.

Berger, A., S. M. Schmid, M. Engi, R. Bousquet, and M. Wiederkehr (2010), Mechanisms of mass and heat transport during Barrovian metamorphism: A discussion based on field evidence from the Central Alps (Switzerland/N-Italy), *Tectonics*, doi: 10.1029/2009TC002622.

Bertotti, G., V. Picotti, D. Bernoulli, and A. Castellarin (1993), From rifting to drifting: tectonic evolution of the South-Alpine upper crust from the Triassic to the Early Cretaceous, *Sedimentary Geology*, *86*(1–2), 53–76, doi:http://dx.doi.org/10.1016/0037-0738(93)90133-P.

Best, M. G., and E. H. Christiansen (2001), *Igneous Petrology*, Blackwell Sci., London.

Billen, M. I. (2008), Modeling the Dynamics of Subducting Slabs, *Annual Review of Earth and Planetary Sciences*, *36*(1), 325–356, doi:10.1146/annurev.earth.36.031207.124129.

Billen, M. I., and M. Gurnis (2001), A low viscosity wedge in subduction zones, *Earth and Planetary Science Letters*, *193*, 227–236.

Borghi, A., M. Gattiglio, F. Mondino, and G. Zaccone (1999), Structural and metamorphic evidence of pre-Alpine basement in the Ambin nappe (Cottian Alps, Italy), *Memorie della Società Geologica Italiana*, *51*(1), 205–220.

Boriani, A., and I. Villa (1997), Geochronology of regional metamorphism in the Ivrea-Verbano zone and Serie dei Laghi, Italian Alps, *Schweiz. mineral. petrogr. Mitt*, *77*, 381–401.

Boutin, R., and R. Montigny (1993), Datation 39 Ar/ 40 Ar des amphibolites du complexe leptyno-amphibolique du plateau d'Aigurande : collision varisque à 390 Ma dans le Nord-Ouest du Massif central français, *Compte Rendu Academie des Sciences de Paris*, *316*, 1391–1398.

Braga, R., H.-J. Massonne, and L. Morten (2007), An early metamorphic stage for the Variscan Ulten Zone gneiss (NE Italy): evidence from mineral inclusions in kyanite, *Mineralogical magazine*, *71*(6), 691–702, doi:10.1180/minmag.2007.071.6.691.

Burg, J. P., a. F. Leyreloup, F. Romney, and C. P. Delor (1989), Inverted metamorphic zonation and Variscan thrust tectonics in the rouergue area (Massif Central, France): P-T-t record from mineral to regional scale, *Geological Society, London, Special Publications*, *43*(1), 423–439, doi:10.1144/GSL.SP.1989.043.01.38.

Bussy, F., M. Sartori, and P. Thélin (1996), U-Pb zircon dating in the middle Penninic basement of the Western Alps (Valais, Switzerland), *Schweizerische Mineralogische Und Petrographische Mitteilungen*, *76*, 81–84.

Bussy, F., J. Hernandez, and J. F. von Raumer (2000), Bimodal magmatism as a consequence of the post-collisional readjustment of the thickened Variscan continental lithosphere (Aiguilles Rouges–Mont Blanc Massifs, Western Alps), *Special Paper 350: The Fourth Hutton Symposium on the Origin of Granites and Related Rocks*, *350*, 221–233, doi:10.1130/0-8137-2350-7.221.

Carminati, E., G. B. Siletto, and D. Battaglia (1997), Thrust kinematics and internal deformation in basement-involved fold and thrust belts: The eastern Orobic Alps (Central Southern Alps, northern Italy), *Tectonics*, *16*(2), 259–271, doi:10.1029/96TC03936.

Carslaw, H. S., and J. C. Jaeger (1959), *Conduction of heat in solids*, second ed., 517 pp., Oxford University Press, London.

Cassinis, G., F. Massari, C. Neri, and C. Venturini (1988), The continental Permian in the southern alps (Italy)-a review, *Zeitschrift fur geologische Wissenschaften*, *16*(11-12), 1117–1126.

Cavazza, W., and F. Wezel (2003), The Mediterranean region-a geological primer, *Episodes*, *26*(3), 160–168.

Chopin, C. (1984), Coesite and pure pyrope in high-grade blue-schists of the Western Alps, *Contrib Mineral Petrol*, *86*, 107–118.

Chopra, P. N., and M. S. Peterson (1981), The experimental deformation of dunite, *Tectonophysics*, *78*, 453–473, doi:10.1016/0040-1951(81)90024-X.

Christensen, U. R. (1992), An Eulerian Tecnique for thermo-mechanical model of lithospheric extension, *Journal of Geophysical Research*, *97*, 2015–2036, doi:10.1029/91JB02642.

Cloos, M. (1993), Lithospheric buoyancy and collisional orogenesis: Subduction of oceanic plateaus, continental margins, island arcs, spreading ridges and seamounts, *Geological Society of America Bulletin*, *105*, 715–737.

Coleman, R., D. Lee, L. Beatty, and W. Brannock (1965), Eclogites and Eclogites: Their Differences and Similarities, *Geological Society of America Bulletin*, *77*, 483–508.

Coleman, R. G. (1971), Plate tectonic emplacement of upper mantle peridotites along continental edges, *Journal of Geophysical Research*, *76*(5), 1212–1222, doi:10.1029/JB076i005p01212.

Colmenares, L., and M. Zoback (2002), A Statistical evaluation of six rock failure.

Compagnoni, R., and S. Ferrando (2010), Paleo-European crust of the Italian western Alps: Geological history of the Argentera Massif and comparison with Mont Blanc–Aiguilles Rouges and Maures, *Journal of the Virtual Explorer, Electronic Edition*, *36*(3), doi:10.3809/jvirtex.2009.00228.

Corsini, M., G. Ruffet, and R. Caby (2004), Alpine and late-hercynian geochronological constraints in the Argentera Massif (Western Alps), *Eclogae Geologicae Helvetiae*, *97*(1), 3–15, doi:10.1007/s00015-004-1107-8.

Cortesogno, L., G. Cassinis, G. Dallagiovanna, L. Gaggero, G. Oggiano, A. Ronchi, S. Seno, and M. Vanossi (1998), The Variscan post- collisional volcanism in Late Carboniferous–Permian sequences of Ligurian Alps, Southern Alps and Sardinia (Italy): a synthesis, *Lithos*, *45*, 305–328.

Costa, S., H. Maluski, and J. M. Lardeaux (1993), 40Ar39Ar chronology of Variscan tectono-metamorphic events in an exhumed crustal nappe: the Monts du Lyonnais complex (Massif Central, France), *Chemical Geology*, *105*(4), 339–359, doi:10.1016/0009-2541(93)90135-6.

Cruciani, C., E. Carminati, and C. Doglioni (2005), Slab dip vs. lithosphere age: No direct function, *Earth and Planetary Science Letters*, *238*, 298–310, doi:10.1016/j.epsl.2005.07.025.

Dal Piaz, G. V. (2001), Geology of the Monte Rosa massif: historical review and personal comments, *Schweizerische Mineralogische und Petrographische Mitteilungen*, *81*(3), 275–303.

dal Piaz, G. V. (2010), The Italian Alps: A journey across two centuries of Alpine geology, *Journal of the Virtual Explorer*, *36*, doi:10.3809/jvirtex.2010.00234.

Dal Piaz, G. V., A. Bistacchi, and M. Massironi (2003), Geological outline of the Alps, *Episodes*, *26*(3), 175–180.

Dale, J., and T. J. B. Holland (2003), Geothermobarometry, P-T paths and metamorphic field gradients of high-pressure rocks from the Adula Nappe, Central Alps, *Journal of Metamorphic Geology*, *21*(8), 813–829, doi:10.1046/j.1525-1314.2003.00483.x.

Delleani, F., M. I. Spalla, G. Rebay, and M. Zucali (2012), Tectonometamorphic evolution of the Ivozio complex (Sesia-Lanzo Zone, Western Alps), *Rendiconti Online Società Geologica Italiana*, *22*, 69–72.

Demange, M. (1985), The eclogite-facies rocks of the Montagne Noire, France, *Chemical Geology*, *50*(1-3), doi:10.1016/0009-2541(85)90119-6.

Desmons, J., and D. Mercier (1993), Passing Through the Briancon Zone, in *Pre-Mesozoic Geology in the Alps*, pp. 279–296.

Desmons, J., R. Compagnoni, and L. Cortesogno (1999a), Pre-Alpine metamorphism of the Internal zones of the Western Alps, *Schweizerische Mineralogische Und Petrographische Mitteilungen*, *79*, 23–39.

Desmons, J., R. Compagnoni, and L. Cortesogno (1999b), Alpine metamorphism of the Western Alps : I. Middle to high T/P metamorphism, *Schweizerische Mineralogische Und Petrographische Mitteilungen*, *79*, 89–110.

di Paola, S. (2001), Eredità litostratigrafica, strutturale e metamorfica paleozoica nel margine interno Europeo (Grandes Rousses e Argentera), ristrutturato durante l'orogenesi Alpina, Ph.D. thesis, Università degli Studi di Milano and Université Claude Bernard Lyon.

di Paola, S., and M. I. Spalla (2000), Contrasting tectonic records in pre-Alpine metabasites of the Southern Alps (lake Como, Italy), *Journal of Geodynamics*, *30*(1-2), 167–189, doi:10.1016/S0264-3707(99)00032-0.

Diella, V., M. I. Spalla, and A. Tunesi (1992), Contrasted thermo-mechanical evolutions in the South- alpine metamorphic basement of the Orobic Alps (Central Alps, Italy), *Journal of Metamorphic Geology*, *10*, 203–219.

Donea, J., and A. Huerta (2003), *Finite Element Methods for Flow Problems*, vol. 1, 350 pp., Wiley, doi:10.1017/CBO9781107415324.004.

Droop, G. T. R. (1983), Pre-Alpine eclogites in the Pennine Basement Complex of the Eastern Alps, *Journal of Metamorphic Geology*, *1*(1), 3–12, doi:10.1111/j.1525-1314.1983.tb00261.x.

Dubois, J., and M. Diament (1997), *Géophysique*, Masson, Paris.

Ducrot, J., J. R. Lancelot, and J. Marchand (1983), Datation U-Pb sur zircons de l'éclogite de La Borie (Haut-Allier, France) et conséquences sur l'évolution ante-hercynienne de l'Europe occidentale, *Earth and Planetary Science Letters*, *62*(3), 385–394, doi:10.1016/0012-821X(83)90009-2.

Dufour, E., J.-M. Lardeaux, and D. Coffrant (1985), éclogites ert granulites dans les Monts du Lyonnais: une èvolution métamorphique plurifaciale éohercynienne, *Compte Rendu Academie des Sciences de Paris*, *300*(4), 141–144.

Duguet, M., N. Le Breton, and M. Faure (2007), P-T paths reconstruction of a collisional event: The example of the Thiviers-Payzac Unit in the Variscan French Massif Central, *Lithos*, *98*(1-4), 210–232, doi:10.1016/j.lithos.2007.04.001.

Edel, J. B., K. Schulmann, E. Skrzypek, and A. Cocherie (2013), Tectonic evolution of the European Variscan belt constrained by palaeomagnetic, structural and anisotropy of magnetic susceptibility data from the Northern Vosges magmatic arc (eastern France), *Journal of the Geological Society*, *170*(5), 785–804, doi:10.1144/jgs2011-138.

Emmanuel, S., and B. Berkowitz (2006), Suppression and stimulation of seafloor hydrothermal convection by exothermic mineral hydration, *Earth and Planetary Science Letters*, *243*(3-4), 657–668, doi:10.1016/j.epsl.2006.01.028.

England, P., and S. Richardson (1977), The influence of erosion upon the mineral facies of rocks from different metamorphic environments, *Journal of the Geological Society*, *143*, 201–213.

England, P., and A. Thompson (1984), Pressure–Temperature–Time Paths of Regional Metamorphism I. Heat Transfer during the Evolution of Regions of Thickened Continental Crust, *Journal of Petrology*, *25*(4), 894–928, doi:10.1093/petrology/25.4.894.

Ernst, W. (1971a), Metamorphic zonations on presumably subducted lithospheric plates from Japan, California and the Alps, *Contributions to Mineralogy and Petrology*, *34*(1), 43–59, doi:10.1007/BF00376030.

Ernst, W., and J. Liou (2008), High- and ultrahigh-pressure metamorphism: Past results and future prospects, *American Mineralogist*, *93*(11-12), 1771–1786, doi:10.2138/am.2008.2940.

Ernst, W. G. (1971b), Do mineral parageneses reflect unusually high-pressure conditions of Franciscan metamorphism?, doi:10.2475/ajs.270.2.81.

Ernst, W. G. (1973), Blueschist metamorphism and P-T regimes in active subduction zones, *Tectonophysics*, *17*, 255–272.

Ernst, W. G. (1999), Metamorphism, partial preservation, and exhumation of ultrahigh-pressure belts, *Island Arc*, *8*(2), 125–153, doi:10.1046/j.1440-1738.1999.00227.x.

Ernst, W. G. (2005), Alpine and Pacific styles of Phanerozic mountain building: subduction-zone petrogenesis of continental crust, *Terra Nova*, *17*, 165–188.

Eskola, P. (1920), The Mineral Facies of Rocks, *Norsk Geologisk Tidsskrift*, *6*, 143–194.

Faccenda, M. (2014), Water in the slab: A trilogy, *Tectonophysics*, *614*, 1–30, doi:10.1016/j.tecto.2013.12.020.

Faccenda, M., and N. S. Mancktelow (2010), Fluid flow during unbending: Implications for slab hydration, intermediate-depth earthquakes and deep fluid subduction, *Tectonophysics*, *494*(1-2), 149–154, doi:10.1016/j.tecto.2010.08.002.

Faccenda, M., G. Minelli, and T. V. Gerya (2009), Coupled and decoupled regimes of continental collision: Numerical modeling, *Earth and Planetary Science Letters*, *278*, 337–349, doi:10.1016/j.epsl.2008.12.021.

Faryad, S. W., F. Melcher, G. Hoinkes, J. Puhl, T. Meisel, and W. Frank (2002), Relics of eclogite facies metamorphism in the Austroalpine basement, Hochgroessen (Speik complex), Austria, *Mineralogy and Petrology*, *74*, 49–73.

Faure, M., A. E. Prost, and E. Lasne (1990), Déformation ductile extensive d'âge namuro-westphalien dans le plateau d'Aigurande, Massif central français, *Bulletin de la Societe Geologique de France*, *1*(8), 189–197.

Faure, M., E. B. Mézème, M. Duguet, C. Cartier, and J. Y. Talbot (2005), Paleozoic tectonic evolution of medio-Europa from the example of the French Massif Central and Massif Armoricain, *Journal of the Virtual Explorer*, *19*, doi:10.3809/jvirtex.2005.00120.

Faure, M., E. B. Mézème, A. Cocherie, P. Rossi, A. Chemenda, and D. Boutelier (2008), Devonian geodynamic evolution the Variscan Belt, insights from the French Massif Central and Massif Armoricain, *Tectonics*, *27*(2), 1–19, doi:10.1029/2007TC002115.

Faure, M., J.-M. Lardeaux, and P. Ledru (2009), A review of the pre-Permian geology of the Variscan French Massif Central, *Comptes Rendus Geoscience*, *341*(2-3), 202–213, doi:10.1016/j.crte.2008.12.001.

Faure, M., A. Cocherie, J. Gaché, C. Esnault, C. Guerrot, P. Rossi, L. Wei, and L. Qiuli (2014), Middle Carboniferous intracontinental subduction in the Outer Zone of the Variscan Belt (Montagne Noire Axial Zone, French Massif Central): multimethod geochronological approach of polyphase metamorphism, *Geological Society, London, Special Publications*, *405*(1), 289–311, doi:10.1144/SP405.2.

Ferrando, S., B. Lombardo, and R. Compagnoni (2008), Metamorphic history of HP mafic granulites from the Gesso-Stura Terrain (Argentera Massif, Western Alps, Italy), *European Journal of Mineralogy*, *20*(5), 777–790, doi:10.1127/0935-1221/2008/0020-1891.

Feybesse, J.-L., J.-M. Lardeaux, V. Johan, M. Tegyey, E. Dufour, B. Lemière, and J. Delfour (1988), La série de la Brévenne (Massif central francais): une unité dévonienne charriée sur le complexe métamorphique des Monts du Lyonnais à la fin de la collision varisque, *Compte Rendu Academie des Sciences de Paris*, *307*(2), 991–996.

Franke, W. (2000), The mid-European segment of the Variscides: tectonostratigraphic units, terrane boundaries and plate tectonic evolution, *Geological Society, London, Special Publications*, *179*(1), 35–61, doi:10.1144/GSL.SP.2000.179.01.05.

Fumasoli, M. (1974), Geologie des Gebietes nördlich und südlich der Jorio-Tonale-Linie im Westen von Gravedona (Como, Italia), Ph.D. thesis.

Gardien, V., and J.-M. Lardeaux (1991), Découverte d'éclogites dans le synforme de Maclas: extension de l'Unité Supérieure des Gneiss à l'Est du Massif Central, *Compte Rendu Academie des Sciences Paris*, *312*, 61–68.

Gardien, V., J.-M. Lardeaux, and M. Misseri (1988), Les péridotites des Monts du Lyonnais (Massif Central Français): témoins privilégiés d'une subduction de lithosphère océanique paléozoique, *Compte Rendu Academie des Sciences de Paris*, *307*, 1967–1972.

Gardien, V., E. Reusser, and D. Marquer (1994), Pre-Alpine metamorphic evolution of the gneisses from the Valpelline series (Western Alps, Italy), *Schweiz. Mineral. Petrogr. Mitt.*, *74*, 489–502.

Gasco, I., A. Borghi, and M. Gattiglio (2010), Metamorphic evolution of the Gran Paradiso Massif: A case study of an eclogitic metagabbro and a polymetamorphic glaucophane–garnet micaschist, *Lithos*, *115*(1-4), 101–120, doi:10.1016/j.lithos.2009.11.009.

Gasco, I., A. Borghi, and M. Gattiglio (2011a), P–T Alpine metamorphic evolution of the Monte Rosa nappe along the Piedmont Zone boundary (Gressoney Valley, NW Italy), *Lithos*, *127*(1-2), 336–353, doi:10.1016/j.lithos.2011.09.007.

Gasco, I., M. Gattiglio, and A. Borghi (2011b), Lithostratigraphic setting and P-T metamorphic evolution for the Dora Maira Massif along the Piedmont Zone boundary (middle Susa Valley, NW Alps), *International Journal of Earth Sciences*, *100*(5), 1065–1085, doi:10.1007/s00531-011-0640-8.

Gebelin, A., G. Martelet, M. Brunel, M. Faure, and P. Rossi (2004), Late Hercynian leucogranites modelling as deduced from new gravity data: The example of the Millevaches massif (Massif Central, France), *Bulletin de la Societe Geologique de France*, *175*(3), 239–248, doi:10.2113/175.3.239.

Gébelin, A., F. Roger, and M. Brunel (2009), Syntectonic crustal melting and high-grade metamorphism in a transpressional regime, Variscan Massif Central, France, *Tectonophysics*, *477*(3-4), 229–243, doi:10.1016/j.tecto.2009.03.022.

Genier, F., F. Bussy, J.-L. Epard, and L. Baumgartner (2008), Water-assisted migmatization of metagraywackes in a Variscan shear zone, Aiguilles-Rouges massif, western Alps, *Lithos*, *102*(3-4), 575–597, doi:10.1016/j.lithos.2007.07.024.

Gerya, T. (2011), Future directions in subduction modeling, *Journal of Geodynamics*, *52*(5), 344–378, doi:10.1016/j.jog.2011.06.005.

Gerya, T. V., and B. Stockhert (2002), Exhumation rates of high pressure metamorphic rocks in subduction channels: The effect of Rheology., *Geophysical Research Letters*, *29*(8), 1–19, doi:10.1029/2002TC001406.

Gerya, T. V., and B. Stöckhert (2006), Two-dimensional numerical modeling of tectonic and metamorphic histories at active continental margins, *International Journal of Earth Sciences*, *90*(2), 250–274, doi:10.1007/s00531-005-0035-9.

Gerya, T. V., and D. A. Yuen (2003), Rayleigh–Taylor instabilities from hydration and melting propel 'cold plumes' at subduction zones, *Earth and Planetary Science Letters*, *212*(1-2), 47–62, doi:10.1016/S0012-821X(03)00265-6.

Giacomini, F., R. Braga, M. Tiepolo, and R. Tribuzio (2007), New constraints on the origin and age of Variscan eclogitic rocks (Ligurian Alps, Italy), *Contributions to Mineralogy and Petrology*, *153*(1), 29–53, doi:10.1007/s00410-006-0131-2.

Giobbi, M. E., A. Boriani, and I. Villa (2003), Pre-Alpine ophiolites in the basement of Southern Alps: the presence of a bimodal association (LAG-Leptyno-Amphibolitic group) in the Serie dei Laghi (N-Italy, Ticino-CH), *Rendiconti Accademia Lincei*, *9*(14), 79–99.

Giobbi, O. E., and A. Gregnanin (1983), The crystalline basement of the "Massiccio delle Tre Valli Bresciane": new petrographic and chemical data, *Memorie della Società Geologica Italiana*, *26*, 133–144.

Giorgis, D., P. Thelin, G. Stampfli, and F. Bussy (1999), The Mont-Mort metapelites: Variscan metamorphism and geodynamic context (Brianconnais basement, Western Alps, Switzerland), *Schweizerische Mineralogische und Petrographische Mitteilungen*, *79*(3), 381–398.

Godard, G. (2001), Eclogites and their geodynamic interpretation: a history, *Journal of Geodynamics*, *32*(1-2), 165–203, doi:10.1016/S0264-3707(01)00020-5.

Godard, G., S. Martin, G. Prosser, J. Kienast, and L. Morten (1996), Variscan migmatites, eclogites and garnet-peridotites of the Ulten zone, Eastern Austroalpine system, *Tectonophysics*, *259*, 313–341.

Gorczyk, W., T. V. Gerya, J. a. D. Connolly, D. a. Yuen, and M. Rudolph (2006), Large-scale rigid-body rotation in the mantle wedge and its implications for seismic tomography, *Geochemistry, Geophysics, Geosystems*, *7*(5), 1–23, doi:10.1029/2005GC001075.

Gorczyk, W., S. Guillot, T. V. Gerya, and K. Hattori (2007), Asthenospheric upwelling, oceanic slab retreat, and exhumation of UHP mantle rocks: Insights from Greater Antilles, *Geophysical Research Letters*, *34*, doi:10.1029/2007GL031059.

Gosso, G., B. Messiga, and M. Spalla (1995), Dumortierite-kyanite relics within the HT-LP country rocks of the Sondalo Gabbro: a record of extension related uplift of HP-rocks, *International Ophiolite Symposium*, p. 55.

Grandjean, V., S. Guillot, and A. Pecher (1996), Un nouveau témoin de l'évolution métamorphique BP-HT post-orogénique hercynienne: l'unité de Peyre-Arguet (Haut-Dauphiné): A new record of the LP-HT late-Variscan metamorphism: the Peyre-Arguet unit (Haut-Dauphiné), *Comptes Rendus de l'Academie de Sciences - Serie IIa: Sciences de la Terre et des Planetes*, *322*(3), 189–195.

Green, H. W., W.-P. Chen, and M. R. Brudzinski (2010), Seismic evidence of negligible water carried below 400-km depth in subducting lithosphere., *Nature*, *467*(7317), 828–831, doi:10.1038/nature09401.

Guillot, S., and R. P. Ménot (1999), Nappe stacking and first evidence of Late Variscan extension in the Belledonne Massif (External Crystalline Massifs, French Alps), *Geodinamica Acta*, *12*(2), 97–111, doi:10.1016/S0985-3111(99)80026-6.

Guillot, S., and R.-P. Ménot (2009), Paleozoic evolution of the External Crystalline Massifs of the Western Alps, *Comptes Rendus - Geoscience*, *341*(2-3), 253–265, doi:10.1016/j.crte.2008.11.010.

Guillot, S., R. P. Menot, and A. Fernandez (1998), Paleozoic evolution of the external crystalline massifs along the Belledonne-Oisans transect (Western Alps), *Acta Universitatis Carolinae Geologica*, *42*, 257–258.

Guillot, S., S. di Paola, R.-P. Menot, P. Ledru, M. I. Spalla, G. Gosso, and S. Schwartz (2009a), Suture zones and importance of strike-slip faulting for Variscan geodynamic reconstructions of the External Crystalline Massifs of the western Alps, *Bulletin de la Societe Geologique de France*, *180*(6), 483–500, doi:10.2113/gssgfbull.180.6.483.

Guillot, S., K. Hattori, P. Agard, S. Schwartz, and O. Vidal (2009b), Exhumation Processes in Oceanic and Continental Subduction Contexts: A Review, in *Subduction Zone Dynamics*, edited by S. Lallemand and F. Funiciello, pp. 175–204, Springer-Verlag Berlin Heidelberg, doi:10.1007/978-3-540-87974-9.

Hacker, B. R. (2006), Pressures and temperatures of ultrahigh-pressure metamorphism: Implications for UHP tectonics and H2O in subducting slabs, *International Geology Review*, *48*(12), 1053–1066, doi:Doi10.2747/0020-6814.48.12.1053.

Haenel, R., L. Rybach, and L. Stegena (1988), *Handbook of Terrestrial Heat-Flow Density Determination*, Kluwer Academic Publishers.

Hauy, R.-J. (1822), *Traité de minéralogie*, second ed., 456 pp., Bachelier et Huzard, Paris.

Hauzenberger, C. A., W. Holler, and G. Hoinkes (1996), Transition from eclogite to amphibolite-faeies metamorphism in the Austroalpine Ulten Zone, *Mineralogy and Petrology*, *58*, 111–130.

Hebert, L. B., P. Antoshechkina, P. Asimow, and M. Gurnis (2009), Emergence of a low-viscosity channel in subduction zones through the coupling of mantle flow and thermodynamics, *Earth and Planetary Science Letters*, *278*(3-4), 243–256, doi:10.1016/j.epsl.2008.12.013.

Henk, A., L. Franz, S. Teufel, and O. Oncken (1997), Magmatic Underplating, Extension, and Crustal Reequilibration: Insights from a Cross-Section through the Ivrea Zone and Strona-Ceneri Zone, Northern Italy, *The Journal of Geology*, *105*(3), 367–377.

Herzberg, C., L. Riccio, A. Chiesa, A. Fornoni, G. O. Gatto, A. Gregnanin, E. M. Piccirillo, and A. Scolari (1977), Petrogenetic evolution of a spinelgarnet-lherzolite in the austridic crystalline basement from Val Clapa (Alto Adige, northeastern Italy), *Memorie degli Istituti di Geologia e Mineralogia dell'Università di Padova*, *XXX*, 6–23.

Heuret, A., and S. Lallemand (2005), Plate motions, slab dynamics and back-arc deformation, *Physics of the Earth and Planetary Interiors*, *149*, 31–51, doi:10.1016/j.pepi.2004.08.022.

Hirth, G., and S. Guillot (2013), Rheology and tectonic significance of serpentinite, *Elements*, *9*(2), 107–113, doi:10.2113/gselements.9.2.107.

Hirth, G., and D. Kohlstedt (2003), Rheology of the upper mantle and the mantle wedge: A view from the experimentalists, *Geophysical Monograph Series*, *138*, 83–105, doi:10.1029/138GM06.

Hofmann, A. W. (1997), Mantle geochemistry: the message from oceanic volcanism, *Nature*, *385*(6613), 219–229, doi:10.1038/385219a0.

Honda, S., and M. Saito (2003), Small-scale convection under the back arc occurring in the low viscosity wedge, *Earth and Planetary Science Letters*, *216*, 703–715, doi:10.1016/S0012-821X(03)00537-5.

Jarrard, R. D. (1986), Relations Among Subduction Parameters, *Review of Geophysics*, *24*(2), 217–284.

Kirby, S. (1983), Rheology of the Lithosphere, *Reviews of Geophysics and Space Physics*, *21*(6), 1459–1487, doi:10.1029/RG021i006p01458.

Konzett, J., C. Miller, R. Armstrong, and M. Thöni (2005), Metamorphic evolution of iron-rich mafic cumulates from the Ötztal-Stubai crystalline complex, Eastern Alps, Austria, *Journal of Petrology*, *46*(4), 717–747, doi:10.1093/petrology/egh095.

Kornprobst, J. (2002), *Metamorphic Rocks and Their Geodynamic Significance. A Petrological Handbook. Petrology and Structural Geology Series*, Kluwer Academic Publishers.

Lafon, J.-M. (1986), Géochronologie U-Pb appliquée à deux segments du Massif central français : Le Rouergue oriental et le Limousin central, Ph.D. thesis, Université Montpellier.

Lallemand, S. (1999), *La subduction ocèanic*, Gordon and Breach Science Publishers.

Lallemand, S., A. Heuret, and D. Boutelier (2005), On the relationships between slab dip, back-arc stress, upper plate absolute motion, and crustal nature in subduction zones, *Geochemistry Geophysics Geosystems*, *6*(9), 1–18, doi:10.1029/2005GC000917.

Lardeaux, J.-M. (2014a), Deciphering orogeny: a metamorphic perspective Examples from European Alpine and Variscan belts - Part II: Variscan metamorphism in the French Massif Central - A review, *Bulletin de la Societe Geologique de France*, *185*(5), 281–310.

Lardeaux, J.-M. (2014b), Deciphering orogeny: a metamorphic perspective. Examples from European Alpine and Variscan belts - Part I: Alpine metamorphism in the western Alps. A review, *Bulletin de la Societe Geologique de France*, *185*(2), 93–114.

Lardeaux, J.-M., and E. Dufour (1987), Champs de déformation superposés dans la chaine varisque. Exemple de la zone nord des Monts du Lyonnais (Massif Central francais), *Compte Rendu Academie des Sciences de Paris*, *305*(2), 61–64.

Lardeaux, J.-M., B. Reynard, and E. Dufour (1989), Granulites à kornérupine ert décompression post-orogénique des Monts du Lyonnais (M.C.F.), *Compte Rendu Academie des Sciences de Paris*, *308*(2), 1443–1449.

Lardeaux, J. M., et al. (2014), The Moldanubian Zone in the French Massif Central, Vosges/Schwarzwald and Bohemian Massif revisited: differences and similarities, *Geological Society, London, Special Publications*, *405*(1), 7–44, doi:10.1144/SP405.14.

Lardeaux, J. M. J., P. Ledru, I. Daniel, and S. Duchene (2001), The Variscan French Massif Central—a new addition to the ultra-high pressure metamorphic 'club': exhumation processes and geodynamic consequences, *Tectonophysics*, *332*(1-2), 143–167, doi:10.1016/S0040-1951(00)00253-5.

Latouche, L., and S. Bogdanoff (1987), Évolution précoce du massif de l'Argentera: apport des éclogites et des granulites, *Géologie alpine*, *63*, 151–164.

Le Bayon, B., P. Pitra, M. Ballevre, and M. Bohn (2006), Reconstructing P-T paths during continental collision using multi-stage garnet (Gran Paradiso nappe, Western Alps), *Journal of Metamorphic Geology*, *24*(6), 477–496, doi:10.1111/j.1525-1314.2006.00649.x.

Le Fort, P. (1973), Geologie du Haut-Dauphine cristallin (Alpes Francaise): Etudes petrologique et structurale de la partie occidentale., Ph.D. thesis, Université Nancy.

Le Voci, G., D. R. Davies, S. Goes, S. C. Kramer, and C. R. Wilson (2014), A systematic 2-D investigation into the mantle wedge's transient flow regime and thermal structure: Complexities arising from a hydrated rheology and thermal buoyancy, *Geochemistry, Geophysics, Geosystems*, *15*(1), 28–51, doi:10.1002/2013GC005022.

Ledru, P., et al. (1989), Où sont les nappes dans le Massif central francais?, *Bulletin de la Societe Geologique de France*, *8*(3), 605–618.

Ledru, P., G. Courrioux, C. Dallain, J. M. Lardeaux, J. M. Montel, O. Vanderhaeghe, and G. Vitel (2001), The Velay dome (French Massif Central): Melt generation and granite emplacement during orogenic evolution, *Tectonophysics*, *342*(3-4), 207–237, doi:10.1016/S0040-1951(01)00165-2.

Li, X.-H., M. Faure, P. Rossi, W. Lin, and D. Lahondère (2015), Age of Alpine Corsica ophiolites revisited: Insights from in situ zircon U–Pb age and O–Hf isotopes, *Lithos*, *220–223*(0), 179–190, doi:http://dx.doi.org/10.1016/j.lithos.2015.02.006.

Liati, A., D. Gebauer, and C. Fanning (2009), Geochronological evolution of HP metamorphic rocks of the Adula nappe, Central Alps, in pre-Alpine and Alpine subduction cycles, *Journal of the Geological Society*, *166*, 797–810, doi:10.1144/0016-76492008-033. Geochronological.

Liégeois, J. P., and J. C. Duchesne (1981), The Lac Cornu retrograded eclogites (Aiguilles Rouges massif, Western Alps, France): evidence of crustal origin and metasomatic alteration, *Lithos*, *14*(1), 35–48, doi:10.1016/0024-4937(81)90035-9.

Liu, L., J. Zhang, H. W. Green, Z. Jin, and K. N. Bozhilov (2007), Evidence of former stishovite in metamorphosed sediments, implying subduction to >350 km, *Earth and Planetary Science Letters*, *263*(3-4), 180–191, doi:10.1016/j.epsl.2007.08.010.

Maggetti, M., and M. Flisch (1993), Evolution of the SiIvretta Nappe, in *Pre-Mesozoic Geology in the Alps*, pp. 469–484.

Maggetti, M., and G. Galetti (1988), Evolution of the Silvretta eclogites: metamorphic and magmatic events, *Schweiz. Mineral. Petrogr. Mitt.*, *68*, 467–484.

Maino, M., G. Dallagiovanna, L. Gaggero, S. Seno, and M. Tiepolo (2012), U-Pb zircon geochronological and petrographic constraints on late to post-collisional Variscan magmatism and metamorphism in the Ligurian Alps, Italy, *Geological Journal*, *47*(6), 632–652, doi:10.1002/gj.2421.

Malavieille, J. (2010), Impact of erosion, sedimentation, and structural heritage on the structure and kinematics of orogenic wedges: Analog models and case studies, *GSA Today*, *20*(1), 4–10, doi:10.1130/GSATG48A.1.

Malavieille, J., S. Guillot, P. Costa, J. M. Lardeaux, and V. Gardien (1990), Collapse of the thickened Variscan crust in the French Massif Central: Mont Pilat extensional shear zone and St. Etienne Late Carboniferous basin, *Tectonophysics*, *177*(1-3), 139–149, doi:10.1016/0040-1951(90)90278-G.

Manzotti, P., and M. Zucali (2013), The pre-Alpine tectonic history of the Austroalpine continental basement in the Valpelline unit (Western Italian Alps), *Geological Magazine*, *150*(1), 153–172, doi:10.1017/S0016756812000441.

Marotta, A. M., and M. I. Spalla (2007), Permian-Triassic high thermal regime in the Alps: Result of late Variscan collapse or continental rifting? Validation by numerical modeling, *Tectonics*, *26*, 1–27, doi:10.1029/2006TC002047.

Marotta, A. M., E. Spelta, and C. Rizzetto (2006), Gravity signature of crustal subduction inferred from numerical modelling, *Geophysical Journal International*, *166*, 923–938, doi:10.1111/j.1365-246X.2006.03058.x.

Marshall, D., D. Kirschner, and F. Bussy (1997), A Variscan pressure-temperature-time path for the N-E Mont Blanc massif, *Contributions to Mineralogy and Petrology*, *126*(4), 416–428, doi:10.1007/s004100050260.

Matte, P. (2001), The Variscan collage and orogeny (480-290 Ma) and the tectonic definition of the Armorica microplate: A review, *Terra Nova*, *13*(2), 122–128, doi:10.1046/j.1365-3121.2001.00327.x.

Meda, M., A. M. Marotta, and M. I. Spalla (2010), The role of mantle hydration into the continental crust recycling in the wedge region, *Geological Society, London, Special Publications*, *332*(1), 149–172, doi:10.1144/sp332.10.

Melcher, F., T. Meisel, J. Puhl, and F. Koller (2002), Petrogenesis and geotectonic setting of ultramafic rocks in the Eastern Alps: constraints from geochemistry, *Lithos*, *65*(1-2), 69–112, doi:10.1016/S0024-4937(02)00161-5.

Menot, R.-P. (1988), The geology of the Belledonne massif : an overview (external crystalline massifs of the Western Alps), *Schweizerische Mineralogische Und Petrographische Mitteilungen*, *68*, 531–542.

Ménot, R.-P., M. Bonhommem, and G. Vivier (1987), Structuration tecto-métamorphique carbonifère dans le massif de Belledonne (Alpes occidentales françaises). Apport de la geochronologie K/Ar des amphiboles, *Schweizerische mineralogische und petrographische Mitteilungen*, *67*, 273–284.

Mercier, L., V. Johan, J.-M. Lardeaux, and P. Ledru (1989), Découverte d'éclogites dans l'artense (M.C.F.) Implications pour la définition des nappes à l'Est du Sillon Houiller, *Compte Rendu Academie des Sciences de Paris*, *308*(2), 315–320.

Mercier, L., H. L. M. van Roermund, and J. M. Lardeaux (1991a), Comparison of PTt paths in allochthonous high pressure metamorphic terrains from the Scandinavian Caledonides and the French Massif Central: Contrasted thermal structures during uplift, *Geologische Rundschau*, *80*(2), 333–348, doi:10.1007/BF01829370.

Mercier, L., J.-M. Lardeaux, and P. Davy (1991b), On the tectonic significance of retrograde P-T-t paths in eclogites of the French Massif Central, *Tectonics*, *10*(1), 131–140, doi:10.1029/90TC02094.

Mercier, L., V. Johan, J.-M. Lardeaux, and P. Ledru (1992), Evolutions tectono-métamorphiques des nappes de l'Aretense (Massif central francais): nouveaux marquers de la collision dans la chaine varisque, *Bulletin de la Societe Géologique de France*, *163*(3), 293–308.

Messiga, B., R. Tribuzio, and F. Caucia (1992), Amphibole evolution in Variscan eclogite-amphibolites from the Savona crystalline massif (Western Ligurian Alps, Italy): controls on the decompressional PTt path, *Lithos*, *27*, 215–230.

Milano, P. F., G. Pennacchioni, and M. I. Spalla (1988), Alpine and pre-Alpine tectonics in the Central Orobic Alps (Southern Alps), *Eclogae Geologicae Helvetiae*, *81*, 273–293.

Miller, C., and M. Thöni (1995), Origin of eclogites from the Austroalpine Ötztal basement (Tirol, Austria): geochemistry and Sm–Nd vs. Rb–Sr isotope systematics, *Chemical Geology*, *122*, 199–225.

Miyashiro, A. (1961), Evolution of metamorphic belts, *Journal of Petrology*, *2*, 277–311.

Miyashiro, A. (1973), Paired and unpaired metamorphic belts, *Tectonophysics*, *17*, 241–254.

Monie, P. (1990), Preservation of Hercynian 40Ar/39Ar ages through high-pressure low-temperature Alpine metamorphism in the Western Alps, *European Journal of Mineralogy*, *2*(3), 343–361, doi:10.1127/ejm/2/3/0343.

Morten, L., P. Nimis, and E. Rampone (2004), Records of mantle–crust exchange processes during continental subduction–exhumation in the Nonsberg-Ultental garnet peridotites (eastern Alps). A review, *Periodico di Mineralogia*, *73*, 119–129.

Mottana, A., M. Nicoletti, C. Petrucciani, G. Liborio, L. De Capitani, and R. Bocchio (1985), Pre-alpine and alpine evolution of the South-alpine basement of the Orobic Alps, *Geologische Rundschau*, *74*(2), 353–366, doi:10.1007/BF01824902.

Nagaya, T., A. M. Walker, J. Wookey, S. R. Wallis, K. Ishii, and J. M. Kendall (2016), Seismic evidence for flow in the hydrated mantle wedge of the Ryukyu subduction zone, *Scientific Reports*, *6*(29981), 29,981, doi:10.1038/srep29981.

Neubauer, F. (1988), The Variscan orogeny in the Austroalpine and Southalpine domains of the Eastern Alps, *Schweizerische Mineralogische Und Petrographische Mitteilungen*, *68*, 339–349.

Nicollet, C. (2010), *Métamorphisme et géodynamique*, 304 pp., Dunod.

Nussbaum, C., D. Marquer, and G. G. Biino (1998), Two subduction events in a polycyclic basement: Alpine and pre-Alpine high-pressure metamorphism in the Suretta nappe, Swiss Eastern Alps, *Journal of Metamorphic Geology*, *16*(591-605).

O'Brien, P. J., and J. Rötzler (2003), High-pressure granulites: Formation, recovery of peak conditions and implications for tectonics, *Journal of Metamorphic Geology*, *21*(1), 3–20, doi:10.1046/j.1525-1314.2003.00420.x.

Paquette, J. L., R. P. Menot, and J. J. Peucat (1989), REE, SmNd and UPb zircon study of eclogites from the Alpine External Massifs (Western Alps): evidence for crustal contamination, *Earth and Planetary Science Letters*, *96*(1-2), 181–198, doi:10.1016/0012-821X(89)90131-3.

Paquette, J. L., P. Monchoux, and M. Couturier (1995), Geochemical and isotopic study of a norite-eclogite transition in the European Variscan belt: Implications for UPb zircon systematics in metabasic rocks, *Geochimica et Cosmochimica Acta*, *59*(8), 1611–1622, doi: 10.1016/0016-7037(95)00067-A.

Peacock, S. M. (1990), Fluid processes in subduction zones, *Science*, *248*, 329–337.

Pérez-Gussinyé, M., T. J. Reston, and J. Phipps Morgan (2001), Serpentinization and magmatism during extension at non-volcanic margins: the effect of initial lithospheric structure, *Geological Society, London, Special Publications*, *187*(1), 551–576, doi: 10.1144/GSL.SP.2001.187.01.27.

Pickering, K. T. (1989), The destruction of Iapetus and Tornquist ' s Oceans, *Geology Today*, *5*(5), 160–166.

Pigazzini, N. (2003), Analisi meso e microstrutturale delle metapeliti a cloritoide, staurolite e andalusite nel basamento sudalpino della val camonica tra sellero e forno d'allione, Ph.D. thesis, Università degli Studi di Milano.

Pin, C., and J. Lancelot (1982), U-Pb dating of an early paleozoic bimodal magmatism in the french Massif Central and of its further metamorphic evolution, *Contributions to Mineralogy and Petrology*, *79*(1), 1–12, doi:10.1007/BF00376956.

Pin, C., and J. J. Peucat (1986), Agés des épisode de métamorphisme paléozoique dans le Massif central et le Massif armorican, *Bulletin de la Societe Géologique de France*, *8*(3), 461–469.

Pin, C., and J. D. Sills (1986), Petrogenesis of layered gabbros and ultramafic rocks from Val Sesia, the Ivrea Zone, NW Italy: trace element and isotope geochemistry, *Geological Society, London, Special Publications*, *24*(1), 231–249, doi:10.1144/GSL.SP.1986.024.01.21.

Polino, R., G. V. Dal Piaz, and G. Gosso (1990), Tectonic erosion at the Adria margin and accretionary processes for the Cretaceous orogeny of the Alps ., *Mémoires de la Societé Géologique de France*, *156*, 345–367.

Quinquis, M. E. T., and S. J. H. Buiter (2014), Testing the effects of basic numerical implementations of water migration on models of subduction dynamics, *Solid Earth*, *5*(1), 537–555, doi:10.5194/se-5-537-2014.

Ranalli, G., and D. C. Murphy (1987), Rheological stratification of the Lithosphere, *Tectonophysics*, *132*(4), 281–295, doi:10.1016/0040-1951(87)90348-9.

Riklin, K. (1983), Kontaktmetamorphose permischer Sandsteine im Adamello-Massiv, Ph.D. thesis.

Roda, M., A. M. Marotta, and M. I. Spalla (2010a), Influence of the thermal state of the overriding plate on the slab dip, *Rend. online Soc. Geol. It.*, *10*, 96–99.

Roda, M., A. M. Marotta, and M. I. Spalla (2010b), Numerical simulations of an ocean-continent convergent system: Influence of subduction geometry and mantle wedge hydration on crustal recycling, *Geochemistry Geophysics Geosystems*, *11*(5), 1–21, doi:10.1029/2009GC003015.

Roda, M., A. M. Marotta, and M. I. Spalla (2011), The effects of the overriding plate thermal state on the slab dip in an ocean-continent subduction system, *Compte Rendu Academie des Sciences Paris*, *343*(5), 323–330, doi:10.1016/j.crte.2011.01.005.

Roda, M., M. I. Spalla, and A. M. Marotta (2012), Integration of natural data within a numerical model of ablative subduction: a possible interpretation for the Alpine dynamics of the Austroalpine crust, *Journal of Metamorphic Geology*, *30*(9), 973–996, doi:10.1111/jmg.12000.

Rode, S., D. Rosel, and B. Schulz (2012), Constraints on the Variscan P-T evolution by EMP Th-U-Pb monazite dating in the polymetamorphic Austroalpine Oetzal-Stubai basement (Eastern Alps), *Z. dt. Ges. Geowiss.*, *163*(1), 43–68, doi:10.1127/1860-1804/2012/0163-0043.

Rondenay, S., G. A. Abers, and P. E. V. Keken (2008), Seismic imaging of subduction zone metamorphism, *Geology*, *36*(4), 275–278, doi:10.1130/G24112A.1.

Rubatto, D., U. Schaltegger, B. Lombardo, F. Colombo, and R. Compagnoni (2001), Complex Paleozoic magmatic and metamorphic evolution in the Argentera massif (Western Alps), resolved with U-Pb dating, *Schweiz. Mineral. Petrogr. Mitt.*, *81*, 213–228.

Rubatto, D., S. Ferrando, R. Compagnoni, and B. Lombardo (2010), Carboniferous high-pressure metamorphism of Ordovician protoliths in the Argentera Massif (Italy), Southern European Variscan belt, *Lithos*, *116*(1-2), 65–76, doi:10.1016/j.lithos.2009.12.013.

Ruh, J. B. (2016), Submarine landslides caused by seamounts entering accretionary wedge systems, doi:10.1111/ter.12204.

Rupke, L. H., J. Phipps Morgan, M. Hort, and J. A. D. Connolly (2004), Serpentine and the subduction zone water cycle, *Earth and Planetary Science Letters*, *223*(1-2), 17–34, doi:10.1016/j.epsl.2004.04.018.

Rüpke, L. H., D. W. Schmid, M. Perez-Gussinye, and E. Hartz (2013), Interrelation between rifting, faulting, sedimentation, and mantle serpentinization during continental margin formation - Including examples from the Norwegian Sea, *Geochemistry, Geophysics, Geosystems*, *14*(10), 4351–4369, doi:10.1002/ggge.20268.

Sassi, R., C. Mazzoli, C. Miller, and J. Konzett (2004), Geochemistry and metamorphic evolution of the Pohorje Mountain eclogites from the easternmost Austroalpine basement of the Eastern Alps (Northern Slovenia), *Lithos*, *78*(3), 235–261, doi:10.1016/j.lithos.2004.05.002.

Scambelluri, M., E. Rampone, R. Braga, and N. Malaspina (2010), The Variscan garnet peridotites from the Eastern Alps (Ulten Zone): records of subduction metasomatism in the mantle wedge, *Journal of the Virtual Explorer, Electronic Edition*, *36*(4), doi:10.3809/jvirtex.2010.00259.

Schaltegger, U. (1994), Unravelling the pre-Mesozoic history of Aar and Gotthard massifs (Central Alps) by isotopic dating : a review, *Schweizerische Mineralogische Und Petrographische Mitteilungen*, *74*, 41–51.

Schellart, W. P., J. Freeman, D. R. Stegman, L. Moresi, and D. May (2007), Evolution and diversity of subduction zones controlled by slab width, *Nature*, *446*, 308–311, doi:10.1038/nature05615.

Schmidt, M. W., and S. Poli (1998), Experimentally based water budgets for dehydrating slabs and consequences for arc magma generation, *Earth and Planetary Science Letters*, *163*, 361–379, doi:10.1016/S0012-821X(98)00142-3.

Schulmann, K., J. Konopásek, V. Janoušek, O. Lexa, J.-M. Lardeaux, J.-B. Edel, P. Štípská, and S. Ulrich (2009), An Andean type Palaeozoic convergence in the Bohemian Massif, *Comptes Rendus Geoscience*, *341*(2-3), 266–286, doi:10.1016/j.crte.2008.12.006.

Schulz, B., and J. F. von Raumer (2011), Discovery of Ordovician-Silurian metamorphic monazite in garnet metapelites of the Alpine External Aiguilles Rouges Massif, *Swiss Journal of Geosciences*, *104*(1), 67–79, doi:10.1007/s00015-010-0048-7.

Schweinehage, R., and H. Massonne (1999), Geochemistry and metamorphic evolution of metabasites from the Silvretta nappe, Eastern Alps, *Memorie Scienze Geologiche*, *51*(1), 191–203.

Siletto, G. B., M. I. Spalla, A. Tunesi, J.-M. Lardeaux, and A. Colombo (1993), Pre-Alpine Structural and Metamorphic Histories in the Orobic Southern Alps, Italy, in *Pre-Mesozoic Geology in the Alps*, pp. 585–598.

Smith, D. C. (1984), Coesite in clinopyroxene in the Caledonides and its implication for geodynamics, *Nature*, *310*, 641–644.

Sobolev, N. V., and V. S. Shatsky (1990), Diamond inclusions in garnets from meta- morphic rocks, *Nature*, *343*, 742–746.

Spalla, M., V. Diella, N. Pigazzini, G. Siletto, and G. Gosso (2006), Significato tettonico della transizione Cld—And nelle metapeliti del Basamento Sudalpino (Alta Val Camonica), *Rend Soc Geol It*, *2*, 182–183.

Spalla, M. I., and G. Gosso (1999), Pre-Alpine tectonometamorphic units in the central southern Alps; structural and metamorphic memory, *3rd workshop on Alpine geological studies.*, (51; 1), 221–229.

Spalla, M. I., J.-M. Lardeaux, G. V. Dal Piaz, G. Gosso, and B. Messiga (1996), Tectonic significance of Alpine eclogites, *Journal of Geodynamics*, *21*(3), 257–285, doi:10.1016/0264-3707(95)00033-X.

Spalla, M. I., D. Zanoni, G. Gosso, and M. Zucali (2009), Deciphering the geologic memory of a Permian conglomerate of the Southern Alps by pebble P-T estimates, *International Journal of Earth Sciences*, *98*(1), 203–226, doi:10.1007/s00531-007-0241-8.

Spalla, M. I., D. Zanoni, A. M. Marotta, G. Rebay, M. Roda, M. Zucali, and G. Gosso (2014), The transition from Variscan collision to continental break-up in the Alps: advice from the comparison between natural data and numerical model predictions, *Geological Society, London, Special Publications*, *405*(1), 363–400, doi:10.1144/SP405.11.

Spalla, M. I. M., E. Carminati, S. Ceriani, A. Oliva, and D. Battaglia (1999), Influence of deformation partitioning and metamorphic re-equilibration on P-T path reconstruction in the pre-Alpine basement of central Southern Alps (Northern Italy), *Journal of Metamorphic Geology*, *17*(3), 319–336, doi:10.1046/j.1525-1314.1999.00199.x.

Spear, F. S. (1993), *Metamorphic phase equilibria and Pressure-Temperature-time paths*, 799 pp., Min. Soc. Am. monograph., Washington.

Spiess, R., B. Cesare, C. Mazzoli, R. &. Sassi, and F. P. Sassi (2010), The crystalline basement of the Adria microplate in the eastern Alps: a review of the palaeos- tructural evolution from the Neoproterozoic to the Cenozoic, *Rendiconti Lincei Scienze Fisiche Naturali*, *21*, 31–50.

Stampfli, G. M. (2002), Paleozoic evolution of pre-Variscan terranes: From Gondwana to the Variscan collision, *364*, 263–280.

Stern, R. J. (2002), Subduction zones, *Reviews of Geophysics*, *40*(December), 1031–1039.

Stöckhert, B., and T. V. Gerya (2005), Pre-collisional high pressure metamorphism and nappe tectonics at active continental margins: A numerical simulation, *Terra Nova*, *17*(2), 102–110, doi:10.1111/j.1365-3121.2004.00589.x.

Tait, J. A., V. Bachtadse, W. Franke, and H. C. Soffel (1997), Geodynamic evolution of the Euroepan fold belt: paleomagnetic and geological constraints, *Geologische Rundschau*, *86*, 585–598.

Tao, W., and R. O'Connell (1992), Ablative Subduction: A Two-Sided Alternative to the Conventional Subduction Model, *Journal of Geophysical Research*, *97*(B6), 8877–8904.

Thélin, P., M. Sartori, R. Lengeler, and J. Schaerer (1990), Eclogites of Paleozoic or early Alpine age in the basement of the Penninic Siviez-Mischabel nappe, Wallis, Switzerland, *Lithos*, *25*, 71–88.

Thélin, P., M. Sartori, M. Burri, Y. Gouffon, and R. Chessex (1993), The pre-Alpine basement of the briançonnais (Wallis, Switzerland), in *Pre-Mesozoic Geology in the Alps*, pp. 297–315.

Thieulot, C. (2014), ELEFANT: a user-friendly multipurpose geodynamics code., *Solid Earth Discussions*, *6*(2), 1949–2096, doi:10.5194/sed-6-1949-2014.

Thoeni, M. (1981), degree and evolution of the alpine metamorphism in the austroalpine unit west of the hohe tauern in the light of K/Ar and Rb/Sr age determinations on micas, *Jahrbuch der Geologischen Bundesanstalt*, *124*, 111–174.

Thoeni, M. (2002), Sm–Nd isotope systematics in garnet from different lithologies (Eastern Alps): age results, and an evaluation of potential problems for garnet Sm–Nd chronometry, *Chemical Geology*, *185*, 255–281.

Thompson, A. B., and P. C. England (1984), Pressure–Temperature–Time Paths of Regional Metamorphism II. Their Inference and Interpretation using Mineral Assemblages in Metamorphic Rocks, *Journal of Petrology*, *25*(4), 929–955, doi:10.1093/petrology/25.4.929.

Thompson, A. B. A. A. B. (1981), The pressure-temperature (P, T) plane viewed by geophysicists and petrologists, *Terra Cognita*, *1*, 11–20.

Torsvik, T. H. (1998), Palaeozoic palaeogeography: A North Atlantic viewpoint, *Gff*, *120*(2), 109–118, doi:10.1080/11035899801202109.

Trench, A., and T. H. Torsvik (1991), A revised Palaeozoic apparent polar wander path for Southern Britain (Eastern Avalonia), *Geophysical Journal International*, *104*, 227–233.

Tumiati, S., M. Thöni, P. Nimis, S. Martin, and V. Mair (2003), Mantle-crust interactions during Variscan subduction in the Eastern Alps (Nonsberg-Ulten zone): Geochronology and new petrological constraints, *Earth and Planetary Science Letters*, *210*(3-4), 509–526, doi:10.1016/S0012-821X(03)00161-4.

Turcotte, D. L., and G. Schubert (2002), *Geodynamics*, 2nd ed., Cambridge University Press, New York.

Uyeda, S. (1987), Chilean vs Mariana type subduction zones with remarks on arc-volcanism and collision tectonics, *Geological Society of America*, *18*, 1–7.

Uyeda, S., and H. Kanamori (1979), Back-arc opening and the model of subduction, *J. Geophys. Res.*, *84*(8), 1049–1061, doi:10.1029/JB084iB03p01049.

van Keken, P. E., S. D. King, H. Schmeling, U. R. Christensen, D. Neumeister, and M.-P. Doin (1997), A comparison of methods for the modeling of thermochemical convection, *Journal of Geophysical Research*, *102*(B10), 22,477, doi:10.1029/97JB01353.

Vavra, G., R. Schmid, and D. Gebauer (1999), Internal morphology, habit and U-Th-Pb microanalysis of amphibolite-to-granulite facies zircons: geochronology of the Ivrea Zone (Southern Alps), *Contributions to Mineralogy and Petrology*, *134*(4), 380–404, doi: 10.1007/s004100050492.

Von Huene, R., and S. Lallemand (1990), Tectonic erosion along the Japan and Peru convergent margins, *Bulletin of the Geological Society of America*, *102*(6), 704–720, doi: 10.1130/0016-7606(1990)102<0704:TEATJA>2.3.CO;2.

von Quadt, A., D. Guenther, R. Frischknecht, R. Zimmermann, and G. Franz (1997), The evolution of pre-Variscan ecloogites of the Tauern Window (Eastern Alps) : a Sm / Nd- , conventional and Laser ICP-MS zircon U-Pb study, *Schweizerische Mineralogische und Petrographische Mitteilungen*, *77*, 265–279.

von Raumer, J., J. Abrecht, F. Bussy, B. Lombardo, R. P. Menot, and U. Schaltegger (1999), The Palaeozoic metamorphic evolution of the Alpine External Massifs, *Schweizerische Mineralogische und Petrographische Mitteilungen*, *79*(1), 5–22.

von Raumer, J. F. (1998), The Palaeozoic evolution in the Alps: From Gondwana to Pangea, *Geologische Rundschau*, *87*(3), 407–435, doi:10.1007/s005310050219.

von Raumer, J. F., R.-P. Menot, J. Abrecht, and G. Biino (1993), The Pre-Alpine Evolution of the External Massifs, in *Pre-Mesozoic Geology in the Alps*, pp. 221–240.

von Raumer, J. F., G. M. Stampfli, and F. Bussy (2003), Gondwana-derived microcontinents — the constituents of the Variscan and Alpine collisional orogens, *Tectonophysics*, *365*(1-4), 7–22, doi:10.1016/S0040-1951(03)00015-5.

von Raumer, J. F., F. Bussy, U. Schaltegger, B. Schulz, and G. M. Stampfli (2013), Pre-Mesozoic Alpine basements—Their place in the European Paleozoic framework, *Geological Society of America Bulletin*, *125*(1-2), 89–108, doi:10.1130/B30654.1.

Yamato, P., P. Agard, E. Burov, L. Pourhiet, L. Jolivet, and C. Tiberi (2007), Burial and exhumation in a subduction wedge: Mutual constraints from thermomechanical modeling and natural P-T-t data (Schistes Lustrés, western Alps), *Journal of Geophysical Research*, *112*, 1–28, doi:10.1029/2006JB004441.

Zalesak, S. (1979), Fully multidimensional flux-corrected transport algorithms for fluids, *Journal of computational physics*, *31*, 335–362.

Zanoni, D., M. I. Spalla, and G. Gosso (2010), Vestiges of lost tectonic units in conglomerate pebbles? A test in Permian sequences of the Southalpine Orobic Alps, *Geological Magazine*, *147*(01), 98–122, doi:10.1017/S0016756809990252.

Zienkiewicz, O. C., and R. L. Taylor (2000), *The Finite Element Method Volume 1 : The Basis*, vol. 1, 708 pp.

Zimmermann, V. R., and G. Franz (1989), Die Eklogite der Unteren Schieferhülle; Frosnitztal/Südvenediger (Tauern, Österreich), *Mittelungen der Östereichischen Geologischen Gesellschaft*, *81*(1988), 167–188.

Zucali, M. (2001), La correlazione nei terreni metamor- fici: due esempi dall'Austroalpino occidentale (Zona Sesia-Lanzo) e centrale (Falda Languard-Campo/ Serie del Tonale), Ph.D. thesis, Università degli Studi di Milano.

Zucali, M., and M. I. Spalla (2011), Prograde lawsonite during the flow of continental crust in the Alpine subduction: Strain vs. metamorphism partitioning, a field-analysis approach to infer tectonometamorphic evolutions (Sesia-Lanzo Zone, Western Italian Alps), *Journal of Structural Geology*, *33*(3), 381–398, doi:10.1016/j.jsg.2010.12.006.

Zucali, M., M. I. Spalla, G. Gosso, S. Racchetti, and F. Zulbati (2004), Prograde LWS-KY Transition During Subduction Of The Alpine Continental Crust Of The Sesia- Lanzo Zone: The Ivozio Complex, *Journal of the Virtual Explorer, Electronic Edition*, *16*(4), 1–21.

Zucali, M., P. Manzotti, V. Diella, C. Pesenti, A. Risplendente, J. Darling, and M. Engi (2011), Permian tectonometamorphic evolution of the Dent-Blanche Unit (Austroalpine domain, Western Italian Alps), *Rendiconti Online Società Geologica Italiana*, *15*, 133–136.